TUDelft

Delft University of Technology

Optimizing hydrographic operations for bathymetric measurements using multibeam echosounders

Mohammadloo, Tannaz H.

DOI
10.4233/uuid:a1bb9cd0-6eef-4665-a910-969d55667f35

Publication date
2020

Document Version
Final published version

Important note
To cite this publication, please use the final published version (if applicable).
Please check the document version above.

Optimizing hydrographic operations for bathymetric measurements using multibeam echosounders

Optimizing hydrographic operations for bathymetric measurements using multibeam echosounders

Dissertation

for the purpose of obtaining the degree of doctor
at Delft University of Technology,
by the authority of the Rector Magnificus Prof. dr. ir. T.H.J.J. van der Hagen,
chair of the Board for Doctorates,
to be defended publicly on
Tuesday 10 November 2020 at 15:00 o'clock

by

Tannaz HAJI MOHAMMADLOO

Master of Science in Geomatics Engineering: Geodesy,
University of Esfahan, Iran
born in Terhan, Iran.

The dissertation has been approved by the promoters.

Composition of the doctoral committee:

Rector Magnificus	chairman
Prof. dr. D. G. Simons	Delft University of Technology, promoter
Prof. dr. ir. M. Snellen	Delft University of Technology, promoter

Independent members:

Prof. dr. ir. G. Vosselman	University of Twente
Prof. dr. ir. P. J. M. Van Oosterom	Delft University of Technology
Prof. dr. L. L. A. Vermeersen	Delft University of Technology
Dr. ir. D. C. Slobbe	Delft University of Technology

Other member:

Dr. J. D. Beaudoin	QPS B.V., Canada

An electronic version of this dissertation is available at
`http://repository.tudelft.nl/`.

To my parents without whom
I would not be here today
and
to Alireza
who always stands by me

Contents

Summary

Detailed information about the sea and river bed is of high importance for a large number of applications, such as marine geology, coastal engineering, safe navigation and offshore construction. Acoustic remote sensing techniques have become extremely attractive for obtaining bathymetry measurements and for mapping the sediment properties, due to their high coverage capabilities and relatively low costs. Among the available tools for remotely mapping the seafloor, the MultiBeam EchoSounder (MBES) belongs to the state-of-the-art technology enabling acquisition of high resolution measurements of bathymetry within a relatively short time period.

Despite the widespread use of MBESs for hydrographic operations and the considerable efforts devoted to optimize these operations, the existing knowledge with regard to the measurement capabilities of the MBES is lacking in some respects. This can lead to an unreliable and inaccurate representation of the seafloor and/or unrealistic estimates of the measurement uncertainties. Moreover, realistic pre-survey predictions of the contribution of the various uncertainty sources affecting the quality of the bathymetric measurements is of importance to ensure sufficient accuracy of the soundings and a correct interpretation of the sediment properties. This thesis thus aims at bringing the insight of the MBES measurement capabilities to a new stage by addressing these issues.

An essential prerequisite for accurate depth measurements is the knowledge of the Sound Speed Profile (SSP). Lacking knowledge of the prevailing SSP leads to refraction artefacts (systematic errors in the derived bathymetry). In this thesis, a method for correcting the refraction artefacts is proposed by employing the redundancy in the MBES measurements obtained from the overlap of adjacent swaths. The application of the SSP inversion method to a data set with existing refraction artefacts showed a successful correction of the depth measurements. In addition, the developed inversion method has neither manipulated the existing morphology nor introduced artificial bathymetric features in areas which do not have refraction induced errors.

New generations of MBESs are able to transmit Frequency Modulated (FM) signals, in addition to the more standard Continuous Wave (CW) signals. The advantages of FM signals are an increase in the achievable swath width while maintaining high range resolution, yielding to enhanced processing capabilities and the possibility to increase the transmitted energy (without deteriorating the range resolution). Despite these advantages, the depth measurements acquired using FM pulses exhibit higher noise levels compared to those derived using CW pulses. In this thesis, the resulting bathymetric uncertainties due to the use of FM pulse have been investigated to evaluate the MBES system performance when using FM signals. There are two contributions to the uncertainties when switching from CW to FM, baseline

decorrelation and the Doppler effect. In this thesis, both of them have been accounted for in the MBES total vertical uncertainty prediction. Although taking the identified error sources into consideration results in a more realistic description of the bathymetric uncertainty as shown in this thesis, accounting for these considerations does require additional knowledge which might not be available prior to a hydrographic survey.

Furthermore, in this research the performance of the bathymetry uncertainty prediction model, as implemented in AMUST (*A priori* Multibeam Uncertainty Simulation Tool), is assessed for modern MBES systems by comparing the model predictions to measured bathymetric uncertainties acquired in different operational environments and for different MBES settings. Two factors are found of importance for a fair and realistic comparison between the measured and predicted bathymetric uncertainties, these are the size of the bottom surface patch and the number of phase samples per beam. If a too large surface patch is considered, the bottom morphology might change, and thus the variations of the bathymetric measurements within a patch do not solely correspond to the uncertainties inherent to the MBES. The optimal size of the surface patch is thus required. As for the number of phase samples, this parameter is used to calculate the contribution of the phase bottom detection method to the bathymetric uncertainty. For the data sets considered, discrepancies were observed between the theoretical and actual number of phase samples resulting in incorrect predictions of the bathymetric uncertainties in case of using the former. It has been found that while, in general, there is a good agreement between the predicted and the measured bathymetric uncertainties, modifications to the model are required for a better model-data agreement, particularly for the outer beam sector and deeper areas. Within this work, the baseline decorrelation, the Doppler effect and decreased signal-to-noise ratio for the outer parts of the swath are accounted for in the echosounder contribution and improvements are observed in capturing the variations of the bathymetric uncertainty with beam angle.

Finally, the last part of this thesis deals with processing and mapping the bathymetric data to a grid. The transformation of the bathymetric measurements to a grid has to be carried out in order to enable efficient data processing while still providing a true representation of the sea and river beds. To this end, different approaches for gridding are considered. For flat areas, the shallowest measured bathymetry is found to be highly influenced by measurement uncertainties, which can be counteracted when using the mean bathymetry. However, the this value underestimates the shallowest bathymetry for areas with slopes. As shown in this thesis, by subtracting the standard deviation of the measurements in a grid cell from the mean, the effect of slopes is accounted for while the influence of measurement uncertainties is decreased compared to the shallowest measured bathymetry.

In conclusion, the contribution of this thesis to the field of MBES bathymetric mapping is to bring the knowledge of the MBES measurements capabilities to a stage such that hydrographic operations are optimized. This leads to a reliable and accurate representation of the bottom and a realistic expectation of the associated uncertainties. Optimizing hydrographic operations is accomplished by correcting

the systematic errors (if present), using a realistic bathymetric uncertainty prediction model and addressing proper distribution of the soundings while ensuring low uncertainties of the measurement. These issues allow for realistic bathymetry maps and need to be accounted for in survey planning.

Samenvatting

Gedetailleerde informatie over zee en rivierbedding is van groot groot belang voor een groot aantal toepassingen, zoals geologische oceanografie, kustwaterbouw, veilige navigatie en offshore bouw. Akoestische teledetectietechnieken zijn uitermate aantrekkelijk geworden voor het verkrijgen van bathymetriemetingen en voor het in kaart brengen van de sedimenteigenschappen, vanwege hun hoge dekkingsvermogen en relatief lage kosten. Onder de beschikbare middelen voor het in kaart brengen van de zeebodem op afstand, behoort de MultiBeam EchoSounder (MBES) tot de state-of-the-art technologie die het mogelijk maakt om met hoge resolutie metingen van bathymetrie in relatief korte periode te doen.

Ondanks het wijdverbreide gebruik van MBES's voor hydrografische operaties en de aanzienlijke inspanningen die zijn geleverd om deze operaties te optimaliseren, ontbreekt de bestaande kennis met betrekking tot de meetcapaciteiten van de MBES in sommige opzichten. Dit kan leiden tot een onbetrouwbare en onnauwkeurige weergave van de zeebodem en/of onrealistische schattingen van de meetonzekerheden. Bovendien zijn realistische voorspellingen van de bijdrage van de verschillende onzekerheidsbronnen die de kwaliteit van de bathymetrische metingen beïnvloeden vooraf van belang om voldoende nauwkeurigheid van de peilingen en een juiste interpretatie van sedimenteigenschappen te verzekeren. Dit proefschrift tracht dus bedoeld om het inzicht van de MBES-meetmogelijkheden naar een nieuwe niveau te brengen door deze problemen aan te pakken.

Een essentiële voorwaarde voor nauwkeurige dieptemetingen is de kennis van het Sound Speed Profile (SSP). Gebrek aan kennis van het heersende SSP leidt tot refractieartefacten (systematische fouten in de afgeleide bathymetrie). In dit proefschrift wordt een methode voorgesteld om de refractieartefacten te corrigeren door gebruik te maken van de redundantie in de MBES-metingen verkregen uit de overlap van aangrenzende stroken. De toepassing van de SSP-inversiemethode op een dataset met bestaande refractie artefacten, gaf een succesvolle correctie van de dieptemetingen. Bovendien had de ontwikkelde inversiemethode noch de bestaande morfologie gemanipuleerd, noch kunstmatige bathymetrische kenmerken geïntroduceerd in gebieden die geen door refractie veroorzaakte fouten hebben.

Nieuwe generaties MBES's kunnen frequentie gemoduleerde (FM) signalen verzenden, naast de standaard Continuous Wave (CW) signalen. De voordelen van FM-signalen zijn een vergroting van de bereikbare strookbreedte met behoud van een hoge resolutie, wat leidt tot verbeterde verwerkingscapaciteiten en de mogelijkheid om de uitgezonden energie te verhogen (zonder de bereikresolutie te verslechteren). Ondanks deze voordelen vertonen de dieptemetingen die zijn verkregen met behulp van de FM-pulsen hogere ruisniveaus in vergelijking met die verkregen met behulp van CW-pulsen. In dit proefschrift zijn de resulterende bathymetrische onzekerheden als gevolg van het gebruik van de FM-puls onderzocht

om de prestaties van het MBES-systeem bij gebruik van de FM-signal te evalueren. Er zijn twee bijdragen aan de onzekerheden bij het overschakelen van CW naar FM, baseline-decorrelatie en het Doppler-effect. In dit proefschrift zijn ze allebei verantwoord in de MBES-voorspelling van de totale verticale onzekerheid. Hoewel het in overweging nemen van de geïdentificeerde foutbronnen resulteert in een realistischer beschrijving van de bathymetrische onzekerheid zoals getoond in dit proefschrift, vereist het verantwoorden van deze overwegingen aanvullende kennis die mogelijk niet beschikbaar is voorafgaand aan een hydrografisch onderzoek.

Daarnast worden in dit onderzoek de prestaties van het bathymetrische onze-kerheids voorspellingsmodel, zoals geïmplementeerd in AMUST (*A priori* Multibeam Uncertainty Simulation Tool), beoordeeld voor moderne MBES door de modelvoor-spellingen te vergelijken met gemeten bathymetrische onzekerheden verworven in verschillende operationele omgevingen en voor verschillende MBES-instellingen. Twee factoren zijn van belang voor een eerlijke en realistische vergelijking tussen de gemeten en voorspelde bathymetrische onzekerheden, dit zijn de grootte van het bodemoppervlak en het aantal fasemonsters per bundel. Als een te groot oppervlak wordt overwogen, kan de bodem morfologie veranderen en komen de variaties van de bathymetrische metingen binnen een vlak niet volledig overeen met de onzeker-heden die inherent zijn aan de MBES. De optimale grootte van het oppervlak is dus vereist. Wat het aantal fasemonsters betreft, deze parameter wordt gebruikt om de bijdrage van de fase bodem detectiemethode aan de bathymetrische onzekerhe-den te berekenen. Voor de beschouwde datasets werden verschillen waargenomen tussen het theoretische en het werkelijke aantal fasemonsters, wat resulteerde in onjuiste voorspellingen van de bathymetrische onzekerheden bij gebruik van de eerste. Hoewel er over het algemeen een goede overeenkomst bestaat tussen de voorspelde en gemeten bathymetrische onzekerheden is het gebleken dat, aanpas-singen aan het model nodig zijn voor een betere overeenkomst tussen het model en de metingen, met name voor de buitenste bundel en diepere gebieden. Binnen dit werk wordt rekening gehouden met de baseline decorrelatie, het Doppler-effect en de verminderde signaal-ruisverhouding voor de buitenste delen van de strook en worden verbeteringen waargenomen in het vastleggen van de variaties van de bathymetrische onzekerheid met de bundelhoek.

Ten slotte gaat het laatste deel van dit proefschrift in op het verwerken en in kaart brengen van de bathymetrische gegevens op een raster. De transformatie van de bathymetrische metingen naar een raster moet worden uitgevoerd om een efficiënte gegevensverwerking mogelijk te maken en toch een waarheidsgetrouwe weergave van de zee- en rivierbeddingen te bieden. Daartoe worden verschillende benaderingen voor rastering overwogen. Voor vlakke gebieden blijkt de ondiepst gemeten bathymetrie sterk beïnvloed te worden door meetonzekerheden, dit kan worden tegengegaan door gebruik van de gemiddelde bathymetrie. Deze waarde onderschat echter de ondiepste bathymetrie voor gebieden met hellingen. Zoals in dit proefschrift wordt aangetoond, wordt door het aftrekken van de standaarddevi-atie van het gemiddelde van de metingen in een rastercel rekening gehouden met het effect van hellingen terwijl de invloed van meetonzekerheden wordt verminderd in vergelijking met de ondiepste die van gemeten bathymetrie.

In conclusie, de bijdrage van dit proefschrift aan het gebied van MBES bathymetrische mapping is om de kennis van de MBES-meetmogelijkheden naar een zodanig niveau te brengen dat hydrografische operaties worden geoptimaliseerd. Dit leidt tot een betrouwbare en nauwkeurige weergave van de bodem en een realistische verwachting van de bijbehorende onzekerheden. Het optimaliseren van hydrografische metingen wordt bereikt door de systematische fouten (indien aanwezig) te corrigeren met behulp van een realistisch voorspellingsmodel voor bathymetrische onzekerheden, waarbij de juiste verdeling van de peilingen wordt aangepakt terwijl lage onzekerheden van de meting worden gegarandeerd. Dit laatste maakt realistische bathymetriekaarten mogelijk en moet in de enquêteplanning worden meegenomen.

Nomenclature

Latin symbols

(a, b)	Sub-arrays a and b
$a_0^{(')}$	(Shifted) intercept of the polynomial function used to model the depth in a surface patch (cell)
a_c	Ratio of the correct to erroneous sound speeds
a_H	Fixed (static) component of the measured heave uncertainty
$a_{X_{(N,V)}}$	Slope in the X direction in navigation (easting) and vessel (across-track) frames
$a_{Y_{(N,V)}}$	Slope in the Y direction in navigation (northing) and vessel (along-track) frames
Az	Beam azimuth angle
b_H	Variable components of the measured heave uncertainty
A	Ensonified footprint, area
A_1	Unit area (defined as $1\,\text{m}^2$)
A_b	Ensonified footprint in beam limited regime
A_p	Ensonified footprint in pulse limited regime
b_p	Beam pattern, directivity pattern
B	Receiver bandwidth
B_{eff}	Receiver effective bandwidth
$B_p(B_{p_T}, B_{p_R})$	Beam pattern, directivity pattern in dB (transmission and reception)
BS	Backscattering strength in dB per m^2 at $1\,\text{m}$
c	True sound velocity in m/s
c_{img}	Complex sound velocity
c_{meas}	Measured sound velocity in m/s
c_n	Sound speed corresponding to the nth sailed track
c_{SSP}	Average sound speed in the water column
c_{tr}	Sound speed at the transducer (surface sound speed)
d	Water depth below the transducer
d_i	Depth of a given cell i
$d_{\text{min},CL}$	Shallowest calculated depth corresponding to CL confidence level
$d_{\text{min,Reg}}$	Shallowest depth using regression coefficients
$\boldsymbol{de}$	Descendants in Differential Evolution optimization
e	Euler's number
e_s	A scalar describing an arbitrary point on the line
EL	Echo level in dB
f_c	Center frequency of the emitted signal
f_d	Difference between the frequency of the Dopplerized received and emitted signals

f_s	Sampling frequency
F_{DE}	Differential Evolution scalar multiplication factor between 0 and 1
G_{DE}	Differential Evolution Energy (objective) function
G	Array acoustic response
H	Total heave
H_{Induced}	Induced heave
H_{Meas}	Measured heave
k	Wavenumber
i	Imaginary unit
I	Acoustic intensity
I_b	Backscatterd acoustic intensity
I_i	Incident acoustic intensity
I_{ref}	Reference intensity equal to $0.67 \times 10^{-18} \text{W/m}^2$
δL	Distance between array elements
$L(L_T, L_R)$	Array length (transmission and reception)
L_b	Distance between two sub-array centers in the interferometry
$\boldsymbol{m}$	Design vector in Differential Evolution optimization
m	Array element (i.e., hydrophone or projector)
$\hat{m}$	Integer phase ambiguity
M	Number of receiving elements
M_z	Bulk grain size in units Φ
n_p	Number of phase samples
NL	Background noise level
$N_{G_{\text{DE}}}$	Differential Evolution number of generations
N_{hits}	Number of depth measurement in a cell
$\boldsymbol{p}$	Partner population in Differential Evolution optimization
p	Acoustic pressure
p_0	Acoustic pressure amplitude at source location
p_{dB}	Acoustic pressure in dB relative to $1\,\mu\text{Pa}$
$p_{c_{\text{DE}}}$	Differential Evolution crossover probability
p_i	Incident acoustic pressure
p_r	Reflected acoustic pressure
p_{ref}	Reference acoustic pressure equal to $1\,\mu\text{Pa}$
p_{rms}	Root-mean-square acoustic pressure
p_t	Transmitted (refracted) acoustic pressure
P	Pitch angle
pg	Processing gain in ratio
PG	Processing gain in dB
P_a	Acoustic power
q_{DE}	Differential Evolution population size
r	True distance to the source
r_{meas}	Measured distance to the source
δr	Spatial delay on array elements at beamforming
R	Roll angle
R_{NT}	Rotation matrix translating from transducer frame T to

	navigation frame N
R_{NV}	Rotation matrix translating from vessel frame V to navigation frame N
R_{VT}	Rotation matrix translating from transducer frame T to vessel frame V
$\mathcal{R}$	Reflection coefficient
s	Transmitted sound pressure signal
$S(S_a, S_b)$	Receiving sound pressure signal (on sub-array a and b)
$S(f)$	Fourier transform of the transmitted signal $s(t)$
SH	Transducer sensitivity in dB re V/µPa
SL	Source level in dB re 1 µPa at 1 m
S_w	Water salinity
t	Time instant
t_D	Two-Way Travel time of signal (from transmission until reception)
t_e	Emission (transmission) instant of a signal sample
$t_{O_{i,n,j}}$	Modeled One-Way Travel time of the jth depth measurement from a given sailed track n in the given cell i
t_r	Receiving instant of a signal sample
$\delta t = t^{\text{shift}}_{S_a, S_b}$	Range-Doppler coupling (for received signals on sub-arrays a and b)
$\mathcal{T}$	Transmission coefficient
T	Pulse length
T_{eff}	Effective pulse length
T_e	Integration time
$T_{O_{i,n,j}}$	Measured One-Way Travel time of the jth depth measurement from a given sailed track n in the given cell i
TL	Transmission loss in dB
TS	Target strength in dB
T_w	Water temperature
$\vec{u}_{(N,T)}$	Unitary directional vector (in navigation and transducer frames)
v_r, v_e	Speed of the array center at reception and emission projected on beam direction
x	Horizontal distance between the receiver and scatterer, across track distance
δx_d	Across-track bathymetry resolution
$[X,Y]_{N_{\text{cent}}}$	Horizontal coordinates of the cell center in navigation frame
$[X,Y]_{N_{\text{LU,LL,RL,RU}}}$	Horizontal coordinates in navigation frame correspondig to upper-left, lower-left, lower-right, and upper-right corners of a cell
$[x,y,z]$	Space coordinates
$[x,y,z]_{\text{Off}}$	Offset coordinates between the transducer and heave or GNSS sensor
$[X,Y,Z]_N$	Coordinates in the navigation frame
$[X,Y,Z]_T$	Coordinates in the transducer frame
$[X,Y,d]_{\text{tr}}$	Transducer coordinates in navigation frame

$[X, Y, Z]_V$	Vessel frame
δy_d	Along-track bathymetry resolution

Greek symbols

α	Attenuation coefficient in dB/m
β	Beam depression angle (angle between the direction of the incoming sound wave and navigation horizontal plane)
β'	Recalculated beam depression angle (angle between the direction of the incoming sound wave and navigation horizontal plane) for the updated sound speed
Γ	Grid cell size
γ	Tapering coefficient in %
γ_1	Skewness
γ_a	Attenuation coefficient in Np/m
γ_a	Spectral component
δr_{res}	Range resolution
δr_s	Range sampling resolution
$\Delta\varphi$	Phase delay or theoretical phase difference
$\widehat{\Delta\varphi}$	Estimated phase difference
η	Spectral strength in units of cm^4
θ	Incident angle (angle between incident wave and surface normal), beam angle for a flat seabed
θ_{crit}	Critical incident angle
θ_{fl}	Incident angle assuming a flat seafloor
θ_m	Actual steering angle
θ_p	Angular position of a scatterer relative to the array normal
θ_{mount}	MBES across-track mounting angle
$\theta_s(\theta_{s_R}, \theta_{s_T})$	Steering angle (at reception and transmission)
$\delta\theta_s$	Error in the steering angle due to the Doppler effect
Θ	Beam angle
$d\Theta$	Angular uncertainty induced due to the uncertainty in the mean sound speed profile at the receiving array
$d\Theta'$	Angular uncertainty induced due to the uncertainty in the mean sound speed profile at the middle boundary
κ	Chirp rate
λ	Acoustic wavelength
μ	Coherence coefficient
ν	Spatial frequency for the direction θ
ν_s	Spatial frequency for the direction θ_s
ρ	Density in kg/m^3
σ_b	Backscattering cross section
σ_d	Total depth uncertainty
$\sigma_{c_{\mathrm{meas}}}$	Uncertainty in measurement of the average sound speed

	in water column
$\sigma_{c_{\text{tr}}}$	Uncertainty in sound speed measurements at receiving array
σ_{Δ_φ}	Standard deviation of the phase difference
$\sigma_{d_{\text{Align}}}$	Depth uncertainty due to the motion sensor and echosounder alignment
$\sigma_{d_{\text{AngMot}}}$	Depth uncertainty due to angular motion sensor measurements
$\sigma_{d_{ES}}$	Depth uncertainty due to the echosounder contribution
σ_{d_H}	Depth uncertainty induced by heave
$\sigma_{d_{\Omega_T}}$	Depth uncertainty due to non-zero along-track opening angle
σ_{d_r}	Depth uncertainty due to the range uncertainties
$\sigma_{d,r_{\text{Doppler}}}$	Depth uncertainty due to uncertainty in estimate of the range shift induced by the Doppler effect
$\sigma_{d_{SS}}$	Depth uncertainty due to the sound speed uncertainties
$\sigma_{d,\theta_{s,\text{Doppler}}}$	Depth uncertainty due to the uncertainty in the beam steering induced by the Doppler effect
$\sigma_{d_{\Theta_{\text{meas}}}}$	Depth uncertainty due to the uncertainties of the beam angle
σ_{d,t_D}	Depth uncertainty due to the uncertainty in the detection instant
$\sigma_{d,t_{\text{Decorr}}}$	Depth uncertainty due to the uncertainty in the detection instant induced by the baseline decorrelation
$\sigma_{H_{\text{Induced}}}$	Uncertainty of the induced heave
$\sigma_{H_{\text{Meas}}}$	Uncertainty of the measured heave
$\sigma_{P_{\text{meas}}}$	Uncertainty of pitch measurements
$\sigma_{\Delta P_{\text{Align}}}$	Uncertainties of the pitch offset value from patch test
$\sigma_{r_{\text{Doppler}}}$	Uncertainty in the range shift estimate due to the Doppler effect
$\sigma_{R_{\text{meas}}}$	Uncertainty of roll measurements
$\sigma_{\Delta R_{\text{Align}}}$	Uncertainties of the roll offset value from patch test
σ_{SSP}	Uncertainty in the measurements of the sound speed profile
σ_t	Target's backscattering cross section
$\sigma_{\theta_{s_c}}$	Uncertainty in the steering angle due to the sound speed fluctuations at the transducer
$\sigma_{\theta_{s,\text{Doppler}}}$	Uncertainty in the beam steering angle due to the Doppler effect
σ_{Θ_c}	Angular uncertainty due to sound speed measurement uncertainty
$\sigma_{\Theta_{\text{SSP}}}$	Angular uncertainty due to non-uniform sound speed profile
$\sigma_{\Theta_{\text{meas}}}$	Uncertainty in the measurements of the beam angle
σ_r	Roughness (interface) scattering
$\sigma_{r_{\text{meas}}}$	Uncertainty of the measured range
σ_v	Volume scattering
σ_{v_r,v_e}	Uncertainty in the speed at reception and emission (transmission) projected on beam direction
$[\sigma_x, \sigma_y, \sigma_z]_{\text{Off}}$	Uncertainties of offset coordinates between transducer and heave sensor
$\hat{\sigma}_v$	Volume scattering parameter
τ	Time delay on array element at beamforming
τ_0	Time difference between emitting and receiving first sample of

	emitted pulse for a receiver located at the center of the array
ϕ	Grazing angle (angle between the incident wave and the surface)
ϕ_{intr}	Angle of intromission
ψ	Phase of the expected value of $S_a S_b^*$ with S_a and S_b the received signals at sub-array a and b
ω	Circular (angular) frequency
$\Omega(\Omega_R, \Omega_T)$	Beam opening angle (at reception and transmission)
ξ, ξ_m	Orientation of the projected true (erroneous) beam vector on the XY-plane of the transducer frame
ζ	Proportionality constant

Mathematical symbols

$\frac{\partial f}{\partial x}$	Partial derivative of function f with respect to variable x
$\boldsymbol{\Lambda}$	Diagonal matrix with diagonal entries the eigenvalues of a positive definite matrix
λ_{ii}	i^{th} eigenvalue of a positive definite matrix
$\Delta(.)$	Laplace operator
$|.|$	Absolute value of a real number or vector
$\|.\|$	Norm of a vector
$<.>$	Mean operator
$\mathbf{U}$	matrix of eigenvectors, where each column corresponds to one of the eigenvalues
$\mathbb{N}$	Set of natural numbers
$*$	Complex conjugate transpose
$\arg(.)$	Argument operator

Statistical symbols

$\mathbf{A}$	$m \times n$ design matrix of the functional model
CL	Confidence level
D_{CL}	Scale factor corresponding to the confidence level CL for calculating confidence interval
$D(.)$	Dispersion operator
$E(.)$	Expectation operator
$\boldsymbol{e}$	m-vector of measurement error
$\hat{\boldsymbol{e}}$	Least-squares estimator of residuals
H_0	Null hypothesis
H_1	Alternative hypothesis
$\mathbf{I} \equiv \mathbf{I}_m$	Identity matrix of order m
$N(\mu, \sigma)$	Normal distribution with the mean μ and standard deviation σ
$\mathcal{U}(0, 1)$	Uniform distribution between 0 and 1

$\mathrm{P}\{x = x_0\}$	Probability that x will be equal to x_0
$\mathbf{Q}_y$	Covariance matrix of $\mathbf{y}$
$\mathbf{x}$	n-vector of unknown parameters
$\hat{\mathbf{x}}$	n-vector (estimate of unknown $\mathbf{x}$)
$\underline{x}$	Random variable
$\mathbf{y}$	m-vector of observable
var(.)	Variance operator
σ^2	Variance of the data
$\hat{\sigma}_y^2$	Estimator of variance component
σ_x	Standard deviation of the random variable $\underline{x}$

Acronyms

General acronyms

ABE	Adaptive Bathymetric Estimation
AMUST	*A priori* Multibeam Uncertainty Simulation Tool
COG	Center Of Gravity
CTD	Conductivity, Temperature, Pressure
CUBE	Combined Uncertainty and Bathymetry Estimator
CW	Continuous Wave
DE	Differential Evolution
DGNSS	Differential Global Navigation Satellite System
DOA	Direction Of Arrival
EOF	Empirical Orthogonal Function
FM	Frequency Modulated
GA	Genetic Algorithm
GN	Gauss-Newton
GNSS	Global Navigation Satellite System
IHO	International Hydrographic Organization
INS	Inertial Navigation Sensor
IQR	Interquartile Range
LIDAR	LIght Detection And Ranging
LINZ	Land Information New Zealand
LFM	Linear Frequency Modulated
MAD	Median Absolute Deviation
MBES	MultiBeam EchoSounder
MVP	Moving Vessel Profiler
NAP	Normaal Amsterdam Peil
NETPOS	NEtherlands POsitioning Service
NOAA	National Oceanic and Atmospheric Administration
NRTK	Network RTK
OWTT	One-Way Travel Time
PDF	Probability Density Function
QINSy	Quality Integrated Navigation System
QPS	Quality Positioning Services
radar	RAdio Detection And Ranging
RTK	Real Time Kinematic
RVU	Random Vertical Uncertainty
RWS	Rijkswaterstaat
SBES	SingleBeam EchoSounder
sonar	SOund Navigation And Ranging

SNR	Signal-to-Noise Ratio
SSP	Sound Speed Profile
SSS	SideScan Sonar
SVD	Singular Value Decomposition
TWTT	Two-Way Travel Time
TRVU	Total Random Vertical Uncertainty
UTM	Universal Transverse Mercator
WGS84	World Geodetic System 1984

Sediment acronyms

cS	clayey Sand
gmS	gravelly muddy Sand
mS	muddy Sand
msG	muddy sandy Gravel
sG	sandy Gravel
sM	sandy Mud

1

Introduction

*A journey of a thousand miles begins
with a single step.*

Laozi

*Innovation is the ability to see change
as an opportunity – not a threat.*

Steve Jobs

This introduction explains the motivation for this thesis, namely to bring the insights in the MultiBeam EchoSounder (MBES) measurement capabilities to a new stage such that the hydrographic operations are optimized in terms of a reliable and accurate representation of the bottom and a realistic expectation of the associated uncertainties. A brief overview of the systems available for these operations with a special focus on the MBES along with the principles of bathymetric measurements with this system is provided. Following this, the various measures taken so far for improving the hydrographic operations are briefly discussed and the aspects still requiring investigation are highlighted. Next, the research objectives are introduced followed by presenting the outline of this thesis.

1.1. Underwater environment

The world oceans cover more than two-thirds of the Earth's surface and hold various types of resources. It is an environment with a highly varied and dynamic flora, fauna and physics and has been a great source of attraction for mankind. The oceans are also of immense importance in sustaining life, controlling climate and facilitating commerce. However, what is lying beneath the sea surface has remained a source of mystery for ages as it is only remotely accessible and difficult to monitor. Today, thanks to modern technology a detailed investigation of the underwater environment can be carried out.

Knowing the morphology and sediment composition of the sea and river bed is of high importance for a large number of human activities at sea, including shipping, offshore activities such as oil and gas exploration, coastal engineering, and marine biology and geology [1–4]. Detailed information about the bottom is thus required to guarantee safe navigation and to enable the discovery and localization of resources.

Methods for monitoring the underwater environment are limited. Traditionally, obtaining information about the distribution of the sediment required an extensive set of grab samples of the sediment and subsequent laboratory analysis. This is a cost intensive, time consuming and locally restricted process. Regarding the bottom topography, traditionally a lead line was used to measure the water depth below the vessel allowing for obstacles avoidance, which is again a time consuming process incapable of providing large coverage of the bottom [5]. Remote sensing approaches, on the other hand, are more appropriate as they provide larger coverage and are more time efficient.

While the terrestrial surfaces can be mapped using radar (RAdio Detection And Ranging) or optical sensors, mapping the bottom of the ocean with a similar spatial resolution requires to a large extent the use of acoustic sensors [6]. The water is a highly dissipative medium, and thus the electromagnetic waves are attenuated extremely strongly. This limits the applicability of these waves to shallow environment and clear waters [7] (for these environments, bathymetric LIDAR (LIght Detection and Ranging) and satellite derived bathymetry [8], derived from satellite imagery, and satellite altimetry, which uses the gravity data [9] and its applicability is not limited to clear waters, can be used). As an alternative, acoustic waves are the most practical waveform for transmitting information in the water as they have significantly lower attenuation resulting in a larger traveled distance [10]. Since the development of the first sonar (SOund Navigation and Ranging) in the beginning of the 20th century, different acoustic systems have been developed for remotely mapping the seafloor. These are the SideScan Sonars (SSSs), SingleBeam EchoSounders (SBESs), and MultiBeam EchoSounders (MBESs) [11], see Fig. 1.1. These systems differ in frequency, aperture and mounting configuration to cover the broad range of applications encountered.

1.2. Underwater acoustic mapping systems

SSS systems are generally regarded as visualization tools and provide high resolution acoustic images of the bottom [11]. The system is often towed behind the vessel at a short distance above the bottom, see Fig. 1.1a. It sends a short pulse in a frequency range between 65 kHz and 500 kHz at grazing incidence, in a narrow beam towards the seabed. The SSS measures the backscattered signal intensity at the seabed as a function of time. The traditional SSS cannot measure the bathymetry[1], except for a rough estimate of its altitude from the echo at nadir. To compensate for this, a second receiving antenna can be used, which adds interferometric capabilities to the SSS [12]. Although the concept is simple, there are a number of issues deteriorating the quality of the bathymetric measurements derived [13–16].

An SBES transmits a short signal (a ping) in a beam of moderate angular aperture (5° to 15°) vertically below the survey vessel, see Fig. 1.1b. The water depth under the SBES is derived using the measured Two-Way Travel Time (TWTT) together with the sound speed. The intensity and shape of the signal are partly determined by the composition of the seafloor and can therefore be used for classification [17–19]. Although the SBES was a significant improvement over the traditional lead line, it was still far from ideal. The system returns only one measurement (sounding) per ping. The spatial resolution of an SBES is not homogeneous between the horizontal and vertical directions with the former dramatically deteriorating with water depth. Obtaining a full coverage of the seafloor with an SBES requires a considerable number of survey lines which is a time-consuming process.
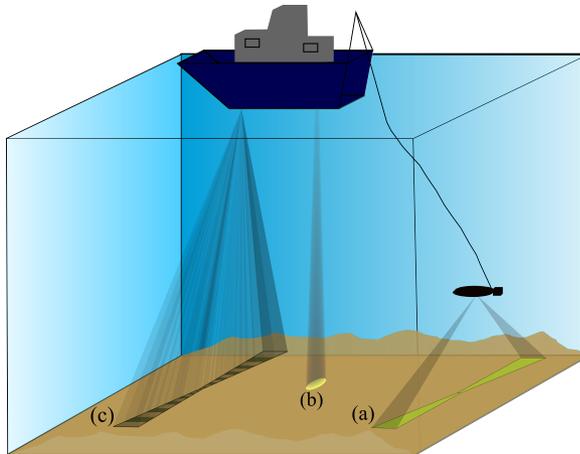
Figure 1.1: Schematic overview of a) SSS, b) SBES and c) MBES geometry.

To overcome the limitations of the SBES, the MBES has been developed. In-

---

[1]Throughout this thesis, the terminologies *bathymetry* and *depth* indicate a value vertically referenced to the chart datum and thus they are used interchangeably. In case the depth relative to the sonar is meant (and not relative to the chart datum), this is explicitly stated.

stead of transmitting and receiving a single vertical beam, an MBES transmits and receives the signal over a wide angular range (the 'swath') perpendicular to the sailing direction (across-track) similar to a SSS, see Fig. 1.1c. The frequency of the acoustic signal depends on the water depth and ranges from 12 kHz for deep water up to 200 kHz, 400 kHz and even 700 kHz for shallow lagoons [20]. Beamsteering at reception enables to measure the travel time of the acoustic signal to the seafloor for a set of predefined beam angles along the swath. The advantage of an MBES over a SBES is that it provides a large coverage of the bottom as it performs a large number of simultaneous measurements across the vessel's path. Similar to the SSS, the MBES uses its wide angular coverage to provide an acoustic image of the seafloor by using the reflected and scattered signal intensity at the seabed which can be employed for sediment classification [21–24]. Therefore, the MBES allows to map large areas in a relatively short time by covering areas up to seven times the water depth [20]. It is thus extensively used nowadays for seafloor mapping, including hydrography and offshore construction applications, and belongs to the cutting-edge technology to acquire high-resolution bathymetric and imaging data over large areas within a relatively short time period.

1.3. Bathymetry measurements

A MBES calculates the depth of a point relative to the sonar by jointly estimating the TWTT and the beam angle of the received signal relative to the vertical axis. For a set of predefined angular directions, the instant of the signal arrival is searched for. This is obtained by searching for the instant corresponding to the maximum amplitude of the received signal from a given direction. One can also obtain the signal arrival time by dividing the receiving array into two sub-arrays and calculating the phase difference of the received signals beamformed in a given direction. Then, the time at which the two signals are in phase (zero phase difference between the two beams formed in a chosen direction) is taken as the arrival time [25].

Using the arrival time of the signal for a given direction and the speed of sound in the water column, the coordinates of the measurements on the sea or river floor are derived. These coordinates are referenced to the position of the sonar. It is thus imperative to simultaneously know the position and attitude of the supporting platform to accurately determine the 3-dimensional geographical coordinates of a sounding.

Similar to any other measured quantity, the bathymetric measurements are contaminated by uncertainties inherent to the MBES and the transmitted signal, operational environment, survey configuration and ancillary sensors [26–29]. As an example, uncertainties in the measurements acquired from the attitude (i.e., roll, pitch and heading) and positioning sensors induce bathymetric uncertainties. Similarly, an uncertainty in the measurements of the sound speed at the sonar head or in the water column leads to an uncertainty in the estimate of the bathymetry. These contributions have to be accounted for to establish a realistic expectation of the integrated mapping system's measurement capabilities, of which the MBES is only one component.

1.4. Motivation

Despite the widespread use of the MBESs for hydrographic operations, the existing knowledge with regards to its measurement capabilities is lacking in some aspects, discussed in the following, potentially leading to an unreliable and inaccurate representation of the seafloor and/or unrealistic estimates of the measurements uncertainties. These can impose hazards to safe navigation or result in inefficiency of offshore activities. Efforts have thus been put forward to improve various aspects of hydrographic operations using the MBESs.

Since the appearance of the MBES in the market in 1977 [30], the system has greatly evolved from various perspectives. These improvements include, but are not limited to, an enhanced bottom coverage, increased number of soundings and attainable swath, improved spatial resolution and the possibility of modifying the operating frequency of the transmitted signal on a ping by ping basis [5, 13, 31–34]. In parallel with the advances made in the MBES technology, the position and motion sensors, processing and computer capabilities have gone through tremendous developments. For example, positioning accuracy has significantly improved with the availability of Real Time Kinematic (RTK) systems (cm-level accuracy for relatively short distance from the base station) and its extension to Network RTK (NRTK) systems (overcoming the limitations of RTK) [35, 36]. With regards to the motion sensors, currently it is possible to achieve an accuracy of 0.01° using inertial sensors tightly coupled with the Global Navigation Satellite System (GNSS), for example see [37, 38]. High accuracies can be obtained under dynamic conditions by determining the residual biases of attitude sensors and navigation timing errors using patch tests [39]. Hughes Clarke [40] investigated different types of dynamic systematic errors inducing faint but pervasive across-track artefacts in the derived bathymetry map. However, there are still some aspects requiring improvements.

As pointed out earlier, MBES bathymetric measurements are derived using the known sound speed in the water column. Knowledge of this parameter might be lacking due to spatially and/or temporally varying water column sound speeds, occurring in salt wedge estuaries, for instance, or insufficient number of Sound Speed Profile (SSP) measurements. As a result, a systematic error in the derived bathymetry is induced. A majority of existing approaches for correcting the bathymetric measurements affected by this lacking knowledge have a number of limitations. For example, they impose constraints on the seafloor morphology [41, 42] which might be violated in real-world situations. The systematic bathymetric error can be prevented using additional measurements acquired by a Conductivity, Temperature, Pressure (CTD) sensor. However, this requires the vessel to be stationary, making it a time-consuming process, and it is thus impractical to obtain these measurements at high rates. As for underway sound speed profiling systems, [43, 44], the issue with sampling frequency is addressed as it is possible to oversample the water column. However, the profiling hardware (as an example the winches and cables) experiences accelerated wear and there is a risk of fouling or grounding of the towed instrumentation with each cast [45].

New generations of MBESs have the option to use Frequency Modulated (FM)

signals, in addition to the more standard Continuous Wave (CW) signals. The advantages of FM signals include an increase in the achievable swath while maintaining a high range resolution, providing a gain in the processing thanks to the matched filtering of the received signal and the possibility of increasing the transmitted energy (without deteriorating the range resolution) [46]. Despite these advantages, MBES measurements acquired with the FM pulse type exhibit higher noise levels compared to those derived using CW, and thus are of a lower quality [47–49]. Research has been carried out to identify the origin of the degradation in the performance of the bathymetric measurements when using the FM pulse type [50, 51], however, the bathymetric uncertainties induced due to their use need to be quantified. Lack of insight in this regard might result in an unrealistic expectation, often too optimistic, of the MBES bathymetric quality using FM pulse shapes.

As was mentioned in Section 1.3, there are various uncertainty sources affecting the quality of the derived bathymetry. Realistic predictions of their contribution prior to a survey is of importance to ensure sufficient accuracy of the soundings and to meet the standards defined by International Hydrographic Organization (IHO). Moreover, a realistic estimate of the bathymetric uncertainties is required for a correct interpretation of the sediment properties when using bathymetric derived indicators for sediment classification, such as depth residuals [23, 52]. Lacking knowledge in this regard can lead to mistakenly classifying the uncertainties and assigning different sediment types to the measurements having actually the same sediment composition, but different uncertainties. Efforts have been thus put forward to assess the uncertainty sources affecting the depth measurements [26, 27, 29, 53, 54]. References [26, 27] developed an *a priori* vertical uncertainty prediction model to quantify the contribution of the various sources. The developed model has been widely used for predicting the uncertainties prior to a survey, as implemented in *A priori* Multibeam Uncertainty Simulation Tool (AMUST) used throughout this thesis. This tool is developed by the Acoustics Group of Delft University of Technology in a close cooperation with the Ministry of Infrastructure and Water Management (Rijkswaterstaat). The uncertainty model of [26, 27] has been also employed for producing bathymetry maps, for example in the Combined Uncertainty and Bathymetry Estimator (CUBE) algorithm developed by Calder and Mayer [28, 55, 56]. The bathymetric uncertainty prediction model of [26, 27] is referred to as the current model in this thesis. Despite the widespread use of this model, far too little attention has been paid to assess its performance for a given operational environment using the state-of-the-art MBES. The rapid developments of the MBES from both design and processing points of views have also increased the need for a better understanding of the performance of such a model.

The derived high density bathymetry measurements obtained from a survey with a MBES are generally transformed into a grid to produce a bathymetry map and to enable efficient data processing. The process of gridding means to average individual measurements within a chosen capture distance from a pre-selected grid node. Ideally, the assigned value to each node within the grid has to represent the average water depth. To this end, triangulation or equidistant gridding can be used [57, 58]. Despite the advantages of the triangulation technique, such as its flexibility

with regards to varying levels of detail, it has a large memory requirement and long processing time. In terms of the equidistant gridding, the main weaknesses of the widely used approaches are that they lead to either a too shallow [28] or too deep estimate of the bathymetry. These can result in unnecessary dredging in navigational channels and/or navigational hazards.

Addressing the above-mentioned aspects of hydrographic operations, which can potentially deteriorate the quality of the MBES derived bathymetry or shape an unrealistic expectation of the MBES measurement capabilities, is the motivation to conduct the research presented in this thesis.

1.5. Research objectives

The aim of this thesis is thus to bring the knowledge of the MBES measurements capabilities to a stage such that the hydrographic operations are optimized in terms of a reliable and accurate representation of the bottom and a realistic expectation of the associated uncertainties. The main research objective can be further broken down into the following research objectives that are pursued in this dissertation.

1. **Correct the bathymetric measurements for the errors induced due to inaccurate or insufficient knowledge about the water column sound speed with no *a priori* constraints on bottom topography or additional sound speed measurements;**

2. **Model and assess the relevance of the bathymetric uncertainties induced due to the use of FM pulse shapes in the framework of the widely used bathymetric uncertainty prediction model of [26, 27], as implemented in AMUST;**

3. **Assess the performance of the widely used bathymetric uncertainty prediction model of [26, 27], as implemented in AMUST, using the state-of-the-art MBES system and identify parameters that require modification to obtain a better model-data agreement;**

4. **Propose methods for gridding the MBES bathymetric measurements to equidistant grids as alternatives to the shallowest measured depth such that safe navigation is not hampered and outliers are rejected simultaneously.**

1.6. Thesis outline

This thesis comprises seven chapters. Four of them (***Chapters 3 to 6***) are mainly composed of published journal articles or conference papers. Each chapter addresses one of the research objectives defined in Section 1.5. A theoretical introduction, covering the basic formulations in underwater acoustics, is presented providing sufficient background knowledge for a better understanding of this thesis and precedes these chapters, given in ***Chapter 2***. The acoustic wave propagation, simple scattering described by Lambert's rule and a more sophisticated approach

1

are briefly discussed. The latter is then used to investigate the impact of the Signal-to-Noise Ratio (SNR) on the bathymetric uncertainties. The working principle of the MBES along with the widely used bathymetric uncertainty prediction model developed by [26, 27], as implemented in AMUST, and employed throughout this thesis in **Chapters 4 to 6**, are explained to avoid repetition.

The first step toward optimizing hydrographic operations and obtaining a reliable and accurate representation of the seafloor is to ensure that the bathymetric measurements are free of systematic dynamic errors. Lacking knowledge about the sound speed in the water column, which introduces concave or convex seafloor distortions referred to as refraction artefacts, prohibits one from achieving this goal. **Chapter 3** presents a method for correcting bathymetric measurements affected by inaccurate water column sound speed (**objective 1**). It employs the redundancy in the MBES measurements obtained from the overlap of adjacent swaths. The inversion method assumes a constant sound speed in the water column and is applied to a survey area in which this assumption is not valid to assess its performance. The proposed method is also applied to a survey area with existing refraction artefacts in some parts enabling a further assessment of its performance in areas with and without refraction artefacts.

Modeling the bathymetric uncertainties induced by the use of FM signals and assessing its relevance, **objective 2**, is carried out in detail in **Chapter 4**. In this chapter the uncertainties induced by two sources identified for the observed increase in the noise level of the bathymetric measurements when using FM pulse shapes [49], i.e., Doppler frequency shift and baseline decorrelation, are modelled and quantified. To also assess whether indeed a degradation in the quality of the bathymetric measurements is expected in case of using FM signals, these contributions are compared to those inherent to the MBES, such as the uncertainties in the measurements acquired from the attitude and positioning sensors. The modeled contribution of switching from the CW to FM pulse shape is also compared to those encountered in reality to validate the developed model.

In order to meet **objective 3**, **Chapter 5** investigates the subject of MBES bathymetric uncertainties in more detail. The predicted bathymetric uncertainties using the model of [26, 27], as implemented in AMUST, are compared to those measured in varying water depths and survey configurations. The comparison between the two allows to identify possible parameters to modify for a better model-data agreement, such as accounting for the SNR and insights gained from **Chapter 4**.

In **Chapter 6** optimizing hydrographic operations in terms of a reliable and accurate representation of the seafloor is addressed from a different perspective (**objective 4**). In this chapter, equidistant gridding of the derived bathymetric measurements is discussed. A number of potential approaches based on the statistical properties of the soundings are proposed as alternatives to the shallowest measured depth and applied to two survey areas. The implications of using each method for flat and non-flat areas are discussed in detail as well.

Finally, **Chapter 7** concludes the thesis, presenting the main results with regard to optimizing hydrographic operations. An outlook for future research drawn from

1

the whole thesis is also included.

Published articles

This dissertation is an article-based thesis. This means that it is mainly composed of publications in journals or conference proceedings. In each article the general theory of underwater acoustics is discussed to a limited extent of relevance to the issue addressed in that article to provide the sufficient background for the reader. A theoretical background about underwater acoustics and the basic formulations, which are not presented in the articles, are thus discussed in *Chapter 2*. The subsequent chapters contain the articles and address the research objectives. There are some repetitions in different chapters, particularly in the introductions. However, the published articles are mostly kept unchanged to allow a reader to read each chapter individually. Regarding the mathematical symbols, nomenclature and terms, some modifications are made with respect to the published articles allowing for a consistent notation throughout this dissertation. Moreover, one will notice references to sections and figures among different chapters added to highlight the relation between the research objectives addressed in the different published articles.

2

Background

*You can't build a great building on a weak foundation.
You must have a solid foundation if you're going
to have a strong superstructure.*

Gordon B. Hinckley

*In this chapter some basic formulations used in underwater acoustics are
explained providing knowledge for a better understanding of the subsequent
chapters. First, the wave equation and its elementary solution are discussed
followed by the various measures of sound. Then, the interaction of sound
with the sediment including reflection, transmission and scattering are dis-
cussed. Next, the simple scattering model described by Lambert's rule and a
more sophisticated approach are briefly explained followed by presenting the
fundamentals of array processing using the most common methods, namely
beamforming and interferometry. Then, a brief description of the various
pulse shapes most often used by the MultiBeam EchoSounder (MBES) along
with the matched filtering process are provided. An overview of the working
principles of the MBES and the approaches adopted by the system for bottom
detection are discussed followed by a brief explanation of the widely used
bathymetric uncertainty prediction model used throughout this thesis. Fi-
nally, the sonar equation and the Signal-to-Noise Ratio (SNR), are explained.*

2.1. Acoustic waves

Sound is a wave phenomenon. A wave in its turn is a disturbance of the equilibrium, spreading or propagating with time through space. Regarding sound, this disturbance is composed of a pressure and density disturbances. The wave consists of regions of compression, where the pressure exceeds the equilibrium value, and regions of rarefaction, where the pressure is less than the original value. These regions move or propagate away from the source (i.e., the particles remain around the stationary position; the disturbance propagates).

The pressure disturbances are described by the acoustic wave equation. The solution of the wave equation, using specific boundary conditions, provides an exact solution of the wave propagation in any medium [59]. The wave equation is derived by combining the principle of the conservation of mass, Newton's second law and using the relation between the density and pressure [59]

$$\Delta p = \frac{\partial^2 p}{\partial x^2} + \frac{\partial^2 p}{\partial y^2} + \frac{\partial^2 p}{\partial z^2} = \frac{1}{c^2}\frac{\partial^2 p}{\partial t^2} \ , \tag{2.1}$$

with Δ the Laplace operator which is the divergence of the gradient of a function in space x, y and z. p and c denote the pressure and the sound speed, respectively. Here, it is assumed that the medium is homogenous[1] in space. Considering a propagating wave in three dimensions in an isotropic[2] and dissipative[3] medium, the solution of Eq. (2.1) for a spherical coordinate system in complex notation reads as

$$p(r,t) = \frac{p_0}{r}e^{i(kr-\omega t)}e^{-\gamma_a r} \ , \tag{2.2}$$

with p_0 and k the pressure amplitude at 1 m away from the source and wavenumber equaling $\frac{\omega}{c}$, respectively. ω is the circular (angular) frequency defined as $\omega = 2\pi f_c$ with f_c the frequency of the acoustic wave. r is the space variable defining the distance from the observer location to the source equaling $r = \sqrt{x^2 + y^2 + z^2}$ for a source at $[0, 0, 0]$. Here, the wavefronts are spheres centered at the source at $r = 0$ with decreasing pressure amplitudes proportional to $1/r$ caused by the acoustic energy spread over the expanding wavefronts, known as spherical spreading. The term $e^{-\gamma_a r}$ accounts for the decrease of the pressure amplitude due to scattering and absorption, known as sound attenuation. While the latter implies energy conversion to some other form (usually heat), the scattering implies a redistribution of energy in angles away from the original propagation direction with no overall loss of acoustic energy [60]. Here, attenuation is defined by the parameter γ_a expressed in Np/m. Most often, the absorption coefficient is expressed as α in dB/m related to γ_a as $\alpha = 20\gamma_a \log e$[4].

---

[1]Homogenous medium is one in which all the medium physical properties are independent of position.
[2]Isotropic medium is one in which there is no preferred direction in space.
[3]Dissipative medium is one in which part of the acoustic wave energy is continuously absorbed, scattered and leaked as it propagates.
[4]In this thesis $\log x$ indicates logarithm base 10, i.e., $\log_{10} x$.

Restricting the wave propagation to a single direction x, i.e., the pressure is independent of the directions y and z. The wave equation (Eq. (2.1)) is then expressed as

$$\frac{\partial^2 p}{\partial x^2} = \frac{1}{c^2}\frac{\partial^2 p}{\partial t^2} \ . \tag{2.3}$$

Its solution in the complex notation form is

$$p(x,t) = p_0 e^{i(kx-\omega t)} \ , \tag{2.4}$$

which can be also expressed in the real notation form by taking the real part of Eq. (2.4) as

$$p(x,t) = p_0 \cos(kx - \omega t) \ , \tag{2.5}$$

with a constant amplitude equaling p_0 and a phase depending on a single direction x. The phase angle of this wave $(kx - \omega t)$ is constant at an arbitrary point in a plane perpendicular to the x axis (propagation direction). This wave is thus called a plane wave.

Plane waves and spherical waves are used to model the propagation of the acoustic waves in the medium. Although the underwater sources are in practice point sources generating waves spherically spreading in all directions, at sufficiently large distance from the source the curvature of the wavefront is negligible. When these conditions are satisfied the plane waves can be assumed for modeling local processes, such as scattering. Spherical waves, on the other hand, are descriptive of the situation where a decrease of the amplitude with the propagation from a point-like source must be accounted for (as an example, accounting for transmission loss in sonar processing) [11].

2.1.1. Measures of sound

Acoustic intensity I (in W/m^2) is defined as the mean energy (consisting of kinetic energy due to particle motion and potential energy due to the work done by the elastic force) per unit time per unit area normal to the direction of propagation [11]. For a plane wave with a pressure amplitude of p_0 or root-mean-square (rms) pressure of p_{rms}, the acoustic intensity is defined as

$$I = \frac{p_0^2}{2\rho c} = \frac{p_{\mathrm{rms}}^2}{\rho c} \ , \tag{2.6}$$

with p_{rms} an effective value which for a plane harmonic wave with amplitude p_0 is expressed as

$$p_{\mathrm{rms}}^2 = <p^2> = \frac{1}{T_e}\int_0^{T_e} p^2 \mathrm{d}t = \frac{p_0^2}{2} \ , \tag{2.7}$$

with $< . >$ the mean operator. T_e is the integration time defined as one period or an integer number of periods. ρ is the density and the value ρc is referred to as characteristic acoustic impedance.

Another measure is the acoustic power P_a received by a surface A, which is defined as

$$P_a = IA = \frac{p_0^2}{2\rho c}A = \frac{p_{\text{rms}}^2}{\rho c}A\,. \tag{2.8}$$

Due to the enormous range of possible measured magnitudes for acoustic intensity and power, they are usually presented on a logarithmic scale, and noted in decibels dB. Decibel denotes 10 times the base-10 logarithm of the ratio of two intensities, i.e., $10\log\frac{I_1}{I_2}$ quantifies the ratio in dB between two intensities I_1 and I_2. Considering the relationship between the acoustic power and pressure, the same ratio is expressed in dB as $20\log\frac{p_1}{p_2}$. Absolute power or pressure levels can be expressed using reference levels. In underwater acoustics, the reference pressure p_{ref} is $1\,\mu\text{Pa}$ (10^{-6} Pa) corresponding to a reference value in intensity of $I_{\text{ref}} = 6.7 \times 10^{-19}\,\text{W/m}^2$ with $\rho = 1000\,\text{kg/m}^3$ and $c = 1500\,\text{m/s}$. The absolute pressure and intensity levels in dB relative to $1\,\mu\text{Pa}$ are thus

$$p_{\text{dB}} = 20\log(\frac{p}{p_{\text{ref}}})\,, \tag{2.9a}$$

$$I_{\text{dB}} = 10\log(\frac{I}{I_{\text{ref}}})\,, \tag{2.9b}$$

where the notation is dB referenced to $1\,\mu\text{Pa}$, commonly referred to as dB re $1\,\mu\text{Pa}$.

2.2. Propagation of sound through water

An acoustic wave propagating through water loses its intensity due to spherical spreading and absorption, Eq. (2.2). The transmission loss, TL, is a dB measure for the decay of the intensity. TL depends on the water column properties and travel distance r from the source and reads as

$$TL = 20\log r + \alpha r\,, \tag{2.10}$$

The first term in Eq. (2.10) accounts for the energy loss due to spherical spreading, see Section 2.1. The attenuation coefficient (α) depends on the temperature, salinity, acidity, depth and pressure and the frequency of an acoustic wave [61, 62].

2.2.1. Non-homogeneous water

Often, a standard value of $1500\,\text{m/s}$ is used as the sound speed in water. However, using this standard value is not always sufficient. In contrast to the open ocean where the sound speed in the water column, referred to as sound speed profile (SSP), is predictable and stable, in coastal and shallow waters (continental shelves) the variations of the SSPs are irregular and hard to predict [41]. Variations of temperature and salinity affect the sound speed in the water. Also the sound speed varies with depth.

- **Temperature:** typically the temperature of the seawater, T_w, decreases from the surface to the seabed resulting in a decrease in the sound speed. The

temperature also depends on time, location and weather condition and thus there are many deviations from the general trend particularly in shallower layers [11]. Currents and tides also locally influence the temperature of the water;

- **Pressure:** an increase in the water depth increases the hydrostatic pressure[5] as well as the density and bulk modulus [63]. Consequently, the sound speed in seawater increases with pressure, and thus with depth;

- **Salinity:** for the major oceans, the salinity, S_w falls mostly between 34.5 and 35 PSU (Practical Salinity Unit), but it can locally vary depending on hydrological conditions [60]. Regarding closed seas, the average value of salinity can be quite different than that of the major oceans depending on the dominance of evaporation or fresh water input [11]. For a given location, salinity does not noticeably vary with water depth except in the shallowest layers. Typically, an increase in the salinity also increases the sound speed in water, there are some exceptions such as Arctic Ocean.

Empirical relations of varying complexity relating water column sound speed to pressure (or depth), salinity and temperature exist. As an example, the following equation given by [64], limited to a 1000 m depth, provides an estimate for the sound speed

$$ c = 1449 + 4.6T_w - 0.055T_w^2 + 0.00029T_w^3 + (1.34 - 0.01T_w)(S_w - 35) + 0.016d \, , \quad (2.11) $$

with c the sound speed (in m/s), T_w the temperature (in °C), d the water depth (in m) and salinity S_w (in PSU). The sound speed in the water column can be also derived directly using a small acoustic transducer and a reflecting surface.

Shown in Fig. 2.1 is a number of SSPs collected over a period of six months (between December 2018 to June 2019) in the Rotterdam waterway. As seen, the sound speed varies over time mainly due to seasonal temperature variations and location dependent salinity variations. The observed variations highlights the importance of regular SSP measurements.

Regarding seawater, it is often a good approximation to consider it horizontally stratified, i.e., the sound speed c is the same everywhere at a given water depth. The medium can be thus divided into a large number of horizontal layers, each of which can be considered homogeneous, with a constant though different velocity of propagation within it [59].

2.3. Interaction of sound with the seafloor

The interaction of the sound with the seabed consists of reflection, transmission and scattering where the contribution of each process depends on the frequency of the acoustic wave and the roughness of the seabed. For a perfectly flat surface,

---

[5]Hydrostatic pressure equals the total weight per unit area of water plus atmosphere supported above the water depth.
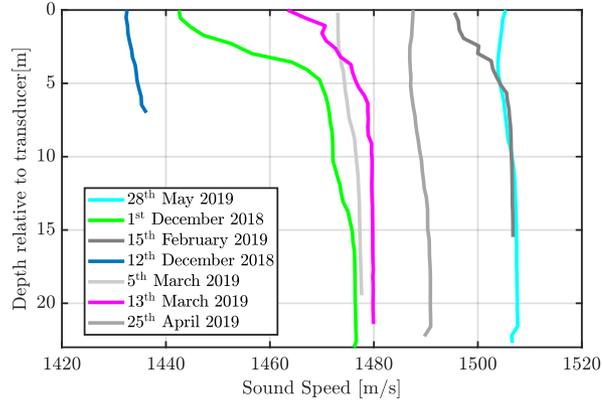
Figure 2.1: Sound speeds in the water column collected over a period of 6 months in the Rotterdam Waterway (The Netherlands). Varying colors indicate different acquisition times and locations in the waterway.

the scattering of the acoustic wave is absent and only reflection and transmission occur. The interface thus acts as a mirror where the major part of the acoustic energy is reflected and the remaining part is transmitted into the second medium. However, a seabed will never be perfectly flat and always exhibits a certain degree of roughness and heterogeneity (or inhomogenity). Consequently, in addition to reflection and transmission, part of the acoustic energy is scattered in all angles. Scattering is most significant when the acoustic wavelength, $\lambda = c/f_c$, is comparable to or smaller than the degree of the roughness and heterogeneity [11]. This implies that at low frequencies scattering becomes less important and the sediment body is often modeled as a layered medium with an impedance contrast between two adjacent layers, whereas models accounting for scattering are essential at high frequencies. Usually, a clean separation between the three processes is not possible and reflection and transmission have to be considered in the scattering model.

2.3.1. Reflection of sound at the seafloor

Assume an acoustic wave propagating in a medium as it arrives at a flat interface between two media with different acoustic impedances (ρc). Its interaction with the interface can be described by a balance between incident, refracted (transmitted) and reflected waves, Fig. 2.2. The propagation of the acoustic wave in the second medium is different than that of the first due to the change in the medium properties. One finds that:

1. The incident wave arriving with an angle ϕ_i relative to the horizontal boundary between the two media, is propagated symmetrically with respect to the interface relative to the normal to the interface with the angle ϕ_r, i.e., $\phi_r = \phi_i$. This phenomenon is referred to as specular reflection. ϕ_i is the angle between the incident wave and the surface (horizontal boundary here), referred to as the grazing angle. The angle $\theta_i = 90 - \phi_i$ is defined as the angle between

the incident wave and the surface normal and is referred to as the incident angle;

2. A part of the incident wave is transmitted (refracted) to the second medium in a direction ϕ_t depending on the change in the sound velocity. The propagation direction ϕ_t can be expressed via Snell's law as

$$\frac{\cos \phi_i}{c_0} = \frac{\cos \phi_t}{c_1} \,, \tag{2.12}$$

with c_0, c_1 the speeds in the first and second medium, respectively.

Extending the situation presented in Fig. 2.2 to the complete water column (i.e., from the surface to the bottom) and considering the water column to be horizontally stratified, Snell's Law can be used at the interfaces between layers to follow the acoustic wave through the medium and to trace out the propagation of wavefronts [7], referred to as ray tracing;
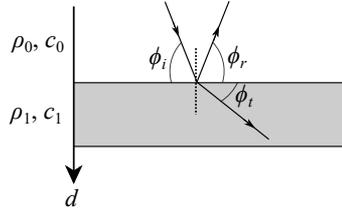
Figure 2.2: Refraction and reflection of wave with variations of the sound speed with water depth.

3. The relations between the incident pressure p_i, reflected pressure p_r and transmitted pressure p_t are given by the reflection coefficient $\mathcal{R} = p_r/p_i$ and the transmission coefficient $\mathcal{T} = p_t/p_i$. For a grazing angle ϕ_i, $\mathcal{R}$ and $\mathcal{T}$ read as

$$\mathcal{R} = \frac{\rho_1 c_1 \sin \phi_i - \rho_0 c_0 \sin \phi_t}{\rho_1 c_1 \sin \phi_i + \rho_0 c_0 \sin \phi_t} \,, \tag{2.13a}$$

$$\mathcal{T} = \frac{2\rho_1 c_1 \sin \phi_i}{\rho_1 c_1 \sin \phi_i + \rho_0 c_0 \sin \phi_t} = \mathcal{R} + 1 \,. \tag{2.13b}$$

Shown with dashed in Fig. 2.3a and Fig. 2.3b are $\mathcal{T}$ and $\mathcal{R}$ as a function of grazing angle, derived from Eq. (2.13), for the interface between water and sandy gravel (sG), muddy sandy gravel (msG), gravelly muddy sand (gmS), muddy sand (mS) and sandy mud (sM), see Table 2.1 for the characteristics of these sediments. For different sediment types the density of the medium (ρ) and corresponding sound speed (c) are derived from the empirical equations established by [65]. The sound speed in the water is assumed to be constant at 1500 m/s. For coarse sediments (e.g., sandy gravel), both the transmission and reflection coefficients are higher

than those of fine sediments (e.g., sandy mud). Sound velocity in the coarse sediments (also referred to as the fast sediments) is larger than that of water implying that the transmitted grazing angle ϕ_t is smaller than the incident wave arriving at angle ϕ_i. However, for the fine sediments (also referred to as slow sediment) the sound speed is mostly smaller than that of water, and thus $\phi_t > \phi_i$.

If $c_1 > c_0$ (fast sediment) there exists a critical angle ϕ_{crit} for which $\phi_t = 0$. Thus, for grazing angles smaller than ϕ_{crit} sound transmission into the second medium is not possible and total reflection occurs (implying that all refracted energy travels horizontally). In a lossless medium, this situation results in $|\mathcal{R}| = 1$. For the situation in which $c_1 < c_0$ a critical angle does not exist, instead, one will have an angle of intromission ϕ_{intr} at which all energy is transmitted into the second medium without any reflection, i.e., $\mathcal{R} = 0$.

In practice however, sediments represent a dissipative medium (attenuation is not zero). Attenuation is accounted for by adding an imaginary part to the real part of the sound speed, c_1, as

$$c_{1_{\text{img}}} = c_1 - \frac{i\gamma_{a_1}|c_1|^2}{\omega} \, , \tag{2.14}$$

with $c_{1_{\text{img}}}$ the complex sound speed and γ_{a_1} the sediment attenuation coefficient in Np/m. ω indicates the angular frequency $\omega = 2\pi f_c$. The expressions for the reflection and transmission coefficients Eq. (2.13) are still valid provided that the complex expression for the sound speed in the second medium Eq. (2.14) is used. It thus follows that in a lossy medium the attenuated acoustic wave can always be transmitted and propagate through the second medium, even below the critical angle. Total reflection does not occur below ϕ_{intr} and $|\mathcal{R}| < 1$, shown with solid in Fig. 2.3.
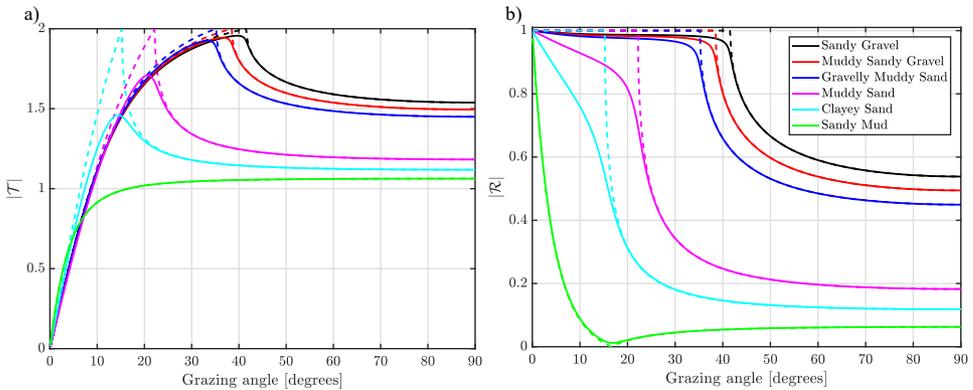
Figure 2.3: Absolute value of transmission (a) and reflection (b) coefficients versus grazing angle for the interface between water and varying sediment type, see Table 2.1 for sediment characteristics. Solid lines show lossless case ($\alpha = 0$) and dashed lines indicate lossy case (α = see the corresponding values in Table 2.1)

Sediment properties affecting the interaction of an acoustic sound wave with the

sediment are referred to as the geo-acoustic parameters. Presented in Table 2.1 are the geo-acoustic parameters corresponding to different sediment types considered in Fig. 2.3. These parameters are defined as the following

- Bulk grain size given as M_z (in phi unit Φ);

- Sound speed c (in m/s);

- Density ρ in (kg/m^3);

- Attenuation coefficient, α, in units of dB/m;

- Volume scattering parameter $\hat{\sigma}_v$, which is a dimensionless quantity;

- Spectral exponent, γ_s, which is a dimensionless quantity;

- Spectral strength η, in units of cm^4.

For sediments, often the empirical equations established by [65] are used to estimate c, ρ and α from the mean grain size. In agreement with recommendations of [66], $\hat{\sigma}_v$, γ_s and η are also related to the mean grain size.

Table 2.1: Typical values for parameters of sandy gravel (sG), muddy sandy gravel (msG), gravelly muddy sand (gmS), muddy sand (mS), clayey sand (cS), and sandy mud (sM) assuming sound speed in the water equaling 1500 m/s and a frequency of 300 kHz.

Sediment type	M_z [Φ]	c [m/s]	ρ [kg/m^3]	α [dB/m]	$\hat{\sigma}_v$ [-]	γ_s [-]	η [cm^4]
sG	-1	2005	2492	136.7	2×10^{-3}	3.25	1.29×10^{-2}
msG	0	1917	2314	136.7	2×10^{-3}	3.25	8.60×10^{-3}
gmS	1	1836	2151	144.3	2×10^{-3}	3.25	5.58×10^{-3}
mS	3	1620	1339	171.39	2×10^{-3}	3.25	2.07×10^{-3}
cS	4	1555	1223	208.74	2×10^{-3}	3.25	1.11×10^{-3}
sM	6	1481	1149	41.91	1×10^{-3}	3.25	5.17×10^{-4}

It should be noted that if the sole mechanism affecting the interaction of an acoustic sound wave with the seafloor was reflection, no echoes would arrive at the MBES. Obtaining measurements from the MBES thus would be impossible. However, apart from reflection, scattering occurs affecting the interaction of an acoustic wave with the sediment.

2.3.2. Scattering of sound at the seafloor

Considering high frequency acoustics, the roughness of the seabed becomes important making the interaction of the acoustic wave with the sediment more complex than the reflection and transmission cases discussed earlier.

When an acoustic wave (assumed locally a plane) hits the seafloor, it is scattered in all directions due to the geometry of the interface irregularities, Fig. 2.4. Part of the incoming wave is reflected with no deformation other than amplitude loss in the specular direction (i.e., coherent reflection). The rest of the energy is scattered in the entire space and part of it is returned back toward the source, referred to as the backscattered signal. It depends on the sediment type, acoustic frequency

and the incident angle [67, 68]. In general, the backscatter strength increases with an increasing grazing angle (decreasing incident angle). Its dependency on the frequency and sediment type is generally more complicated than that on the grazing angle [33, 34, 69].

The relative importance of the specular and backscattered components depends on the surface roughness in terms of the acoustic wavelength. This means that a surface appearing rough to short acoustic wavelength might appear smooth to long acoustic wavelengths. For a smooth bottom, the specular component is relatively large and the scattering component is small. For a rough bottom a reverse situation holds, i.e., small specular and large scattering components.
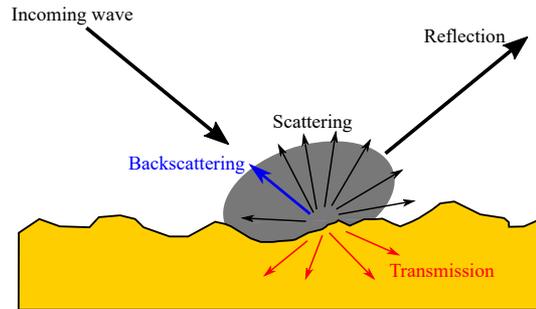
Figure 2.4: Reflection, transmission and scattering of an incoming acoustic wave due to seafloor roughness.

The scattering is described by the fundamental ratio called scattering cross section. In this thesis, the backscattering cross section is defined as the ratio between the intensity of the sound backscattered by a unit surface measured at a distance 1 m from the acoustic source $I_b(\phi_i)$ and the incident wave intensity $I_i(\phi_i)$ of a plane wave, see Fig. 2.5, and is expressed as

$$\sigma_b(\phi_i) = \frac{I_b(\phi_i)}{I_i(\phi_i)} \ .$$

(2.15)

Commonly, the intrinsic scattering property of an interface is described by the backscatter strength $BS(\phi_i)$ (in dB per m^2 at 1 m) related to the backscattering cross section as

$$BS(\phi_i) = 10 \log \sigma_b(\phi_i) \ .$$

(2.16)

The definition of the backscattering cross section and backscattering strength correspond to a unit surface (1 m^2). When quantifying scattering from an arbitrary surface A (as an example, the instantaneously ensonified area of a sound pulse on the sediment), the target's backscattering cross section $\sigma_t(\phi_i)$ (dimensionless[6])

---

[6]Throughout this thesis the scattering cross section is defined as a dimensionless ratio of two intensities in agreement with the Applied Physics Laboratory model (APL model), [66, 70]. In [71] it is mentioned that the scattering cross section can be also defined as the ratio of the scattered power to the incident intensity.

and target strength $TS(\phi_i)$ (in dB at $1\,\mathrm{m}$) are considered which are related to the backscattering cross section and backscattering strength via the instantaneously ensonified area as

$$\sigma_t\,(\phi_i) = \sigma_b\,(\phi_i)\,\frac{A}{A_1}\;,\qquad\qquad\qquad (2.17\mathrm{a})$$

$$TS(\phi_i) = BS(\phi_i) + 10\log\frac{A}{A_1}\;,\qquad\qquad (2.17\mathrm{b})$$

respectively. The term $A_1 = 1\,\mathrm{m}^2$ is the reference unit. Here, it is assumed that the backscattering cross section and backscattering strength are constant over the ensonified area A.
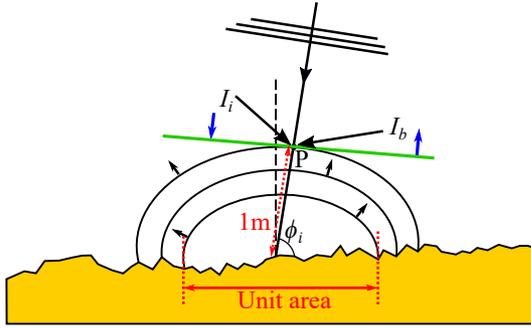
Figure 2.5: Conceptual definition of the backscatter strength and backscattering cross section.

Lambert's rule

A frequently used expression for the BS is the so-called 'Lambert rule'. This rule provides a specific grazing angle dependency of the backscatter strength according to which many rough surfaces behave. Assume that a plane wave with intensity equaling I_i impinges on an surface A at a grazing angle equaling ϕ_i. The intensity intercepted is $I_i\sin\phi_i$. The Lambert rule model states that the scattered intensity can be considered proportional to the sine of the angle of scattering (scattering grazing angle ϕ_s). The backscattered intensity, $I_b(\phi_i)$ at a unit distance can be thus expressed as [71],

$$I_b(\phi_i) = \zeta I_i(\phi_i)\sin\phi_i\sin\phi_i\;,\qquad\qquad (2.18)$$

with ζ a proportionality constant. The backscatter strength (in dB per m^2 at $1\,\mathrm{m}$) is thus of the form

$$BS(\phi_i) = 10\log\zeta + 10\log\sin^2\phi_i = BS_0 + 20\log\sin\phi_i\;,\qquad (2.19)$$

where $\zeta\;(BS_0)$ expresses the frequency and sediment type dependency of the BS. Practically observed values for BS_0 range between $-40\,\mathrm{dB}$ per m^2 at $1\,\mathrm{m}$ to $-10\,\mathrm{dB}$ per m^2 at $1\,\mathrm{m}$ [11]. An average value of $-29\,\mathrm{dB}$ per m^2 at $1\,\mathrm{m}$ is a guideline first

guess when estimating the BS from the Lambert's rule [72]. Despite its simplicity, Lambert's rule provides a good first approximation of the backscatter strength and is in good agreement with observations of the backscatter strength in many cases. Field observations of scattering from rough interfaces (rock as an example), indicate the applicability of Lambert's rule for the entire angular range. However, for fine sediments, the applicability is limited to oblique and grazing angles [11]
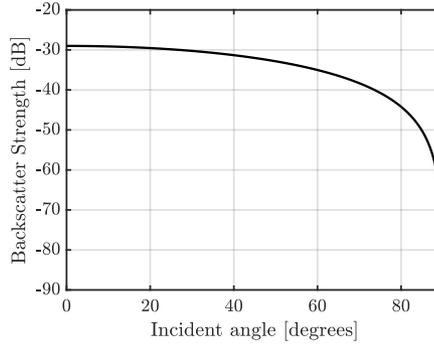
Figure 2.6: Backscatter strength as a function of incident angle as predicted by Lambert's rule with BS_0 equal to $-29\,\mathrm{dB}$ per m^2 at $1\,\mathrm{m}$.

Sophisticated backscatter strength modeling

Although Lambert's rule provides a good first approximation of the backscatter strength, it has shortcomings. It has a sine squared dependency on the grazing angle which sometimes fails to fit data [73]. Therefore, more complex backscatter strength models have been developed. These models distinguish between the interface roughness scattering $\sigma_r(\phi_i)$ and volume scattering $\sigma_v(\phi_i)$ with both contributions depending on the sediment type and grazing angle. $\sigma_r(\phi_i)$ (also referred to as interface scattering or roughness scattering) is caused by the relief of the interface. $\sigma_v(\phi_i)$ is caused by the transmission of the incident wave into the sediment and volume heterogeneities. The backscattering cross section and backscatter strength are thus expressed as

$$\sigma_b(\phi_i) = \sigma_r(\phi_i) + \sigma_v(\phi_i)\,, \tag{2.20a}$$
$$BS(\phi_i) = 10\log(\sigma_r(\phi_i) + \sigma_v(\phi_i))\,, \tag{2.20b}$$

with $\sigma_r(\phi_i) = F(\phi_i, f_c, \rho, c, \alpha, \eta, \gamma_s)$ and $\sigma_v(\phi_i) = F(\phi_i, f_c, \rho, c, \alpha, \hat{\sigma}_v)$. This means that the model requires eight input parameters discussed in Section 2.3.1.

In this thesis the APL-model [66], a modified version of the model developed by [74], is used. The model assumes a semi-infinite, dissipative, homogenous sediment without layering or gradients. For interface scattering, the relation between the acoustic wavelength and the interface is crucial which can be quantified by the Rayleigh parameter, which depends on the interface relief amplitude. A high Rayleigh parameter corresponds to an acoustically rough interface, which causes

considerable sound scattering and a negligible contribution from the coherent re-
flection. A low Rayleigh value, on the other hand, indicates an acoustically smooth
interface with a dominant contribution from coherent reflection.

In the APL-model the interface roughness scattering is modeled by a synthesis
between three different models [66]:

1. The Kirchhoff approximation is valid for smooth to moderately rough bottoms
   (e.g., clay to sand) and large grazing angles (near normal incidence);

2. The composite roughness approximation is valid for smooth to moderately
   rough bottoms (e.g., clay to sand) and small grazing angles (away from normal
   incidence);

3. The large-roughness scattering cross section is used for rough bottoms (e.g.,
   gravel and rock) and is an empirical expression.

To ensure a smooth transition between the validity domain of each model, an in-
terpolation is used.

The contribution of volume scattering σ_v incorporates refraction for a perfectly
flat water-sediment interface and attenuation in a statistically homogeneous medium.
It is further generalized to allow for the effect of absorption in the transmission co-
efficient and to correct for the acoustic shadowing and bottom slope correction
[66]. The actual scattering due to the sediment heterogeneities is based on the
volume scattering parameter $\hat{\sigma}_v$ derived empirically by comparing model predic-
tions to measured BS data. The empirical approach to sediment volume scattering
is in contrast to the approach adopted for interface scattering where the spectral
exponent and spectral strength are measurable quantities [66].
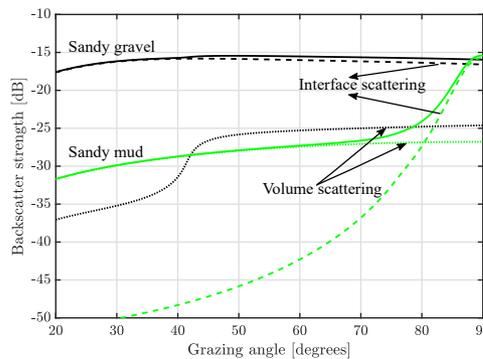
Figure 2.7: Backscatter strength as a function of grazing angle as calculated using the APL-model at
300 kHz for sandy mud and sandy gravel. The contributions of interface scattering and volumes scat-
tering are shown by dashed and dotted lines as well. Same geoacoustic parameters as used in Fig. 2.3
and presented in Table 2.1 are employed.

Fig. 2.7 shows the backscatter strength curves for the roughest (sandy gravel,
$M_z = -1\Phi$) and smoothest (sandy mud, $M_z = 6\Phi$) sediments listed in Table 2.1.

Individual contributions from the interface scattering (dashed) and volume scattering (dotted) are also visualized. Visualized in Fig. 2.8 are the typical backscatter curves for the same geoacoustic parameters as used in Fig. 2.3 and presented in Table 2.1. Based on Fig. 2.7 and Fig. 2.8, a number of observations can be made.

- The backscatter strength decreases with a decreasing grazing angle (i.e., increasing incident angle);

- For sediments with small grain size (large M_z e.g., sandy mud) roughness scattering mainly contributes for angles close to nadir, whereas volume scattering dominates for oblique and grazing incidence;

- For the larger grain size sediments (i.e., small M_z e.g., sandy gravel) the main contributor to the total backscattering is the roughness scattering due to limited penetration into the sediment;

- For muddy sand and clayey sand the difference in the backscatter strength is less pronounced hampering the discrimination between these sediment types based on the backscatter strength;

- For the input parameters and sediment types considered here, there is an overlap in the backscatter curves of all sediment types for the most outer part of the angular range, small grazing angles. An overlap in the backscatter curve for sediments smoother than gravelly muddy sand (blue) is also observed for the angular range close to nadir, i.e., large grazing angles.
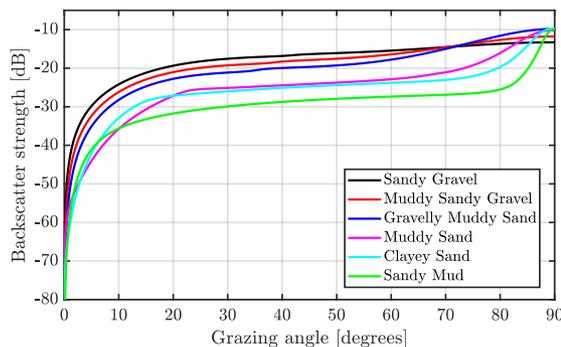
Figure 2.8: Backscatter strength as a function of grazing angle as calculated with the APL-model at 100 kHz for sediment types of Table 2.1.

It should be noted that according to [74] the APL-model is valid for frequencies ranging from 10 kHz to 100 kHz. The limitation is mainly caused by the roughness scattering model. For example, the Kirchhoff and composite roughness approximations, used to model the roughness scattering in the APL-model, require an acoustically relative smooth surface. This means that the radii of curvature of the scattering interface must be smaller than the acoustic wavelength, which might be

violated at high frequencies. However, throughout this dissertation the focus is mostly on fine sediments. Such sediments have a smoother interface than those encountered for coarse sediments. In addition, volume scattering dominates over interface scattering for the majority of the angular range [74]. Based on these arguments, modeling at frequencies higher than 100 kHz (for the systems considered in this thesis the frequency ranges from 100 kHz to 400 kHz) is assumed to be applicable [69].

2.4. Fundamentals of array processing

2.4.1. Beamforming

When using an active sonar, the system serves as a sound source (projector) and a receiver (hydrophone). Upon reception, beamforming is applied, which allows for maximizing the acoustic response for a given direction [11]. Beamforming can be also considered as a spatial filter, enabling separation of the desired part of the signal coming from a given direction from the unwanted part coming from other directions [60] and filtering out the latter.

Beamforming in active sonars requires the existence of at least two receiver or hydrophone elements. Consider a linear array made of M elements equally distanced with δL, aligned along the x-axis ($y = z = 0$) and an acoustic plane wave impinging on the array, see Fig. 2.9. The output of the array, i.e., the sum of the signals of the receiver elements (acoustic pressure), is maximum if the wavefront is parallel to the array (i.e., the acoustic wave comes from a direction perpendicular to the array) implying that all the hydrophone elements receive the signal at the same time leading to constructive interference after the summation. Now, assume that the wavefront impinges with an angle θ relative to the plane of the array (angle between the direction of propagation and the normal to the surface, i.e., incident angle defined in Section 2.3.1), see Fig. 2.9. For this situation, the path difference between elements results in a difference in the arrival times of the signal at the elements, for example, the signal is received at hydrophone 1 later than hydrophone 0. Consider $\delta r_1, \delta r_2, ..., \delta r_{M-1}$ to be the perpendicular distances from each array element to the wavefront, the angle θ can be expressed as

$$\sin \theta = \frac{\delta r_1}{\delta L} = \frac{\delta r_2}{2 \delta L} = \dots . \tag{2.21}$$

The time delay for the receiver element m referenced to the first element (hydrophone 0) thus equals

$$\tau_m = \frac{m \delta L \sin \theta}{c} \quad m = 0, ..., M - 1 , \tag{2.22}$$

corresponding to a phase delay of

$$\Delta \varphi_m = \omega \tau_m = \frac{2\pi f_c}{c} \delta r_m = 2\pi \Big(\frac{\sin \theta}{\lambda} \Big) m \delta L \quad m = 0, ... M - 1 , \tag{2.23}$$

where the term $\frac{\sin \theta}{\lambda}$ is referred to as spatial frequency ν with units m^{-1}.
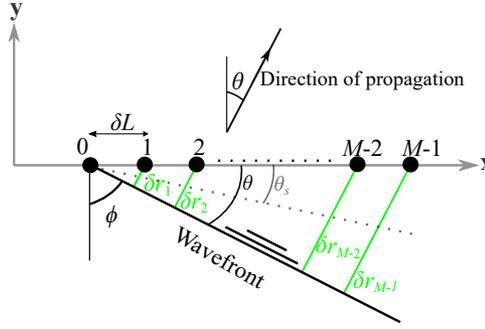
Figure 2.9: Line array of M equidistant hydrophones. Also indicated is the plane wavefront impinging the array with an angle θ with respect to x-axis. The plane wave is received on element 1 later than on element 0 by the time delay equaling τ_1. Indicated with the dashed gray is the array steered in the direction θ_s.

For the situation discussed so far (Fig. 2.9), the acoustic array response with respect to the incoming wave direction is obtained by summation over output response of all receiver elements and writing the phase delay of the signal in complex notation ($e^{i2\pi\nu m\delta L}$) as (modified from [71])

$$G(\nu) = (1 + e^{i2\pi\nu\delta L} + e^{i2\pi\nu 2\delta L} + \cdots + e^{i2\pi\nu(M-1)\delta L}) = \sum_{m=0}^{M-1} e^{i2\pi\nu m\delta L} . \qquad (2.24)$$

The concept of the phase delays is used to focus the array towards a given direction. To this end, the array is steered electronically via posing an appropriate phase delay or time delay to each array element. This means that for a steering angle of θ_s relative to the x-axis, i.e., $\nu_s = \sin\theta_s/\lambda$, the appropriate delays are such that the differences in travel times for the incoming wave (direction θ) are corrected leading to a maximization of the output pressure. The electronic phase delay for the mth array element in complex notation thus equals $e^{-2\pi i\nu_s m\delta L}$ and the acoustic array response for a steered direction θ_s with respect to the incoming wave direction θ reads as

$$G(\nu, \nu_s) = \sum_{m=0}^{M-1} e^{i2\pi(\nu-\nu_s)m\delta L} . \qquad (2.25)$$

The beam pattern is defined as the squared magnitude of the normalized array response, $G(\nu, \nu_s)$, [71]

$$b_p(\nu, \nu_s) = \left| \frac{\sum_{m=0}^{M-1} e^{2\pi i(\nu-\nu_s)m\delta L}}{M} \right|^2 . \qquad (2.26)$$

The beam pattern of Eq. (2.26) can be also expressed in terms of the incidence

angle of the incoming wave θ and steering angle θ_s as

$$b_p(\theta, \theta_s) = \left| \frac{\sum_{m=0}^{M-1} e^{ik(\sin\theta - \sin\theta_s)m\delta L}}{M} \right|^2 , \tag{2.27}$$

with k the wavenumber equaling $\frac{2\pi}{\lambda}$.

   Shown in Fig. 2.10 is the beam pattern expressed in dB ($10 \log b_p(\theta, \theta_s)$) for two steering angles derived from Eq. (2.26). The array consists of 256 elements with the total length of 0.1 m. The spatial resolution of the beamforming is defined by its main lobe, quantified as the half power width or -3 dB beamwidth Ω, and can be approximated as [60]

$$\Omega(\theta_s) = \frac{\lambda}{L \cos\theta_s} , \tag{2.28}$$

implying that the width of the main lobe increases by $1/\cos\theta_s$ with increasing steering angle, as seen in Fig. 2.10. The beam pattern has its main peak at $\sin\theta = \sin\theta_s$. The secondary peaks located next to the main lobe are referred to as the sidelobes. The sidelobes are unwanted as they result in undesired sensitivity of the array for directions other than the steering direction. Reduction of the sidelobe level is accomplished by applying different weights to the received signals on different receiving elements, referred to as array shading. Array shading selectively attenuates the received signal from some hydrophones relative to the others, reducing the sensitivity of the array for directions outside the main lobe. Varying weighting functions can be used, such as Cosine ($\cos^n$), Hamming and Tukey [60]. However, the disadvantage of weighting is widening of the main lobe of the beam pattern.
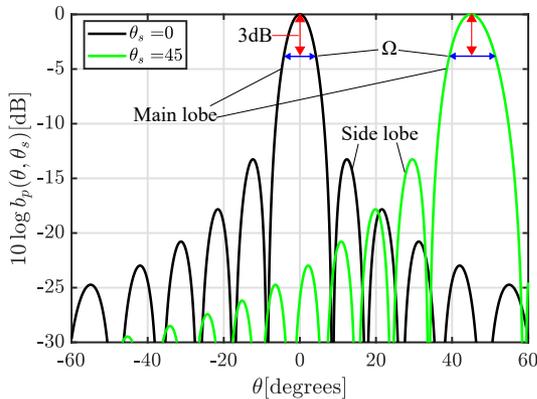
Figure 2.10: Beam pattern of an array of 0.1 m with 256 elements. The frequency of the transmitted signal and the sound speed in the water equal 100 kHz and 1500 m/s, respectively. Two steering angles of 0° (black) and 45° (green) are considered.

2.4.2. Interferometry

Interferometry is based on the constructive and destructive interference of two or more waves (acoustic or electromagnetic waves). For two receivers, receiving a signal of single source, the phase difference between the two signals depends on the difference in path lengths from the source to the receivers. In underwater acoustics, this principle is applied by measuring the phase difference between two closely spaced receivers to retrieve the difference in the path delay and to infer the corresponding angle of arrival. Limiting the situation discussed in Section 2.4.1 to two receivers, Eq. (2.23) can be rewritten as, (see Fig. 2.11)

$$\Delta\varphi = \frac{2\pi}{\lambda}\delta r = \frac{2\pi}{\lambda}\delta L \sin\theta \, . \tag{2.29}$$
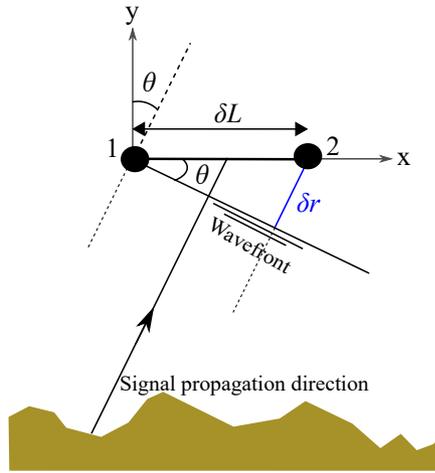
Figure 2.11: Geometry of interferometry. δL is the distance between the two receivers. θ is the direction of the incoming signal relative to the surface normal.

Thus, by measuring the phase difference, the angle of arrival can be determined. In practice, the phase difference $\Delta\varphi$ is estimated using an interferometric estimator based on the two complex signal envelopes received on the two array elements, s_1 and s_2, at a given time sample as [63]

$$\widehat{\Delta\varphi} = \arg(s_1 s_2^*) \, , \tag{2.30}$$

with * the complex conjugate operator. The values given by the complex $\arg$ operator are between $[-\pi, \pi]$. Thus, the relation between $\Delta\varphi$ and $\widehat{\Delta\varphi}$ is not direct, i.e., $\widehat{\Delta\varphi} = \mod\left(\frac{2\pi}{\lambda}\delta L \sin\theta, 2\pi\right)$ with $\mod$ the modulo operation. A counter of phase rotation $\hat{m}$ is thus introduced and $\widehat{\Delta\varphi}$ is related to $\Delta\varphi$ as

$$\widehat{\Delta\varphi} \pm 2\pi\hat{m} = \frac{2\pi}{\lambda}\delta L \sin\theta \quad \hat{m} \in \mathbb{N} \, , \tag{2.31}$$

with $\hat{m}$ the integer phase ambiguity. The estimated phase difference thus becomes ambiguous and discontinuous, referred to as phase jumps. The direction of arrival is expressed as

$$\sin\theta = \sin^{-1}\left(\frac{\widehat{\Delta\varphi}}{k\delta L} \pm 2\pi\hat{m}\right) \quad \hat{m} \in \mathbb{N}\,, \tag{2.32}$$

with $\mathbb{N}$ the set of natural numbers. To address the phase ambiguity problem, occurring as soon as δL (commonly referred to as the baseline length in the interferometry) is larger $\lambda/2$ [13] a number of approaches can be adopted. An interested reader can refer to [13, 15] for more information of different methods to resolve the phase ambiguity. In this thesis, this issue shall not be considered anymore and it is assumed that the phase difference is measured without ambiguity.

Theoretically, interferometry is a powerful and efficient technique, requiring only two receivers without needing beamforming for source localization. However, there are some practical constraints. These include unacceptable errors in case of unresolved phase ambiguities, sensitivity of phase measurements to various noise sources (see Chapter 4) and the dependency of the quality and accuracy of the measured phase difference on the baseline length and arrival angle relative to the interferometer normal axis.

2.5. Active sonar signal processing

Two types of signals are commonly used for the MBES systems, namely, Continuous Wave (CW) and Frequency Modulated (FM) signals which are briefly explained in this section.

2.5.1. Continuous wave pulse shapes

A CW pulse shape is the most commonly used waveform in MBES. This pulse shape consists of a harmonic wave with the center frequency f_c transmitted during a limited duration T. It can be expressed as a pressure wave in the form of [60]

$$s(t) = \begin{cases} \sqrt{2}p_{\mathrm{rms}}\cos(2\pi f_c t) & 0 < t < T \\ 0 & \text{otherwise} \end{cases}. \tag{2.33}$$

The frequency spectrum of such a wave is composed of two sinc functions centered at the frequencies of $\pm f_c$ [63]. Fig. 2.12 visualizes a CW pulse shape in the time domain (Fig. 2.12a) and its normalized spectrum in the frequency domain (Fig. 2.12b).

The $-3\,\mathrm{dB}$ bandwidth, i.e., the bandwidth corresponding to a $3\,\mathrm{dB}$ reduction of power from its maximum, is commonly and conveniently approximated as [11]

$$B \approx \frac{1}{T}\,. \tag{2.34}$$

For the frequency range of interest in underwater acoustics (from $12\,\mathrm{kHz}$ to
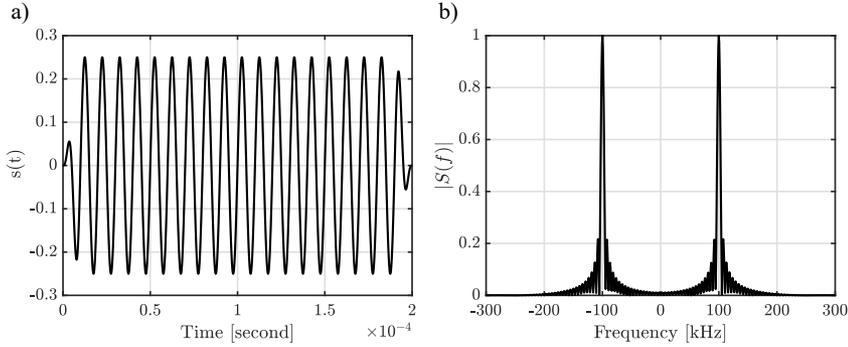
Figure 2.12: CW pulse shape with a center frequency of 100 kHz, duration of 200 μs and $p_{\mathrm{rms}} = 0.176\,\mu\mathrm{Pa}$ in the a) time domain and b) frequency domain.

700 kHz) and pulse lengths ranging from 0.1 ms to 10 ms, the ratio of $\frac{B}{f_c}$ is small (narrowband signals).

Range resolution is the ability of a sonar to distinguish between two or more objects at the same angular direction to the sonar but at different ranges. The range resolution depends mainly on the bandwidth of the transmitted pulse, derived from Eq. (2.34) for a CW pulse shape, and the type and size of the target. For a CW pulse with a duration of T the range resolution δr_{res} reads as

$$\delta r_{\mathrm{res}} = \frac{cT}{2} \; , \tag{2.35}$$

where the factor 2 in the denominator implies using an active sonar, and thus the difference in distance between two objects is travelled twice. Theoretically, high range resolution can be obtained using very short CW pulses. However, pulses cannot be made too short as they must contain enough energy to be detectable against the noise. The main advantage of a CW pulse is simplicity of its generation and processing, along with acceptable performance in many applications. Due to their narrow frequency band, it is cheap, easy and efficient to use. However, the main drawback of CW pulses is that to ensure high resolution, short pulse length is required and thus the Signal-to-Noise ratio (SNR) is compromised.

2.5.2. Frequency modulated pulse shapes

An FM pulse, also referred to as chirp, is a signal with increasing (up-chirp) or decreasing (down-chirp) frequency with time. In underwater acoustics, Linear Frequency Modulated (LFM) pulses are widely used and thus discussed here[7]. An up-chirp FM signal with a center frequency of f_c, bandwidth of B and pulse duration of T can be expressed as a pressure wave in the form of

$$s(t) = \begin{cases} \sqrt{2}p_{\mathrm{rms}} \cos\left(2\pi\left[(f_c - \frac{B}{2})t + \frac{\kappa}{2}t^2\right]\right) & 0 < t < T \\ 0 & \text{otherwise} \end{cases}, \tag{2.36}$$

---

[7]Throughout this the term FM is used for referring to LFM unless otherwise stated.

with κ the chirp rate equaling $\kappa = B/T$ and $f_c - B/2$ the minimum frequency. The instantaneous frequency of such a signal is obtained from

$$f(t) = f_c - \frac{B}{2} + \kappa t \; . \tag{2.37}$$

If the product TB is large enough, the spectrum of such an FM pulse can be approximated by a rectangular function with the width equaling the bandwidth B [46, 49]. It has been shown that for $TB > 10$, 95% of the signal's energy is included in the frequency range $|f - f_c| \leq B/2$. When $TB > 100$, the percentage increases to 99% [75]. Visualized in Fig. 2.13 is an FM pulse shape in the time domain, Fig. 2.13a, and its normalized spectrum in the frequency domain, Fig. 2.13b.
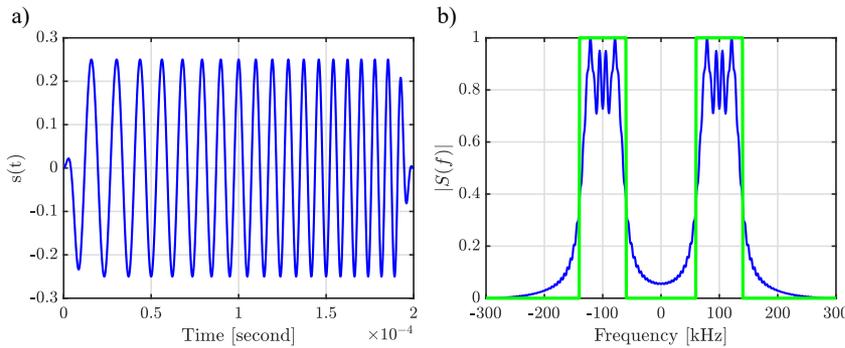
Figure 2.13: FM pulse shape with a center frequency of 100 kHz, bandwidth of 80 kHz, duration of 200 µs and $p_{\mathrm{rms}} = 0.176\,\mu\mathrm{Pa}$. Shown with green is the approximated rectangular spectrum for the FM pulse.

2.5.3. Matched filtering

Matched filtering is a signal processing technique, which is used to detect a known signal disrupted by noise. In sonar and radar systems it is most often applied to modulated signals. The matched filtering, also referred to as pulse compression, correlates the received signal with a replica of the transmitted pulse. The resulting correlation is a measure of the similarity between the two signals. If the received signal is the delayed version of the transmitted pulse (the shape of the signal is similar), the correlation function only has a peak at the time corresponding to the delay. When the matched filtering is used, a pulse with an effective duration of $1/B$ with B being the bandwidth of the signal is obtained. This implies that using a signal with large bandwidth leads to a very good range resolution. The range resolution after the matched filtering is defined as

$$\delta r_{\mathrm{res}} = \frac{c}{2B} \; . \tag{2.38}$$

Shown in Fig. 2.14c and Fig. 2.14d are the matched filtered output for a CW signal with a frequency of 1000 Hz and duration of 0.01 s (see Fig. 2.14a) and an

FM signal with the same frequency and duration and a bandwidth equaling $600\,\text{Hz}$ (see Fig. 2.14b), respectively. For the CW signal, the bandwidth equals the inverse of the pulse duration (see Eq. (2.34)). Therefore, applying the matched filtering does not improve the range resolution. Regarding the FM signal, the energy after the matched filtering is compressed over a duration of $1/B$ (for the pulse considered this equals $0.0017\,\text{s}$) instead of spreading over a duration of T ($0.01\,\text{s}$), and thus the range resolution is improved.
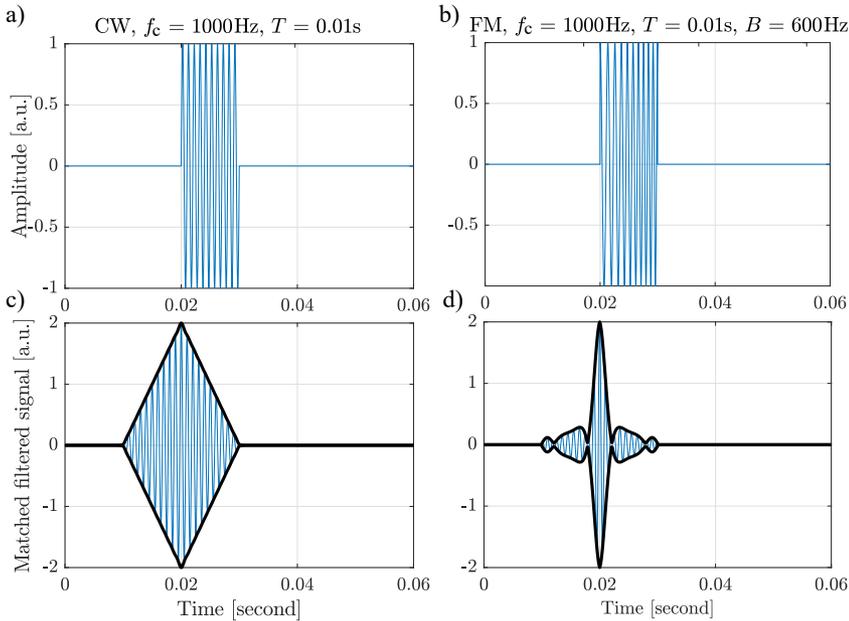
Figure 2.14: a) CW signal with a center frequency of $1000\,\text{Hz}$ and duration of $0.01\,\text{s}$ with c) its matched filtered output, b) FM signal with a center frequency of $1000\,\text{Hz}$, duration of $0.01\,\text{s}$ and bandwidth of $600\,\text{Hz}$ with d) its matched filtered output, shown with the black in are the envelope of the matched filtered signal.

As the bandwidth of the FM signal increases, the effective duration becomes smaller, resulting in a higher range resolution. Illustrated in Fig. 2.15 is the matched filtered output for two FM pulses with the same center frequency and pulse duration and different bandwidths. The FM signal with larger bandwidth (green) has a smaller effective duration (narrower main lobe) and consequently a higher range resolution. The gain due to the matched filtering is equal to SNR at the output of the filter divided by that the input, expressed either in ratio, pg, or decibels $PG = 10\log pg$ [60] and is expressed as

$$pg = BT \,. \tag{2.39}$$

For a CW pulse shape, no PG is expected and the SNR at the receiver output is equal to that of the input, and hence matched filtering is not applied when using this

pulse shape. Regarding an FM signal, an increase in the SNR due to the matched filtering is expected and T and B can be increased independently leading to a high processing gain compared to a CW pulse. However, the matched filtering process for FM pulses imposes a heavier processing burden than that of CW.
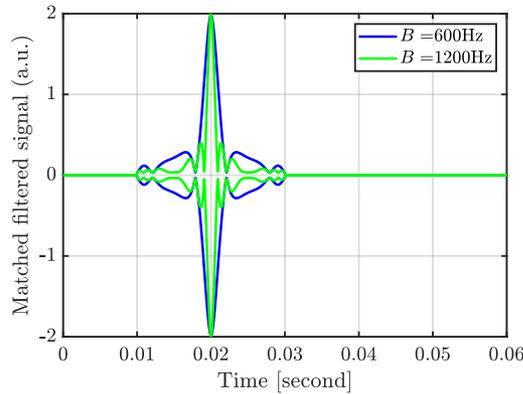
Figure 2.15: Output of matched filtering (pulse compressed) for two FM signals with a center frequency of 1000 hertz, duration of 0.01 s with varying bandwidths of 600 Hz (blue) and 1200 Hz (green).

2.6. Multibeam echosounder theory

2.6.1. General information

The MBES is an active sonar mounted on a vessel hull or underwater vehicle and consists of a transmission and reception module. These two, which form the sonar head, can be either separated (e.g., R2Sonic 2026 in Fig. 2.16b) or both located in one unit (e.g., Kongsberg EM2040C in Fig. 2.16a).

The transmission module of a MBES consists of an array of projectors and associated electronics. Similarly, the reception array consist of receiving transducers (array of hydrophones) and associated electronics. Most of the underwater acoustic transducers make use of the piezoelectric properties of some crystals, natural or synthetic (ceramics) to transmit and receive an acoustic signal [11]. When an electrical field is applied to a piezoelectric material, a mechanical deformation occurs, which in turn generates an acoustic wave. Upon reception, the reverse situation holds.

The transmission unit is basically in charge of signal generation (shape, duration, level and frequency), power amplification and impedance matching [11]. The transmission electronics must also control the transmission sector characteristics, its aperture and tilt based on the configuration parameters and information from the platform motion. The reception unit consists of the hydrophone array, preamplifier, Analog to Digital Convertor (ADC) and filters. This unit performs digitization from the electrical voltage to digitized values. The reception unit is also responsible for beamforming, frequency filtering, elementary bathymetry measurement,

correction of the platform motion (roll stabilization) and correction of the acoustic path refraction via ray tracing.

To obtain the bathymetry and backscatter measurements accurately, the MBES has to receive and process data from several ancillary sensors, see Fig. 2.16c. These are

- **Positioning systems** to obtain the accurate geographical location of the vessel. Different positioning techniques can be used with varying degrees of accuracy, from Global Navigation Satellite Systems (GNSS) (~meter-level of accuracy) to Differential GNSS (DGNSS) (~decimeter-level accuray) to Real Time Kinematic (RTK) (~centimeter-level accuracy) [36]. Nowadays, GNSS in RTK or preferably Network RTK modes are used;

- **Motion sensors** for angular measurements (heading, roll, pitch and heave) and corrections of the vessel movement;

- **Sound velocity profiler** for correcting the acoustic path between the sonar and seafloor (see Section 2.2.1);

- **Sound velocity probe at the receiving module** for accurate beamforming (see Section 2.4.1).
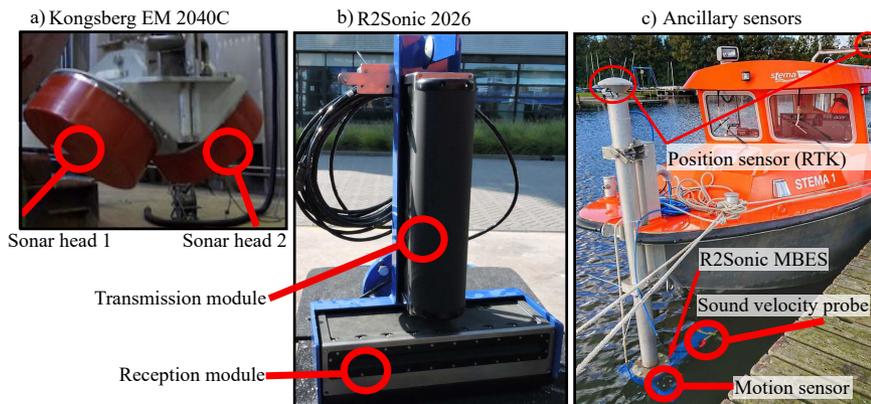
Figure 2.16: a) High frequency dual-head Kongsberg EM2040C MBES (200 kHz to 400 kHz), b) High frequency single-head R2Sonic 2026 MBES (90 kHz to 450 kHz). c) An example of the ancillary sensors. This figure is taken from [76].

A MBES transmits and receives beams over a wide angular range (the 'swath') at each time instant (ping) with a small width in the along-track direction Fig. 2.17. Beamforming at reception creates numerous receiving beams steered at different across-track directions (see Section 2.4.1). This allows one to have simultaneous measurements from adjacent portions of the seafloor independently.

Three shapes of the receiving array are usually employed in MBES systems, i.e., horizontal linear, V-shaped and U-shaped. The horizontal linear array is the simplest

configuration (e.g., R2Sonic 2026 in Fig. 2.16b). However, it may cause installation problems on the hull due to large steering angles required for the outer part of the swath. V-shaped arrays, commonly referred to as dual head MBES, consist of two linear arrays mounted at a certain angle relative to each other, working independently (see e.g. the Kongsberg EM2040C in Fig. 2.16a with two sonar heads). This configuration allows for large steering angles and thus increases the swath width. Moreover, the simplicity in the processing is preserved as this array is based on two linear arrays. U-shaped arrays have a circular section enabling beamforming for an angular subset of the array orthogonal to the intended beam direction.
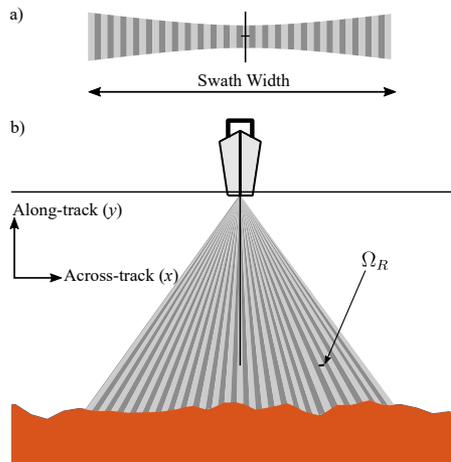
Figure 2.17: Schematic overview of the MBES measurements along with swath width in the across-track direction. a) Top view, b) Side view with the across-track beam opening angle Ω_R.

For the spacing of the beams, two modes are usually used [77]:

- An equiangular spacing leads to a uniform spacing between the beam angles. This means that the resulting spacing on the bottom is not uniform along the swath. For beams close to nadir, the beam spacing is smaller and the density of the measurements is higher. However, as one moves toward the outer parts of the swath, the spacing increases, leading to a decrease in the density of the measurements;

- An equidistant mode leads to a uniform spacing on the bottom meaning that the spacing between the beams across the swath is equal. The beam angles are thus adjusted to fulfill such requirement.

2.6.2. Multibeam echosounder bathymetric measurements

A MBES calculates the depth relative to the sonar by estimating the Two-Way Travel Time (TWTT) t_D for a known beam angle Θ. Θ is defined with respect to the vertical (nadir) and thus equals θ for a flat seafloor and horizontal array as shown

in Fig. 2.18. The beam angle Θ differs from the steering angle at reception θ_s by the mounting angle of the MBES and also by the roll angle derived from the motion sensor. The latter holds in case the MBES applies real time roll correction.

For a constant sound speed in the water column, the acoustic ray path from the MBES to a point on the seafloor is linear, and thus the range r equals $r = \frac{ct_D}{2}$. The corresponding depth relative to the MBES d and across-track distances x from nadir are expressed as (see Fig. 2.18)

$$d = r \cos \Theta = \frac{ct_D}{2} \cos \Theta \,, \tag{2.40a}$$

$$x = r \sin \Theta = \frac{ct_D}{2} \sin \Theta \,. \tag{2.40b}$$

However, in reality the sound speed in the water column varies with temperature, pressure and salinity, see Section 2.2.1. Therefore, the acoustic path has to be reconstructed using ray-tracing.
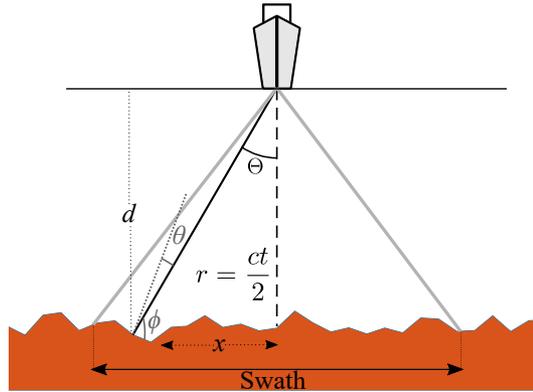
Figure 2.18: Measurements of the pair (t_D, Θ) for bathymetry measurements as done in the MBES

Resolution

The MBES along-track resolution, δy_d for bathymetry is defined by the beam opening angle at transmission, representing the $-3\,\text{dB}$ width of the main lobe as

$$\delta y_d = r\Omega_T \,, \tag{2.41}$$

with $\Omega_T = \frac{\lambda}{L_T}$ beam opening angle in the along-track direction and L_T the length of the transmission array.

The across-track resolution of MBES derived depth measurements is determined by projecting the across-track beam opening angle on the seafloor and reads as

$$\delta x_d = \frac{d\Omega_R}{\cos^2 \Theta} \,, \tag{2.42}$$

with Ω_R the across-track beam opening angle (beam opening angle at reception) equaling $\Omega_R = \frac{\lambda}{L_R \cos \theta_s}$ with L_R the receiving array length. As the steering angle increases (outer parts of the swath), the beam opening angle increases, and thus the across-track resolution is worsened. In reality, the bathymetry across-track resolution limits the attainable swath width for systems using conventional beamforming.

2.6.3. Bottom detection

As mentioned in Section 2.6.2, the depth below the MBES and the across track distance from nadir are determined using t_D and Θ, i.e., the pair (t_D, Θ). For MBES systems the beam angle Θ is considered to be known and the arrival time of the signal is determined for a set of predefined beam angles. This can be done using either amplitude or phase information of the received signal.

Amplitude detection

To perform amplitude detection with the MBES, the instant corresponding to the maximum energy or Center Of Gravity (COG) of the received signal envelope beamformed in a given direction is estimated. Signal arrival time t_D in the COG approach is estimated from the acoustic pressure as [78]

$$t_D = \frac{\sum_i t_i p(t_i)}{\sum_i p(t_i)} \, , \tag{2.43}$$

with t_i a time sample and $p(t_i)$ the pressure of the received beamformed signal in a given direction at the time instant t_i. Shown in Fig. 2.19 is the beamformed pressure signal at 300 kHz for different steering angles. As seen, the peak corresponding to the main lobe can be clearly identified for the beam steered at 11° (and to some extent for 31°). For beam angles close to nadir, any of the amplitude detection techniques performs well. However, with increasing beam angle the peak of the echo envelope becomes less sharp. The detection instant is thus derived using COG calculation. Illustrated in Fig. 2.20 is an example of t_D estimation based on the COG (dotted blue) and the instant corresponding to the maximum energy of the signal (dotted dashed gray) along with the true arrival instant (dashed black) for a beam steered 10° from nadir. Here, the estimate based on COG is closer to the true arrival time than the one based on the maximum energy of the signal.

The results shown here are without taking the effect of SNR into account. An interested reader is referred to [29, 78, 79] for a discussion on the effect of varying parameters, such as pulse length and SNR, on the calculation of the COG.

Phase detection

As one moves toward the outer parts of the swath, i.e., increasing beam steering angle, the echo time spreading becomes very wide, as an example see the signals at 51° and 61° in Fig. 2.19. Therefore, the instant derived based on amplitude detection (either using the COG or maximum intensity of the signal) does not provide an accurate and a reliable estimate, see the dotted blue and dotted dashed gray
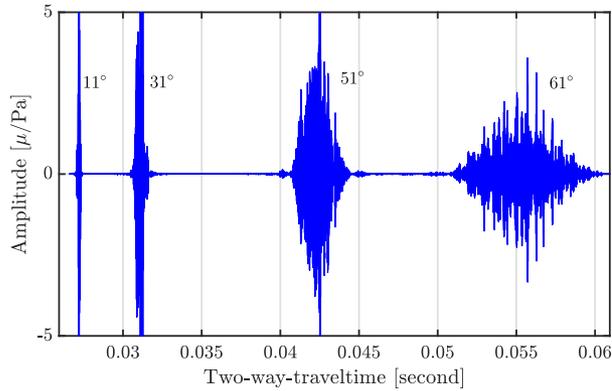
Figure 2.19: Modeled pressure signal steered at 11°, 31°, 51° and 61° assuming a MBES with a center frequency of 300 kHz transmitting a CW pulse with the duration of 50 μs and a clayey sand bottom ($M_z = 4\Phi$). The signals associated with the different steering angles are separated signals arriving at different time instances and plotted on the same time axis.
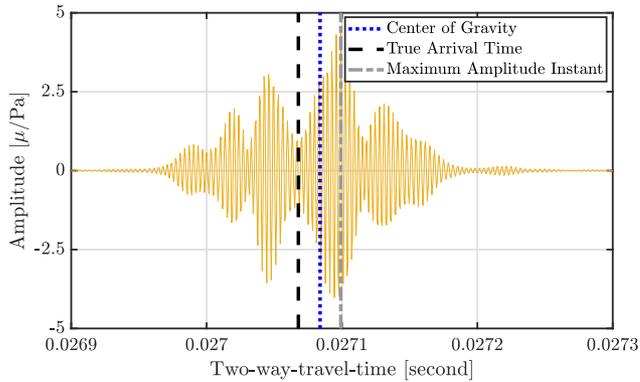
Figure 2.20: Modeled pressure signal steered at 10° for the same transmitted signal and bottom properties considered in Fig. 2.19. Shown with dotted blue and dotted dashed gray are the estimates of t_D based on COG and the instant corresponding to maximum energy of the signal, respectively. The true arrival time is shown by dashed black.

lines in Fig. 2.21. An alternative technique is to use phase detection which is based on interferometry and phase difference measurements discussed in Section 2.4.2.

To perform phase detection with a MBES, the array of length L is divided in two sub-arrays where the distance between the centers of these two sub-arrays, i.e., baseline length, is usually taken as a half or one-third of the array length. The received signals on the two sub-arrays are beamformed for a same angular direction. As a next step the phase difference Eq. (2.30) between the complex envelope of the received signal on the two sub-arrays is calculated.

For the two beamformed signals in a given steering direction, when the footprint on the seafloor is located at an angular direction equal to the steering direction,

the range from the footprint to each sub-array is equal, and thus the phase difference equals zero. Therefore, a phase difference of zero (zero-phase crossing) represents the estimate of the arrival time t_D. Fig. 2.21 visualizes $\widehat{\Delta\varphi}$ as a function of time (orange). As $\widehat{\Delta\varphi}$ is intrinsically noisy, the zero-phase crossing (solid magenta) is calculated by fitting a low-order polynomial to the estimated phase difference using the least-squares method (solid green) and thus the instantaneous phase fluctuations are smoothed. Although this reduces the uncertainty of the arrival time estimate (its standard deviation is proportional to $1/\sqrt{n_p}$), the resolution is deteriorated, i.e., the estimated t_D is no longer a local one as a series of neighboring samples is used. Therefore, a trade-off has to be made between uncertainty and resolution. An elaborated discussion on modeling the standard deviation of the phase measurements due to the physical structure of the returned signal can be found in [16, 29].
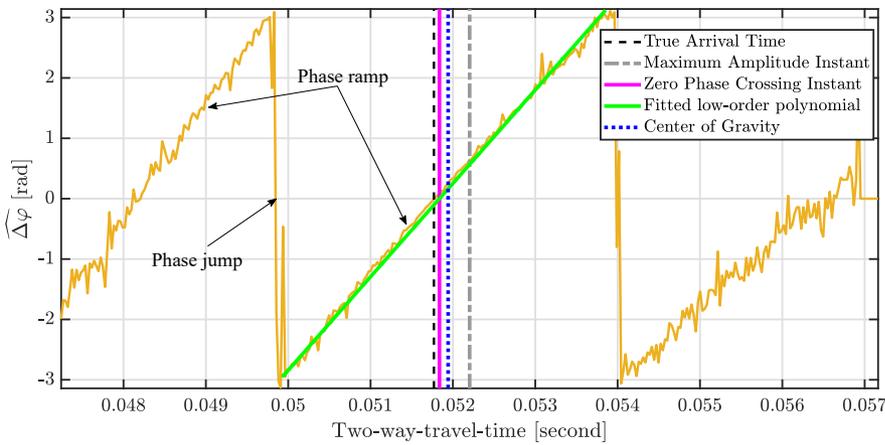
Figure 2.21: Phase difference $\widehat{\Delta\varphi}$ between a simulated pressure signal measured at the two sub-arrays (orange) for the same transmitted signal and bottom properties considered in Fig. 2.19. Both sub-arrays consist of 128 elements and the distance between the centers of these sub-arrays equals 0.25 m. The phase difference is calculated from the beamformed signals at 61°. The instants corresponding to the maximum amplitude of the signal (dotted dashed), estimate of the COG (dotted blue), zero-crossing of the phase difference (solid magenta) and the true arrival time (black dashed) are illustrated. A second-order polynomial is fitted to the phase difference to identify the zero-crossing (green).

As mentioned, when using the measurements of the phase difference, one should account for the phase ambiguity, $\hat{m}$ in Section 2.4.2 which can be accomplished using different techniques. These ambiguities, also referred to as the phase jumps, are shown as discontinuities in the phase measurements in Fig. 2.21. Between these jumps, the so-called phase ramps are located containing the actual zero-crossing. Here, the estimated arrival time using the COG detection method is used to locate the correct phase ramp. In general, since the prerequisite for phase detection using MBES is to beamform the received signal in a given steering direction, one can assume that these received signals are narrow enough to give a non-ambiguous estimate of the zero-phase crossing [79]. Limiting the processing to

the beamformed signals also minimizes the effect of footprint shift, a phenomenon that occurs due to the fact that the different sub-arrays receive simultaneous echo contributions coming from slightly shifted parts of the seafloor [16].

2.7. Multibeam echosounder bathymetric uncertainty modeling

Applications of MBES depth measurements are numerous, including offshore activities, dredging operations, safe navigation, and the study of marine geological and biological systems [23, 80–82]. The MBES bathymetric measurements and its derivatives, such as depth residuals, (along with backscatter measurements) are often used for obtaining the required information. However, similar to any type of measured quantity, they are contaminated by uncertainties. In this section, different uncertainty sources affecting the quality of MBES derived depths are discussed.

As discussed in Section 2.6.2, the depth of a sounding from the transducer is determined using the pair (t_D, Θ). The situation depicted in Fig. 2.18 assumes zero roll and pitch angles of the vessel. It also assumes zero across-track angle under which the MBES is mounted. This means that for the situation shown in Fig. 2.18, Θ equaled the beam steering angle relative to the transducer normal Eq. (2.40). Now assume a roll angle of the vessel and an across-track angle under which the MBES is mounted on the vessel equal R and θ_{mount}, respectively, see Fig. 2.22. The beam angle Θ with respect to nadir (depth-axis) can be defined as $\Theta = \theta_s + R + \theta_{\mathrm{mount}}$. Considering this definition and P as the pitch angle, Eq. (2.40)a still holds and is rewritten as

$$d = r \cos P \cos(\theta_s + R + \theta_{\mathrm{mount}}) = r \cos P \cos \Theta . \tag{2.44}$$
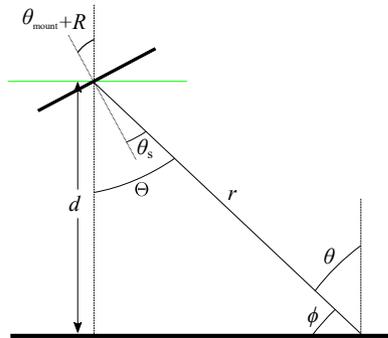
Figure 2.22: Schematic of the MBES array, illustrating the angles of relevance for calculating the depth relative to the MBES.

Here, it is assumed that the distance between the transmission and reception arrays is negligible in relation to the distance between the MBES and the seafloor, and hence no distinction is made between them. The bathymetric uncertainty sources can be categorized as

1. Echosounder contribution, $\sigma_{d_{ES}}$, due to the uncertainties in the measurements of the range between the transducer and a point on the seafloor (composed of the travel time of the signal and speed of sound) and angle of impact of the incoming sound wave at the transducer. The non-zero beam opening angle in the along-track direction also contributes to the $\sigma_{d_{ES}}$;

2. Angular motion sensor contribution, $\sigma_{d_{AngMot}}$, due to the uncertainties in roll and pitch measurements and imperfectness of their corrections;

3. Motion sensor and echosounder alignment contribution, $\sigma_{d_{Align}}$, due to the discrepancies between the roll and pitch angle measurements at the motion sensor and the transducer;

4. Sound speed contribution, $\sigma_{d_{SS}}$, due to the sound speed uncertainties at the receiving array (for beamforming) and those of the water column (for ray tracing);

5. Heave contribution, σ_H, due to the uncertainties in the heave measurements and those from roll and pitch uncertainties. In case of using GNSS for vertical positioning, the uncertainty of the heave measurements is replaced by the uncertainty of the vertical component of the GNSS.

Assuming the above contributors are uncorrelated, the corresponding total depth uncertainty relative to the MBES reads as

$$\sigma_{\hat{d}}^2 = \sqrt{\sigma_{\hat{d}_{ES}}^2 + \sigma_{\hat{d}_{AngMot}}^2 + \sigma_{\hat{d}_{Align}}^2 + \sigma_{\hat{d}_{SS}}^2 + \sigma_H^2} \, . \tag{2.45}$$

Here, a short description of the contributions is given. An interested reader may refer to [26, 27] for a complete derivation of all the relevant equations.

Before proceeding, a comment on the vessel coordinate system is in order. In references [26, 27] a right handed coordinate system with positive Y-axis to the port and positive X-axis to the bow of the vessel was considered. The z-axis thus points to the up direction. The definition of the vessel coordinate system is not unique and the manufacturers of the software acquisition system and post-processing can define a different coordinate system. As an example, the Quality Positioning Services (QPS) BV, products of which are used in thesis for data acquisition, defines the vessel coordinate system to be right handed with positive X-axis to the starboard and positive Y-axis to the bow (Z-axis thus points to the up direction). Throughout the thesis, this coordinate system is adopted. Therefore, equations presented in this section differ from those of [26, 27]. This means that the y coordinate defined by [26] is the $-x$ coordinate defined by QPS and the x coordinate of [26] is the y coordinate of QPS.

2.7.1. Echosounder contribution

The echosounder contribution, $\sigma_{d_{ES}}$, can be divided into uncertainties in range σ_{d_r} and beam angle $\sigma_{d_{\Theta_{meas}}}$ along with the contribution of the along-track beam opening

angle $\sigma_{d_{\Omega_R}}$. σ_{d_r} is given by

$$\sigma_{d_r}^2 \approx (\cos P \cos \Theta)^2 \left(\sigma_{r_{\mathrm{meas}}}^2 + \left(\frac{r_{\mathrm{meas}}}{c_{\mathrm{meas}}}\right)^2 \sigma_{c_{\mathrm{meas}}}^2 \right), \qquad (2.46)$$

with r_{meas} and c_{meas} the measured range and speed of sound, respectively. Eq. (2.46) is valid under the assumption that the true sound speed in the water does not deviate too much from the measured average sound speed in the water column. $\sigma_{c_{\mathrm{meas}}}$ is the uncertainty in the measurement of the average sound speed. The uncertainty in the measured range $\sigma_{r_{\mathrm{meas}}}$ depends on the type of MBES and is affected by sampling resolution and pulse length and is given by [26, 27]

$$\sigma_{r_{\mathrm{meas}}}^2 = \left(\frac{\delta r_s}{2}\right)^2 + \left(\frac{cT}{4}\right)^2, \qquad (2.47)$$

with δr_s and cT the range sampling resolution and the pulse length (in m), respectively. The first term reflects the uncertainty induced by a finite sampling rate. There are a number of issues arising with this term:

1. The term 'range sampling resolution' is often mixed up with the term 'range resolution', see Eq. (2.35). The former is calculated from the sampling frequency or sampling rate, which is the number of signal samples per second, as $\delta r_s = c/f_s$ with f_s the sampling frequency. The range resolution, on the other hand, is the ability of a sonar to distinguish between two or more objects at the same angular direction to the sonar but at different ranges. It increases with increasing pulse length and is accounted for in the calculations of the depth random uncertainty, see the second term in Eq. (2.47);

2. Another issue related to the range sampling resolution is the sampling frequency. The reported value for this parameter is the output sampling frequency which is different from the one used for applying the bandpass filters and beamforming with the latter being higher. Knowledge of this value is thus required;

3. The term used for describing the uncertainty in the range measurements, Eq. (2.47), is found to overpredict the uncertainties [27]. Therefore, this term is scaled by 0.707 compared to [26].

Depth uncertainty due to the uncertainty in the measurements of the beam angle $\sigma_{d_{\Theta_{\mathrm{meas}}}}$ is obtained from

$$\sigma_{d_{\Theta_{\mathrm{meas}}}}^2 = \left(r \sin \Theta \cos P\right)^2 \sigma_{\Theta_{\mathrm{meas}}}^2, \qquad (2.48)$$

where $\sigma_{\Theta_{\mathrm{meas}}}$ depends on the bottom detection method (see Section 2.6.3), i.e., amplitude or phase detection, and the type of transducer array and reads as

$$\sigma_{\Theta_{\mathrm{meas}}} = \begin{cases} \frac{1}{12}\Omega_R & \text{Amplitude detection} \\[2mm] \frac{0.2}{\sqrt{n_p}}\Omega_R & \text{Phase detection} \end{cases}, \qquad (2.49)$$

with Ω_R the across-track beam opening angle, i.e., beam opening angle at reception. n_p indicates the number of phase samples, defined as [83]

$$n_p = \frac{\frac{d\Omega_R}{\cos^2\Theta}}{\frac{cT}{2\sin\Theta}} \ . \tag{2.50}$$

Eq. (2.49) does not take the effect of a particular pulse shape into account. An alternative approach presented in [54, 84] does account for the pulse shape in determining uncertainties in the detection instant in the interferometry step, i.e., relevant for the phase detection. This is accomplished using the coherence coefficient which is a measure for the correlation between the two received signals at the two sub-arrays, see Chapter 4.

In references [26, 27] the selection of the bottom detection method was based on n_p. If $n_p > 12$, phase detection was used, otherwise amplitude detection was chosen as the detection method. However, this criterion does not hold for modern MBES systems and the selection of the bottom detection method is based on their performance. Throughout this thesis, this approach is taken. This means that the angular measurement uncertainties induced by both detection techniques are calculated and the technique with the smaller uncertainty is chosen.

An additional point concerns the across-track beam opening angle. In references [26, 27], the beam opening angle in the across-track direction was assumed constant, and was derived from the manufacturer specification (i.e., corresponding to the opening angle at nadir). However, as the beam steering angle increases, the length of the array projected on the steering direction decreases leading to an increase in the beam opening angle, see Eq. (2.28). The beam opening angle also varies with frequency, i.e., it decreases with an increasing frequency. To account for these issues, Eq. (2.28) is used in Eq. (2.49).

As discussed in Section 2.6.2, Eq. (2.41), the beam opening angle in the along-track direction Ω_T limits the depth resolution, i.e., the resolution is deteriorated with increasing Ω_T. For a non-flat seafloor, non-zero opening angle in the along-track direction results in a depth uncertainty. The actual error due to Ω_T depends on the variation of the water depth in the area. Since this variation is unknown, a scenario depicted in Fig. 2.23 is assumed, in which the range at the outer beam is equal to the depth below the vessel. The resulting depth uncertainty is

$$\sigma_{d_{\Omega_T}} = d\left(1 - \cos\frac{\Omega_T}{2}\right) . \tag{2.51}$$

The total contribution of the echosounder to the depth uncertainty is thus obtained from

$$\sigma^2_{d_{\mathrm{ES}}} = \sigma^2_{d_r} + \sigma^2_{d_{\Theta_{\mathrm{meas}}}} + \sigma^2_{d_{\Omega_T}} . \tag{2.52}$$

2.7.2. Angular motion contribution

In general, roll R and P are measured by the motion sensor on the vessel. Their uncertainties contribute to the uncertainties in the depth measurements $\sigma^2_{d_{\mathrm{AngMot}}}$.
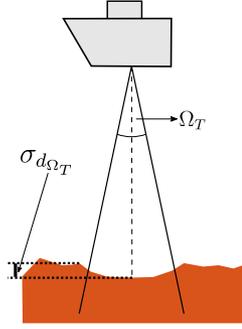
Figure 2.23: Side view with beam opening angle in the along-track direction Ω_T and the resulting depth uncertainty $\sigma_{d_{\Omega_T}}$.

These contributions are denoted by $\sigma_{R_{\text{meas}}}$ and $\sigma_{P_{\text{meas}}}$, respectively. The resulting depth uncertainty is derived from

$$\sigma_{d_{\text{AngMot}}} = (r \cos P \sin \Theta)^2 \sigma_{R_{\text{meas}}}^2 + (r \sin P \cos \Theta)^2 \sigma_{P_{\text{meas}}}^2 . \qquad (2.53)$$

2.7.3. Motion sensor and transducer misalignment contribution

When considering the angular contribution, one should take into account that ideally the measurements made by a MBES must be relative to the true vertical and heading reported by the motion sensors. Upon installation of these sensors on the vessel, achieving a perfect alignment is not possible. Therefore, an additional calibration process, referred to as patch test, must be performed to derive actual offsets. Inaccuracy of the pitch and roll offset values derived from the patch test ($\sigma_{\Delta P_{\text{Align}}}$ and $\sigma_{\Delta R_{\text{Align}}}$, respectively) induces a depth uncertainty $\sigma_{d_{\text{Align}}}$ derived from

$$\sigma_{d_{\text{Align}}}^2 = (r \cos P \sin \Theta)^2 \sigma_{\Delta R_{\text{Align}}}^2 + (r \sin P \cos \Theta)^2 \sigma_{\Delta P_{\text{Align}}}^2 . \qquad (2.54)$$

A brief discussion on the motion stabilization available in the MBES and its effect on the depth uncertainty prediction is in order. Roll stabilization is a mechanism for ensuring a uniform swath width and avoiding any gaps between adjacent survey lines and is applied upon reception (during the beamforming process). As for the pitch stabilization, it is done by steering the transmit beam forward and backward (in the along-track direction) and ensures equal density around the reference angle [85]. In case roll and pitch stabilization are applied, additional uncertainties emerge due to the imperfectness of these stabilization process. A second pair of roll (alignment) uncertainties, $\sigma_{R_{\text{meas}}}$ and $\sigma_{\Delta R_{\text{Align}}}$, and pitch (alignment) uncertainties, $\sigma_{P_{\text{meas}}}$ and $\sigma_{\Delta P_{\text{Align}}}$, are added to Eq. (2.53) and Eq. (2.54).

2.7.4. Sound speed contribution

The contribution of the sound speed uncertainties to the angular uncertainty can be divided into two terms corresponding to sound speed uncertainty at the receiving array $\sigma_{\theta_{sc}}$ and in the sound speed profile $\sigma_{\Theta_{\mathrm{SSP}}}$ as

$$\sigma_{\Theta_c}^2 = \sigma_{\theta_{sc}}^2 + \sigma_{\Theta_{\mathrm{SSP}}}^2 . \tag{2.55}$$

For $\sigma_{\theta_{sc}}$, the angle Θ is not of importance, but the steering angle has to be considered. Following [26, 27] the corresponding uncertainty is obtained from

$$\sigma_{\theta_{sc}}^2 = \left(\frac{\tan\theta_s}{c_{\mathrm{tr}}}\right)^2 \sigma_{c_{\mathrm{tr}}}^2 , \tag{2.56}$$

with c_{tr} the sound speed at the receiving array and $\sigma_{c_{\mathrm{tr}}}$ its uncertainty.

In order to quantify the contribution of $\sigma_{\Theta_{\mathrm{SSP}}}$, various models can be used. In [27], this term is based on a two-layered representation of the sound speed profile assuming equal thickness of both layers, see Fig. 2.24. The angular uncertainty induced by uncertainty in the mean sound speed profile at the receiving array is thus approximately half of that at the middle boundary, see $\mathrm{d}\Theta$ and $\mathrm{d}\Theta'$ in Fig. 2.24. Using this and differentiating the Snell's law at the middle boundary of the two layers with respect to the beam angle in the second layer (Θ'), the angular uncertainty induced by the non-uniform sound speed profile is obtained from

$$\sigma_{\Theta_{\mathrm{SSP}}}^2 = \left(\frac{\tan\Theta}{2c_{\mathrm{SSP}}}\right)^2 \sigma_{\mathrm{SSP}}^2 , \tag{2.57}$$

with c_{SSP} the average sound speed in the water column derived from the SSP and σ_{SSP} its corresponding uncertainty. The resulting bathymetric uncertainty reads as

$$\sigma_{d_{\mathrm{SS}}}^2 = (r\cos P \sin\theta)^2 \left(\sigma_{\theta_{sc}}^2 + \sigma_{\Theta_{\mathrm{SSP}}}^2\right) . \tag{2.58}$$

2.7.5. Heave contribution

Heave H is the motion of the heave sensor relative to its mean vertical position over a predefined time period. The heave at the transducer is obtained from the measured heave by the sensor, H_{Meas}, and the induced heave by roll and pitch of the vessel H_{Induced}. The latter is due to the fact that the heave sensor and the transducer are not located at the same position. The heave at the transducer is thus expressed as

$$H = H_{\mathrm{Meas}} + H_{\mathrm{Induced}} , \tag{2.59}$$

with the uncertainty σ_H derived from

$$\sigma_H^2 = \sigma_{H_{\mathrm{Meas}}}^2 + \sigma_{H_{\mathrm{Induced}}}^2 . \tag{2.60}$$
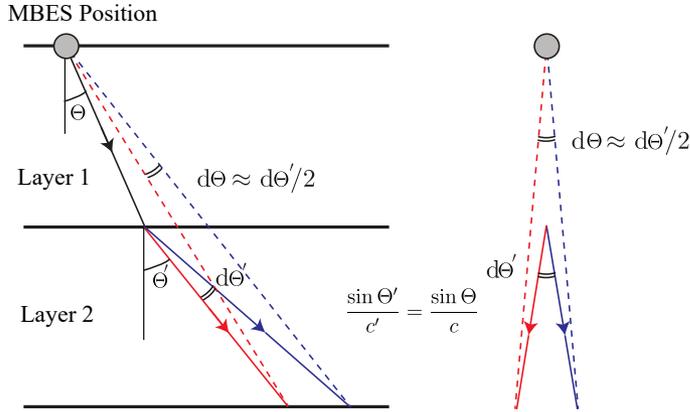
Figure 2.24: Schematic representation of two-layer sound speed profile representation with equal thickness of the both layers.

The term $\sigma^2_{H_{\text{Meas}}}$ is obtained from the manufacturers' specification as

$$\sigma^2_{H_{\text{Meas}}} = \max\left(a^2_H, (b_H H_{\text{Meas}})\right)^2 , \qquad (2.61)$$

with a_H and b_H a fixed (static) and variable (function of peak-to-peak heave height) component. The induced heave is expressed as

$$H_{\text{Induced}} = -y_{\text{Off}} \sin P + x_{\text{Off}} \sin R \cos P + z_{\text{Off}}(1 - \cos R \cos P) , \qquad (2.62)$$

and its uncertainty is derived from

$$\begin{aligned}
\sigma^2_{H_{\text{Induced}}} = &(y_{\text{Off}} \cos P + x_{\text{Off}} \sin R \sin P - z_{\text{Off}} \cos R \sin P)^2 (\sigma^2_{P_{\text{meas}}} + \sigma^2_{\Delta P_{\text{align}}}) \\
&+ (-x_{\text{Off}} \cos R \cos P - z_{\text{Off}} \sin R \cos P)^2 (\sigma^2_{R_{\text{meas}}} + \sigma^2_{\Delta R_{\text{align}}}) \\
&+ \sin^2 P \sigma^2_{y_{\text{Off}}} + \sin^2 R \cos^2 P \sigma^2_{x_{\text{Off}}} + (1 - \cos R \cos P)^2 \sigma^2_{z_{\text{Off}}} ,
\end{aligned}$$
$$(2.63)$$

with x_{Off}, y_{Off} and z_{Off} the offset coordinates between the transducer and heave sensor and $\sigma_{x_{\text{Off}}}$, $\sigma_{y_{\text{Off}}}$ and $\sigma_{z_{\text{Off}}}$ the corresponding uncertainty in the measurements of these offsets. It should be noted that in case vertical positioning is carried out using GNSS, instead of $\sigma^2_{H_{\text{Meas}}}$, the z-component of the uncertainty of GNSS (from manufacturers' specification) is used.

To reference the measurements derived from the MBES to a datum of interest, in addition to the heave contribution, corrections for dynamic draft and datum are required. Throughout this thesis, all datasets are acquired with the acquisition software Quality Integrated Navigation System (QINSy), which is developed by QPS BV. The vessels were equipped with GNSS sensors on-board, receiving correction signals from Real-time Kinematic (RTK) services. GNSS RTK provides one with accurate position and ellipsoidal height of the GNSS antenna with an accuracy of a few centimeters in the WGS84 reference frame. The seafloor depth relative to the chart

is then derived using the ellipsoidal height, GNSS antenna and transducer offsets from the vessel COG and chart datum shift, obtained from chart datum models, see as an example [86, 87]. Their corresponding uncertainties can potentially affect the depth uncertainty. Generally, the chart datum uncertainty adds an additional term to Eq. (2.45), however, there are exceptions which will be discussed in Chapters 5 and 6. (An interested reader might also refer to [88] for more information on various depth processing algorithms available in QINSy). Using GNSS RTK for calculating the seafloor depth implies that the water surface level is directly of no relevance and accounting for height offsets, such as dynamic draft, height above draft reference and tide, is not necessary for this method (however, knowledge of the water surface level is required for computing the entry location for the sound speed profile, and hence it indirectly affects the estimated depth). This means that to obtain the depth uncertainty relative to the chart datum it is not necessary to add their contribution to Eq. (2.45). Heave measurements (short-term variations in the transducer's depth) are, however, used within the processing software to calculate the height of the vessel's center of gravity between two position updates (because the MBES and Inertial Navigation Sensor (INS) have higher update rate than many GNSS system). Therefore, the accuracy of heave measurement acquired by the INS contributes to the uncertainty in the estimate of the depth.

2.7.6. Confidence levels and confidence regions

In order to evaluate the depth uncertainty, confidence intervals are determined describing the 1-dimensional interval in which a specific percentage, confidence level CL, of the measurements is expected to fall. Throughout this thesis, when calculating the corresponding confidence regions, it is assumed that the depth is a univariate random variables normally distributed $N(\mu_d, \sigma_d)$ with mean, $\mu_d = 0$, and a standard deviation σ_d, conforming Sections 2.7.1 to 2.7.5. The confidence interval is then defined by the boundaries $\pm D_{CL}\sigma_d$, with D_{CL} a scaling factor which depends on the confidence level derived from the normal inverse cumulative distribution function for a given confidence level. Table 2.2 provides the confidence intervals for three confidence levels for the 1-dimensional case of random depth uncertainty.

Table 2.2: Confidence levels and regions of the random depth uncertainty.

CL	$\pm D_{CL}\sigma_d$
68%	$\pm 0.9945\sigma_d$
95%	$\pm 1.9600\sigma_d$
99.7%	$\pm 2.9677\sigma_d$

2.8. Sonar equation

Different phenomena and effects belonging to underwater sound propagation affect the design and operation of sonar equipment. These effects can be logically and conveniently grouped together by the sonar equation [71]. The sonar equation can be used to predict the performance of a sonar, as an example its detection

probability. Another application of the sonar equation is in sonar design, where a pre-established requirement (such as range) needs to be met in the design of the equipment. Moreover, as discussed in Section 2.3.2, the backscatter strength depends on the composition of the seafloor, grazing angle of the incoming wave and the acoustic frequency [89] and it contains useful information about the sediment properties [25, 80]. However, before any useful information can be extracted from the received echo level (EL) at the MBES, an appropriate processing is required as EL is not only dependent on the seafloor backscattering strength, but is actually affected by the measurement configuration (transmission range and angle), water column properties and the hardware and software settings of the sonar (directivity patterns and receiving processing) [34, 90, 91]. The terms affecting the backscatter strength are expressed by the sonar equation. Following [90, 91] the received echo level EL as a function of time is expressed as

$$EL = SL + Bp_T(f_c, \theta_{s_T}) - 2TL + BS(f_c, \phi) + 10 \log \frac{A}{A_1}$$
$$+ PG + SH(f_c) + Bp_R(f_c, \theta_{s_R}) \,, \tag{2.64}$$

with SL the source level (in dB re $1\,\mu$Pa at $1\,$m) modulated by the transmission directivity pattern $Bp_T(f_c, \theta_{s_T})$ as a function of f_c and the transmission angle (steering angle) θ_{s_T} with respect to the sonar axis. $Bp_R(f_c, \theta_{s_R})$ indicates the directivity pattern at reception expressed as a function of f_c and the receiving angle θ_{s_R} with respect to the sonar axis. PG (in dB) is the receiver gain applied by the receiver electronics, see Section 2.5.3 and Eq. (2.39). SH accounts for the sensitivity of the transducer with respect to f_c (in dB re V/μPa). The received echo level EL is a result of signal scattering and reflection within the instantaneously ensonified area A on the seafloor. As the $BS(f_c, \phi)$ is defined per unit area, the ensonified area A is accounted for by the term $10 \log A/A_1$ with A_1 the unit area of $1\,$m^2. The transmission loss TL accounts for the energy loss of an acoustic wave propagating through the water column, see Sections 2.1 and 2.2 (Eq. (2.2) and Eq. (2.10)). Here, the factor 2 accounts for the two-way transmission loss in dB, see Section 2.2. $BS(f_c, \phi)$ is the backscatter strength in dB per m^2 at $1\,$m^8.

Before proceeding, a comment on the calculation of the ensonified area is in order. The ensonified area A is affected not only by the sonar characteristics but also by the seabed morphology, i.e., the across-track a_x and along track a_y slopes. The ensonified footprint area in the pulse limited A_p and beam limited A_b regimes are thus given as [92]

$$A_p = \Omega_T r \frac{c T_{\text{eff}}}{2 \sin(\theta_{\text{fl}} - a_y) \cos a_x} \,, \tag{2.65a}$$

$$A_b = r^2 \Omega_T \Omega_R \,, \tag{2.65b}$$

---

[8]Here, the dependency of the backscatter strength, directivity patterns at transmission and reception and sensitivity of the transducer on the frequency are made explicit. Generally in case of using monochromatic signals (e.g., MBES) the common notations for these parameters do not explicitly include the frequency dependency.

with T_{eff} the effective pulse length and θ_{fl} the incident angle on the flat seabed. The footprint used in Eq. (2.64) is selected based on $A = \min(A_p, A_b)$. The across-track and along-track slopes can be calculated from the bathymetric measurements using the approach presented in [92], see Chapter 5. As discussed in Section 2.7 the beam angle Θ differs from the steering angle at reception θ_{S_R} by the mounting angle of the MBES and also by the platform motion in case of applying real-time roll correction. Ω_T and Ω_R indicate the along-track and across-track beam opening angles given in Eq. (2.28). For a constant array length, the beam opening angle varies with frequency.

Non-zero values for the slopes imply that the incident angle on the actual seabed, θ, is different from that of the flat θ_{fl} (reported by the sonar), and the former can be calculated from θ_{fl} using the approach discussed in [92].

Signal-to-Noise ratio

The Signal-to-Noise Ratio (SNR) expresses the relative importance of the contribution of the expected received echo level and the perturbing noise. It is an important parameter affecting the performance of the sonar in detection and sonar design. The output SNR for active sonar is expressed as [71]

$$SNR = EL - NL \, , \tag{2.66}$$

with NL the background noise level in dB re 1 µPa in the processing band B of the sonar receiver. For MBES systems this can be due to noise (the sound that reaches the receiver while there is no sonar transmission and no target) or reverberation (the sound that while, there are not targets reaches the receiver as a result of sonar transmission). The noise comprises of the ambient noise and platform self-noise. The former originates from outside the system stemming from natural or man-made causes. Sonar self-noise is the noise generated by the receiving platform and consists mainly of machinery noise (from the vessel's motor), propeller noise, and hydrodynamic noise, see [11, 60] for a detailed discussion.

3

Correcting multibeam echosounder bathymetric measurements for errors induced by inaccurate water column sound speeds

An error doesn't become a mistake until you refuse to correct it.

Orlando Aloysius Battista

The objective of this chapter is to correct the bathymetric measurements affected by inaccurate knowledge regarding water column sound speed. The method exploits the redundancy in the MultiBeam EchoSounder (MBES) measurements obtained from the overlap of adjacent swaths and searches for the sound speeds profiles that minimize the difference between depth measurements along the overlapping swaths. Therefore, it does not impose unrealistic constraints on the seafloor morphology and does not rely on additional measurements as opposed to the majority of the existing approaches.

The central role of water column sound speed in bathymetric measurements is discussed in the first part of this chapter followed by presenting the two optimization methods used, i.e., Differential Evolution (DE) and Gauss Newton (GN). The inversion method assumes a constant sound speed in the water column. To assess the sensitivity of the method to this assumption, it is then applied to a data set with large variations in the Sound Speed Profile (SSP) where the assumption is clearly violated. Next, the impact of varying overlap percentages between the adjacent sailed tracks is assessed. Lastly, both DE and GN are applied to a data set with existing refraction artefacts to investigate their performance in practice and to compare them.

3.1. Introduction

Currently MultiBeam EchoSounder (MBES) systems are widely used for conducting bathymetric surveys. They allow for efficient surveying of large areas and offer the possibility of complete bottom coverage. A MBES sends out an acoustic pulse along a wide swath perpendicular to the sailing direction. Beam steering at reception allows for determining the travel-time of the signals for a set of predefined beam angles [29], Section 2.4.1. For each ping, water depths along the swath are derived from the combination of travel times and beam angles, provided that the local Sound Speed Profile (SSP) in the water column is known [95], see Section 2.6.2.

In principle, towed systems, such as a Moving Vessel Profiler (MVP) or a Conductivity, Temperature, Pressure (CTD) sensor [43, 44] can be used to acquire SSP measurements. However, they are not widely used due to the risk of fouling or grounding of the towed instrumentation with each cast [45]. Instead, non-towed systems are often used where the speed of sound in the water is measured by lowering a velocimeter or CTD sensor in the water as deep as possible. To perform such a measurement, the vessel needs to remain stationary. This makes the SSP acquisition a time-consuming process, and it is thus impractical to obtain these measurements at high rates. While infrequent acquisition of SSPs is expected to play a minor role in environments with little variations of sound speeds (both temporally and spatially), it is expected to have large effects on the depth measurements in highly dynamic environments. For these environments the varying presence of salt and fresh water results in large variations in the SSP leading to systematic errors in the estimate of depth.

The effect of using erroneous sound speeds on derived bathymetry has been discussed by numerous scholars. References [96] and [97] examined the effect for a flat transducer (zero roll and mounting angle). References [96] and [98] have shown that for a MBES with zero mounting angle and roll, the varying error terms induced by the erroneous sound speed profile cancel out each other at 45° beam angle, and thus regardless of the SSP, the measured depth is always equal to the true depth for this angle. Reference [40] studied the impact of erroneous SSPs for a tilted array and has shown that the angular error depends on the sign and magnitude of roll and is thus related to the motion time series. References [99] and [45] designed a numerical simulation tool to assess the impact of water column variability on sounding uncertainty without any requirement for soundings. Reference [100] created a map of the depth uncertainty using raytracing based on the spatial variability of two popular oceanographic data sources. Such a tool has allowed identification of areas with high water column variability and evaluation of the seasonal variations on environmental based errors. Approaches to compensate for a lack of sound speed information have been studied and range from reducing the need of sound speed information to gathering additional sound speed information. Reference [101] proposed an equivalent yet, simplified representation for the SSP which can significantly increase the speed of the ray tracing algorithm.

One can also deal with a lack of SSP information by filling the gaps between

the succeeding measurements. Reference [102] developed a model for generating mean SSPs for any location in the world using global oceanic databases. However, the SSP derived can deviate from that acquired at the time of the measurements, particularly in small-scale highly dynamic environments. A number of approaches have been proposed using model predictions of the prevailing water column SSP in such circumstances. Such a method has been incorporated in the Adaptive Bathymetric Estimation (ABE) method, introduced by [103] and extended by the same authors in [104], using estimates of the SSP based on a model for the bathymetry using the Extended Kalman Filter. Reference [105] used an oceanographic model that incorporates surface and internal waves with a high spatio-temporal resolution to generate SSPs for refraction correction. When deriving depth estimates from the measured travel times, however, such a database might not be always available.

Effort has been put forward to correct the MBES derived depths affected by refraction artefacts. Reference [41] presented a refraction correction algorithm in a post-processing context. The method takes into account the nadir data of either two neighboring parallel sailed tracks or crossing tracks. It then searches for refraction coefficients of a two-layer SSP bringing the outer parts of the sailed tracks as close as possible to the seafloor observed at nadir. The method thus assumes that the shape of the swath corrected for refraction artefacts is aligned with the nadir depths of surrounding sailed tracks. However, this assumption can be violated if a large angular coverage (large swaths) is considered, i.e., real bathymetric features might exist at the outer parts of the swath which do not exist at nadir. Reference [42] adopted a relatively similar approach by using the measured depth and considering it as the true depth for the outer parts of the swath. This true depth, in combination with other parameters such as beam angle and Two-Way Travel Time (TWTT), was used to invert for the constant gradient SSPs. Reference [106] proposed an inversion method using Empirical Orthogonal Functions (EOFs) and Genetic Algorithm (GA).

It is a standard practice to carry out MBES surveys with at least a small overlap between adjacent swaths (derived from adjacent sailed tracks). The overlap between the swaths depends on the water depth, line spacing, MBES beamwidth and the order of the survey, see [107]. As an example, National Oceanic and Atmospheric Administration (NOAA) [108] recommends 10% to 20% overlap between the adjacent swath and Land Information New Zealand (LINZ) suggests 200% and 100% swath coverage to meet the LINZ special and Linz-1 orders [109], respectively. The time between measuring two overlapping swaths typically amounts to maximum several hours, but this can vary greatly for differing water depths and survey types. Since generally sediment transport does not occur in a period less than several days (bottom features such as mega ripples and sand waves are not expected to vary within this relatively short period), the bottom can be assumed stable over the course of the survey. Consequently, in the absence of systematic errors the depths as determined from the measured travel times along the two overlapping swaths must be equal at equal points on the seafloor. However, for environments with strong variations in the water column SSP, sometimes significant differences are found. For modern well-calibrated MBES systems, these differences

are in general due to the use of an erroneous sound speed profile stemming from a lack of sound speed information.

In this chapter we propose a method for estimating the sound speed and depth that fully employs the redundancy of the overlapping MBES swaths. Assuming negligible depth variations due to seafloor dynamics and minimizing the contribution of systematic error sources affecting the depth measurements, sound speeds are estimated by minimizing the difference between the water depths along the overlapping parts. This process (optimizing the sound speeds) is carried out using DE, [110], and GN, [111]. The former can be classified as a meta-heuristic method making few or no assumptions about the problem being optimized and can search very large spaces. DE was found to be an efficient global optimization method to solve inversion problems in underwater acoustics and is generally more efficient than the original GA when searching for the global optimum of a real geo-acoustic inversion problem [112, 113]. DE is often used for multi-dimensional real-valued functions and does not require calculating the gradient of the problem being optimized. However, a large number of forward calculations is required to obtain the optimal solution. A faster alternative is to use a gradient-based optimization method, such as GN, with the risk of converging to a local minimum. GN is used to solve non-linear least squares problems and is a modified version of the Newton's method with the advantage of not requiring the second derivatives of the optimization problem.

Within this chapter, a simple description of the water column sound speed, i.e., constant sound speed, is assumed. A complex environment with varying SSP in the water column (salt wedge estuary) is considered and the performance of the method with the assumption of constant SSP is assessed. As a next step, the proposed method is applied to an area with refraction artefacts. The comparison is also made between the two optimization approaches, i.e., DE and GN.

This chapter is organized as follows. In Section 3.2 the method for reducing the SSP induced bathymetric errors is introduced. Section 3.3 gives the description of the MBES data sets used. The data were acquired during a routine bathymetric survey, i.e., they reflect standard practice. In Section 3.4 the results and discussion regarding the application of the inversion algorithm are presented, followed by the conclusions drawn in Section 3.5.

3.2. Correcting sound speed induced bathymetric errors

3.2.1. Role of water column sound speeds in MBES bathymetric measurements

Insufficient knowledge about the water column sound speed hampers correct determination of water depths in two ways and results in a concave (also referred to as smiley or curved upward) or convex (also referred to as frowny or curved downward) seabed surface distortion (Here, a simple situation is considered with a constant sound speed over the entire water column. However, the approach

presented is not limited to such an assumption).

- **Effect on Sound propagation**: sound is impinging on the MBES at angle θ_s with respect to the normal of the MBES, see Fig. 3.1. One can determine the location on the seafloor from which the sound is scattered to the transducer using θ_s, MBES mounting angles (heading, pitch and roll between the transducer and vessel frames, Appendix A) and SSPs. An error in the SSP will thus result in an erroneous estimate of this location;

- **Effect on Beamsteering**: the MBES transmits a sound pulse over a wide range of angles perpendicular to the sailing direction. Beamforming at reception is applied for discriminating between the directions from which the sound impinges at the MBES after backscattering from the seafloor. For a linear array made of independent receiving elements located at equal distances, beamforming in direction θ_s for a receiving element m comes down to applying a time delay τ_m of (Section 2.4.1, Eq. (2.22))

$$\tau_m = \frac{m \delta L \sin \theta_s}{c} \quad m = 0, \ldots, M-1 , \tag{3.1}$$

with δL the distance between the individual receiving elements of the receiver array. Employing an erroneous sound speed for the beamsteering, referred to as c_m, instead of the true one, c, thus introduces errors in the time delays applied. Consequently, the beam actual steering angle, θ_m, differs from the steering direction aimed for, θ_s.
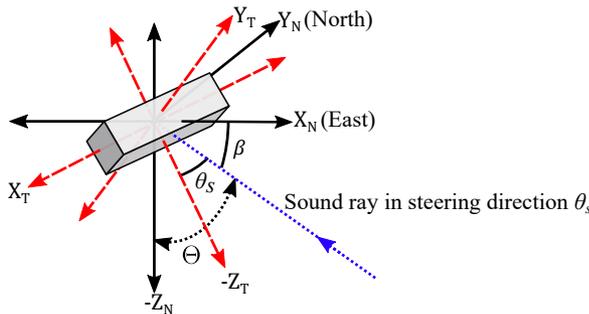
Figure 3.1: MBES measurement configuration schematic. X_T, Y_T and Z_T denote the transducer frame. X_N, Y_N, Z_N indicate the navigation frame. θ_s and β are the beam angles relative to the MBES normal and navigation horizontal plane respectively. Θ indicates the beam angle relative to Z_N.

3.2.2. Optimization methods considered

Fig. 3.2a shows the MBES survey geometry, consisting of a number of tracks that have been sailed parallel to each other, such that the MBES swaths from the adjacent sailed tracks have a certain overlap with each other. The MBES measurements

consist of measured TWTT for all beams. Fig. 3.2b shows the depths along a cross-section for a situation where the SSPs used are erroneous, resulting in depth differences at the overlapping parts. Assuming calibrated mounting offsets and accurate (high quality) tide observations, heave, and draft or 3-dimensional positioning with Global Navigation Satellite System (GNSS), the remaining difference in the water depths at the overlapping parts is mostly attributable to the use of incorrect SSPs allowing for its estimation through optimization of an objective function. Hereto, the optimized sound speeds are derived by minimizing the depth differences along the overlapping parts of the adjacent swaths. To account for the variations of the sound speed with time and position, for each sailed track a unique sound speed is searched for. This means that for a part of the survey area where the depth measurements from N overlapping swaths exist, the search should be carried out for unknown parameters needed for the description of N SSPs.
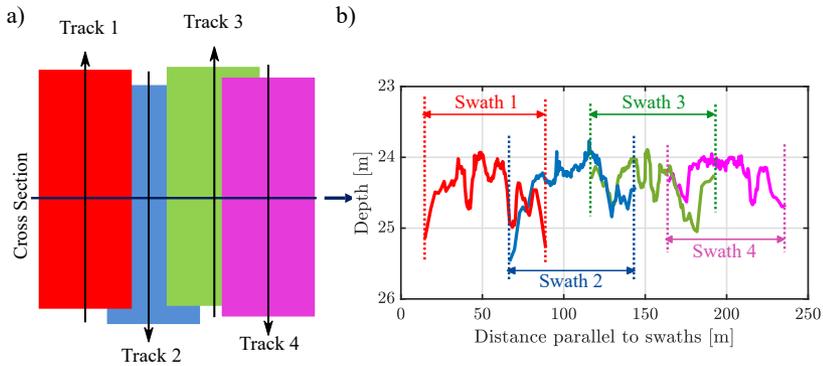
Figure 3.2: a) Schematic of a survey configuration. The arrows indicate the sailing direction, b) Example of difference in the estimated bathymetry, vertically referenced to the chart datum, due to insufficient information about the water column sound speed for the cross section containing depth measurements from four sailed tracks.

Differential Evolution

Differential Evolution (DE) is a global optimization method and is a variant of the well-known Genetic Algorithm (GA). The following steps are taken for its implementation. For a number of consecutive pings in a given sailed track, the part of the seafloor where the depth measurements from this track and its adjacent ones overlap is considered and is referred to as a 'segment' in the remainder of this chapter. For quantifying the agreement in the water depths at the overlapping parts, a grid aligned to the mean heading of the pings in the track under consideration is defined, i.e., X and Y axis of the grid are assumed to be perpendicular and parallel to the heading direction, respectively, see Fig. 3.3a. The DE energy (objective) function is defined as

$$G_{\text{DE}}(\boldsymbol{x}) = \sum_{i=1}^{I} \sqrt{\frac{\sum_{n=1}^{N} \sum_{j=1}^{J_{i,n}} (d_{i,n,j}(\boldsymbol{x}) - \bar{d}_i(\boldsymbol{x}))^2}{\sum_{n=1}^{N} J_{i,n}}} \, , \qquad (3.2)$$

where I is the total number of grid cells in the segment considered (as an example 100 cells in Fig. 3.3a) and $J_{i,n}$ is the total number of measurements of a given sailed track (n) located within a given cell (i). x contains the parameters needed for the description of the N SSPs for the segment under consideration. For the current contribution, constant sound speed profiles are assumed. This means that x contains N unknown sound speeds, for the example shown in Fig. 3.3a we have thus $N = 3$. $d_{i,n,j}$ is a single depth (j) from a given track located in a given cell and $\bar{d}_i$ is the weighted mean of $d_{i,n,j}$ with the weight function being the inverse cubed horizontal distance between the location of the measurements and the cell center. Fig. 3.3b illustrates the situation for one cell within the grid which contains the depth measurements from three sailed tracks (shown with varying colors).
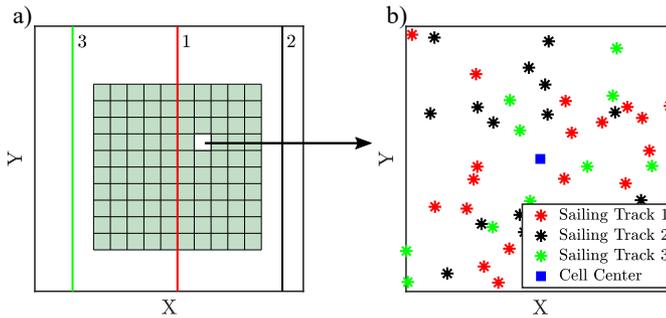
Figure 3.3: a) Schematic overview of the grid considered for a segment of the survey area and b) a cell in the grid which contains the depth measurements from three adjacent sailing tracks.

When an update value for the nth sound speed is available, the beam vector, see Fig. 3.1, has to be re-pointed, and consequently $d_{i,n,j}$ is recalculated. Traditionally, re-pointing a beam to account for an update of the sound speed at the transducer is done by correcting the raw steering angles θ_s reported by the transducer followed by recalculating the beam launch angle, β in Fig. 3.1, [114, 115]. However, in this chapter the refraction correction is applied to the launch angle, without having to recalculate θ_s. This leads to an increase in the processing speed, see Appendix A. The energy function, $G_{\text{DE}}(x)$ calculated for each segment, is minimum when the depth variations for the cell are minimized. This implies that the depths corresponding to the measurements from adjacent sailed tracks have become closer to each other. Consequently, minimization of the energy function gives the sound speeds which provide the maximum agreement between water depths for the segment considered. In order to locate the minimum of Eq. (3.2), use is made of DE [110]. Details on this algorithm are provided by [116], see Appendix B for a brief explanation of DE. The lower and upper bounds for the unknown sound speeds are assumed 1400 m/s and 1600 m/s respectively. The performance of global optimization methods, i.e., their success in locating the global optimum in an efficient way, is dependent on a number of so-called setting parameters. For the DE, these are

- Population size q_{DE}

- Multiplication Factor F_{DE}

- Crossover Probability $p_{c_{\mathrm{DE}}}$

- Number of Generations $N_{G_{\mathrm{DE}}}$

These setting parameters have to be set beforehand to maximize the probability to locate the global optimum. Here, the best values for these parameters while preserving the computational efficiency were found to be $q_{\mathrm{DE}} = 16$, $F_{\mathrm{DE}} = 0.6$, $p_{c_{\mathrm{DE}}} = 0.55$ and $N_{G_{\mathrm{DE}}} = 10N$ [116].

Gauss Newton

The method presented above describes an approach to reduce SSP induced errors by searching for SSPs maximizing the agreement in water depths along the overlapping parts covered by adjacent sailed tracks. In principle, DE allows for an arbitrary SSP parameterization. However, it requires a significant number of forward calculations.

For reducing the computational effort, instead of DE, the Gauss Newton (GN) method can be used for the optimization. For DE optimization, the parameters searched for were the SSPs per sailed track located within the segment under consideration. For GN, a different approach is taken, where both the SSPs and water depths are considered unknown and the aim is to minimize the function

$$G_{\mathrm{GN}} = \sum_{i=1}^{I} \sum_{n=1}^{N} \sum_{j=1}^{J_{i,n}} (t_{O_{i,n,j}} - T_{O_{i,n,j}})^2 \, , \tag{3.3}$$

where $t_{O_{i,n,j}}$ and $T_{O_{i,n,j}}$ are the modeled and measured One-Way Travel Time (OWTT) (TWTT/2) of the jth depth measurement from a given sailed track located in a given cell (i), respectively. The model for calculating $t_{O_{i,n,j}}$ accounts for the effects of the sound speed on the beamsteering and propagation through the water column. Assuming each cell in the overlapping part is a horizontal plane with the normal vector of $[0, 0, 1]$, the intersection of a given depth measurement (j) in a given track with the plane can be computed, see Fig. 3.4. The equation of the plane with this normal vector containing the center of the given cell reads as

$$d = d_i \, , \tag{3.4}$$

where d is the depth of an arbitrary point on the plane and d_i is the depth of a given cell (i). Eq. (3.4) implies that the depth in a cell is constant (it can vary from one cell to another). The vector form of the equation defining a given depth measurement (j) in a given track (n) transmitted from the MBES, i.e., the equation of a line passing through the MBES at the time of transmission of a given beam with the directional vector of $\vec{u}_N$, reads as (see the dashed lines in Fig. 3.4)

$$\begin{bmatrix} X \\ Y \\ d \end{bmatrix} = \begin{bmatrix} X \\ Y \\ d \end{bmatrix}_{\mathrm{tr}} + \vec{u}_N e_s \, , \tag{3.5}$$

where e_s is a scalar describing an arbitrary point on the line, and $\vec{u}_N$ is given in Eq. (A.1). The vector $[X, Y, d]_{\text{tr}}^T$ contains the transducer horizontal coordinates and depth for the depth measurement j in the track n. To clarify this, take Fig. 3.4 as an example which illustrates a cell i in the overlapping part of the two adjacent sailed tracks (referred to as 1 and 2) containing the depth measurements from both of them. The indices j_1 and j_2 indicate a depth measurement from sailed tracks 1 and 2 with their associated unit vectors in the navigation frame $(\vec{u}_N)_{j_1}$ and $(\vec{u}_N)_{j_2}$ respectively. For the intersection of Eq. (3.5) with the seafloor, $X = X_{i,n,j}$, $Y = Y_{i,n,j}$ and $d = d_{i,n,j}$ are considered, with $X_{i,n,j}$ and $Y_{i,n,j}$ the horizontal position of a depth measurement for a given sailed track located in a given cell. The intersection of this line with the plane is derived by substituting Eq. (3.5) in Eq. (3.4) and solving for e_s ($e_s = -\frac{d_{\text{tr}} - d_i}{z_N}$ with $z_N = -\sin\beta$ the third component of the beam unit vector in the navigation frame, see Eq. (A.1)). Substituting e_s in Eq. (3.5) and considering the measured depth to the seafloor, the OWTT can be modeled as

$$t_{O_{i,n,j}} = \frac{d_{\text{tr}_{n,j}} - d_i}{c_n \sin(\beta'_{i,n,j}(c_n))} \,, \tag{3.6}$$

with c_n the sound speed corresponding to the nth sailed track. $\beta'_{i,n,j}(c_n)$ is the launch (depression) angle (see Fig. 3.1) which is a non-linear function of the sound speed and the $'$ indicates that it has been recalculated using the updated sound speed. As mentioned, unknowns to be determined are the sound speeds of the sailed tracks located in the segment and the depths of the cells center, i.e., c_n and d_i. It is seen from Eq. (3.6) that there exists a nonlinear relation between the unknowns and modeled travel times. By linearizing Eq. (3.6) one gets

$$E\{y\} = A(x) \quad D\{y\} = \sigma_y^2 I \,, \tag{3.7}$$

where $x = \left[d_1, d_2, ..., d_I, c_1, c_2, ..., c_N\right]^T$ is $I + N$-vector containing the unknowns. y indicates the vector of the length $\sum_{n=1}^{N} J_{i,n}$ containing the measured-minus-modeled OWTT. $\sigma_y^2 I$ is the covariance matrix of y with σ_y^2 the variance of the data and I an identity matrix of order $\sum_{n=1}^{N} J_{i,n}$. A is the linearized design matrix of the size $\sum_{n=1}^{N} J_{i,n} \times (I + N)$. Its columns indicate the partial derivatives of Eq. (3.6) with respect to the unknown parameters (x) as

$$\frac{\partial t_{O_{i,n,j}}}{\partial d_i} = \frac{-1}{c_n \sin\left(\beta'_{i,n,j}(c_n)\right)}$$

$$\frac{\partial t_{O_{i,n,j}}}{\partial c_n} = \frac{\left(d_i - d_{\text{tr}_{n,j}}\right)\left(\frac{\partial \beta'_{i,n,j}(c_n)}{\partial c_n} \cot\left(\beta'_{i,n,j}(c_n)\right) + \frac{1}{c_n}\right)}{c_n \sin\left(\beta'_{i,n,j}(c_n)\right)} \,. \tag{3.8}$$

Solving for x in a least-squares sense conform Eq. (3.3) requires an iterative GN approach, see for example [117].
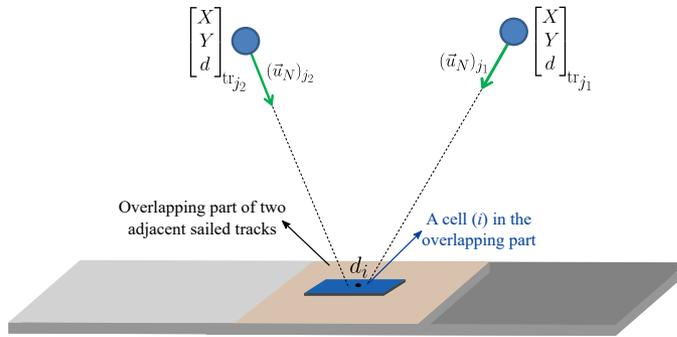
Figure 3.4: Schematic overview of a cell in the overlapping part of the two adjacent sailed tracks (1 and 2) in the navigation frame. Roll, pitch and heading are not shown here for the sake of clarity. Indices j_1 and j_2 indicate two depth measurements from the sailed tracks 1 and 2 respectively.

It should be highlighted that although the apparent formulation of the objective functions used in GN and DE is different, they both seek to minimize the depth variations located at the overlapping areas of adjacent sailed tracks. For the DE, this is done by minimizing the difference between depth measurements. As for the GN, minimizing the quadratic sum of the differences between the modeled and measured OWTTs directly results in minimized quadratic difference between modeled and measured depths as depths measurements are a scaled variant of the OWTTs. This indicates that the above two methods are conceptually equivalent.

3.3. Description of data sets

For assessing the performance of the SSP inversion method, two data sets were used. The first one was acquired by Rijkswaterstaat in the Nieuwe Waterweg, the Netherlands, which is a ship canal from het Scheur (a branch of the Rhine-Meuse-Scheldt delta) west of the town of Maassluis to the North Sea at Hook of Holland. The data was acquired on 19/01/2010 using a Reson 8125 MBES and covers an area of $270\,000\,\mathrm{m}^2$ consisting of 19 sailed tracks with water depth varying from $3.5\,\mathrm{m}$ to $26\,\mathrm{m}$, vertically referenced to Normaal Amsterdams Peil (NAP), see Fig. 3.5. The data set was acquired from $10\,\mathrm{h}$ and $45\,\mathrm{min}$ to $13\,\mathrm{h}$ and $34\,\mathrm{min}$ (the time span of around $2\,\mathrm{h}$ and $45\,\mathrm{min}$). Fig. 3.6 illustrates the water level with respect to NAP for the Maeslantkering zeezijde tide station (closest station to the survey area). During this period, the maximum water level variation for this station was around $0.16\,\mathrm{m}$. The bottom morphology is not expected to change to a noticeable extent. The survey area is characterized by a sand wave field which is traversing the sill plates of the Maeslantkering storm surge barrier and is considered to be a salt wedge estuary with a strongly stratified water mass in which fast flowing surface river water is predominantly fresh and bottom water is predominantly salty with a pronounced pycnocline at the interface between the two layers [99]. The four SSPs acquired during the survey (ebb tide) are shown in Fig. 3.7. It is clearly seen that the SSPs are not constant (variations of around $25\,\mathrm{m/s}$ with depth). The

overlapping percentage (the portion of the swath corresponding to one sailed track covered by the swath of adjacent sailed track) between the two adjacent tracks was close to 70%, enabling the assessment of the effect of the varying percentages of the overlap on the method's performance.
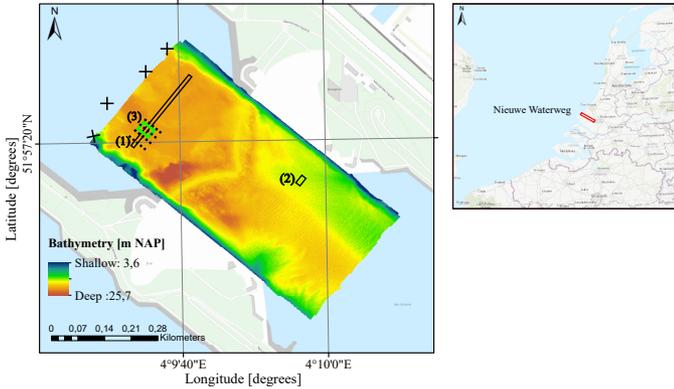
Figure 3.5: Bathymetry and location of the survey area (Nieuwe Waterweg, the Netherlands). The bathymetry map, vertically referenced to NAP, was derived from Qimera post-processing software developed by Quality Positioning Services (QPS) BV. The location of the measured SSPs is shown by black crosses. The areas indicated by 1, 2 and 3 and the sailed tracks shown by dashed lines will be investigated further.
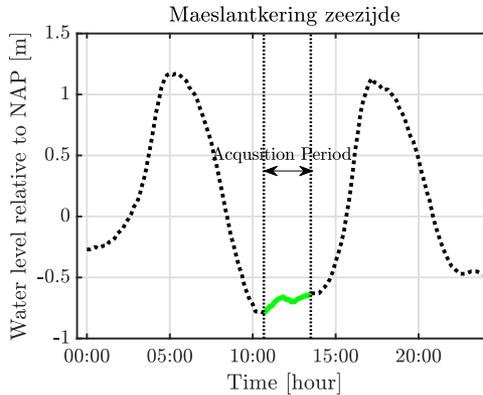
Figure 3.6: Water level with respect to NAP vertical datum for the closest tide station to the data set acquired in Nieuwe Waterweg during the data acquisition period.

The second data set considered in this chapter was acquired in the Bedford Basin, Halifax, Nova Scotia, Canada using a multi-frequency R2Sonic 2026 MBES on 02/05/2017 from 13 h and 17 min to 16 h and 58 min. This data set was used as one of the primary data sets in R2Sonic's Multi-Spectral Challenge [34, 118]. The frequencies used during the data acquisition equaled 100 kHz, 200 kHz and 400 kHz. To avoid depth variations due to varying signal penetration with frequency [94] (see
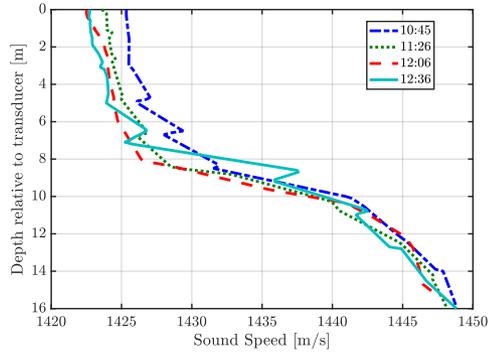
Figure 3.7: The four measured SSPs for the survey area Nieuwe Waterweg.

also [69] for a detailed discussion on the effect of signal penetration on the measured multi-frequency backscatter and bathymetry), the results here are presented considering only the frequency of 200 kHz. The data covers an area of around 1 840 000 m^2 and consists of 13 sailed tracks with approximately 50% survey overlap. The depth in the survey area ranges from 13 m to 90 m, vertically referenced to Lowest Astronomical Tide (LAT), see Fig. 3.8. The SSPs acquired during the survey are also illustrated in Fig. 3.9. The SSPs vary over the water column from 1448 m/s to 1464 m/s. The survey itself is small relative to the entire Bedford Basin. The basin is an estuary situated at the northwest end of Halifax Harbor and is blocked from full ocean circulation by a narrow and shallow sill [119]. This data set was chosen as the refraction problem only exists in the northeast of the survey area. It is thus important to assess whether the application of the SSP inversion method to the complete survey area corrects for the refraction problem only in the areas needed or it affects the bathymetry in the remaining parts without refraction induced errors. The latter results in misinterpretation of the bottom morphology. Also, the varying morphology within the survey area makes this data set interesting for assessing the performance of the inversion method.

3.4. Results

A sailed track within the survey area was divided into subsets consisting of 20 consecutive pings. The method considers the part of the seafloor where the depth measurements from these pings in the track under consideration and its adjacent ones overlap, referred to as the segment. The resolution of the grid defined in both directions was equal and taken as 10% of the average depth of the measurements located in the segment, Section 3.2.2. This value was chosen as such to ensure the availability of a sufficient number of soundings for calculating the statistics within a cell in a segment under consideration. Assuming constant SSPs and that the depth measurements corresponding to N sailed tracks are located in this segment, N sound speed are derived (one per sailed track). Afterwards, the next 20 pings are considered and the same approach is applied.
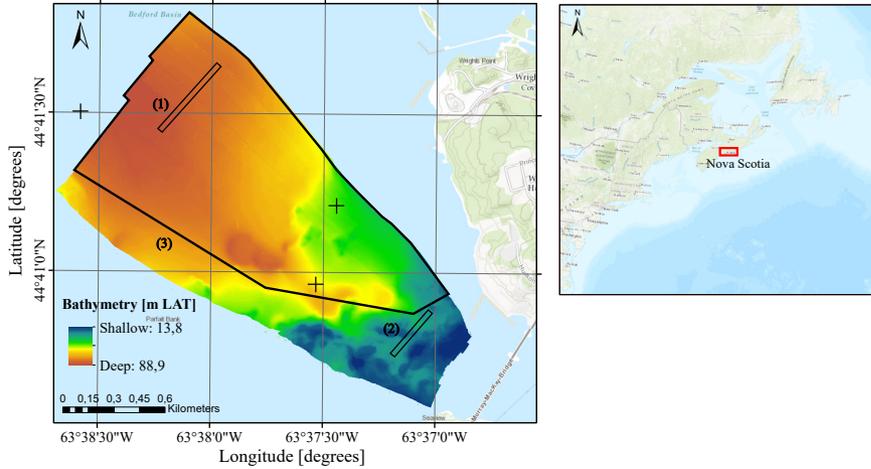
Figure 3.8: Bathymetry and location of the survey area (Bedford Basin, Canada), vertically referenced to LAT. The bathymetry map was derived from Qimera post-processing software developed by Quality Positioning Services (QPS) BV. The location of the SSPs acquired are also shown by black crosses. Areas indicated by 1, 2 and 3 will be investigated further.
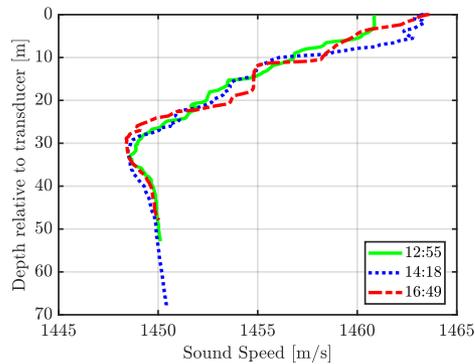
Figure 3.9: The three measured SSPs for the survey area Bedford Basin.

The performance of the inversion method has been assessed using two indicators:

1. **Difference between the depth measurements**: in general the standard deviation gives a measure of the inversion method's precision, however, there is also a need to assess the method's accuracy, i.e., its unbiasedness. To this end, a data set free of refraction artefacts was considered and artificial artefacts were introduced (assuming erroneous sound speeds in the water column). The SSP inversion method was applied to the resulting erroneous depths and the difference between the depths derived after applying the SSP inversion and the original ones was assessed;

2. **Standard deviation of the depth measurements for each cell of the grid**: if the refraction artefacts do not exist, the standard deviation of the depth measurements in a cell reflects the uncertainty of these measurements (due to the uncertainties inherent to the MBES) and those induced by the bottom morphology. However, if the refraction artefacts exist, smiley or frowny features appear and the discrepancies between the depth measurements from the adjacent sailed tracks increase resulting in an increase in the standard deviation. This value can be seen as a measure of the precision of the SSP inversion algorithm.

3.4.1. Applying Differential Evolution based SSP inversion method to Nieuwe Waterweg

The high quality data set acquired in the Nieuwe Waterweg is free from refraction artefacts. As seen from Fig. 3.7, the sound speed in the water column varies with depth. We therefore considered the erroneous SSPs by increasing the measured SSPs by 15 m/s for the upper part and decreasing it by 12 m/s for the lower part of the water column. Also a random Gaussian noise with a standard deviation of 0.2 m/s was added to the sound speeds. This value represents the uncertainty in the SSP measurements in different locations (inland waterways and the North Sea). Using the resulting SSPs, ray tracing was carried out and the depths were determined. The SSP inversion method assuming a simple representation of the sound speed in the water column was applied to the data affected by the refraction artefacts.

To assess the two surfaces (i.e., original and the one after application of SSP inversion), two small parts of the survey area consisting of around 20 consecutive pings were chosen, see the black rectangles indicated by 1 and 2 in Fig. 3.5. Area 1 is located in a relatively flat part. Area 2, however, is located in an area where the morphological features exist. Shown in Fig. 3.10a and Fig. 3.11a are the original depth measurements derived from raytracing using measured SSPs. Varying colors indicate different sailed tracks. Using the erroneous SSPs, ray tracing was again carried out and the corresponding depths are calculated. For area 1 (Fig. 3.10b), the resulting refraction artefacts are clearly evident (smiley features appears at the overlapping parts). Regarding area 2 where the bathymetric features exist, the erroneous SSPs lead to an incorrect interpretation of the bottom morphology, see Fig. 3.11b.

Fig. 3.10c and Fig. 3.11c show the depths recalculated after applying the method. A visual comparison between the recalculated depths after the inversion and the original ones, Fig. 3.10a and Fig. 3.11a, suggests that although the assumption of constant SSPs was not valid for the data set considered, the inversion method successfully recovered the original surface. For 98% and 90% of the depths in areas 1 and 2 the difference between the original depths and those derived after SSP inversion was less than 0.023 m and 0.035 m, respectively. These differences are quite small relative to typical errors associated with MBES systems. This also indicates that at least for these two areas, the application of the SSP inversion method

did not affect the bottom morphology such that nonexistent bathymetric features appear or the existing morphology changes.
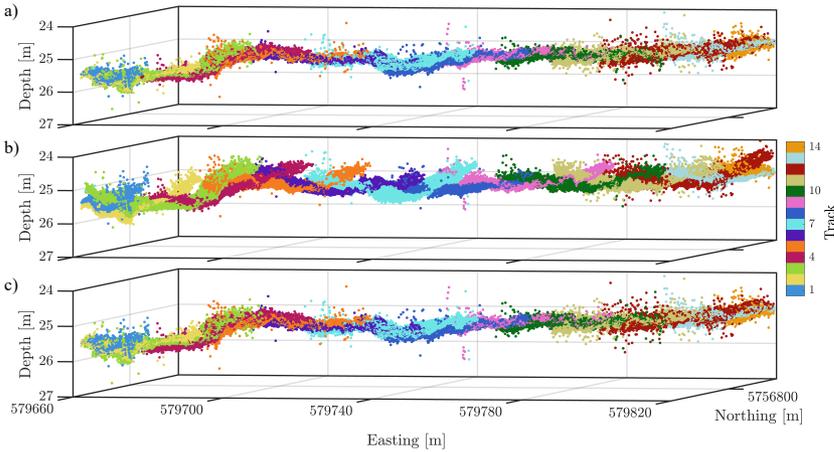
Figure 3.10: Depths (vertically referenced to NAP) within area 1 in Fig. 3.5 consisting of 20 pings derived from the a) original SSPs, b) erroneous SSP and c) results of the SSP inversion. Varying colors indicate different sailed tracks.
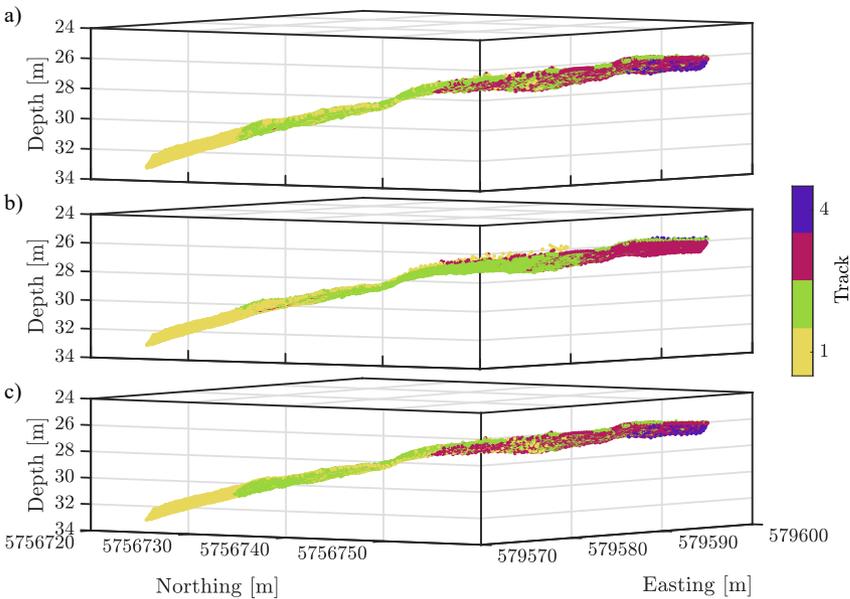
Figure 3.11: Depths (vertically referenced to NAP) within area 2 in Fig. 3.5 consisting of 20 pings derived from the a) original SSPs, b) erroneous SSP and c) results of the SSP inversion. Varying colors indicate different sailed tracks.

As a next step, the difference between the original surface and the one de-
rived after the SSP inversion (indicator 1) was assessed for the full area. Shown in
Fig. 3.12 is the histogram of the differences between the original depth measure-
ments and those recalculated after the SSP inversion (indicated by $\underline{x}$ as a random
variable) along with its normal distribution fit (red curve). The mean and standard
deviation of the differences are 0.009 m (vertical solid blue line), $E(\underline{x})$, and 0.024 m,
$\sigma_{\underline{x}}$, respectively. The differences have to be tested from the statistical point of
view to assess whether they are statistically significant. To this end, the null and
alternative hypotheses were considered as $H_0 : E(\underline{x}) = 0$ versus $H_1 : E(\underline{x}) \neq 0$.
Provided that the number of samples is sufficiently large, based on the central
limit theorem one can state that the sample average of these random variables is
normally distributed with the mean zero and standard deviation of $\sigma_{\underline{x}}$. A 95% con-
fidence interval for a given sample is thus obtained by $-1.96\sigma_{\underline{x}} < \bar{E}(\underline{x}) < 1.96\sigma_{\underline{x}}$,
i.e., -0.048 m<0.009 m<-0.048 m. Therefore, the differences between the original
and inverted depths are not statistically significant.
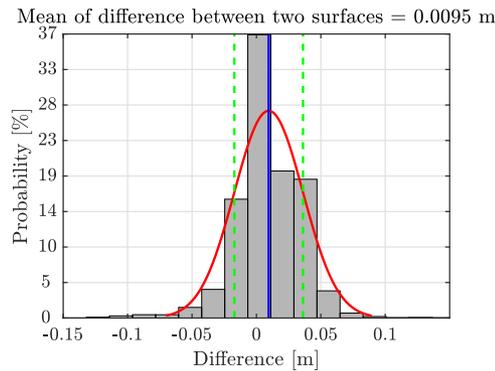
Figure 3.12: Histogram of the difference between original depths and those derived after the SSP
inversion and its normal distribution fit (red curve). Shown with the vertical solid blue line is the mean of
the differences. The vertical dashed green lines indicate the 68% confidence interval of the differences.

Indicator 2 introduced earlier for the assessment of the SSP inversion method is
the standard deviation of the depths after applying the SSP inversion. A grid with
a cell size of 0.25 m $\times$ 0.25 m was defined for the full survey area (this cell size can
be different from those defined for each segment of the data for applying the SSP
inversion method). The standard deviation of the original depth measurements
located in each cell was calculated and was assigned to the cell center. For the
depths derived assuming erroneous SSPs and those recalculated after the applica-
tion of the inversion method, the standard deviation was also determined. Shown
in Fig. 3.13a is the map of the difference between the standard deviation of the
original depths and those based on the erroneous SSPs where a positive value in-
dicates a larger standard deviation of the latter. Using erroneous SSPs results in a
noticeable increase in the standard deviation, as seen from the increase (red parts)
for the overlapping parts of the sailed tracks. The mean value of the standard devi-
ation over the entire area increases from 0.113 m to 0.202 m. Fig. 3.13b illustrates

the map of the difference between the standard deviation of the original depth measurements and those recalculated after SSP inversion. A visual comparison indicates almost equal depth standard deviation of the two.
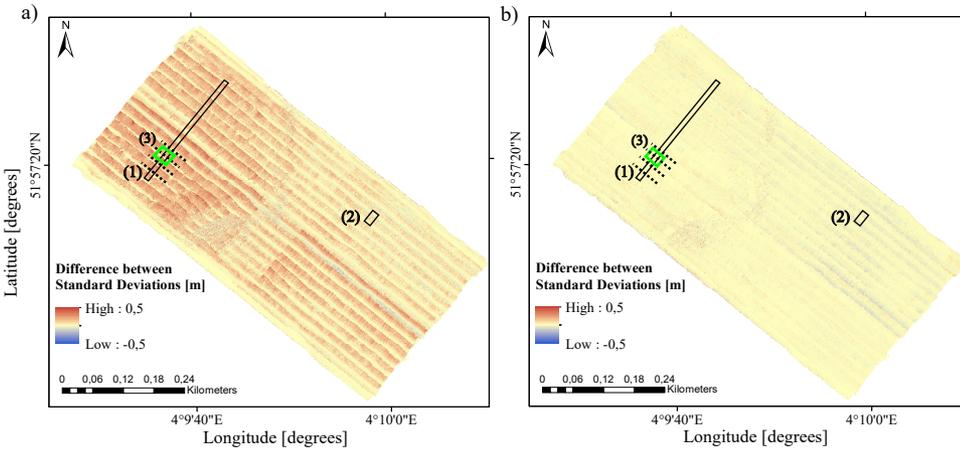
Figure 3.13: Difference between the standard deviation of the original depth measurements of Nieuwe Waterweg (vertically referenced to NAP) and those a) derived assuming erroneous SSPs, and b) recalculated after applying the DE inversion method. The areas indicated by 1, 2 and 3 are the same as those shown in Fig. 3.5 and. The sailed tracks shown by black dashed lines will be investigated further.

The results presented so far were derived from the application of DE, see Section 3.2.2. No significant differences were found between the results of applying DE and GN based SSP inversion methods to this data set.

3.4.2. Investigating the effect of overlap percentage

For the functionality of the SSP inversion method (either DE or GN), overlap between the adjacent swaths is required. An important issue to investigate is the impact of varying overlap percentages. To this end, a small area consisting of 50 pings, indicated as 3 with green rectangle in Figs. 3.5 and 3.13 was used where the soundings from four tracks (indicated by dashed lines) were located within the area. To define the varying percentages of overlap, three different scenarios, I, II and III were considered, see Fig. 3.14. Three sailed tracks indicated as L1, L2 and L3 are shown in this figure. The scenarios are as follows:

- **Scenario I**: Overlap exists between three lines, L1, L2 and L3. Fig. 3.14a shows this scenario in which these lines and the maximum available swath width were used. This resulted in the overlap of 70% between L1 and L2 (L1 and L3 have 42% of overlap). Additionally, L1 and L2 overlap percentage was reduced to 55% by reducing the most outer beam to 49°. Therefore, for this scenario, two overlap percentages of 70% and 55% between L1 and L2 were considered;

- **Scenario II**: Overlap exists between L1 and L2, but L3 drops out, see Fig. 3.14b.

The overlaps of 40% and 35% were obtained by reducing the most outer beam to 40° and 38° respectively;

- **Scenario III**: L2 line was excluded, and hence overlap exists between L1 and L3, see Fig. 3.14b. Overlap percentages of 30%, 18%, 12% and 9% between L1 and L3 were obtained by reducing the most outer beams to 55°, 51°, 49° and 48° respectively.

3
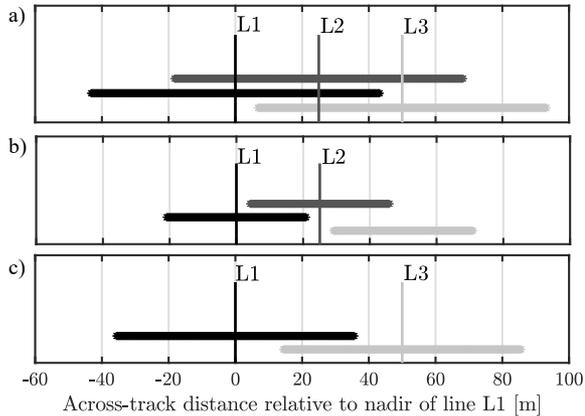
Figure 3.14: Schematic overview of the overlap between the three sailed tracks for 3 scenarios, a) overlap exist between L1, L2 and L3 lines (Scenario I), b) overlap exist between L1 and L2 (Scenario II), c) L2 is excluded and the overlap exist between L1 and L3 (Scenario III). Varying shades of gray indicate the swaths for different sailed track.

For the calculations presented in Fig. 3.14, the water depth and line spacing equaled 25 m. Shown in Fig. 3.15 is the depth standard deviation for the area indicated as 3 in Figs. 3.5 and 3.13 after applying the SSP inversion method for the situations with an overlap of a) 70%, Scenario I with the maximum swath width, and b) 30%, Scenario III derived from excluding every other sailed track while reducing the swath with to 55°. Generally, a reduction in the overlap increases the depth standard deviation. As the overlap decreases, the inversion is carried out using the soundings mostly from the beams close to nadir. These beams are less affected by the erroneous sound speeds than the outer beams, and hence not only are there less depth measurements constraining the estimate, but also is the geometry such that the objective function is less sensitive to the changes in the unknowns, see [116].

Shown in Table 3.1 is the standard deviation of the difference between the original depths and those derived after applying the inversion method for varying overlap percentages. As expected, a decrease in the overlap percentage increases the standard deviation. For overlap percentages decreasing from 70% to 35%, the standard deviation only slightly increased. For an overlap of less than 35%, a more rapid increase was found.
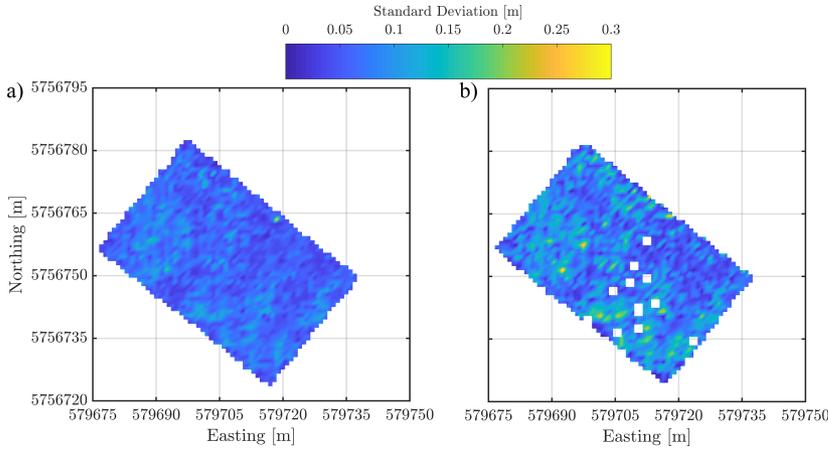
Figure 3.15: Depth standard deviation for area indicated as 3 in Fig. 3.5 after applying the SSP inversion for a grid with the cell size of 0.25 m × 0.25 m using a) 70% overlap and b) 30% overlap between the adjacent sailing tracks.

Table 3.1: Standard deviation of the difference between the original depths and those derived after applying the inversion algorithm for varying percentage of overlap (one-sided) for area 3 (Fig. 3.5).

Overlap percentage (%)	70	55	40	35	30	18	12	9
Depth standard deviation [m]	0.024	0.027	0.029	0.031	0.042	0.054	0.056	0.061

3.4.3. Illustration of use of the proposed method in practice: application to Bedford Basin

As mentioned in Section 3.3, bathymetry measurements to the northeast of the Bedford Basin survey area were affected by the unknown or erroneous SSPs. Shown in Fig. 3.16a is the standard deviation of the depth measurements (vertically referenced to LAT) gridded using a cell size of 3 m × 3 m. The map indicates a larger standard deviation for the outer beams to the northeast of the survey area, see the three sailed tracks shown in this figure as an example.

Generally speaking, there are a number of error sources with a similar signature as the refraction induced errors. Before applying the proposed inversion method, one should ensure that these contributors have not affected the data set. Besides the uncertainties inherent to the MBES, the contributors affecting the quality of the derived depths can be categorized as static and dynamic. A detailed discussion on the various systematic error sources can be found in reference [120]. The static contributor with a similar signature as the refraction is roll misalignment between the MBES and Inertial Navigation Sensor (INS). The correction of the static systematic errors is most often carried out using the patch tests, which examines the repeatability of the system over a pre-defined patch of the seafloor. For the Bedford Basin survey, the patch test was carried out, and therefore these systematic errors, if present, were excluded. The other group of systematic errors are the dynamic ones, producing errors that vary either with the period of the ocean wave spectrum
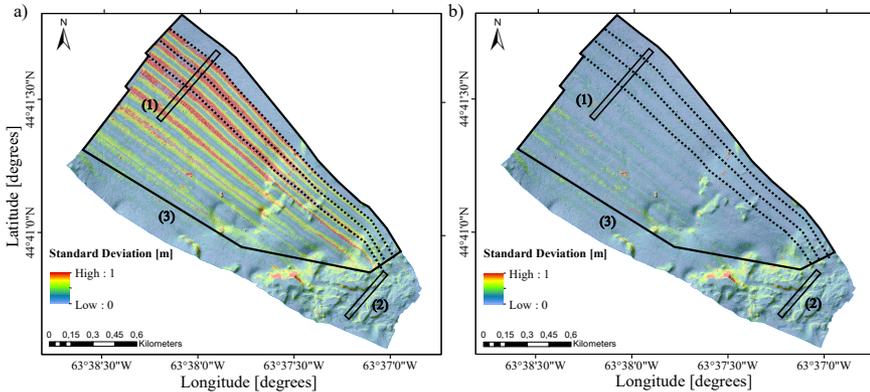
Figure 3.16: Standard deviation of depth measurements (vertically referenced to LAT) in Bedford Basin a) using the measured SSPs and b) after applying DE based SSP inversion method. The areas indicated by 1, 2 and 3 are investigated further. The dashed lines indicate 3 sailed tracks.

or with the long period acceleration of the vessel [40]. The dynamic errors having the same characteristics as the refraction induced error are motion scaling problems (correlating with roll), time delays in the motion sensor output (correlating with roll rate) and imperfect alignment of the roll/pitch axes with the MBES reference frame (correlating with pitch). These errors can be identified using correlation analysis between the motion time series and depth derivatives. Careful examination of the motion time series has revealed no signatures of the dynamic systematic. Therefore, it is concluded that the observed increase in the differences toward the outer parts of the swath is not caused by systematic error sources.

Applying the DE based SSP inversion method and recalculating the bathymetry with the estimated sound speeds corrects for the refraction effect, see Fig. 3.16b. The method also reduces the standard deviation in other areas where the effect of unknown/erroneous sound speed is less noticeable. The remaining larger uncertainties for the overlapping parts of the swaths in some areas can be due to the increasing inherent MBES uncertainties with beam angle or contribution of the bottom morphology.

To assess the two surfaces in more detail, two parts of the survey area consisting of approximately 20 pings with and without apparent artefacts were chosen, see the areas indicated by 1 and 2 in Figs. 3.8 and 3.16 respectively. Shown in Fig. 3.17 are the depths for an area with refraction artefacts (area 1) a) before and b) after the application of the DE inversion method. The DE SSP inversion method clearly corrects the smiley feature observed in the surface derived from the measurements.

Concerning area 2, as seen from the bathymetry map of Fig. 3.8, morphological features exist to the southeast of the survey area where the depth gets shallower. No refraction problem observed in this area and the variations of the standard deviations are mostly due to the inherent uncertainties of the MBES and morphological features. This is thus an interesting area for the assessment of the SSP inversion method accuracy, i.e., to assess whether the application of the method in an area
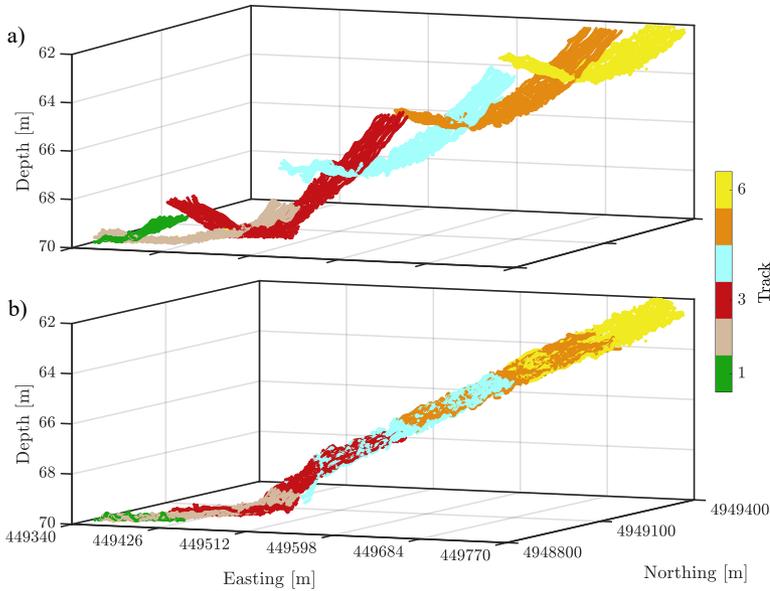
Figure 3.17: Depths (vertically referenced to LAT) within the area consisting of 20 pings indicated as 1 in Fig. 3.16 based on the a) measured SSPs and b) result of DE based SSP inversion. Varying colors indicate different sailed tracks.

without refraction artefacts introduces either artificial bathymetric features or manipulates the existing ones. Fig. 3.18 illustrates the depths derived a) before and b) after applying the DE based SSP inversion for the area indicated by 2 in Fig. 3.16. The depths based on the measured SSPs and those optimized at the overlapping parts of the swaths are in good agreement with the mean and standard deviation of 0.003 m and 0.078 m respectively. Based on the Chebyshev's inequality, [117], which is used in case of having an unknown distribution for a random variable, one can state that there is no evidence that the original depth and those recalculated after the inversion are different from a statistical point of view.

The histogram of the depth standard deviation for the area indicated as 3 in Figs. 3.8 and 3.16 is presented in Fig. 3.19 using the bathymetry derived from a) the measured SSPs and b) recalculated after applying the DE based SSP inversion. The mean and standard deviation of the depth standard deviation after applying the inversion method decreased by a factor of around 2.8 compared to the situation where the measured SSPs were used. This indicates that the standard deviation not only does get closer to zero but also does vary less from one cell to another.

3.4.4. Comparison between Differential Evolution and Gauss Newton based SSP inversion methods

As discussed, the SSP inversion method can be implemented using either DE or GN based optimization approaches. The former is more powerful as it searches for the
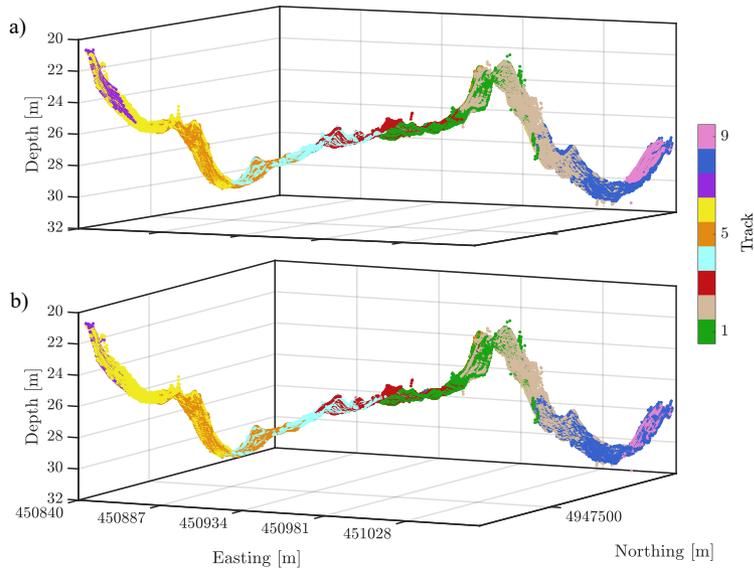
Figure 3.18: Depths (vertically referenced to LAT) within the area consisting of 20 pings indicated as 2 in Fig. 3.16 based on the a) measured SSPs and b) result of DE based SSP inversion. Varying colors indicate different sailed tracks.
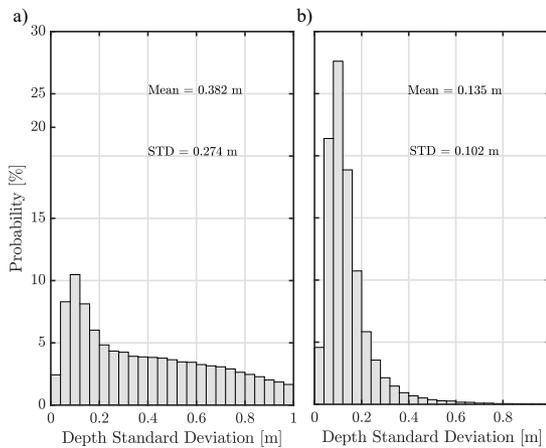
Figure 3.19: Histograms of the standard deviation of the depths derived from a) measured SSPs and b) recalculated after applying the DE based SSP inversion.

global minima as opposed to the latter which can get trapped at local minimum. As an example, if the starting point is too far from the global optimum, GN is not a suitable approach for localizing it. Moreover, developing the existing model to account

for more complicated representations of the SSP in the water column (potentially for the future developments of the SSP inversion method) is more straightforward with DE than GN. This is due to the fact that the former only requires updating the parameter space while the latter needs updating the observation equations and the Jacobian matrix. However, GN has the advantage of being faster than DE. The computational complexity of GN is in the order of $O(n^3)$ with n being the number of sound speeds to be optimized plus the number of cells. Calculating the computational complexity of DE in terms of the big O notation ($O(...)$) is not trivial, because many other parameters such as the population size and multiplication factor also contribute to its performance. Therefore, instead of big O notation representation, we assessed the computational complexity of both methods by comparing the time it took to run them on the same data sets. The comparison indicates that the GN is faster that DE by a factor varying from 3.3 to 5. This observation is a result of both algorithmic complexity and implementation related effects.

3.5. Conclusions

In this chapter, a method for reducing the MBES bathymetric errors induced due to an erroneous/insufficient knowledge of the water column sound speed was presented. The method takes advantage of the overlap between the adjacent sailed tracks and optimizes the sound speeds minimizing the difference between the depth measurements at these overlapping parts. For the optimization, two methods, i.e., DE and GN, were used. For the DE, the search is carried out for those sound speeds in the water column (assuming constant) resulting in minimum variations of the depth standard deviation along overlapping parts of adjacent swaths. This approach allows for arbitrary parameterizations of the water column SSP. A drawback, however, is the large number of forward calculations. Alternatively, GN can be used where the optimization is carried out by minimizing the sum of the squares of the difference between modeled and measured OWTT.

A complex environment with varying water column sound speed and free of refraction artefacts was considered and the refraction artefacts were introduced assuming erroneous SSPs. Applying the method based on the assumption of constant sound speed to this survey area indicated a good agreement between the original depth measurements and those derived after applying the inversion to the data artificially contaminated by refraction errors. The mean and standard deviation of the differences were 0.009 m and 0.024 m, respectively. This means that even for a situation in which the sound speed varies with depth, the inversion method based on a simple representation of the water column SSP can give reasonable results.

The impact of varying overlap percentages between the adjacent sailed tracks was assessed by considering a small area consisting of 50 pings where the soundings from four sailed tracks were located within the area. Various overlap percentages were obtained by reducing the swath width, excluding sailed tracks from the analysis or a combination of both. It was shown that, in general, the reduction of the overlap percentage increases the standard deviation of the difference between the original depths and those derived after applying the inversion method. However,

this increase occurs more rapidly for the overlap percentages of less than 35%. For larger values, the reduction of the overlap percentage only slightly increases the standard deviation.

The inversion method was also applied to a data set with existing refraction artefacts at some parts of the survey area. Applying the method corrected for the apparent refraction artefacts. The method also reduced the standard deviation in other areas where the effect of unknown/erroneous sound speed was less notice-able. For areas without refraction artefacts, the method introduced neither artificial bathymetric features nor manipulates the existing ones. The mean of the differ-ences between the depths before and after applying the inversion method for this area was 0.003 m with a standard deviation of 0.078 m.

For a constant water column sound speed, no significant difference was found between the results of the DE and GN. The latter was however faster by a factor varying from 3.3 to 5. The advantage of using DE for the optimization lies on its flexibility with regards to SSP parameterizations. If one wants to consider a more complicated representation of the sound speed in the water column, GN becomes inefficient as it involves calculating the derivatives.

4

Multibeam echosounder bathymetric measurements: implications of using frequency modulated pulses

It is far better to foresee even without certainty than not to foresee at all

Henri Poincare

The objective of this chapter is to elaborate on the implications of using Frequency Modulated (FM) pulse shapes for bathymetric measurements. The increasing interest in their use due to maintaining high resolution at larger ranges necessitates the assessment of the associated bathymetric uncertainties. Despite the advantages gained by using FM signals (Section 2.5), MultiBeam EchoSounder (MBES) measurements acquired in this mode exhibit higher noise level than those derived using Continuous Wave (CW).

This chapter begins by modeling the effect of using FM pulse shape on MBES bathymetric measurements, i.e., Doppler frequency shift and baseline decorrelation. Next, these contributions are quantified for situations of relevance for MBES bathymetric measurements on the continental shelf and ship dynamics associated to rough and calm sea-states. Following this, the bathymetric uncertainties induced due to the use of FM signals are compared to the total predicted bathymetric uncertainty considering only the contributors inherent to the MBES. Finally, a comparison is made between the modeled and measured depth uncertainties when switching from CW to FM signals.

4.1. Introduction

Modern MBES have the option to use FM signals, in addition to the more standard CW signals. FM signals enable emitting long pulses, while keeping a high ranging resolution [46]. The latter is obtained by matched filtering the received echo signals (Section 2.5.3). The long pulse allows for measurements at larger ranges, resulting in an increase in the attainable swath. Despite the advantages gained by using FM signals, it has been observed that switching from CW to FM can result in noisier bathymetric measurements [47–49, 122]. A number of potential sources for the degradation in the performance of bathymetric measurements due to the use of FM signals have been identified in references [49, 50, 123].

The first cause is related to the Doppler effect. Since the MBES is in a constant movement, the received signals will be affected by a Doppler frequency shift. When this received Doppler Shifted signal is matched filtered, using as replica the emitted signal, the matched filtered output will be affected by this difference in frequency, resulting in a bias in the estimate of the arrival time. In general, this bias is corrected for in the MBES processing, using the speeds of the transducers at transmission and reception [124]. Still, the imperfect knowledge of the speeds, and thus the imperfect correction, gives rise to uncertainties in the MBES derived depths.

In addition, the frequency shift as introduced by the Doppler effect also has an impact on the beamsteering (Section 2.4.1), resulting in uncertainties in the steering angle. This second effect, however, also holds for CW pulses and is in general not compensated for (Ø. Aasbø, Kongsberg personal communication, August 2017). An uncertainty in the steering angle gives rise to uncertainties in the estimated depths which is of importance in the prediction of the total uncertainty budget carried out prior to a survey with an MBES (Section 2.7); an underestimation of the contribution of the Doppler effect potentially leads to an optimistic expectation of the depth uncertainties.

The second origin of potential effects on bathymetric uncertainties, stemming from the use of FM signals, is the baseline decorrelation. The phenomenon of baseline decorrelation is encountered in the MBES interferometry step (Section 2.4.2), applied when using phase detection (Section 2.6.3). For the interferometry step, the full MBES receiving array is divided into two sub-arrays and the phase difference of the signals arriving at the two sub-arrays is determined. The time at which the two signals are in phase is taken as the arrival time and the angle corresponding to this zero phase difference is referred to as the Direction of Arrival (DOA) [125]. For MBES, the DOA is assumed to be known. For other systems, e.g., full interferometric systems, other effects such as footprint shift can also be of importance. Expressions for uncertainties in these cases, based on the Cramer-Rao lower bound, can be found, for example in references [126–129].

The backscattered signals received by these two sub-arrays are slightly different due to the different angular directions, and consequently the coherence between the two received signals is reduced. This degradation in coherence, negatively affecting the quality of the phase estimates, is a purely random process [130] which cannot be compensated for. This effect has been addressed in a number of studies,

for example in references [16, 79, 130, 131], for different environments. Based on different measurement configurations and signals considered, different outcomes were found regarding the importance of the baseline decorrelation. In reference [49] the effect has been studied nicely and thoroughly specifically for the MBES using FM pulses, and expressions were derived for quantifying the uncertainty in MBES bathymetric measurements due to baseline decorrelation for both FM and CW pulses. For the situation considered in [49], consisting of a water depth of around 200 m and a 73 kHz MBES, it has been found that the phase difference uncertainty (which results in bathymetry uncertainty) due to baseline correlation is higher for FM pulses than for CW pulses. This indicates that indeed the baseline decorrelation is a factor potentially contributing to a degradation in the bathymetric measurements when switching from CW to FM pulses.

In this chapter the analysis of [49] is extended to a shallow water configuration (around 60 m), of relevance to marine environments typically encountered on the continental shelf, and a high frequency MBES system (a center frequency of 300 kHz). Both above mentioned contributions, i.e., the effects of Doppler and baseline decorrelation, are quantified for this environment. This provides insight in their relative importance. Another important step in this paper, in addition to the analysis of [49], is to investigate if for these types of environments indeed a degradation in bathymetric measurements due to the use of FM pulses is expected. To this end, the contribution of the Doppler effect is compared to all other uncertainties inherent to MBES bathymetric measurements, i.e., range measurement, roll and steering angle, pitch angle, beam opening angle and sound speed profile (Section 2.7). For this, use is made of predictions of the total propagated uncertainty based on [26] and [27]. To assess the agreement of the modeled uncertainties with those encountered in measurements, depth measurements in both FM and CW modes acquired during a survey in the Westerschelde estuary, the Netherlands, using EM2040C dual head are analyzed.

A preliminary study on the effect of using FM pulses on the uncertainty of the MBES derived depth was presented in [121], mainly investigating the sensitivity to various pulse shapes. In the present chapter, focus is on a realistic MBES so that the results can be compared with measurements. In addition, the considered uncertainties are compared to other sources of uncertainty in MBES bathymetric measurements.

The chapter is organized as follows. Section 4.2 focuses on the expected effects of the use of FM signals. In Section 4.3 the contributions of Section 4.2 are quantified for a realistic situation followed by a discussion on their relative contribution to the total bathymetric uncertainties in Section 4.4. The results from real measurements are presented in Section 4.5 and the conclusions are drawn in Section 4.6.

4.2. Modeling the effect of using FM signal on MBES bathymetric uncertainties

Considering the use of either CW or FM pulse shapes, the only difference in the processing is the fact that for the FM signal matched filtering, i.e., pulse compression, is applied at reception. This is illustrated in the diagram of Fig. 4.1.
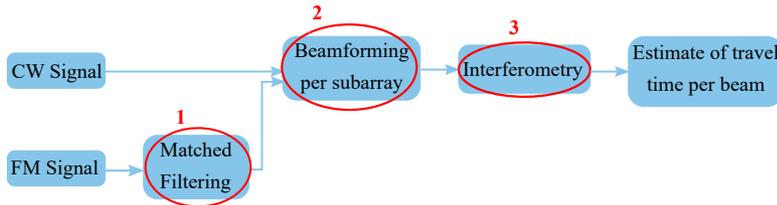
Figure 4.1: Flow diagram of the MBES processing chain. Indicated with ellipses are the three processing steps that are considered in this chapter with respect to potential influence of using an FM pulse on the quality of the MBES derived estimates of water depth.

The potential causes for the degradation in MBES bathymetric measurement performance due to the use of FM signals, as indicated by the ellipses in Fig. 4.1, are:

1. The MBES is in constant movement. Consequently, the received signal shape is affected by Doppler effects. When applying matched filtering (Section 2.5.3) to the received signal using as the replica the emitted signal without Doppler, an error is introduced;

2. The Doppler effect also affects the beamsteering (Section 2.4.1) since the delays applied assume the frequency of the signal without the presence of Doppler. However, this effect also exists for CW signals;

3. In the interferometry step the full array is divided into two sub-arrays and the phase shifts as a function of time between the beamformed signals for a given steering direction at these two sub-arrays are determined. The time at which this phase shift is zero corresponds to the return from the seafloor at the beam angle exactly equaling the beamsteering angle. The estimates of the phase shifts, and therefore the zero-crossing, are deteriorated by noise (intrinsic and additive). Whereas the improved Signal-to-Noise Ratio (SNR) (reduction of relative contribution of additive noise), for FM signals will reduce this noise, references [49] and [50] suggested that the sidelobes of the matched filtered FM signal will increase the noise (intrinsic noise increases), see Section 2.5.3 and Fig. 2.15.

4.2.1. Doppler frequency shift

In this subsection the effect of the Doppler frequency shift on the MBES measurements is addressed, thereby quantifying the effects indicated by 1 and 2 in Fig. 4.1. The Doppler frequency shift stems from the movement of the MBES transducer

when emitting and receiving the signal. Consider a single scatterer (a point) at angular position θ_p relative to the array normal, see Fig. 4.2. The distance between the two sub-array centers (hereafter denoted a and b) is referred to as the baseline length denoted by L_b. The speeds of the array center at emission and reception projected on the beam direction are v_e and v_r, respectively. It is assumed that there is no rotation around the array center, an interested reader is referred to as [49] for a situation where the rotation is taken into account.
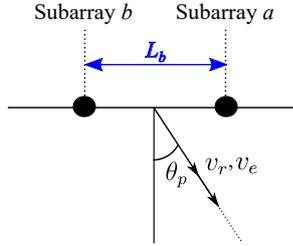
Figure 4.2: Geometrical configuration considered. The figure is based upon figures from Ref. [49].

The time difference between emitting and receiving the first sample of the emitted pulse for a receiver located at the center of the array is denoted by τ_0. Since the signal samples span the pulse length and the receiver and transmitter are in movement over the pulse length, the time needed for the signal to travel from source to receiver changes over the pulse length.

Consider now the signal sample received at the instant t_r, which corresponds to the signal sample transmitted at the instant t_e where both times are defined as the elapsed time since the start of the transmission. The following equations relate these two instances for the two sub-arrays a and b, respectively.

$$c(t_r - t_e) = c\tau_0 - v_e t_e - v_r(t_r - \tau_0) - \frac{L_b}{2}\sin\theta_p , \qquad (4.1a)$$

$$c(t_r - t_e) = c\tau_0 - v_e t_e - v_r(t_r - \tau_0) + \frac{L_b}{2}\sin\theta_p , \qquad (4.1b)$$

with c the speed of sound in the water. Considering the point on the seafloor is located in the far-field (which is a valid assumption for the typical values for the frequencies used in MBES and the water depth considered here, around 60 m), the curvature of the wave front can be neglected. For the array center and $t_e = 0$, one finds $t_r = \tau_0$, i.e., the Two-Way Travel Time (TWTT) of the first sample from and to the array center. For all subsequent times, the above expressions model the change in the received signal due to the movement of the transducer at emission and reception. Using Eq. (4.1) the received signals can be expressed as [49]

$$S_a(t) = s\left(\frac{k_{r1}}{k_e}(t - \tau_0) + \frac{1}{k_e}\frac{L_b\sin\theta_p}{2c}\right) \text{ with } k_e = 1 - \frac{v_e}{c}, \ k_{r1} = 1 + \frac{v_r}{c} , \quad (4.2a)$$

$$S_b(t) = s\left(\frac{k_{r2}}{k_e}(t - \tau_0) - \frac{1}{k_e}\frac{L_b\sin\theta_p}{2c}\right) \text{ with } k_{r2} = 1 + \frac{v_r}{c} , \qquad (4.2b)$$

with s the emitted signal shape (Sections 2.5.1 and 2.5.2). It is seen that the received signals are delayed and distorted, i.e., affected by Doppler, versions of the transmitted signal.

Doppler effect on matched filtered signals

The resulting Doppler frequency shift affects the matched filtering output (Section 2.5.3). Small Doppler mismatches, where the matched filtered signal is Doppler shifted but the replica is not, do not change the general matched filter output shape and reduce the amplitude very little for FM pulses [132]. However, the maximum of the matched filter output is shifted in time. Thus, uncompensated Doppler frequency shifts change the estimate of the TWTT; this is the so-called range-Doppler coupling[133]

$$t^{\text{shift}} = -f_d \frac{T}{B} \, , \tag{4.3}$$

with t^{shift} the shift in the location of the maximum of the matched filter output with respect to the undopplerized matched filter output. f_d is the difference between the frequency of the received and emitted signals (reflecting the Doppler effect) equaling $f_d = f_c(1 + v_r/c)(1 - v_e/c)^{-1} \approx f_c(v_r + v_e)/c$ where f_c is the center frequency of the signal. B and T are the total signal bandwidth and pulse duration, respectively. It is assumed that the MBES transducer speeds are much smaller than c. In case the exact value for f_d is considered instead of the approximation, the resulting t^{shift} will be in agreement with reference [134].

The maxima of signals S_a and S_b after matched filtering are thus shifted with shifts $t_{S_a}^{\text{shift}}$ and $t_{S_b}^{\text{shift}}$ equaling

$$\delta t = t_{S_a}^{\text{shift}} = t_{S_b}^{\text{shift}} = -\frac{v_e + v_r}{c} f_c \frac{T}{B} \, , \tag{4.4}$$

with δt the expected shift in the estimate of the TWTT. Thus, the first impact of the Doppler effect is a time shift in the estimated arrival time, and thus the estimated range equaling $-f_c T \frac{v_e + v_r}{2B}$. In principle, the time shift (range shift) due to the range-Doppler coupling can be compensated in the post-processing mode if the speeds are known [135], (Ø. Aasbø, Kongsberg personal communication, August 2017). However, an uncertainty in these speeds results in an uncertainty in the correction applied, leading to an uncertainty in the estimated bathymetry.

Doppler effect on beamforming

When beamforming, the signals as received on the different receiving elements are delayed and then summed. The delay is such that it reflects the expected differences in the arrival times for the different receiving elements. The delay can be either applied on the signals in the time or frequency domain. The latter corresponds to applying a phase shift, Section 2.4.1. Movement of the transducer affects the received signal. Not accounting for this in the time delay or phase shift will, in turn, have an influence on the beamforming output. This effect exists both for FM and for CW pulses.

The derivations below consider the array to consist of two elements (a and b) distanced by L_b. For the times at which the signals are received at sub-arrays a and b, we can write

$$t_r(c + v_r) = t_e(c - v_e) + \tau_0(c + v_r) - \frac{L_b}{2} \sin \theta_p , \qquad (4.5a)$$

$$t_r(c + v_r) = t_e(c - v_e) + \tau_0(c + v_r) + \frac{L_b}{2} \sin \theta_p , \qquad (4.5b)$$

or

$$t_r = \tau_0 + t_e \frac{c - v_e}{c + v_r} - \frac{L_b}{2} \frac{\sin \theta_p}{c + v_r} , \qquad (4.6a)$$

$$t_r = \tau_0 + t_e \frac{c - v_e}{c + v_r} + \frac{L_b}{2} \frac{\sin \theta_p}{c + v_r} , \qquad (4.6b)$$

respectively. The first term in Eq. (4.6) is the time between the emission of the first signal sample and its arrival at the full array center. The term in the middle indicates the compression or expansion of the signal corresponding to the Doppler shift in frequency. The last term of these two equations indicates the time shifts that need to be applied when steering in direction θ_p. However, the time delays applied in the MBES are different and do not account for the speed of the transducer, i.e., they account only for the speed of sound c and not for the full $(c + v_r)$ terms, resulting in a difference between the steering angle aimed for and that obtained θ_s. The following holds

$$\frac{L_b \sin \theta_s}{c} = \frac{L_b}{2} \frac{\sin \theta_p}{c + v_r} + \frac{L_b}{2} \frac{\sin \theta_p}{c + v_r} \Leftrightarrow \sin \theta_s \approx \sin \theta_p (1 - \frac{v_r}{c}) . \qquad (4.7)$$

The term $1 - v_r/c$ is derived using the Taylor series expansion of $1/(1 + v_r/c)$ with $|v_r/c| \ll 1$ around the point zero, truncated after the first-order term. Using the Taylor series expansion of $\sin^{-1}[\sin \theta_p (1 - v_r/c)]$ around the point $\sin \theta_p$, again truncated after the first order term, results in the following expression for the error in the steering angle

$$\delta \theta_s \approx \frac{1}{\sqrt{1 - \sin^2 \theta_p}} \frac{v_r}{c} \sin \theta_p = -\frac{v_r}{c} \tan \theta_p , \qquad (4.8)$$

indicating that when steering at θ_s a scatterer located at the angular position θ_p is localized. This bias is equal for CW and FM signals. In contrast to the effect of Doppler on the matched filtered signals which is often taken into account in the post processing, the angular bias in the beamsteering is not corrected for (Ø. Aasbø, Kongsberg personal communication, August 2017). This bias in the angle estimate varies from ping to ping and is as such in this research considered as a contribution to the depth uncertainty considering v_r as the random variable.

Doppler effect on MBES bathymetric measurements

Finally, the uncertainty in the bathymetric measurements as introduced by the Doppler frequency shift can be determined from the expression given in Eq. (2.44) and repeated here

$$d = r \cos P \cos \Theta \,, \tag{4.9}$$

with d the depth below the transducer at the instant of the measurements, P the pitch angle. The beam angle Θ with respect to the depth-axis is defined as $\theta_s + R + \theta_{\mathrm{mount}}$ with R the roll and θ_{mount}, see Fig. 2.22.

In case there is an uncertainty in the steering angle due to the Doppler effect, $\sigma_{\theta_{s,\mathrm{Doppler}}}$, an uncertainty in the bathymetry, $\sigma_{d,\theta_{s,\mathrm{Doppler}}}$, is introduced. The expression for the contribution of this uncertainty is obtained from

$$\sigma_{d,\theta_{s,\mathrm{Doppler}}}^2 = (r \cos P \sin \Theta)^2 \sigma_{\theta_{s,\mathrm{Doppler}}}^2 = (r \cos P \sin \Theta)^2 \frac{\mathrm{var}(v_r)}{c^2} \tan^2 \theta_p \,, \tag{4.10}$$

where $\sigma_{\theta_{s,\mathrm{Doppler}}}$ is determined by applying error propagation to Eq. (4.8) and $\mathrm{var}(v_r)$ denotes the variations in the speed at the reception which in this case corresponds to the variance of v_r.

Similarly, an uncertainty in the estimate of the range shift due to the Doppler effect (stems from the uncertainties in the estimate of the transducer speeds), $\sigma_{r_{\mathrm{Doppler}}}$, results in a bathymetric uncertainty $\sigma_{d,r_{\mathrm{Doppler}}}$. For the bathymetric uncertainty we have

$$\sigma_{d,r_{\mathrm{Doppler}}}^2 = (\cos P \cos \Theta)^2 \sigma_{r_{\mathrm{Doppler}}}^2 = (\cos P \cos \Theta)^2 \left(f_c \frac{T}{\sqrt{2}B}\right)^2 \sigma_{v_r}^2 \,. \tag{4.11}$$

Here, it is assumed that the uncertainty in the speed at transmission and reception are equal with σ_{v_r} the uncertainty in the speed at the reception. This is a valid assumption for the situations where the TWTT is short compared to the typical period of change in the wave motion (the ocean wave period spectra is larger than 4 s [40, 136]), and thus the speeds at transmission and reception are almost equal. However, for deeper water where the TWTT can be several seconds, these speeds are different and the error propagation should be applied separately to them. $\sigma_{d,r_{\mathrm{Doppler}}}$ only occurs when using FM pulses. However, the bathymetric uncertainty induced by the error in the beamsteering, Eq. (4.10), holds for both CW and FM pulses.

4.2.2. Baseline decorrelation

Signals arriving from scatterers located in the signal footprint (instantly ensonified area) overlap in time, i.e., the signals received at one instant of time result from contributions of all scatterers within the signal footprint. Hence, the footprint can be considered as a source dimension with its own directivity pattern. This fluctuation and the fact that the two sub-arrays observe the bottom along slightly different angular directions result in a decorrelation between the two received signals. This

decorrelation is referred to as baseline decorrelation which is an intrinsic noise origin (inherent component of the acoustical signal),[29] and increases as the size of the footprint gets larger (due to the more fluctuating directivity pattern). Due to the presence of sidelobes in the matched filtered FM signal, its footprint gets larger compared to that of CW, see Section 2.5.3 and Fig. 2.15, leading to an increase in the contribution of the baseline decorrelation [49, 50]. Reference [27] accounts for the depth uncertainty induced by the interferometry step (phase detection), see Sections 2.4.2 and 2.6.3, through an uncertainty in the angle estimate given in Eq. (2.48)

$$\sigma^2_{d_{\Theta_{\text{meas}}}} = \left(r \sin \Theta \cos P\right)^2 \sigma^2_{\Theta_{\text{meas}}} , \tag{4.12}$$

where the depth uncertainty due to the baseline decorrelation $\sigma_{d,\Theta_{\text{Decorr}}}$ is taken into account through $\sigma_{\Theta_{\text{meas}}}$, i.e., a random uncertainty in the measurement of the beam angle. In case of phase detecion, reference [27] defines $\sigma_{\Theta_{\text{meas}}}$ as

$$\sigma^2_{\Theta_{\text{meas}}} = \left(\frac{0.2\Omega_{R,0}}{\sqrt{n_p}}\right)^2 , \tag{4.13}$$

with Ω_{R_0} the beam opening angle in the across-track direction in case no steering is applied. As mentioned in Section 2.7.1, the beam opening angle in the across-track direction is considered constant in references [26, 27], derived assuming zero steering. Thus, here we use the term Ω_{R_0} to distinguish between the constant zero steering used here and that of varies with beam angle, see Eq. (2.28). n_p is the number of phase samples obtained from Eq. (2.50) by Substituting Ω_{R_0} for Ω_R as

$$n_p = \frac{\frac{d\Omega_{R_0}}{\cos^2 \Theta}}{\frac{cT}{2 \sin \Theta}} . \tag{4.14}$$

An alternative approach is to account for the baseline decorrelation through an uncertainty in the estimate of the phase difference zero-crossing (in the interferometry step), Section 2.4.2 and Fig. 2.21. In this chapter, use is made of the coherence coefficient μ, [49, 50, 131], for the MBES interferometry step defined as

$$\mu = \frac{S(f)^2 \left(f_c \frac{L_b}{2d} \frac{cos^2\Theta}{\tan \Theta}\right)}{S(f)^2(0)} , \tag{4.15}$$

where $S(f)$ denotes the Fourier transform of the transmitted signal $s(t)$. $s(t)$ may be the actual envelope of the narrow-band signal (CW) or the envelope obtained after pulse compression of the modulated signal (FM). As the coherence coefficient is dependent on the signal parameters (shape and f_c), it is not known beforehand how this decorrelation affects CW signals compared to FM signals.

From [137], the following expression for the variance of the phase difference is

obtained

$$
\sigma_{\Delta\varphi}^2 = \frac{1 - |\mu|^2}{1 - (|\mu|\cos\psi)^2}\left(\frac{\pi^2}{4} - \pi\sin^{-1}(|\mu|\cos\psi) + (\sin^{-1}(|\mu|\cos\psi))^2\right)
$$
$$
+ \frac{1}{2}\sum_{j=1}^{\infty}\frac{1 - |\mu|^{2j}}{j^2}\,,
\tag{4.16}
$$

where μ is calculated from Eq. (4.15) and ψ is the phase of the expected value of $S_a S_b^*$, $\psi = \arg(S_a S_b^*)$, Eq. (4.2) (zero at the theoretical instant of detection) with * being the complex conjugate operator.

The expression for the bathymetric uncertainty induced by the uncertainty in the time estimate due to the baseline decorrelation $\sigma_{d_{t_{\mathrm{Decorr}}}}^2$ is obtained from [49]

$$
\sigma_{d_{t_{\mathrm{Decorr}}}}^2 = \frac{(d\sigma_{\Delta\varphi})^2}{\left(2\pi f_c\frac{L_b\cos\Theta}{c\tan\Theta}\right)^2 n_p}\,.
\tag{4.17}
$$

Typically Eq. (4.12) or Eq. (4.17) are used to account for the bathymetric uncertainty induced by interferometry. We now investigate to what extend they agree. As first step Eq. (4.13) is substituted in Eq. (4.12) with the across-track beam opening angle (with zero steering) equaling $\Omega_{R_0} = \lambda/L = c/(f_c L)$, where L is the total length of the acoustic array which is different from the baseline length (L_b). The latter is chosen to be one-third of the total array length [49]. This substitution leads to the following expression

$$
\sigma_{d,\Theta_{\mathrm{meas}}}^2 = \frac{(0.2d)^2}{\left(3f_c\frac{L_b}{c\tan\Theta}\right)^2 n_p}\,.
\tag{4.18}
$$

It is clear that Eqs. (4.17) and (4.18) are in agreement (the part $\left(d/(\frac{f_c L_b\sqrt{n_p}}{c\tan\Theta})\right)^2$ is similar in both expressions), except for a coefficient Q. In the case where Eqs. (4.17) and (4.18) are used, this coefficient equals $\sigma_{\Delta\varphi}/(2\pi\cos\Theta)$ and 0.2/3, respectively. $\sigma_{\Delta\varphi}$ is dependent on the pulse shape. In Section 4.4 the agreement between both expressions is quantified.

An additional point to highlight is the effect of additive noise. The above considerations have not taken into account the deteriorating effect of additive noise affecting the outer beams. The nature of the additive noise makes its prediction complicated, [11, 66], requiring information on the acoustic backscatter returned to the MBES. The backscatter strength returned to the sonar is the result of a complex interaction of the acoustic pulse transmitted and the often inhomogeneous seafloor, see as an example [138] and [139]. The nature of the energy returned carries important information about the seafloor characteristics and physical properties and can be used for seafloor classification [80, 140]. However, the backscatter strength

might not be known before the data acquisition and no closed form expressions can be derived. Still, in Sections 4.3 and 4.4, the total coherence coefficient due to both noise origins is assessed to obtain insight into the impact of the additive noise. Additionally, this uncertainty source is also discussed in Section 4.5, where real measurements acquired in the FM and CW modes are analyzed.

4.3. Quantifying contributions of Doppler effect and baseline decorrelation to MBES bathymetric uncertainty

This section aims at the quantification of the potential effects of the Doppler frequency shift and baseline decorrelation on the bathymetric uncertainty. The situation considered is that of 60 m water depth, and a high-frequency MBES (300 kHz). The MBES considered reflects the EM2040C dual head. Currently, this system is in widespread use for monitoring continental shelf waters. CW and FM specifications and the characteristics of the Kongsberg EM2040C MBES are presented in Table 4.1 and Table 4.2 [141], respectively. The modeling was carried out for the medium and very long CW pulse lengths available in EM2040C, i.e., 0.145 ms and 0.6 ms. The former is often used for shallow waters and the latter was employed here to assess the impact of lengthening the pulse (consequently larger footprint). For the FM, a pulse with a total duration of 3 ms was considered.

For the CW pulse, a Hanning function was applied. With regards to the tapering value of the FM signal, Kongsberg considers a varying tapering value between 10% and 50% [Ø. Aasbø, Kongsberg personal communication, August 2017]. In this chapter, the modeling was carried out using the smallest (nearly rectangular shape) and largest tapering values to assess the effect of signal smoothing.

With regards to the bandwidth used, the EM2040C transmits FM pulses with a bandwidth of a few kHz [Ø. Aasbø, Kongsberg personal communication, August 2017]. We focused on an effective bandwidth of 2.615 kHz and 3.615 kHz, Table 4.1 (calculated from the total bandwidth as $B_{\mathrm{eff}} = B(1 - 0.625 \times \gamma/100)$ with γ the tapering value in % [63]). The same relationship holds for the total and effective pulse lengths. The length of the baseline L_b was assumed to be 0.12 m which is one-third of the theoretical array length (based on the beam opening angle), corrected for the shading.

Table 4.1: CW and FM specification for EM2040C.

Parameter	CW	FM	FM	FM
Tapering value [%]	100	10	50	50
Center frequency [kHz]	300	300	300	300
Total pulse length [ms]	0.145 and 600	3	3	3
Total bandwidth [kHz]		2.790	3.803	5.258
Effective bandwidth [kHz]		2.615	2.615	3.615

Table 4.2: Characteristics of a EM2040C dual head used as input for the predictions of MBES inherent depth uncertainties.

Parameter	Value
Number of beams	400
Beamspacing mode	equiangle
Swath Width [°]	130
Mounting angle of transducer [°]	34.73 for starboard, 35.29 for port
Beamsteering reference angle [°]	0
Along-track opening angle [°]	1
Across-track opening angle at nadir [°]	1
Range resolution [m]	0.018

4

4.3.1. Doppler frequency shift

For modeling the effects of the Doppler frequency shift, the uncertainty and variance of the MBES transducer speeds at transmission and reception are needed. To this end, positioning and attitude data acquired during two measurement campaigns were used. One data set was acquired in the North Sea (Cleaver Bank area) on 05/11/2013 in rough weather conditions. To assess the impact of the weather condition on the Doppler effect, we also analyzed the data set from the Plymouth Sound area, United Kingdom, acquired on 12/10/2004 in a calmer weather condition compared to the Cleaver Bank data. The water depth assumed for the predictions of the Doppler induced depth uncertainty was 60 m.

Shown in Fig. 4.3a is the variation of the speeds at transmission projected on the beam direction for different beam angles over a sailing track with relatively constant heading for the rough (black) and calm (green) sea states. The reason for considering one track line with constant heading and not the full survey area was that for the projection of the speeds on the beam direction, the rotation from the navigation frame to vessel frame is required, which can be significantly unstable when making turns and changing sailing direction [135].

The impact of the weather condition is clearly visible. Rough weather conditions result in larger variations of the projected speeds over the varying beam angles compared to calm conditions. Larger values for calm sea state for the beams close to nadir are due to the higher vessel speed during the data acquisition (4.63 m/s for calm and 3.06 m/s for the rough sea state). It is also seen that the variations of the speeds projected are not perfectly symmetric with respect to the nadir (this behavior was also observed in [135]) for either data sets due to the vessel rolling during data acquisition (this was confirmed by obtaining a symmetric variations with respect to the beam angle from a simulation with zero roll angle).

As mentioned, for the bathymetric uncertainty due to imperfect corrections of the Doppler effect in the matched filtering process, the uncertainty in the estimate of the speeds is required. To obtain an estimate for this value, a Monte Carlo simulation was run where the projected speeds were calculated assuming that the measurements from the motion and positioning sensors and offsets are normally distributed with a standard deviation specified by Kongsberg to meet the accuracy

requirement of the EM2040C system (K. Jensen, Kongsberg personal communication, June 2018). The uncertainties of roll, pitch, heading, and heave equaled 0.02°, 0.05°, 0.02° and 0.05 m or 5% of the depth, whichever is highest, respectively. Moreover, the accuracy of transducer and motion sensors offsets were assumed to be 0.02 m, 0.02 m, 0.005 m and 0.05 m, 0.05 m, 0.05 m in the vessel coordinate system with positive x to the starboard, positive y to the bow and positive z toward the up direction. Shown in Fig. 4.3b are the uncertainties in the estimate of the speeds for both sea states. It is seen that for the rough conditions, the uncertainties are in general higher than those of the calm.
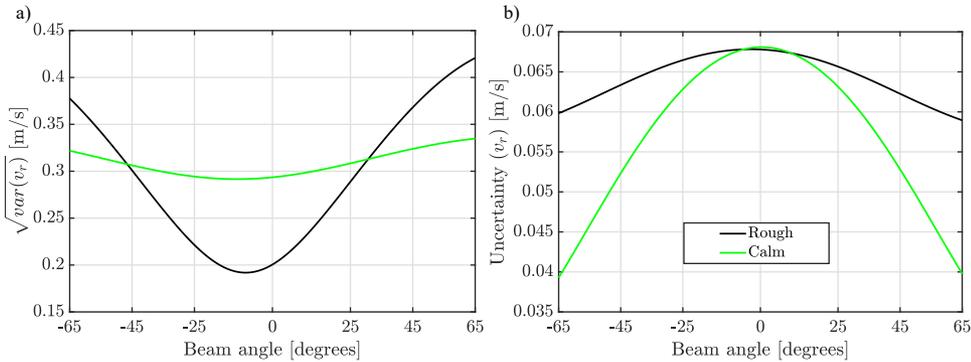
Figure 4.3: a) Square root of the variations and b) uncertainties in the estimate of the speeds at transmission projected on the beam direction for different beam angles for rough (black) and calm (green) sea states.

Using these variations and uncertainties of the speeds, the MBES bathymetric uncertainty induced by the uncertainty in the Doppler effect was calculated using Eqs. (4.10) and (4.11). It should be noted that theoretically the calculation of the depth uncertainty induced by the imperfect Doppler correction requires both the uncertainties in the estimate of the speeds at transmission and reception, see Eq. (4.4). However, considering a water depth of around 60 m, the maximum TWTT for the most outer beam equaling 65° is approximately 0.2 s. This is considerably shorter than the typical period of the waves (around 4 s), and the speeds at the reception and transmission are thus almost equal. This was also verified from the two data sets. Fig. 4.4 shows the resulting bathymetric uncertainty, referred to as the Random Vertical Uncertainty (RVU), for CW and FM pulses. Although when using a CW pulse (Fig. 4.4a), matched filtering is not applied, the variations of the speeds still induce an uncertainty in the measurements. This corresponds to an uncertainty in the beam steering angle which is currently not corrected for in the MBES processing. It is seen that for the calm sea state, the depth uncertainty for the CW pulse is nearly 85% of that of the rough sea state for the most outer beams.

For the FM pulse there is, in addition to the error in the beam angle, also an uncertainty in the travel time estimation, see Fig. 4.4b. The depth uncertainty due to beam steering (dashed curves) is independent of the pulse shape and is equal for both CW and FM pulses. However, the depth uncertainty due to the imperfectness
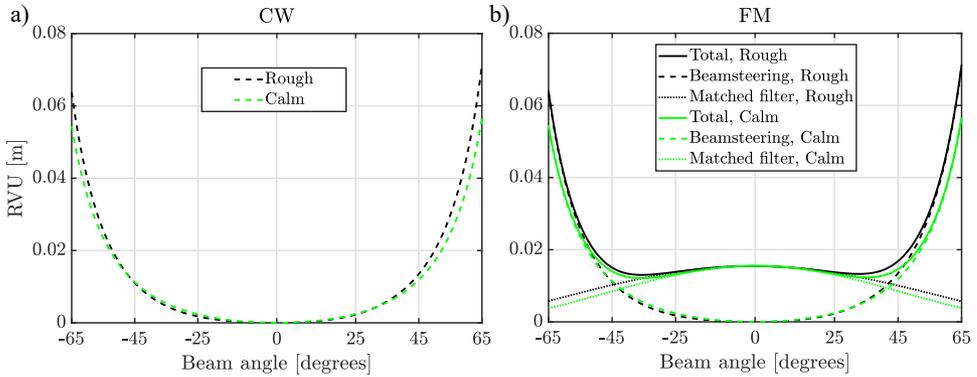
Figure 4.4: a) RVU due to the Doppler effect for a CW pulse with the duration of 0.145 ms and b) RVU due to the Doppler effect for an FM pulse with an effective bandwidth of 2.615 kHz and an pulse length of 3 ms for a rough (black) and more calm (green) sea states.

of Doppler range correction occurs only for FM pulses (dotted curves in Fig. 4.4b) and depends both on the bandwidth and pulse length of the signal. Widening the bandwidth (or increasing the tapering value) of the FM pulse decreases the contribution of this uncertainty source. Compared to the depth uncertainty due to the beamsteering which is a first-order effect, the contribution of the uncertainty due to the imperfectness of the Doppler range bias estimation, a second-order effect, is much smaller. Both effects and their sum are shown for FM, see Fig. 4.4b. As expected, the rough sea state worsens the situation, i.e., for the most outer beams the uncertainty is increased by a factor of 1.2 and the dominant contributor is the error due to the beamsteering. It should be noted that not accounting for the Doppler effect in the matched filtering would increase this contribution typically by a factor of 10.

4.3.2. Baseline decorrelation

Eqs. (4.15) and (4.16) are used to calculate the coherence coefficient, Fig. 4.5a, and the standard deviation of the phase difference between the sub-arrays a and b over the phase ramp, Fig. 4.5b, as a function of the beam angle, respectively.

As can be seen for the CW pulse with the duration of 0.145 ms, the coherence coefficient is the highest leading to the lowest noise over the phase ramp (dashed curves in both frames of Fig. 4.5). However, an increase in the pulse length leads to a decrease in the coherence coefficient and increase in the standard deviation of the phase estimate, as seen for the two CW pulses with different durations. This can be explained by the increasing signal footprint and the resulting decreasing coherence level.

With regards to the FM pulse, the coherence coefficient (and the noise over the phase ramp) is more controlled by the bandwidth and the tapering values instead of the pulse length. Increasing the tapering value results in an increase in the coherence coefficient (decrease in the noise over the phase ramp) as the sidelobe
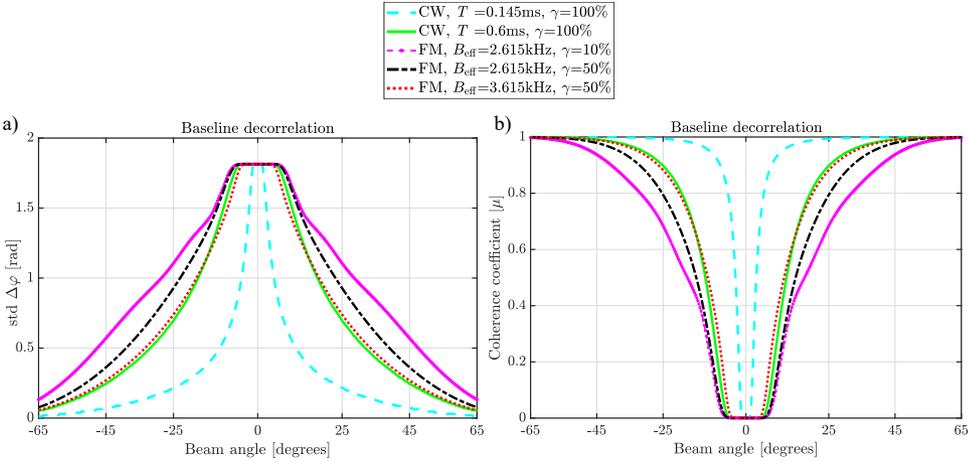
Figure 4.5: a) coherence coefficient considering the baseline decorrelation and b) predictions of $\sigma_{\Delta\varphi}$ due to the baseline decorrelation for CW and FM pulses with different specifics. For the echosounder a baseline L_b of 0.12 m was used ($\psi = 0$).

level is reduced. Moreover, widening the bandwidth of the FM signal, again leads to an improvement in the coherence coefficient which is expected as the effective pulse length decreases (compare the three FM pulses in both frames of Fig. 4.5). An increase in the pulse length of the FM signal while the bandwidth and the tapering coefficient remain unchanged does not affect the coherence coefficient. This is due to the equal effective pulse lengths of the two pulse-compressed signals and, consequently, equal footprints and coherence coefficients.

The comparison between the coherence level of CW and FM pulses due to the baseline decorrelation reveals that, for an effective bandwidth of 2.615 kHz and both tapering values, the coherence coefficient of the CW pulse is higher than that of FM. However, the coherence level and consequently noise over the phase ramp do fully depend on the pulse specifications and are not solely a matter of using CW or FM pulses. As an example, if we consider the FM pulse with a tapering value and effective bandwidth of 50% and 3.615 kHz (dotted curve), respectively, the coherence level due to the baseline decorrelation becomes very close to that of the CW pulse with a pulse length of 0.6 ms.

Although smoothing the FM signal and shortening the CW pulse improve the coherence coefficient, it also reduces the transmitted energy level and hence SNR is deteriorated. As mentioned in Section 4.2, modeling the SNR (additive noise contribution) prior to the survey is a complicated task requiring information on bottom characteristics. However, to obtain insight into the impact of SNR on the standard deviation of the phase difference, a simulation has been performed. SNR modeling is carried out using the well-known active sonar equation [11] assuming a maximum transmitted energy level of EM2040C available (equaling 204.5 dB re μPa at 1 m, K. Jensen, Kongsberg personal communication, June 2018) and a sandy mud bottom, see Table 2.1 for its characteristics. The total backscatter strength is mod-

eled as the result of a contribution from volume backscattering and rough interface backscattering, Section 2.3.2 [66]. It can be shown that the total coherence coefficient is the product of baseline decorrelation coherence coefficient and additive noise coherence coefficient [49, 51]. The standard deviation of the phase estimate is now derived substituting this total coherence coefficient in Eq. (4.16).

Shown in Fig. 4.6 is the standard deviation of the phase estimate resulting from both additive noise and baseline decorrelation. It is seen that for the CW pulse with the longer pulse length, the standard deviation of the phase difference is affected by the additive noise for a smaller range of outer beams. This is due to the higher target strength (increased by an increase in the ensonified area) and lower noise level (inversely proportional to the signal duration). For the two FM pulses with the same tapering coefficients, the additive noise deteriorates the uncertainty in the phase estimate for the outer beams in a similar manner. With regards to the FM pulse with 10% tapering value (nearly rectangular) an increase in the uncertainty of the phase estimate due to the additive noise occurs for a negligible range of outer beams compared to the two other FM pulses considered. Thus, it is seen that although using a smoother FM pulse shape increases the uncertainty on the phase estimate for the outer beam due to the reduced SNR, it decreases the uncertainty due to the baseline decorrelation, and hence a trade-off has to be made between the sidelobe reduction achieved at the cost of an increase in the additive noise.
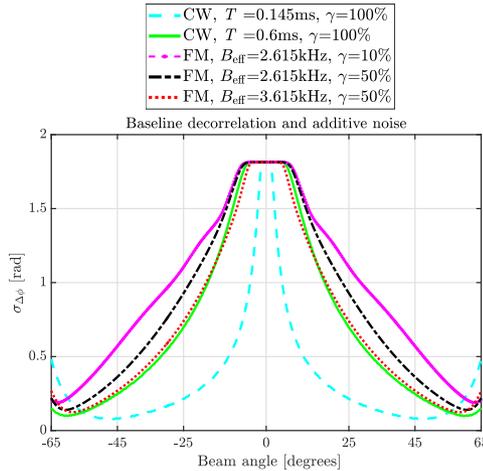
Figure 4.6: Predictions of $\sigma_{\Delta\varphi}$ due to the baseline decorrelation and additive noise for CW and FM pulses with different specifics. For the echosounder a baseline L_b of 0.12 m was used ($\psi = 0$).

The final bathymetric uncertainty due to the baseline decorrelation is determined using Eq. (4.17) and is shown in Fig. 4.7a. From this figure, but also from those shown previously, it is clear that the effect of baseline decorrelation on the bathymetric uncertainty is based on the pulse shape and is not solely a matter of using a FM or CW pulse; compare the FM pulse with the largest effective bandwidth and CW pulse with the longest duration. Moreover, the bathymetric uncertainty due to the

baseline decorrelation increases up to a certain beam angle and then decreases. Depending on the pulse specifications, the standard deviation of the phase difference is nearly constant for the range of beam angles. The denominator Eq. (4.17) thus plays an important role for the beam angles within this range and controls the shape of the bathymetry uncertainty curve (the denominator decreases with the beam angle and consequently the depth uncertainty increases). However, for the beam angles out of this range, the standard deviation decreases rapidly and the rate of its decrease is more dominant than the decreasing rate of the denominator.

To obtain the total depth uncertainty induced by the uncertainty in the detection instant for the different pulses, the signal pulse length has to be also taken into account. This is due to inability to separately distinguish instantaneous contributors located within the resolution cell (delimited by the pulse duration) as they are all received at the same time [29]. This means that at a given instant of reception relative to the transmission, the target echo contains simultaneous contributions from all scatterers included inside a resolution cell, which is determined by the pulse length. Inside this resolution cell, the instantaneous contributors cannot be distinguished separately. Under the assumption of uniformly distributed contributors within the resolution cell (which is a valid assumption if geometrically equidistributed scatterers are considered [29]) the uncertainty in the estimation of the arrival time is $T/\sqrt{12}$ (classical result for a uniform distribution [142]). Considering r in Eq. (4.9) as the multiplication of the sound speed and the $\mathrm{TWTT}/2$ and applying the error propagation gives the estimate of the induced uncertainty due to this contributor as $cT\cos P\cos\Theta/(4\sqrt{3})$, and its square is added to Eq. (4.17). The combined depth uncertainty due to the baseline decorrelation and signal duration is shown in Fig. 4.7b. It is seen that for the CW pulse with the shortest and longest durations, the vertical uncertainty due to the uncertainty in the detection instant is the lowest and highest, respectively. For the two FM pulses with different tapering values, the depth uncertainty is nearly the same. However, as the effective bandwidth increases, the uncertainty decreases. Although the depth uncertainty due to the baseline decorrelation for the FM pulses with a smaller effective bandwidth is higher than that of the CW pulse with a duration of 0.6 ms, the depth uncertainty due to the uncertainty in the detection instant of the former is lower than that of the latter. This is due to the fact that for the FM signal, the effective pulse length after the matched filtering is used to determine the contribution of the signal duration in the detection instant which is much smaller than the original pulse length of the FM (3 ms) and CW with a pulse length of 0.6 ms.

Shown in Fig. 4.7c is the depth uncertainty induced by the combined effect of baseline decorrelation (intrinsic), additive noise, and the signal duration, and hence is a more comprehensive representation of the depth uncertainty due to the uncertainty in the detection instant for the different pulse types. It is seen that for the CW pulse with the shortest duration, the additive noise deteriorates the bathymetric uncertainty for the outer beams (this deterioration was also observed in the estimate of the phase difference, see Fig. 4.6). Regarding the CW pulse with the longest duration and the three FM pulse shapes, no noticeable difference was observed compared to Fig. 4.7b (where only the uncertainty induced by the

baseline decorrelation and signal duration were considered).
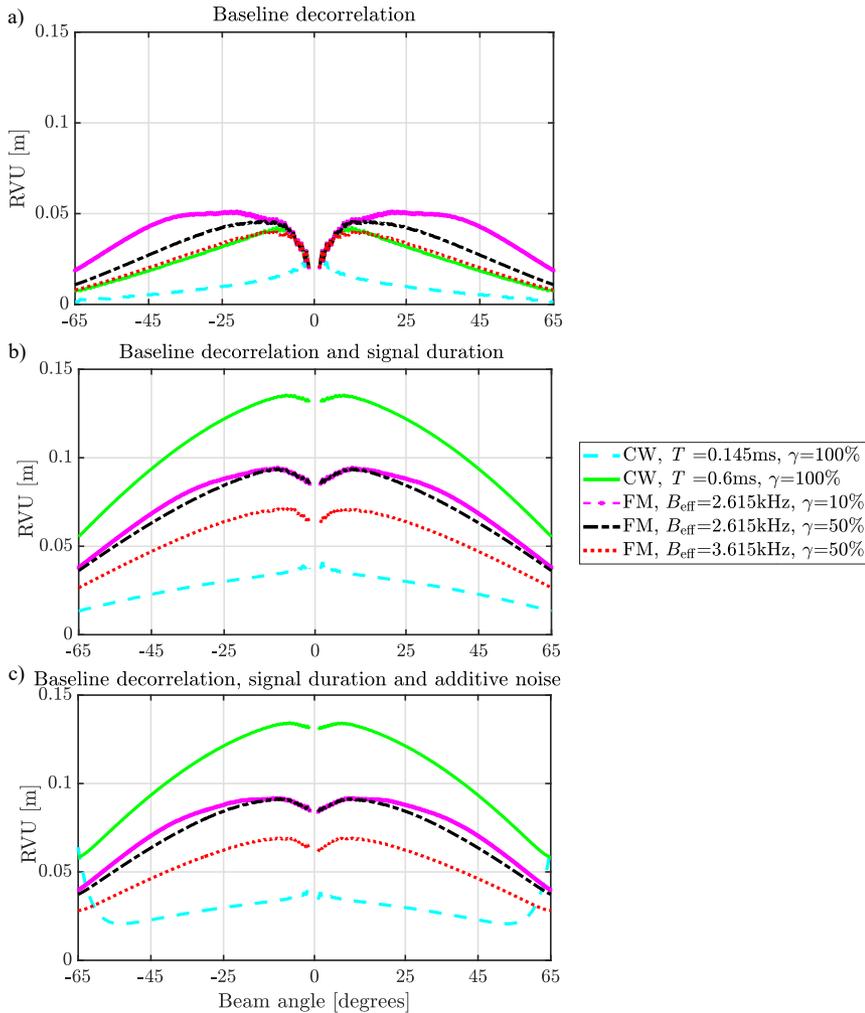
Figure 4.7: Predicted bathymetric uncertainty due to the a) baseline decorrelation, b) baseline decorrelation and signal duration, and c) baseline decorrelation, signal duration and additive noise for CW and FM pulses with different specifics.

As mentioned, the backscatter strength is related to seabed characteristics such as sediment bulk density, seafloor roughness, volume heterogeneity, and discrete scatterers [89] and the SNR (and consequently the additive noise) is thus differ for varying sediment types. To obtain a better understanding of this effect on the additive noise, two sediment types, i.e., clay and sandy gravel, representative of fine and coarse sediments are considered (see Table 2.1 for the characteristics of the sediments). The depth uncertainty induced by the combined effect of the baseline decorrelation, signal duration and additive noise for the CW pulse with

the duration of 0.145 ms (cyan) and the FM pulse with the effective bandwidth of 2.615 kHz and 10% tapering value (magenta) considering these two sediments are shown in Fig. 4.8. To highlight the effect of additive noise, the level of transmitted power is assumed to be 20 dB lower than the maximum power available at the transmission. It is seen that for the fine sediment (clay) shown with solid curve, the additive noise deteriorates the RVU to a larger extent than that of the coarse sediment (sandy gravel) shown with dashed curve which is due to the higher SNR of the latter resulting from the higher backscatter values [80, 143].
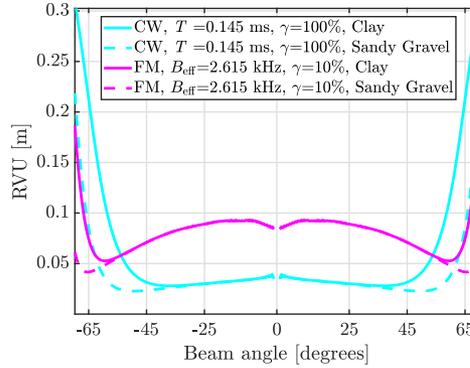
Figure 4.8: Predicted bathymetric uncertainty due to the baseline decorrelation, signal duration and additive noise for a CW pulse of the duration 0.145 ms (cyan) and an FM pulse with an effective bandwidth of 2.615 kHz and 10% tapering value (magenta) for clay (solid) and sandy gravel (dashed) sediments.

4.4. Assessment of the relative contribution of the effects of Doppler and baseline decorrelation

In this section the bathymetric uncertainties induced by the baseline decorrelation and Doppler effect are compared to the total depth uncertainty predicted. For the prediction of the total bathymetric uncertainty, use is made of references [26, 27] considering only the contributors relative to the MBES transducer, see Section 2.7 for the description of the equations used. The uncertainty prediction model was developed under the assumption of independent contributors and flat seafloor. Modeling the uncertainties for a non-flat seafloor requires information regarding the bottom prior to the data acquisition, which is not always feasible.

It should be noted that in Section 2.7, the depth uncertainty contributors are categorized into echosounder, angular motion sensor, motion sonar and transducer alignment, sound speed and heave. Another approach for grouping the depth uncertainty sources considered in this chapter is to categorize them as range measurements Eq. (2.46), roll and steering angle (Eq. (2.48), first term in Eqs. (2.53), (2.54) and (2.58)), pitch angle (second term in Eqs. (2.53) and (2.54)), along-track opening angle (Eq. (2.51)), sound speed profile (the second term in Eq. (2.58)) and

heave. The resulting Total Random Vertical Uncertainty (TRVU) again is calculated using the square root of the sum of the squares of the individual contributors.

As discussed in Section 4.2.2, reference [27] accounts for the depth uncertainty induced by the interferometry step through an uncertainty in the angle estimate given in Eq. (2.48). However, the depth uncertainty due to the interferometry step can be also accounted for by fully taking the pulse shape into consideration using the coherence coefficient. The corresponding depth uncertainty is thus obtained from the uncertainty in the detection instant induced by the baseline decorrelation (with or without additive noise) and signal duration, σ_{d,t_D}. Thus, the uncertainty in the range measurements is expressed as

$$\sigma_{d_r}^2 = \sigma_{d,t_D}^2 + (\cos P \cos \Theta)^2 \left(\frac{r_{\text{meas}}}{c}\right)^2 \sigma_{c_{\text{meas}}}^2 , \qquad (4.19)$$

where $\sigma_{d,t_D}^2 = \sigma_{d,t_{\text{Decorr}}}^2 + \left(cT \cos P \cos \Theta / \left(4\sqrt{3}\right)\right)^2$.

Uncertainty with regards to the vessel heave (combination of the measurement uncertainty of heave and the induced heave) and variation in the water level induce uncertainty in the depth estimation. The contribution of the former depends on the relative location of the MBES transducer and the vertical reference unit and does not solely depend on the MBES in contrast to other sources discussed above. The uncertainty due to the variations in the water level and that of the Global Navigation Satellite Systems (GNSS) also do not depend on the MBES. As the focus here is on the contributors relevant to the depths relative to the MBES transducer, these sources have been excluded from the calculation of the TRVU.

It should be noted that for the calculation of TRVU, the contribution of the Doppler effect has not been considered. This enables us to investigate the magnitude of the underestimation of the depth uncertainty that occurs in case of not accounting for the Doppler induced uncertainty. Presented in Fig. 4.9 is the predicted bathymetry uncertainty due to the total and individual uncertainty sources (68% confidence level) for a CW pulse with a duration of 0.145 ms and an FM pulse with an effective bandwidth of 2.615 kHz.

The characteristics of the EM2040C (Table 4.2) were used as the input parameters to predict the uncertainty in the bathymetry measurement for a given depth (60 m) as shown in Fig. 4.9. In addition to the characteristics of the MBES, the characteristics of the sound speed measurements and the motion sensor are also of great importance. Phins [37] was used as the Inertial Navigation Sensor (INS) for providing position, true heading, attitude, speed, and heave. Roll and pitch accuracies of the system are 0.01° (the misalignment accuracies are assumed to be 0.02°). The sound velocity profiler is a miniSVP manufactured by Valeport. The accuracy of the system indicated by the manufacturer is 0.02 m/s [144]. However, from measurements in different locations (inland waterways and the North Sea), the uncertainty was found to be 0.2 m/s, and hence this value is chosen as a more realistic description of the system accuracy. A constant sound speed of 1500 m/s in the water column and 1505 m/s at the receiver array are assumed. It should be highlighted that the uncertainty predictions presented in Fig. 4.9 are based on the
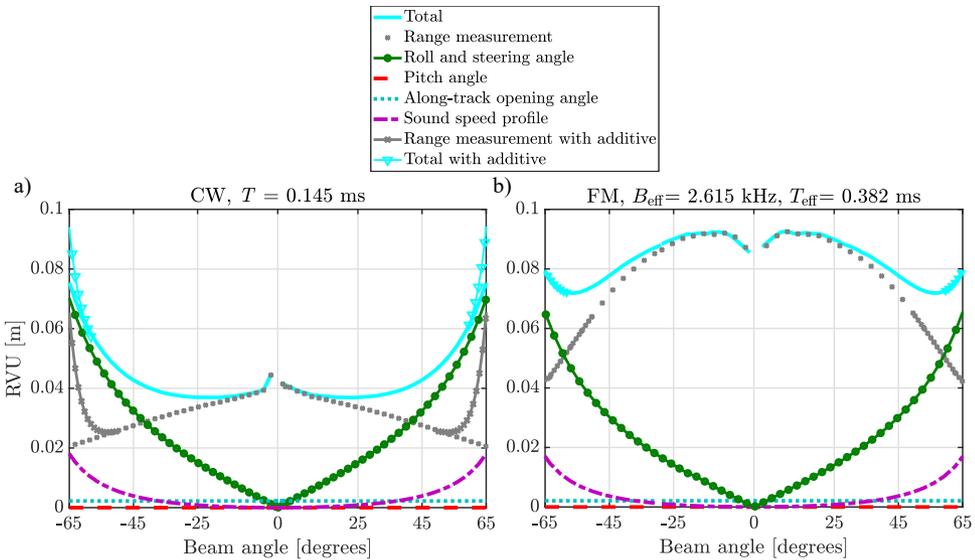
Figure 4.9: Predicted bathymetric uncertainties. Here, the contribution of heave, dynamic draft, and tidal corrections are not considered, a) a CW pulse with a duration of 0.145 ms and b) an FM pulse with an effective bandwidth of 2.615 kHz.

specifications discussed and illustrated in Table 4.1 and are not to be viewed as the uncertainty predictions applicable to a different scenario.

For the FM pulse, the contribution of the uncertainties in the range measurements (grey cross markers), i.e., baseline decorrelation and the signal duration, is higher than that of CW which is due to its longer pulse length. The additive noise consideration does not affect the depth uncertainty for the FM pulses with the specifics considered here; the uncertainty due to the range measurements with and without additive noise coincide. However, for the CW pulse with the duration of 0.145 ms, if the contribution of the additive noise is considered, the range measurements uncertainties (solid grey with cross markers) increase for $\pm 55°$ beam angles onward, Fig. 4.9a, exceeding that FM for the most outer beams. As mentioned, regarding the contribution of other sources of uncertainty as derived by references [26] and [27], no distinction is made between CW and FM pulses.

As can be seen from Fig. 4.9, the maximum TRVU without considering the additive noise (solid cyan) is nearly 0.08 m for both pulse types. While the TRVU for the most outer beams is nearly equal for CW and FM pulses, for the inner beam it is larger for the FM pulse due to the larger uncertainty in the range measurements making it a dominant contributor to the TRVU. Again, if the additive noise is considered for the CW pulse, the maximum TRVU (solid cyan with downward pointing triangle markers) will increase for the outer beams (the central sector is not affected by additive noise as the baseline decorrelation is the dominant source of uncertainty for these beams) and for the most outer beams the TRVU would be slightly larger than that of FM.

With regards to the uncertainties induced by the Doppler effect in case of using the FM (with an effective bandwidth of 2.615 kHz) and CW pulses (with a duration of 0.145 ms) in a rough weather condition (dashed (for CW) and solid (for FM) in Fig. 4.4a and Fig. 4.4b, respectively), one can expect uncertainties of around 0.065 m at $\pm 65°$, respectively. Comparing the TRVU to those induced by Doppler when using FM and CW, the maximum Doppler effect is nearly 82% of the total uncertainty budget. Hence, it is important to consider the uncertainty induced by the former to obtain a realistic description of the bathymetry uncertainty. With regards to the calm sea state, the contributions are 68% of the TRVU.

As mentioned, for the calculation of the uncertainties due to the range measurements we have used the uncertainties induced by the baseline decorrelation (with or without additive noise contribution) in the interferometry step, see Eq. (4.17), where $\sigma_{\Delta\varphi}^2$ is due to the baseline decorrelation. However, reference [27] took a different approach which was discussed in Section 4.2.2. It has been shown that these two approaches are in agreement, see Eq. (4.17) and Eq. (4.18) except for a coefficient Q equaling $\sigma_{\Delta\varphi}/(2\pi\cos\Theta)$ and $0.2/3$, respectively. Shown in Fig. 4.10 is this coefficient for both expressions. For the CW pulse with the shortest duration, the factor based on the baseline decorrelation is larger than that of [27] for beam angles up to $\pm 15°$, and hence using the latter for these beams leads to an underestimation of the uncertainties. However, as the duration of CW pulse increases, the baseline decorrelation increases and the underestimation occurs for a broader range of inner beams in case of using Eq. (4.18). With regards to the FM pulse shapes with nearly a rectangular shape (lowest smoothing), the coefficient Q based on baseline decorrelation is larger than the one based on Eq. (4.18) for almost the complete swath. However, transmitting a smoother signal and widening the effective bandwidth, decreases the range where the underestimation of the uncertainties occur.
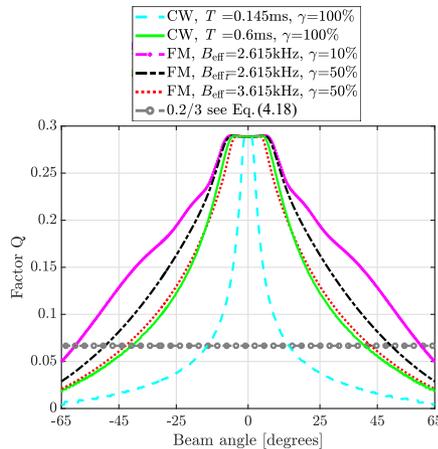
Figure 4.10: Estimated coefficient Q used for predicting the baseline decorrelation for FM and CW pulses with different specifics and the coefficient Q as in reference [27].

4.5. Analysis of MBES experimental data in CW and FM modes

To assess the agreement between the modeled and measured uncertainties, a survey was carried out on 17/08/2017 in the Westerschelde Estuary, the Netherlands, connecting the Scheldt River to the North Sea. The data were acquired using the EM2040C dual head in both CW and FM modes with a center frequency of 300 kHz and pulse lengths of 0.145 ms and 3 ms (effective bandwidth of 2.615 kHz), respectively. The sea state during the measurement was rough. The bathymetry within the area varies between 46 m and 71 m, vertically referenced to Normaal Amsterdams Peil (NAP), and is shown in Fig. 4.11. The equiangular beam spacing with the normal detector mode was used. Filters and gains available in EM2040C were turned off. For a detailed description of the filters available and Kongsberg recommendations, one can refer to [145] and [146].
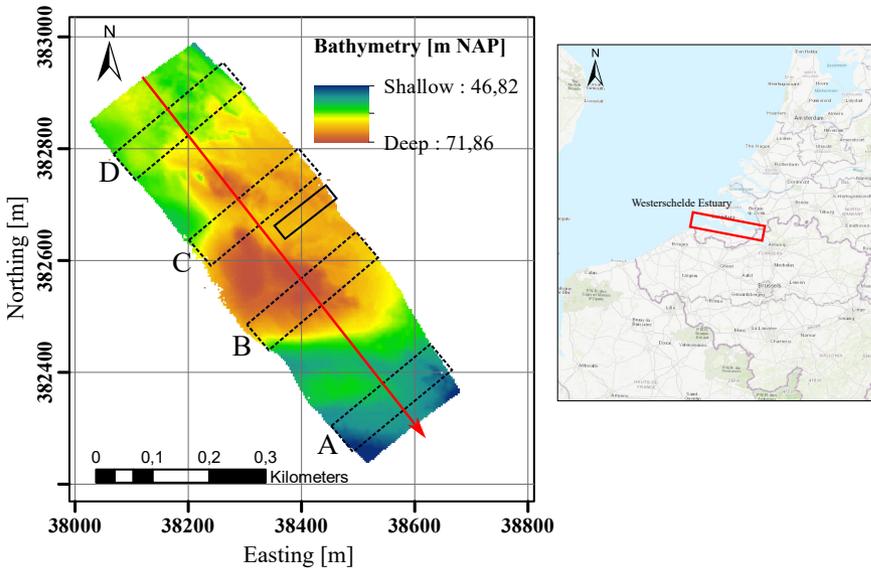
Figure 4.11: Bathymetry map (vertically referenced to NAP) and the location of the survey area in the Westerschelde Estuary, the Netherlands. The black dashed and solid rectangles indicate the areas used for later plots. The red arrow shows the sailing direction.

From Sections 4.2 and 4.4 we do expect equal depth uncertainties for both CW and FM induced by the Doppler effect due to the beamsteering. However, when the FM pulse is used an additional uncertainty due to the imperfectness of the Doppler-range correction occurs. With regards to the uncertainties induced by the baseline decorrelation and signal duration (see Fig. 4.7a and Fig. 4.7b), it is concluded that for the CW pulse used during the survey, the uncertainties due to the above-mentioned sources are smaller than those of the FM with either of the tapering values (as the exact tapering value is not known) and bandwidths. Regarding the uncertainties induced by the baseline decorrelation, additive noise and signal

duration, Fig. 4.7c, for the CW pulse used during the survey the uncertainties due to this source can get larger than those of FM for the outer beams. In addition to the uncertainty sources discussed, one might suspect that the loss of dual swath capability due to the duty-cycle limitations is another contributor to the deterioration of the quality of the bathymetric measurements [147]. However, the pulse length was not so long such that the duty-cycle of the transmitter is exceeded, and hence this issue is not of relevance.

Shown in Fig. 4.12 is the standard deviation of the depth measurements for four different areas indicated by the black rectangles in Fig. 4.11 as **A** (a and b), **B** (c and d), **C** (e and f), and **D** (g and h). These results are derived based on a grid with a cell size of $0.5\,\mathrm{m}\times 0.5\,\mathrm{m}$. For each cell each the standard deviation is obtained from the depth measurements located in a cell. Darker color corresponds to larger depth standard deviation. While Fig. 4.12a, c, e, and g represent the situation for the FM pulse, Fig. 4.12b, d, f, and h, illustrate the surfaces derived from the measurements using the CW pulse. These figures are composed of separate sets of measurements, i.e., one track used one pulse type only and the sailing direction was the same for both pulse types. It is seen that the measurements in the FM mode are in general noisier than their CW counterparts. It is also seen from all frames of Fig. 4.12 that the standard deviation in each cell strongly correlates with the seabed morphology, see the larger standard deviation for non-flat bottoms.
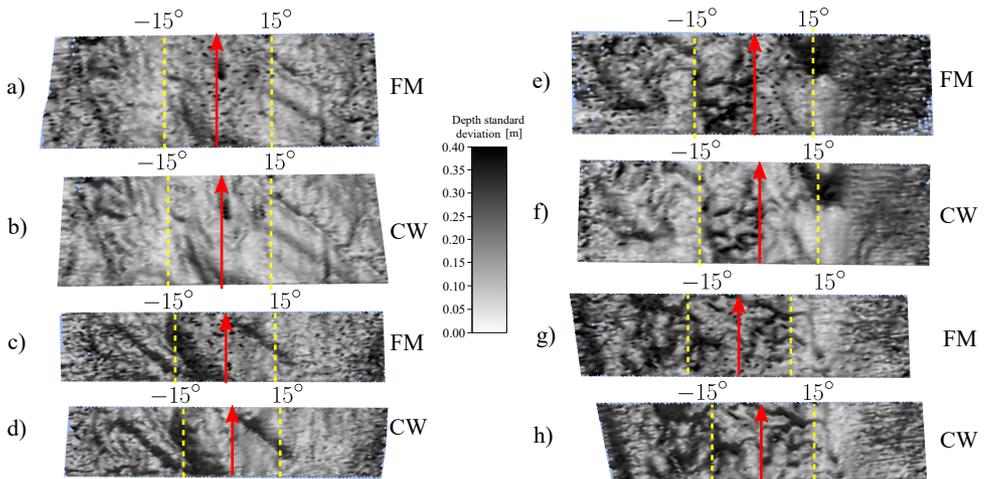
Figure 4.12: Standard deviation of the depth measurement for the areas shown with the dashed rectangles in Fig. 4.11 in case of using FM and CW pulses, area (a) **A** with FM, (b) **A** with CW, (c) **B** with FM, (d) **B** with CW, (e) **C** with FM, (f) **C** with CW, (g) **D** with FM, (h) **D** with CW. This figure is produced using Qimera processing software (developed by Quality Positioning Services (QPS) BV). The red arrows show the sailing direction. The dashed yellow lines show $\pm15°$ beam angles.

It has been mentioned earlier that here the predictions were derived (based on the model of references [26, 27]) assuming a flat seafloor. Thus, to have a fair comparison between the predicted (from the model) and real (from the depth

measurements) bathymetric uncertainties, flat parts of the survey area were cho-
sen. Within the survey area, the region satisfying this condition to some extent
was the starboard of the black rectangle indicated as **B** in Fig. 4.11 corresponding
to Fig. 4.12c and Fig. 4.12d. As the port side exhibits significantly larger standard
deviation compared to the starboard due to the presence of the morphological fea-
tures, it was excluded from the comparison. Still, for the starboard, the bottom was
not completely flat. Another area considered for the comparison of the predicted
and measured uncertainties was the solid rectangle indicated by **E** in Fig. 4.11 (cor-
responding to the port sides) which was relatively flat. Areas **B** and **E** contained
110 and 50 pings, respectively, which was assumed sufficient to provide a reliable
estimate of the standard deviation.

As a first step, the variation of the measured speeds at transmission was con-
sidered. The speeds in easting, northing, and down direction were stored in the
Network Attitude datagram and they were projected on the beam direction using
the motion and position sensor outputs. Shown in Fig. 4.13 is the variation of the
speeds over the survey area for different beam angles. Also indicated, for illus-
tration purposes, is the speed used for the model predictions in the Sections 4.3
and 4.4. The difference for the FM and CW pulses is due to slightly different sea
state conditions and ship attitudes over the two tracks. As for the uncertainties of
the speed estimates, the maximum allowable uncertainties indicated by Kongsberg
for is 0.03 m/s in all directions, i.e., easting, northing, and downward (K. Jensen,
Kongsberg personal communication, June 2018). However, this is seen to be lower
than the uncertainties from Fig. 4.3a. Still Fig. 4.3a was derived using the uncer-
tainties of the equipment used for the survey in August 2017 for both pulse types
and thus are considered to represent the real uncertainties.
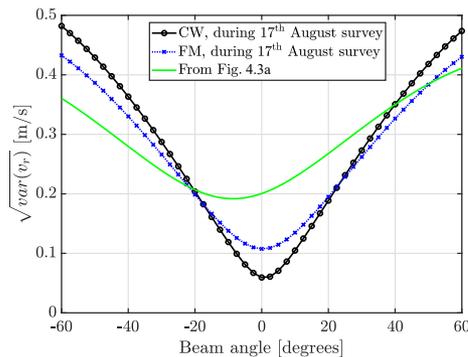
Figure 4.13: Square root of the speeds variations.

To calculate the Doppler effect on beamsteering (existing for both CW and FM
pulses) and matched filtering (only for FM pulses), a bin size of 2° was consid-
ered and the average beam angle and depth of the soundings per bin, along with
the measured variation and uncertainties of the speeds were used in Eqs. (4.10)
and (4.11). Shown in Fig. 4.14a and Fig. 4.14b are the predicted depth uncertain-
ties induced due to the use of CW and FM pulses for the starboard of the area

indicated by **B** in Fig. 4.11, respectively.
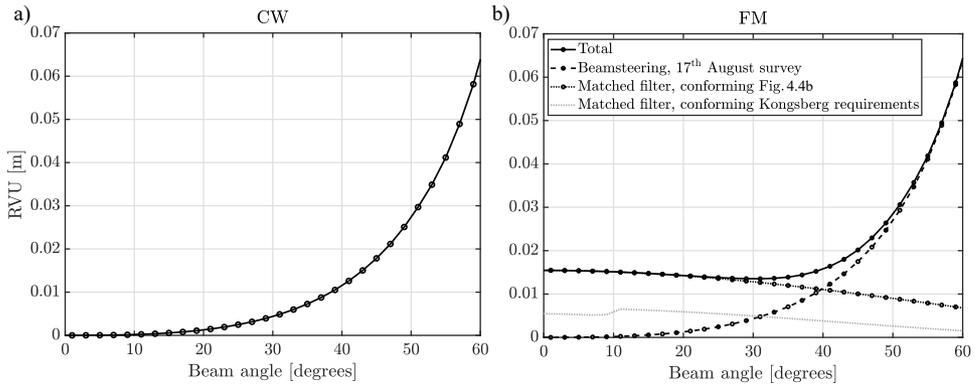
Figure 4.14: a) RVU due to the Doppler effect for the CW pulse and b) RVU due to the Doppler effect for the FM pulse (with circles) and RVU due to Dopplerized matched filter for the FM pulse according to the Kongsberg requirements (dotted light) for the starboard of the area **B** in Fig. 4.11.

Comparing Fig. 4.14a with Fig. 4.4a, slightly higher uncertainties are found as expected from Fig. 4.13. Shown with the light dashed gray in Fig. 4.14b are the uncertainties due to the matched filtering in case of using the Kongsberg specifications, indicating that in practice uncertainties due to the Doppler in matched filtering are twice as high. A similar situation also holds for the area **E** in Fig. 4.11.

The other source of uncertainty affecting the quality of MBES bathymetric measurements differently when using CW and FM pulses, is the baseline decorrelation, see the developed model and its quantification for the operational environment in Sections 4.3 and 4.4, respectively. It should be noted that, as discussed, except for the uncertainties due to the baseline decorrelation, the second-order Doppler effect (imperfectness of Doppler correction), and signal duration, the contribution of the other uncertainty sources to the depth measurements uncertainties are equal for both pulse shapes. Therefore, to eliminate the effect of these contributors, for the remainder of this chapter, the difference between the CW and FM pulses are considered, i.e., the effect of switching from CW to FM. Ideally, for this analysis, the data in both modes have to be acquired simultaneously. If the time interval between the data acquisition in FM and CW modes amounts to several days, the difference between the depth measurements acquired in both modes is not solely affected to the pulse type as the bottom features can vary due to sediment transport. However, for the data set analyzed here, the time interval between measuring the two track lines with varying pulse type was around 45 min. The features such as ripples and sand waves are thus not expected to vary within this period, i.e., sediment transport does not occur to a significant extent. Still, a small effect might be observed due to this phenomenon.

To assess the performance of the model developed for quantifying the effect of baseline decorrelation, use was made of the quality factor stored in the datagrams during the data acquisition. The quality factor, stored in the raw range and angle

datagram (datagram 78), is defined in reference [124] as the standard deviation of the range divided by the detected range. The parameters affecting this standard deviation are thus the signal noise at the detection instant and the uncertainty in the estimate of the zero-crossing from the linear fit to the phase difference measurements, see Section 2.6.3. Fig. 4.15a and Fig. 4.15b illustrate with circles the measured difference between the standard deviation of the detected range projected on the depth axis for the FM and CW pulses derived from the quality factor for the phase detection for areas **E** and **B** in Fig. 4.11. Shown with the solid curve is the modeled difference between the standard deviation of the detected range induced by the baseline decorrelation for FM and CW pulses, see Eq. (4.17) and Fig. 4.7a. For beam angles larger than $\pm 15°$, the behavior of the modeled differences follows those measured. For beam angles close to the nadir, the interferometry, ill-adapted to too short time signals is replaced by the amplitude detection, which is the detection of the echo arrival time based on the analysis of signal envelope [29] (Section 2.6.3). The effect of different pulse shapes on the amplitude detection was not addressed here.
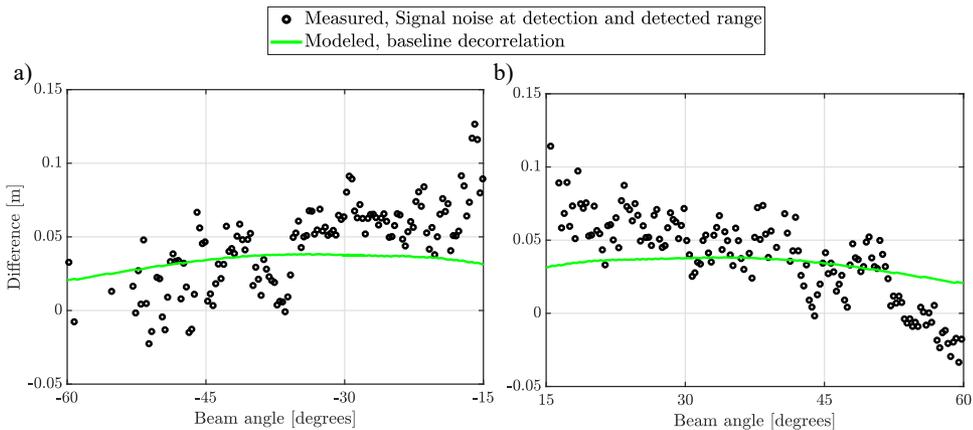
Figure 4.15: Modeled (solid curve) and measured (circles) difference between the uncertainty of the detected range projected on the depth axis using FM and CW pulses for a) area **E** and b) area **B** in Fig. 4.11.

As a final step, the comparison between the modeled and measured differences between the standard deviation of the final depth measurements using FM and CW pulses was carried out. Again, a bin size of 2° was considered and the variations of the depth measurements for different bins were obtained. Fig. 4.16a and Fig. 4.16b visualize with solid black with circles the difference between the standard deviation of the depth measurements using FM and CW, where the positive values indicate a higher standard deviation for the FM than that of CW, for areas **E** and **B**, respectively. Shown with the dashed with crosses is the predicted difference accounting for all aspects addressed in Sections 4.3 and 4.4. For illustration purposes, the curves without accounting for signal duration and/or additive noise are also shown.

This indicates that including the contribution of the signal duration affects the

beams close to the nadir the most. The comparison between the full model and measured curves indicates a relatively good agreement for the areas considered (**E** and **B** in Fig. 4.11). This indicates that accounting for the depth uncertainties due to the uncertainties in the Doppler range correction and the combined effect of the baseline decorrelation and the signal duration can capture the observed difference in the vertical uncertainty when switching from CW to FM for a flat seafloor to a certain extent. The discrepancies between the model and the measured differences are associated to the bottom morphology. It can also be seen that the effect of additive noise on the differences is almost negligible considering the specifications of the pulse used during the survey.
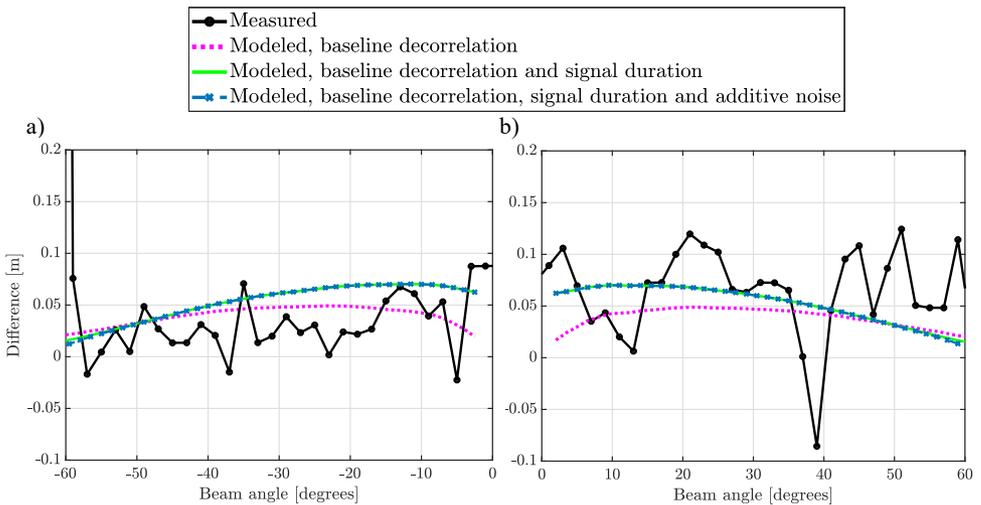
Figure 4.16: Difference between the standard deviation of depth measurements using FM and CW pulses as measured (solid curve with circle markers) and modeled using baseline decorrelation (dotted) plus the signal duration (solid curve) plus the additive noise (dashed curve with cross markers), i.e., $\sigma_{\mathrm{FM}} - \sigma_{\mathrm{CW}}$, for a) area **E** and b) area **B** in Fig. 4.11.

4.6. Conclusions

New generations of MBESs are able to transmit both FM and CW pulse shapes, whereas in the past the only pulse used was CW. FM pulses allow for measurements at larger ranges resulting in an increase in the attainable swath. However, in contrast to the expectations, in some cases the quality of the bathymetry measurements was reported to deteriorate when switching from CW to FM. Two origins have been identified for the increase in the depth variations when using FM: the Doppler frequency shift due to the motion of the MBES sensor and baseline decorrelation. In this chapter, the depth uncertainties induced by both effects were quantified for the EM2040C dual head in a shallow water environment (water depth of approximately 60 m) and rough and calm sea states. The contribution of the Doppler effect was compared to the depth uncertainty induced by the uncertainties in the

range measurements (due to the baseline decorrelation and signal duration and additive noise), roll and steering angle, pitch angle, along track opening angle, and sound speed profile, which are the contributors relevant to the depths relative to the MBES. Measurements acquired in FM and CW modes using EM2040C dual head were analyzed to validate the uncertainty prediction model. Based on the results of the modeling and real measurements, the following conclusions can be drawn:

- The bathymetric uncertainty induced by the Doppler effect in the beamsteering process is equal for both pulse types and as is not corrected for by the manufacturer, its contribution is a first-order effect. For the rough sea state, the vertical uncertainty induced by this source can be up to 82% of the TRVU (for the calm condition the contribution is 80% of the rough sea state). To take its contribution into account in the bathymetry uncertainty model, an additional term in the expression describing the random depth uncertainty due to the uncertainty in the roll and steering angle is needed;

- The bathymetric uncertainty resulting from the imperfectness of the correction applied to counteract the Doppler frequency shift occurs only for the FM pulse shape and thus its associated uncertainty is a second-order effect. Its contribution to the TRVU is much smaller than the contribution of the Doppler effect on the steering. In order to consider its contribution, the term defining the random depth uncertainty due to the uncertainty in the measured distance has to be modified;

- Taking these contributions into account in the uncertainty prediction model allows one to have a more realistic description of the bathymetry uncertainty. These terms do, however, require knowledge of the transducer motion and are sea state dependent;

- The baseline decorrelation induces an uncertainty in the estimation of the phase difference leading to an uncertainty in the derived depth. For the FM and CW pulse specifications considered in this chapter, the depth uncertainty for the former is larger than that of the latter (except for the FM pulse with an effective bandwidth and tapering values of 3.615 kHz and 50%, respectively). However, this does not mean that the depth uncertainty is higher for FM than that of CW irrespective of the pulse shape. For the CW pulse, the bathymetric uncertainty due to the baseline decorrelation decreases with shortening pulse length. Widening the bandwidth and increasing the tapering coefficient of FM pulse (reduction of the sidelobes) also lead to a decrease in the depth uncertainty induced by this uncertainty source;

- Although using a shorter CW pulse improves the coherence between the two received signals leading to a decrease in the uncertainty induced by the baseline decorrelation, it also reduces the received acoustic energy. Hence, the SNR deteriorates. From the simulation of SNR for a flat muddy sand bottom it was found that for the CW pulse with the shortest duration, the worsening of the SNR dominates the depth uncertainty for the outer beam sector (larger

than $\pm 55°$) and the final bathymetric uncertainty for this pulse type can be larger than those of FM for these beams. The exact behavior depends on the sediment type and source level;

- Finally, measurements indicate that indeed the use of FM pulses can result in a noisier bathymetry. To assess the agreement between the measured and modeled uncertainty, two relatively flat areas consisting of a number of pings were chosen. Good agreement was found between the measured and predicted effect of switching from CW to FM pulses.

4

5

Assessing the performance of the multibeam echosounder bathymetric modeling

A lack of information cannot be remedied by any mathematical trickery.

Cornelius Lanczos

Prediction is very difficult, especially about the future.

Niels Bohr

This chapter seeks to assess the performance of the MultiBeam EchoSounder (MBES) bathymetric uncertainty modeling (see Section 2.7) by comparing the modeled and measured uncertainties. Realistic prediction of the contribution of different uncertainty sources affecting the depth measurements is of importance for a realistic expectation of the measurements capabilities. Although models have been developed, there is a need to assess their performance for a given operational environment using the state-of-the-art MBES.

The chapter begins by presenting a method for obtaining depth uncertainties from the measurements such that a fair comparison with the modeled uncertainties can be made. Following this, the modeled and measured uncertainties are compared for varying water depth and pulse length. Possible reasons for discrepancies observed are given and the improvements achieved in the model-data agreement by accounting for them are discussed.

5.1. Introduction

Reliable representation of the sea- and river-floor bathymetry is of high importance for a large number of applications, such as maintaining safe navigation, marine geology, off-shore construction and habitat mapping [2, 151, 152]. Acoustic remote sensing with MultiBeam EchoSounder (MBES) systems has been extensively used for delivering such information due to the systems' capability to map large areas in a relatively short period of time. The system transmits an acoustic pulse (ping) in a wide swath perpendicular to the sailing direction [29]. Beamforming at reception enables determining the Two-Way Travel Time (TWTT) of the received signal for a set of predefined beam angles. The depth measurements are derived from the TWTT per beam and the sound speed in the water [95]. However, similar to any type of measured parameter, the derived depths are affected by different sources of uncertainty, such as those in the sound speed, motion and atitude sensors.

Obtaining a realistic *a priori* estimate of the depth uncertainties is of importance for a number of applications, such as the production of bathymetric maps. In the literature, a number of approaches to obtain these estimates, and to subsequently use them are described. References [26, 27] developed an *a priori* vertical uncertainty prediction model to quantify the contribution of the various sources. The developed model has been widely used for predicting the uncertainties prior to a survey, as implemented in *A priori* Multibeam Uncertainty Simulation Tool (AMUST) used throughout this chapter. The uncertainty model of [26, 27] has been also employed for producing bathymetry maps, for example in the Combined Uncertainty and Bathymetry Estimator (CUBE) algorithm developed by Calder and Mayer [28, 55, 56]. They used *a priori* standard deviations of the soundings derived from the uncertainty prediction model of [26, 27] as an input to construct a grid over a survey area and to assign an estimate of depth and its uncertainty to each grid node. A reliable and accurate bathymetry map with its associated uncertainty is essential for applications such as bridge risk management and coastal inundation modeling [153, 154]. Moreover, a realistic uncertainty description is also a key for survey planning to assess whether the required survey standards can be met in a specific measurement campaign.

In addition to the early uncertainty prediction model of [26, 27], effort has been put forward to address the contribution of other uncertainty sources of relevance to the MBES bathymetric measurements not accounted for in the developed model. Since the establishment of the model of [26, 27], impressive developments have been realized in MBES systems, such as enabling the use of Frequency Modulated (FM) pulse shapes, using sophisticated bottom detection methods or filters [145, 146]. In reference [54, 149], the vertical uncertainties induced by the use of FM pulse shapes were quantified and their relevance for MBES bathymetric uncertainty predictions was assessed. Reference [29] proposed a unified definition of a quality factor for sonar bathymetry measurements. This is an *a posteriori* estimator of the local relative depth uncertainty derived from signal features available from the standard MBES signal processing (phase or amplitude detection). The proposed

quality factor is only a part of the total quality of the sounding linked to the signal processing, and other uncertainty contributors have not been taken into account. A Monte-Carlo simulation [155] or an empirical approach [156] can be used to quantify the uncertainties of the gridded bathymetric map derived from compiling bathymetric data with heterogeneous cover and varying ranges of uncertainties. Reference [157] investigated the impact of varying parameters, such as the vessel speed, swath width, track configuration and density of the measurements, on the final grid using a virtual survey simulator.

Apart from the direct application of the depth measurements for map production, [158], derivatives of the bathymetric measurements, such as slope and bathymetry position index can be used for sediment classification purposes [159, 160]. References [23, 52] have combined the so-called depth residuals (related to the depths' standard deviation) with backscatter strength measurements to increase the discrimination performance of the sediment classification methods and, in addition, to solve the ambiguity in the relationship between backscatter value and median grain size [24]. Recently, reference [69] has investigated the effect of frequency dependent signal penetration on multi-frequency MBES bathymetry and backscatter. The authors have used the bathymetry uncertainty to assess the statistical significance of the changes in the measured depth differences (between the various frequencies) with incident angle. Lacking information with regard to the uncertainties inherent to the MBES can lead to misinterpretation. As an example, it can lead to mistakenly classifying the uncertainties and assigning different sediment types to measurements having actually the same sediment composition, but different uncertainties.

Despite an impressive amount of research carried out toward theoretical and empirical modeling of the MBES bathymetric uncertainties, there has been little effort to validate the often used bathymetry uncertainty prediction model of [26, 27] in varying conditions (either environmental or MBES settings). Comparison between the measured and modeled uncertainties provides one with insight into how realistic the modeling is and can also give directions for future improvements of the bathymetric uncertainty prediction model. This can be also beneficial for the approaches relying on the modeled uncertainty to give an estimate of the soundings' uncertainty in a grid, such as the CUBE method [28, 56, 158]. These issues have motivated us to assess the agreement between the modeled (from [26, 27]) and measured vertical uncertainties for one of the current state-of-the-art MBES systems.

To this end, a dedicated survey was carried out by the Ministry of Infrastructure and Water Management of the Netherlands (Rijkswaterstaat), RWS. The survey areas considered were selected such to differ in water depth, while the water depth was close to constant within each area. This allows for experimentally investigating the effect of water depth on the uncertainties and to compare the measured trends with those predicted. The second parameter that was changed during the survey was the pulse length, as this parameter is known to have an important influence on the uncertainties.

This chapter is organized as the following. In Section 5.2, a method for obtaining the depth uncertainties from the measurements such that a fair comparison with the modeled uncertainties can be made is presented. The description of the data

sets is given in Section 5.3. We present the results in Section 5.4 and discuss the relevant issues. Concluding remarks of this chapter are given in Section 5.5.

5.2. Modeling and measuring bathymetric uncertainties

5.2.1. Modeling approach

As mentioned, the predictions of the depth uncertainty induced by varying sources are derived from the model presented in [26, 27]. This model is developed under the assumption of independent contributors (total uncertainty is the square root of sum of the squares of the individual uncertainty sources) and a flat bottom. The bathymetric uncertainty sources can be categorized as [150]

1. Echosounder contribution, $\sigma_{d_{ES}}$, due to the non-zero beam opening angle in the along-track direction, uncertainties in the measurements of the range (between the transducer and a point on the seafloor) and the angle of impact of the incoming sound at the transducer. The latter depends on the method used within the MBES processing chain for bottom detection, i.e., using the amplitude and phase of the received signal. The former is obtained either from the maximum amplitude of the received signal or the center of gravity of the signal envelope after beamforming [78]. As for the phase detection, the full MBES receiving array is divided into two sub-arrays [29]. First, the received signals on both sub-arrays are beamformed focusing the two sub-arrays in a desired direction. The time at which the two signals are in phase (zero phase difference between the two beams formed in a chosen direction) is then taken as the arrival time [29];

2. Angular motion sensor contribution, $\sigma_{d_{AngMot}}$, due to the uncertainties in roll and pitch measurements and imperfectness of their corrections;

3. Motion sensor and echosounder alignment contribution, $\sigma_{d_{Align}}$, due to the discrepancies between roll and pitch angle measurements at the motion sensor and the transducer;

4. Sound speed contribution, $\sigma_{d_{SS}}$, due to the sound speed uncertainties at the transducer array and those in the water column;

5. Heave contribution, σ_H, due to the uncertainties in the heave measurements and those induced due to the vertical motion of the transducer with respect to the vertical reference unit caused by the angular motions of the vessel. In case of using Global Navigation Satellite System (GNSS) for vertical positioning, the uncertainty of the heave measurements is replaced by the uncertainty of the vertical component of the GNSS.

Assuming the above uncertainty sources are uncorrelated, the total depth uncertainty relative to the MBES is expressed as

$$\sigma_d = \sqrt{\sigma_{d_{\text{ES}}}^2 + \sigma_{d_{\text{AngMot}}}^2 + \sigma_{d_{\text{Align}}}^2 + \sigma_{d_{\text{SS}}}^2 + \sigma_H^2} \,. \tag{5.1}$$

The equations for quantifying the contributions of the uncertainty sources are not presented here and an interested reader can refer to Section 2.7 where the relevant equations are given and references [26, 27] for derivation of these equations and detailed discussion.

5.2.2. Determining the measured bathymetric uncertainties

As mentioned, the uncertainty prediction model is based on the assumption of a flat seafloor. Therefore, when comparing the modeled predictions with measurements, areas have to be selected with minimum variation in the water depth. Still, small changes in water depth might be present. To mitigate the contribution of these small variations to the measured uncertainties such that they are comparable to the modeled uncertainties, the approach described in the following is taken.

Measurements in a discrete surface patch on the bottom $d_i = f(X_{V_i}, Y_{V_i})$, $i = 1, 2, ..., N_{\text{hits}}$ (with N_{hits} the number of soundings in a surface patch) are considered. The surface patch includes a few angles around the central beam angle and a few consecutive pings. X_{V_i}, Y_{V_i} and d_i indicate the across-track and along-tack coordinates in the vessel frame along with the depth of the ith sounding located in the surface patch, respectively. The surface patch is modeled assuming either a plane (with three unknowns) or bi-quadratic polynomial (with six unknowns). Thus, we have [92]

$$d = f(X_V, Y_V) = a_0 + a_{X_V} X_V + a_{Y_V} Y_V + (a'_{X_V} X_V^2 + a'_{Y_V} Y_V^2 + a'_{X_V Y_V} X_V Y_V) \,, \tag{5.2}$$

where the term in the parentheses is used when considering a bi-quadratic polynomial and discarded otherwise. The unknown parameters can be derived from the least-squares method [142]. The least-squares estimate of the unknown parameters $x = \left[a_0, a_{X_V}, a_{Y_V}, (a'_{X_V}, a'_{Y_V}, a'_{X_V Y_V})\right]^T$ for a linear model of observation equations, $E\{y\} = Ax$ with E and A the expectation operator and the design matrix, respectively, and y the vector containing the observations $y = [d_1, d_2, ..., d_{N_{\text{hits}}}]^T$, is

$$\hat{x} = (A^T Q_y^{-1} A)^{-1} A^T Q_y^{-1} y \,, \tag{5.3}$$

where A is of the size $N_{\text{hits}} \times 3(6)$ with its ith row being $A_i = \left[1, X_{V_i}, Y_{V_i}, (X_{V_i}^2, Y_{V_i}^2, X_{V_i} Y_{V_i})\right]$. $Q_y = \sigma_y^2 I$ is the covariance matrix of y, with σ_y^2 the variance of the data and I an identity matrix. For this special structure of covariance matrix (independent and identically distributed errors), Eq. (5.3) is simplified to $\hat{x} = (A^T A)^{-1} A^T y$. The least-

squares estimate of the variance component is

$$\hat{\sigma}_y^2 = \frac{\hat{e}^T \hat{e}}{N_{\text{hits}} - 3(6)} \, ,$$ (5.4)

with $\hat{e} = \mathbf{A}\hat{x} - y$ the N_{hits}-vector of the least-squares residuals [142]. The square root of the variance component gives the estimate of the standard deviation of the depth measurements in which the potential remaining presence of the slopes has been accounted for.

5.3. Description of the data sets

For validating the depth uncertainty model, a survey was carried out by RWS in the Oosterschelde estuary (Eastern Scheldt), the Netherlands. This estuary is located in the province of Zeeland, between Schouwen-Duiveland and Tholen on the north and Noord-Beveland and Zuid-Beveland on the south. The EM2040C dual head, [141] from Kongsberg was used with the dual swath acquisition and the equiangular beamspacing mode [77], see Table 5.1.

A brief discussion on the systems used for data acquisition and bathymetry processing is in order. A critical element for accurate estimation of the depth below the transducer is the Sound Speed Profile (SSP) in the water column which varies both spatially and temporally. Therefore, sufficient and accurate measurements of SSPs are required. To ensure the former, the surveyor was asked to acquire a new SSP in case of a difference of more than 2 m/s between the surface sound speed value and the sound speed from the latest full SSP [108]. The sound velocity profiler was manufactured by AML oceanographic and the uncertainty of its measurements as indicated by the manufacturer is 0.02 m/s [161]. However, from measurements in different locations (inland waterways and the North Sea), the uncertainty was found to be 0.2 m/s, and hence this value was chosen as a more realistic description of the system's uncertainty and is used to quantify the resulting depth uncertainty. The sound speed profiles acquired for both data sets were almost constant in the water column equaling 1515 m/s. This value was thus used in the uncertainty prediction model for the sound speed in the water column and at the receiving array.

The data sets were acquired using the Quality Integrated Navigation System (QINSy) (developed by Quality Positioning Services, QPS BV) and GNSS sensors received the correction signal from Real-time Kinematic (RTK) services, Netherlands Positioning Service (NETPOS) in the Netherlands. GNSS RTK provides one with accurate position and ellipsoidal height of the GNSS antenna with an accuracy of a few centimeters in the WGS84 reference frame. The seafloor depth relative to the chart is then derived using the ellipsoidal height, GNSS antenna and transducer offsets from the vessel center of gravity (COG) and chart datum shift, obtained from chart datum models, see as an example [86, 87]. Since NETPOS was used during the data acquisition, the antenna's vertical coordinate is obtained in NAP (Normaal Amsterdam Peil). This means that the uncertainty induced by the chart datum has been already included in the vertical positioning uncertainty, and hence there is no

need to add this as a separate contributor to Eq. (5.1). Using GNSS with NETPOS for calculating the seafloor depth implies that the water surface level is directly of no relevance and accounting for height offsets, such as dynamic draft, height above draft reference and tide, is not necessary for this method (however, knowledge of the water surface level is required for computing the entry location for the sound speed profile, and hence it indirectly affects the estimated depth). This means that to obtain the depth uncertainty relative to the chart datum it is not necessary to add their contribution to Eq. (5.1). Heave measurements (short-term variations in the transducer's depth) are, however, used within the processing software to calculate the height of the vessel's center of gravity between two position updates (because the MBES and Inertial Navigation Sensor (INS) have higher update rate than many GNSS system). Therefore, the accuracy of heave measurement acquired by the INS contributes to the uncertainty in the estimate of the depth. Phins manufactured by iXblue [37] was used as the INS for providing position, true heading, attitude, speed, and heave. The roll and pitch uncertainties of the system are 0.01° (similarly the misalignment uncertainties are assumed to be 0.01°).

Generally speaking, degradation in the quality of the MBES bathymetric measurements is not solely due to the uncertainties inherent to the MBES. Also systematic error sources, categorized as static and dynamic, exist (see [120] for a detailed discussion and [158] for a brief explanation). These errors lead to depth errors through systematic rise and fall of all the beams, see [120] and [40]. Correcting the measurements for the systematic errors is carried out using patch tests, correlation analysis between the motion time series and depth derivatives or assessing the agreement between the depth measurements at the overlapping parts of the adjacent swaths [93, 96]. By using these investigation tools, we concluded that the variations of the depth measurements were not caused by the systematic error sources.

For the data acquisition, a Continuous Wave (CW) pulse type was used with a total pulse length (T) of 27 µs, 54 µs and 134 µs (corresponding to the effective pulse length of $T_{\text{eff}} = 37\%T$, [63]) enabling analysis of the effect of the varying pulse length. Measurements were taken in depths of around 10 m and 30 m, along tracks of nearly 760 m and 640 m length, respectively. Shown in Fig. 5.1 are the bathymetry maps vertically referenced to Normaal Amsterdams Peil (NAP), derived from Qimera (manufactured by QPS BV), for the water depths of 10 m, (c), and 30 m, (d). These are based on the measurements with a pulse length of 54 µs. The bathymetry maps using other pulse lengths were also derived, but show no differences, and hence are not shown here. The location of both data sets was chosen such that they represent a flat seafloor to comply with the assumptions behind the model. However, as seen from the bathymetry maps of the survey areas and their zoomed in versions (Fig. 5.1), small-scale variations of the bathymetry still exist indicating that the assumption of the flat seafloor is not fully valid and the approach presented in Section 5.2.2 is thus used to eliminate the corresponding contribution from the measurements. It should be noted that approach presented in Section 5.2.2 account for the effect of potential along- and across-track slopes within a surface patch, however, the bottom morphology might change from one

patch to another. Therefore, it is decided to consider a small area consisting of a number of patches, i.e., not the full survey area, to minimize the variations of the bottom morphology when calculating the measured bathymetric uncertainties, see the black rectangles in Fig. 5.1e and Fig. 5.1f. In this chapter it is assumed that the effect of potentially remaining small-scale bathymetry variations can be neglected in the modeling.

Table 5.1: Characteristics of EM2040C [141] in the dual head configuration.

Parameter	Value
Center frequency [kHz]	300
Theoretical array length [m]	0.407
Number of beams (dual swath) [#]	800
Beamspacing mode	equiangular
Maximum swath width [°]	130
Mounting angle of transducer [°]	39.89 for Starboard, 40.57 for Port
Beamsteering reference angle [°]	0
Along-track opening angle [°]	0.9
Across-track opening angle at nadir [°]	0.9
Range resolution [m]	0.02525
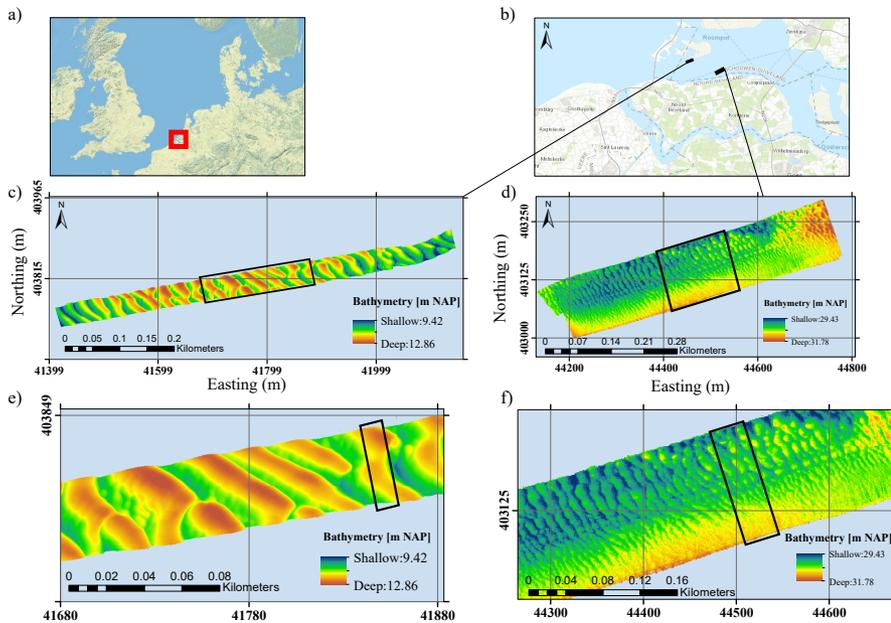
Figure 5.1: Study areas a) North Sea, b) South-West of the Netherlands showing the Oosterschelde estuary (Eastern Scheldt) and the location of the two data sets. Bathymetry maps, vertically referenced to NAP, of the survey area for c) 10 m water depth with the grid cell size of 0.25 m × 0.25 m, d) 30 m water depth with the grid cell size of 1 m × 1 m, e) zoomed in on the black rectangle shown in (c) and f) zoomed in on the black rectangle shown in (d). The bathymetry maps correspond to the measurements with a pulse length of 54 μs and equiangular beamspacing mode. The black rectangles in e) and f) indicate the areas considered for the depth uncertainty calculation.

5.4. Results and discussion

For the calculation of the vertical uncertainties, the size of the surface patch on the bottom is of importance. If a too large surface patch is considered, the variations of the measured uncertainties within a patch cannot be solely associated to the uncertainties inherent to the MBES as the small-scale roughness of order higher than that used for the fit affects the vertical uncertainties. One the other hand, if a too small surface patch is considered, the number of the measurements falling within a patch is small and a robust estimate of the variance component, Eq. (5.4), cannot be obtained. Therefore, an optimal size for the surface patch is required. To this end, five different patch sizes of 2.5°, 2°, 1.5°, 1°, 0.5° in the across-track by 7 pings in the along-track directions were considered. Shown in Fig. 5.2 is the mean value of the vertical uncertainty over the swath (from −65° to 65°) for different patch sizes in a water depth of 10 m (gray) and 30 m (black). It is seen that the largest decrease in the vertical uncertainty occurs by decreasing the size of the patches in the across-track direction from 2.5° to 2° for both water depths. For the deeper water, a further decrease in the patch size to 1° results in a further decrease in the vertical uncertainty. However, it is seen that decreasing the patch size further to 0.5° increases the vertical uncertainty. For a water depth of 10 m, the vertical uncertainties are almost the same for the patch sizes of 2° and 1.5° followed by the increase in the vertical uncertainties for a further decrease in the patch size. The increase in the uncertainties for too small patch sizes indicates that the number of measurements within patches are not enough for the extraction of the required statistics. Based on this result, patch sizes of 1.5° by 7 pings and 1° by 7 pings were chosen for the measurements in a water depth of 10 m and 30 m respectively.
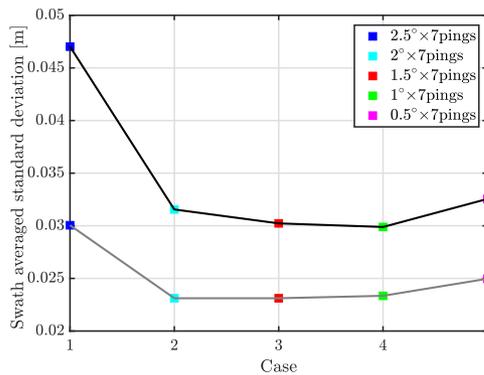
Figure 5.2: Mean value of the vertical uncertainty for different patch sizes in the across-track direction (squares with varying colors) for water depths of 10 m (gray line) and 30 m (black line) and a pulse length of 54 μs.

The calculation of the measured bathymetric uncertainties was carried out by fitting a bi-quadratic or linear function to the measurements within each surface patch. The degree of the fit function (bi-quadratic or linear) was chosen based upon the curvature, which is a measure of the surface patch deviation from a flat plane.

For the data acquired, it was seen that the absolute curvature larger than 0.2°/m corresponds to gradual slopes. Therefore, for a surface patch with curvature smaller than this threshold a linear function was used for the fit, otherwise a bi-quadratic fit was employed.

5.4.1. Trends visible in measured bathymetric uncertainties

Before comparing the modeled and measured uncertainties, the latter as obtained from the measurements with varying pulse lengths is presented in Fig. 5.3 for water depths of a) 10 m and b) 30 m to obtain an insight into the expected effect of different parameters.

1. As the depth increases, generally the vertical uncertainty increases (compare Fig. 5.3a and Fig. 5.3b), except for the longest pulse length;

2. An increase in the pulse length leads to an increase in the standard deviation due to the deterioration of the range resolution and increase in baseline decorrelation with increasing pulse length, see Chapter 3 and [54];

3. In general, lengthening the pulse results in using the amplitude detection, Section 5.2.1 and Section 2.6.3, for a larger range of beam angles around nadir. As an example, compare the transition point of around $\pm15°$ for a water depth of 30 m and a pulse length of 134 μs to that of around $\pm4°$ for the same water depth and a pulse length of 54 μs. The reason for this change in the transition point for varying pulse length is the changing nature of the baseline decorrelation with the pulse length [54]. For beam angles close to nadir and long pulse lengths, the entire main beam is ensonified at any one instant implying that the scattered return is received from a wide range of angular directions corresponding at least to the width of the main beam. Thus , the estimate of the phase difference zero-crossing (in the interferometry step), Section 2.6.3, becomes uncertain. Therefore, the amplitude detection is used for the bottom detection. Another contributing factor to the quality of the zero-crossing estimate is the Signal-to-Noise Ratio (SNR) where longer pulse lengths have a higher values of the SNR due to the increased energy of the transmitted signal. Based on the results presented, it can be seen that the increased SNR for longer pulse lengths does not compensate for the increased uncertainty due to the baseline decorrelation (blue markers are always above the others).

5.4.2. Comparing modeled and measured uncertainties

The modeled bathymetric uncertainties are derived using the characteristics of the MBES and its settings during the data acquisition, see Table 5.1, uncertainties of the sound speed measurements and motion sensors, Section 5.3, and environmental related parameters. It should be highlighted that the uncertainty predictions
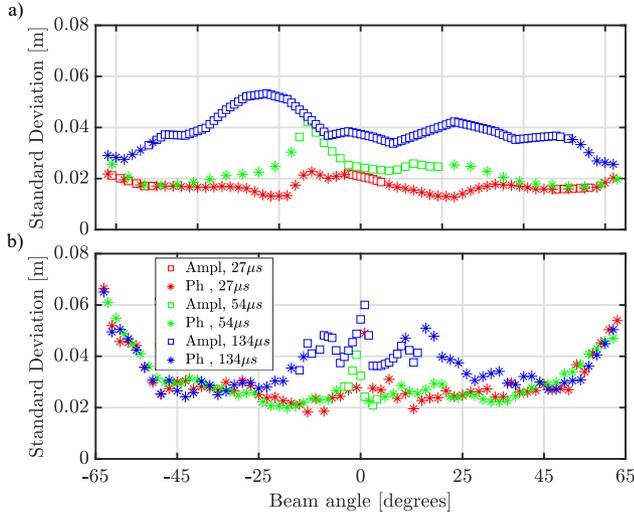
Figure 5.3: Standard deviation of the depth measurements for water depths of a) 10 m and b) 30 m, with a pulse length of 27 µs (red), 54 µs (green) and 134 µs (blue). The transition from the amplitude to phase detection is shown by changing the square marker to asterisk.

presented here are based on these specifications and are not to be viewed as the uncertainty predictions applicable to a different scenario.

Generally, information regarding the majority of the input parameters is reliable. However, in the expression used for predicting the bathymetric uncertainty due to the uncertainty in the phase bottom detection [26, 27], the number of phase samples, n_p, is used. This is given in [83] as

$$n_p = \frac{\frac{d\Omega_R}{\cos^2\Theta}}{\frac{cT}{2\sin\Theta}} \, , \tag{5.5}$$

where Θ indicates the angle between the received beam and nadir (depth-axis) [149]. Ω_R is the across-track beam opening angle (the beam opening angle at reception), which increases with an increasing steering angle for the outer beams, see Table 5.1 for its value at nadir. How well this equation represents the actual number of phase samples is questionable as there is no information with regard to the approach taken by Kongsberg for deriving the number of phase samples per beam. Presented in Fig. 5.4 with gray is the prediction of the bathymetric uncertainty for the situations in which the number of phase samples within the beam footprint was derived using Eq. (5.5). Shown with black and green are the bathymetric uncertainties obtained using the number of phase samples extracted from the data, [124], and those measured respectively. It is seen that in case of using the theoretical number of phase samples, large discrepancies occur. Particularly for the middle sector of the swath with the prediction overestimating the measured uncertainties. Using the number of phase samples obtained in practice for predicting the bathy-

metric uncertainties reduces this discrepancy to a noticeable extent. Therefore, for the comparison between the modeled and measured bathymetric uncertainties, the number of phase samples obtained in practice is used in the prediction model.
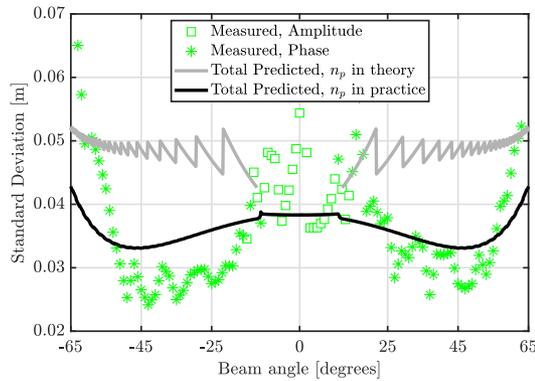
Figure 5.4: Predictions of total bathymetric uncertainty for a water depth of 30 m and a pulse length of 134 μs using the number of phase samples obtained from Eq. (5.5) (gray) and extracted from the data (black). Shown with green markers are the measured vertical uncertainties. The transition from amplitude to phase detection is shown by changing the square marker to asterisk.

Shown in Fig. 5.5 are the modeled and measured bathymetric uncertainties for the area indicated by the black dashed rectangle in Fig. 5.1e for a water depth of 10 m with a pulse length of 27 μs, (a), 54 μs, (b), and 134 μs, (c). It should be noted that for the bottom detection method (amplitude or phase), the approach documented in the data was taken.

Both the measured and predicted depth uncertainties increase with increasing pulse length. In general, the uncertainties derived from the prediction model are in a good agreement with those encountered in reality with larger discrepancies occurring for the beams where the amplitude detection was used. The measured bathymetric uncertainty slightly increases with an increasing beam angle which is captured by the prediction model.

As discussed in Section 5.4.1, lengthening the pulse duration results in using the amplitude detection for a larger range of beams around nadir, and consequently the model underestimates the bathymetric uncertainties for a broader range of beams, compare Fig. 5.5a and Fig. 5.5c. The most dominant source of uncertainty is predicted to be the echosounder contribution, see the solid back line with circle markers. As discussed in Section 5.2.1 this contribution is divided into three terms see [149, 150]:

1. Uncertainties in the range measurements;

2. Uncertainties in the angle of impact of the incoming sound wave with the MBES;

3. non-zero along-track beam opening angle.

There is no difference for the first and third contributions between amplitude and phase detection. However, the expression for the second term differs. In case of using amplitude detection, the uncertainty in the across-track angular measurements is a constant term equaling $\frac{1}{12}\Omega_R$ [26, 27]. Comparing the measured and predicted uncertainties suggests that this term requires modification.
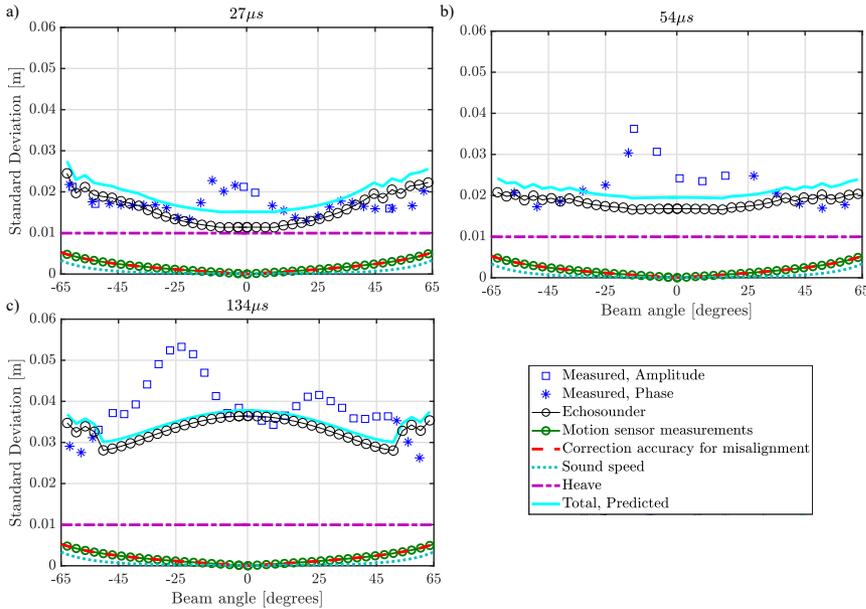
Figure 5.5: Bathymetric uncertainty derived from the measurements (blue markers) and those predicted for a water depth of 10 m and a pulse length of a) 27 μs, b) 54 μs and c) 134 μs. The change from amplitude to phase detection in the data is shown by switching from square markers to asterisks with the same color. The location of this switch was similarly applied in the modeling.

An additional point to clarify is the term referred to as range sampling resolution used in the calculation of the contribution of the range measurements to the bathymetric uncertainty. The range sampling resolution is defined as $\delta r_s = c/f_s$ with f_s the sampling frequency. The reported value for f_s is the output sampling frequency, different from the one used for applying the bandpass filters and beamforming with the latter being higher. Knowledge of this value is required for correct calculation of the contribution of the range measurements to the bathymetric uncertainty. If the sampling frequency used for the bottom detection would be in the order of MHz, the contribution of the range error becomes negligible. Throughout this thesis, lacking detailed information on the sampling frequency of relevance, the maximum output sample rate of EM2040c equaling 60 kHz was used for the predictions, corresponding to a contribution varying from 0.009 m at nadir to 0.0008 m for the most outer beam to the bathymetric uncertainty.

Shown in Fig. 5.6 are the modeled and measured depth uncertainties for the area indicated by dashed line in Fig. 5.1f for a water depth of 30 m and pulse

lengths of 27 µs, (a), 54 µs, (b), and 134 µs, (c). Compared to the shallower water depth, for the two pulse lengths of 27 µs and 54 µs the discrepancy between the modeled and measured uncertainties increases. This can partly indicate that the prediction model cannot fully capture the depth dependency of the bathymetric uncertainties. For the pulse with the longest duration, relatively good agreement is obtained between the predicted and measured uncertainties for the middle sector of the beams. With regards to the variations of the bathymetric uncertainty with beam angle, in contrast to the data acquired in a water depth of 10 m, the measured uncertainties show a pronounced dependency on the beam angle. This behavior is captured to a limited extent by the prediction model.
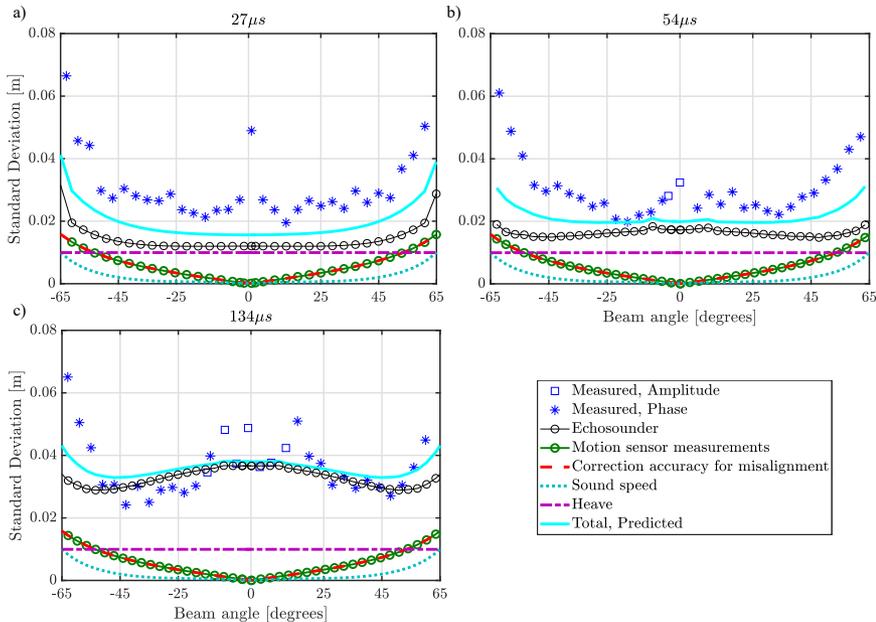
Figure 5.6: Bathymetric uncertainty derived from the measurements (blue) and those predicted for a water depth of 30 m and a pulse length of a) 27 µs, b) 54 µs and c) 134 µs. The change from amplitude to phase detection in the data is shown by switching from square markers to asterisks with the same color. The location of this switch was similarly applied in the modeling.

5.4.3. Improving model-data agreement by accounting for the most recent insights in the contributors to MBES bathymetric uncertainties

In order to improve the agreement between the predicted and measured uncertainties, particularly for deeper waters, the contribution of the following uncertainty sources are of importance:

1. **Doppler effect**: since the MBES is constantly moving, the received signals are affected by a Doppler frequency shift. This frequency shift has an im-

pact on the beamsteering, resulting in uncertainties in the steering angle. An uncertainty in the steering angle gives rise to uncertainties in the estimated depths. As such, an underestimation of the contribution of the Doppler effect potentially leads to an optimistic expectation of the depth uncertainties, see [54]. This contribution increases with water depth and beam angle;

2. **Baseline decorrelation**: as shown by [54], the phenomenon of baseline decorrelation occurs in the MBES interferometry step for phase detection due to slightly different received signals by the two sub-arrays resulting from different angular directions. Thus, the coherence between the two received signals is affected. As the water depth increases this coherence is reduced (due to a larger signal footprint and consequently a more fluctuating directivity pattern) and thus the quality of the phase estimates is negatively affected resulting in an increase in the bathymetric uncertainty.

The current expressions used for the depth uncertainty prediction, [26, 27], do not account for the contribution of the Doppler effect. However, the baseline decorrelation is accounted for in an approximate way, not accounting for the specific pulse characteristics [54]. Here it will be investigated to what extent these two factors modify the model-data agreement for the cases considered.

As discussed in reference [54], accounting for the contribution of the Doppler effect requires knowledge of the speed of the array center at emission and reception of the signal projected on the beam direction and weather condition during the data acquisition. The weather condition during the survey was calm and the vessel and MBES used for the survey were those employed in reference [54]. We thus made use of the values derived by them for the calm weather condition, see Fig. 4.3 in Section 4.3 and [54].

To quantify the effect of baseline decorrelation on MBES bathymetric measurements in the interferometry step, the standard deviation of the phase difference needs to be calculated [137]. Parameters required for this calculation are the actual pulse shape of the transmitted signal (CW pulse shape used here with the center frequency presented in Table 5.1) and the length of each sub-array used in the interferometry step, equaling 0.12 m for the case considered, i.e., one-third of the theoretical array length corrected for the shading.

Shown in Fig. 5.7 and Fig. 5.8 are the measured and predicted depth uncertainties for a water depth of 10 m and 30 m, respectively, with varying pulse lengths where both the Doppler effect (light green circles) and baseline decorrelation are considered. The baseline decorrelation has now been considered within the echosounder contribution (solid black line with circle markers). The depth uncertainty induced by the motion sensor, correction accuracy for misalignment, sound speed, and heave are equal to those of Fig. 5.5 and Fig. 5.6 and thus not shown here.

From Fig. 5.7, it is seen that the contribution of the echosounder decreases with an increasing beam angle (as the coherence between the two received signal increases with an increasing beam angle), in contrast to Fig. 5.5 where an increase in the uncertainty with beam angle was observed. This indicates that accounting
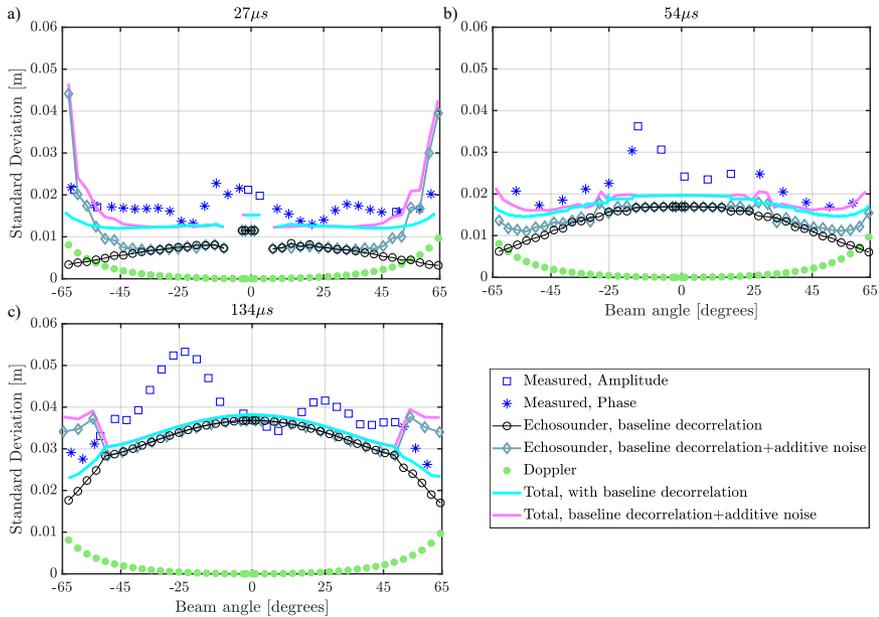
Figure 5.7: Bathymetric uncertainty derived from the measurements (blue markers) and those predicted considering the uncertainty induced by the Doppler effect and baseline decorrelation without (cyan) and with (light pink) additive noise for a water depth of 10 m and a pulse length of a) 27 μs, b) 54 μs and c) 134 μs. The change from amplitude to phase detection in the data is shown by switching from square markers to asterisks with the same color. The location of this switch was similarly applied in the modeling. The depth uncertainties induced by motion sensor measurements, correction accuracy for misalignment, sound speed, and heave are equal to those of Fig. 5.5 and thus are not shown here.

for the baseline decorrelation in the approximate way as carried out in references [26, 27] and shown in Fig. 5.7 overestimates the uncertainties. It is also seen that although the total bathymetric uncertainty (cyan) decreases, the magnitude of the reduction is lower than that of the echosounder contribution which is due to the compensation of the decrease by an increasing contribution of the Doppler effect with beam angle. Considering the fact that the longest pulse length used here was shorter than the shortest CW pulse used in reference [54], the results obtained here are in agreement with those of Fig. 4.10 in Section 4.4 and [54]. Compared to the situation where these contributions were not considered, the variations of the bathymetric uncertainty with beam angle as seen in the measurements are captured better (compare the solid cyan curve corresponding to the total predicted uncertainty in this figure to that of Fig. 5.5).

Also for the 30 m water depth, a decrease in the contribution of the echosounder is observed (see Fig. 5.8). With regard to the total bathymetric uncertainty, in contrast to the shallower depth where a decrease was seen, here no noticeable change is observed except for the pulse length of 54 μs where an increase occurs. The almost equal uncertainties (compare Fig. 5.6 and Fig. 5.8) means that the decrease in the contribution of the echosounder is canceled out by the increase in

the contribution of the Doppler effect. Compared to the measured uncertainties, still an underestimation occurs, however, accounting for the Doppler effect and baseline decorrelation, can improve the performance of the uncertainty prediction model in capturing the increase of the measured uncertainties with beam angle, see Fig. 5.8b.
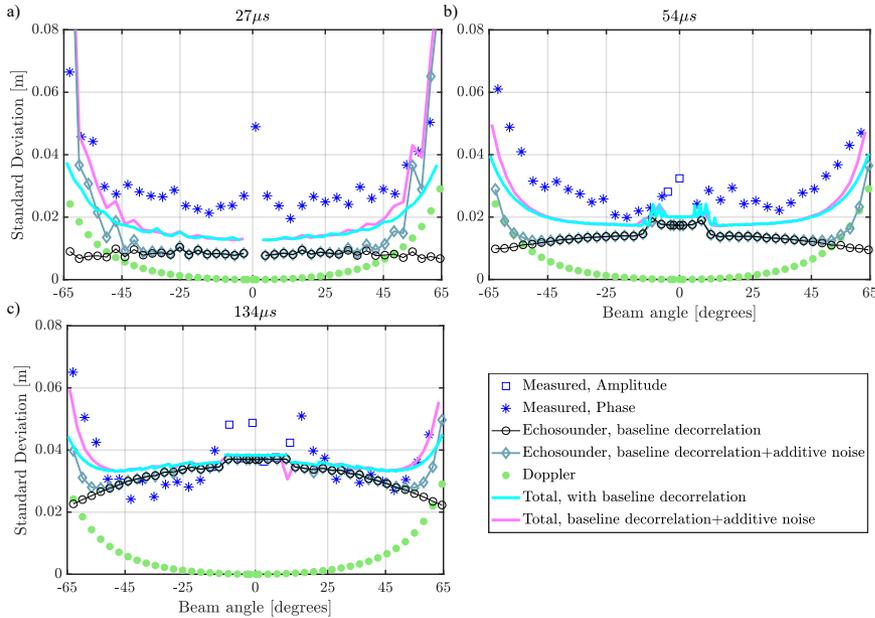
Figure 5.8: Bathymetric uncertainty derived from the measurements (blue markers) and those predicted considering the uncertainty induced by the Doppler effect and baseline decorrelation without (cyan) and with (light pink) additive noise for a water depth of 30 m and a pulse length of a) 27 µs, b) 54 µs and c) 134 µs. The change from amplitude to phase detection in the data is shown by switching from square markers to asterisks with the same color. The location of this switch was similarly applied in the modeling. The depth uncertainties induced by motion sensor measurements, correction accuracy for misalignment, sound speed, and heave are equal to those of Fig. 5.6 and thus are not shown here.

Although accounting for the baseline decorrelation and Doppler effect has improved the performance of the prediction model in capturing the dependency of the depth uncertainties to the beam angle in some cases, still discrepancies between the predicted and measured vertical uncertainties remain. A potential contributor deteriorating the quality of the bathymetric measurements toward the outer parts of the swath is the decreased SNR, due to the additive noise [49, 54]. The uncertainty prediction model assumes an infinite SNR, which is violated in reality. Here, we will investigate to what extent the additive noise contribution modifies the vertical uncertainty predictions for the cases considered. The SNR expresses the relative importance of the contribution of the expected received echo level and the perturbing noise and is given by the sonar equation [71]. The nature of the additive noise makes its prediction complicated as it requires information on the backscatter strength returned to the MBES which is dependent on the composition

of the seabed, angle of incidence, acoustic frequency, seafloor roughness, volume heterogeneity and bulk density [89]. The backscatter strength received is the result of a complex interaction of the transmitted acoustic signal and the often inhomogeneous seafloor [138, 139]. Here, the total backscatter strength is modeled as the result of a contribution from volume backscattering and rough interface backscattering based on the model of reference [66]. *A priori* knowledge of the survey areas indicated a very soft sediment, and thus clayey sand was assumed for modeling the backscatter strength, see Table 2.1 for sediment properties. Indeed, the need for information on the sediment composition makes the prediction of the contribution of the additive noise complicated as such information might not be always available. For the calculation of the SNR, the transmitted source level also needs to be known. Here, this was assumed to be 20 dB lower than the maximum power available at the transmission (K. Jensen, Kongsberg personal communication, June 2018). The transmission loss, noise level or reverberation level inside the receiver band, transmission and reception directivity patterns, sensitivity of the transducer with respect to center frequency, and the receiver gain applied by the receiver electronics are the other parameters required for the calculation of the SNR. The joint impact of the SNR and baseline decorrelation was then derived following reference [49]. Added to Fig. 5.7 and Fig. 5.8 with solid light blue lines with diamond markers, and solid light pink lines are the echosouder contribution accounting for the uncertainties induced by the baseline decorrelation and additive noise and the resulting total depth uncertainty, respectively.

For a water depth of 10 m, compared to the situation where the contribution of additive noise was discarded, no noticeable change is observed for the inner and middle sector of the beams, i.e., this means that the prediction model still (slightly) underestimates the measured uncertainties. However, as expected from the nature of the additive noise, the predicted depth uncertainty for the outer beams increases. This increase improves the ability of the prediction model in capturing the variation of the bathymetric uncertainty with beam angle. Regarding the longest pulse length, a slight over-prediction occurs when accounting for the additive noise contribution.

As for the deeper survey area and the two shorter pulse lengths Fig. 5.8a and Fig. 5.8b, although still an underestimation occurs for the inner and middle beam sector, the increase of the bathymetric uncertainties with increasing beam angle is now well predicted. As for the longest pulse length, a very good agreement between the predicted and measured depth uncertainties is obtained for all the beam angles which was expected as the discrepancy observed between the modeled and measured uncertainties discarding the contribution of the additive noise was mainly concerned with the most outer beams.

5.5. Conclusions

Predicting the uncertainty of MBES bathymetric measurements is an important and almost standard step in the planning of MBES surveys. Models have been developed to fulfil such a purpose enabling one to assess whether the required survey

standards can be met in a specific measurement campaign for a given combination of measurement equipment, MBES and environmental settings. Since the development of these models, the MBES systems have been significantly improved. Moreover, new insights into the uncertainty sources affecting the quality of depth measurements have been obtained, such as the contribution of the baseline decorrelation, Doppler effect and additive noise.

This chapter has focused on assessing the performance of the widely used bathymetric uncertainty prediction model of [26, 27], as implemented in AMUST, by comparing the predicted uncertainties to those measured using different pulse lengths and water depths. To obtain the measured bathymetric uncertainties such that a fair comparison can be made with those modeled, a number of issues have been found of importance as the following:

1. The size of the bottom surface patches, used for the calculation of the measured bathymetric uncertainty accounted for the potential presence of the small-scale depth variations, has to be chosen carefully. If a too large surface patch is used, the bottom morphology might change within a patch to an extent which cannot be captured by the fitting process. Therefore, the derived bathymetric uncertainty does not solely depend on the uncertainties inherent to the MBES. On the other hand, if a too small surface patch is used, the number of soundings within a patch might not be enough to give a robust estimate of the required statistics. The optimal size of the surface patch varies with water depths and was found by comparing the bathymetric uncertainty corresponding to different patch sizes;

2. The number of phase samples within each beam is required for the calculation of the bathymetric uncertainty induced due to the phase bottom detection technique. The comparison between the theoretical number of samples and those obtained in practice revealed large discrepancies, and thus the latter is used for a realistic comparison between the measured and predicted bathymetric uncertainties.

Based on the comparison between the measured and predicted uncertainties, the following conclusions can be drawn:

- In general, the magnitude of the bathymetric uncertainties derived from the prediction model of [26, 27] are in good agreement with those measured. However, discrepancies were observed with increasing water depth and for the outer beams;

- The model tends to underestimate the measured uncertainties for the beams where the amplitude detection was used as the bottom detection method. As the pulse length increases, a larger range of beam angles around nadir uses this bottom detection method, and hence the underestimation occurs for a wider portion of the swath;

- The most dominant contributor to the depth uncertainty has been found to be the echosounder contribution, and hence as a first step toward improving

the model, the contributions of the baseline decorrelation and Doppler effect were added to this contribution. The comparison between the situations with and without accounting for these error sources has indicated a decrease in the contribution of the echosunder in case of the former. The effect on the total bathymetric uncertainty depends also on the magnitude of the Doppler effect (as the reduction in the contribution of the baseline decorrelation with beam angle is counteracted by an increase in the Doppler induced depth uncertainty);

- Accounting for the contributions of the Doppler effect and baseline decorrelation in general improves the performance of the prediction model in capturing the variations of the uncertainty with beam angle. The agreement between the modeled and measured uncertainties for the outer parts of the swath is further improved by accounting for the decreased SNR. This, however, requires knowledge of the pulse shape, speed of the array at reception and transmission of the signal and sediment characteristics which might not be always available;

- Based on the insights obtained by accounting for the contribution of the baseline decorrelation and Doppler effect, one can conclude that the relatively good model-data agreement obtained without accounting for these contributions might have been a coincidence. This occurs as a consequence of accounting for the baseline decorrelation in an approximate manner and discarding the contribution of the Doppler effect; for the situations considered here it was found that the contribution of the baseline decorrelation when accounted for the pulse shape and Doppler effect counteract each other. However, for a different environmental condition, survey configuration or pulse shape, this might not occur. Consequently, not accounting for these contributions in the uncertainty prediction model leads to incorrect predictions;

- Overall, this contribution shows that the current capabilities of modeling the MBES bathymetric uncertainties in a computationally efficient way (error propagation) provides estimates that are in good agreement with those obtained experimentally.

6

Using alternatives to determine the shallowest depth for bathymetric charting: case study

Discovering the unexpected is more important than confirming the known.

George E. P. Box

In the previous chapters the overall objective was to account for either the systematic or random sources of uncertainty affecting the bathymetric measurements. This was accomplished by introducing a method to correct for the systematic error induced by lacking knowledge of the water column sound speed, Chapter 3. Random depth uncertainties induced by different pulse types and sources inherent to the MultiBeam EchoSounder (MBES) were also elucidated, in Chapters 4 and 5. However, this chapter seeks to optimize hydrographic operations in terms of a reliable and accurate representation of the seafloor from a different perspective. Here, the focus is to grid the MBES bathymetric measurements, free of systematic errors, accompanied by their associated uncertainties.

In the first part of this chapter methods for gridding MBES measurements to equidistant grids are proposed as alternatives to the shallowest measured depth which is affected by outliers. The latter reflects the approach often taken when using new MBES measurements to obtain a gridded bathymetry map. The alternative approaches considered use a combination of the mean and standard deviation of soundings, and the regression coefficient from the best fitted plane. Following this, the proposed methods are applied to two data sets and the feasibility along with the implications of using each method are discussed in detail.

This chapter has been published in Journal of Surveying Engineering [158]. Some of its contents have also been presented in International Hydrogaphic Review [162].

6.1. Introduction

Reliable information about the sea- and river-bed bathymetry is of high interest for a large number of applications, such as maintaining safe navigation, building off-shore constructions and making nautical charts. Nowadays, MultiBeam EchoSounders (MBESs) provide high spatial coverage at relatively limited costs, and hence have been extensively used for bathymetric measurements. The amount of data generated by a MBES depends on the ping rate and the number of beams in the across track direction. As an example, for a Kongsberg EM3002 MBES the maximum ping rate is 40 Hz and the number of beams in the single head mode is 254, which results in an incoming data flow of approximately 36.5 million data points per hour [163]. Therefore, reduction of the data is necessary for computationally effective processing.

A number of scholars have studied approaches for producing the bathymetry map from the soundings collected in a survey which will be discussed in the subsequent paragraphs. Within the present chapter, we present and compare a number of methods for producing such maps (without the need for an *a priori* knowledge of the measurements uncertainties) and investigate their feasibility.

Often-used approaches for the data reduction are to use triangulation or equidistant grids [57, 58]. Triangular based gridding is appropriate when having measurements at discrete points. It is flexible with respect to the different levels of detail, i.e., a denser triangle pattern is an indication of more detailed relief information. However, this method has large memory requirements, long processing time and requires sophisticated geometric computations [164]. The advantages of equidistant grids are their simplicity and low memory requirements. The use of equidistant points enables storing only the depth values [165]. Hence, in case an area is homogeneously surveyed by a MBES, equidistant griding is often the preferred method. Within this chapter, considering that areas are homogeneously surveyed by MBES systems, only equidistant grids are considered.

An often-used method for assigning depths to the grid of high density bathymetry data is to use the shallowest (minimum) measured depth within a cell [164]. The advantage of this approach is that the method preserves the shallowest depth, of high importance for safe navigation. The disadvantage, however, is that these shallowest depths can correspond to outliers and consequently, the resulting charted soundings can be (significantly) shallower than the true depth in the area. It is sometimes seen that measurements from the less-reliable outer beams, subjected to the largest uncertainties, are selected as the depths to be charted. They are thus more frequently shoaler than other measurements in the area [28]. In order to mitigate the effect of measurement errors on the charted depths, it is possible to use other statistics derived from the data. A straightforward approach is to use the mean value [164]. However, a problem associated with assigning the mean depth is that hazardous objects might left undetected, and hence safe navigation is prohibited [162]. A more advanced approach for assigning a depth to a set of predefined nodes is to use the Combined Uncertainty and Bathymetry Estimator (CUBE) algorithm developed by references [28, 55]. This approach constructs a

grid over a survey area and assigns to each grid node an estimate of depth and its uncertainty. Use is made of an *a priori* standard deviation for the soundings based on the uncertainty model of [26]. At a node, soundings are integrated to obtain an estimate of the depth and uncertainty using an optimal Kalman filter. Within this chapter, the main focus is on approaches which do not need an *a priori* estimate of the standard deviation of the soundings and use the statistics derived from the measurements. However, a comparison between the approaches presented and CUBE is made to assess their agreement and possible discrepancies. Moreover, the bathymetric uncertainties derived from the measurements are compared to those modeled using references [26, 27], which is also used in CUBE to define *a priori* estimate of the sounding uncertainties. This provides one with insight into how realistic is the modeling and can also give direction for the future improvements.

The survey areas considered in this chapter are located in the Netherlands. The Netherlands is the home of international river basins, such as Scheldt and Ems which run through the country towards the North Sea and the Wadden Sea. These rivers and the estuaries connecting them to sea are used for inland waterway transport within the Netherlands but also between the Netherlands and neighboring countries. A shallowest depth has to be guaranteed to keep the rivers navigable but also to ensure that the ships can carry maximum cargo. Currently for the production of the charts, the Dutch Ministry of Infrastructure and Water Management (RWS) uses the shallowest depth at its measured position from the point cloud of the MBES depth measurements. The resulting unequal spacing between the points results in high memory requirements. In addition, assigning the shallowest depth can result in an artificially shallow grid as discussed above. Within this chapter, the use of alternative techniques for mitigating these two drawbacks is investigated. Whereas the first issue can be easily solved by no longer considering the location of the shallowest depth, but the cell center instead, the second issue requires more careful consideration. This issue, i.e., to assign to each cell a depth value that optimally represents the actual average water depth, is investigated by considering a number of methods for shallowest depth determination and applying them to two different survey areas located in the Westerschelde estuary connecting the Scheldt River to the North Sea, i.e., an important shipping route to the port of Antwerp, Belgium. The resulting grids are compared to their shallowest and mean counterparts. This work is part of an effort to investigate future data management for bathymetric measurements in the Netherlands.

6.2. Description of methods for determining the shallowest depth

In general, when using a MBES system, the density of the measurements acquired is high, see Table 6.1 for the data sets considered in this chapter. Consequently, several soundings are located within a single cell, provided that a large enough cell size is considered. Here, a cell size Γ is considered in both easting and northing directions, i.e., the resolution of the grid in both directions is equal. The number of soundings in each cell is indicated by N_{hits}. These sounding are collected in

the observation vector $\boldsymbol{y}$ as $\boldsymbol{y} = [d_1, d_2, ..., d_{N_{\text{hits}}}]^T$. The shallowest measured depth corresponds to the minimum of $\boldsymbol{y}$.

Table 6.1: Covered area, number of soundings, number of cells and the MBES employed for the two areas (A and B).

Parameter	Survey Area	
	A	B
Area (m^2)	4758203	4492155
Soundings (#)	58777805	114934172
Cells (#)	4758203	4492155
MBES	Norbit WMBS	EM3002D

6.2.1. Shallowest depth based on mean and standard deviation

As mentioned, the problem associated with the shallowest depth is that it is not necessarily a good observable, as no averaging is carried out to mitigate the effect of measurement errors. However, using the mean depth, $\text{E}\{\boldsymbol{y}\}$ with E the expectation operator, neglects the presence of slopes. Therefore, $d_{\min,CL}$ is proposed where $\sigma_{\boldsymbol{y}}$ is the square root of the variance of the data (the standard deviation of the depth measurements in a cell). $d_{\min,CL}$ is expressed as

$$d_{\min,CL} = \text{E}\{\boldsymbol{y}\} - D_{CL}\sigma_{\boldsymbol{y}}\,, \tag{6.1}$$

where D_{CL} is the scale which depends on the confidence level (representing confidence interval) and derived from the normal inverse cumulative distribution function for a given confidence level (the number of times that the standard deviation is subtracted), see Section 2.7.6. For example, $d_{\min,68.3\%}$ denotes the shallowest depth in the 1-$\sigma_{\boldsymbol{y}}$ confidence interval ($CL = 68.3\%$ confidence level). Within this chapter only $D_{CL} = 0$ and $D_{CL} = 1$ (with $D_{CL} = 0$ the mean depth) are considered.

6.2.2. Shallowest depth based on the regression coefficients

As a second approach, where the potential presence of slopes along the cell surface is explicitly accounted for, a linear function (plane) is fitted to the depth measurements as

$$f(X_N, Y_N) = a_0 + a_{X_N}X_N + a_{Y_N}Y_N - d = 0\,. \tag{6.2}$$

where X_N, Y_N and d are the easting and northing coordinates of a sounding in the navigation frame (geographical coordinate system) in a cell respectively. Here, the geographical coordinate system considered is Universal Transverse Mercator (UTM). a_{X_N} and a_{Y_N} are regression coefficients, representing slopes in easting and northing directions, respectively, and a_0 is the intercept.

With the unknown parameters contained in the vector $\boldsymbol{x} = [a_0, a_{X_N}, a_{X_N}]^T$ and the observation vector $\boldsymbol{y}$, i.e., the soundings in a cell, the linear model of observation equations can be written as

$$\text{E}\{\boldsymbol{y}\} = \mathbf{A}\boldsymbol{x} \quad \text{D}\{\boldsymbol{y}\} = \sigma_{\boldsymbol{y}}^2\mathbf{I}\,, \tag{6.3}$$

with E and D the expectation and dispersion operators respectively. $\sigma_y^2 \mathbf{I}$ is the covariance matrix of $\mathbf{y}$ with σ_y^2 the variance of the data and $\mathbf{I}$ an identity matrix of size N_{hits}. $\mathbf{A}$ is the design matrix of the size $N_{\text{hits}} \times 3$ of which its ith row is $\mathbf{A}_i = [1, X_{N_i}, Y_{N_i}]$. The unknown parameters can be derived by minimizing the quadratic error ($\|\mathbf{e}\|^2$ with the assumption $\text{E}\{\mathbf{e}\} = 0$). The least-squares estimate of the 3-vector of unknowns can be then obtained as [142]

$$\hat{\mathbf{x}} = (\mathbf{A}^T \mathbf{A})^{-1} \mathbf{A}^T \mathbf{y} . \tag{6.4}$$

Substituting easting and northing of the measurements in the matrix $\mathbf{A}$ leads to rank deficiency of the normal matrix ($\mathbf{A}^T \mathbf{A}$), also referred to as numerical instability, due to the difference in the magnitude of the columns of the design matrix. To solve this problem, the equation of the plane can be alternatively defined as

$$
\begin{aligned}
f(X_N, Y_N) = a_{X_N}(X_N - \text{E}\{X_N\}) + a_{Y_N}(Y_N - \text{E}\{Y_N\}) - d \\
+ \underbrace{(a_0 + a_{X_N}\text{E}\{X_N\} + a_{Y_N}\text{E}\{Y_N\})}_{a_0'} = 0 ,
\end{aligned} \tag{6.5}
$$

where $\text{E}\{X_N\}$ and $\text{E}\{Y_N\}$ are the mean (expected) values of the easting and northing in a cell. Thus, the unknown parameters are now of the form $\mathbf{x} = [a_0', a_{X_N}, a_{X_N}]^T$.

Using Eq. (6.4) with $\mathbf{A}_i = [1, X_{N_i} - \text{E}\{X_N\}, Y_{N_i} - \text{E}\{Y_N\}]$ as the design matrix, one can determine the unknown parameters. The least-squares estimator of observables ($\hat{\mathbf{y}}$) and of residuals ($\hat{\mathbf{e}}$) follows from

$$\hat{\mathbf{y}} = \mathbf{A}\hat{\mathbf{x}} \tag{6.6a}$$
$$\hat{\mathbf{e}} = \mathbf{y} - \mathbf{A}\hat{\mathbf{x}} , \tag{6.6b}$$

with $\hat{\mathbf{y}}$ and $\hat{\mathbf{e}}$ the depth measurements projected onto the range space of the matrix $\mathbf{A}$ (the plane) and the deviation of the bottom topography from the best-fitted plane, respectively. Based on the assumption $\text{E}\{\mathbf{e}\} = 0$, the expectations of the least-squares estimate of the unknowns, observables and residuals is $\text{E}\{\hat{\mathbf{x}}\} = x$, $\text{E}\{\hat{\mathbf{y}}\} = \mathbf{A}x$ and $\text{E}\{\hat{\mathbf{e}}\} = 0$. The depth residuals are normally distributed with zero mean and their corresponding the standard deviation. This standard deviation along with the least-squares estimate of the observables is used to construct a confidence interval for the identification and rejection of the outliers [166].

The depths at the four corners of a cell can be derived using a_{X_N} and a_{Y_N} and the intercept (determined from substituting Eq. (6.4) in Eq. (6.2)) where the easting and northing of these corners are

$$
\begin{aligned}
X_{N_{\text{LU}}} = X_{N_{\text{LL}}} = X_{N_{\text{cent}}} - \frac{\Gamma}{2} , \\
Y_{N_{\text{RL}}} = Y_{N_{\text{LL}}} = Y_{N_{\text{cent}}} - \frac{\Gamma}{2} , \\
X_{N_{\text{RU}}} = X_{N_{\text{RL}}} = X_{N_{\text{cent}}} + \frac{\Gamma}{2} , \\
X_{N_{\text{RL}}} = X_{N_{\text{LU}}} = Y_{N_{\text{cent}}} + \frac{\Gamma}{2} ,
\end{aligned} \tag{6.7}
$$

where the subscripts LU, LL, RL and RU denote the upper-left, lower-left, lower-right and upper-right corners, respectively. $X_{N_{\mathrm{cent}}}$ and $Y_{N_{\mathrm{cent}}}$ indicate the position of the cell center. The shallowest depth based on the regression coefficients ($d_{\mathrm{min,Reg}}$) reads as

$$d_{\mathrm{min,Reg}} = \min(d_{\mathrm{LU}}, d_{\mathrm{LL}}, d_{\mathrm{RL}}, d_{\mathrm{RU}}) \,, \qquad (6.8)$$

where $\min(d_{\mathrm{LU}}, d_{\mathrm{LL}}, d_{\mathrm{RL}}, d_{\mathrm{RU}})$ indicates the shallowest depth among the four depths at the corners of the cell. Theoretically, $d_{\mathrm{min,Reg}}$ is a more realistic representative of the true shallowest depth in a cell compared to the one based on the standard deviation and mean depth as it explicitly takes the effect of potential slopes into account. One can subtract the standard deviation of the depth residuals (which is an indication of the deviation of the bottom topography from the best fitted plane), from Eq. (6.8) to ensure a safety margin.

6.3. Description of the data sets

To assess the effect of using different methods for shallowest depth determination as introduced in the previous section, two areas in the Westerschelde estuary were considered. The data sets were provided by RWS. These data sets were chosen as they contain regions with significant importance for navigation, related to very shallow depths. Fig. 6.1 shows the bathymetry of the areas. For the sake of convenience, the areas Honte (omgeving Put van Borssele) and Pas van Terneuzen (Springergeul ankergebied) are referred to as A and B, respectively. The depth, vertically referenced to Normaal Amsterdams Peil (NAP), varies from 2.5 m to 66.20 m in area A and from 5.10 m to 17.70 m in area B. In area A a dredged navigational channel exists (see Fig. 6.1) where the relatively deep area inside the trenches is maintained by constant dredging and maintaining the slopes. Hence, it is interesting to assess the bathymetry in this region using the different approaches for obtaining the shallowest depth. Regarding area B, it is seen from Fig. 6.1 that two sets of sand dunes exist, one in the deepest part of the survey area and the other in the shallower part. It is important to investigate the impact of using the different measures for shallowest depth on the mapping of sand dunes. Table 6.1 presents the size of the areas, number of soundings, number of cells and the MBES used. Illustrated in Fig. 6.2 is the map of the number of soundings and bathymetric standard deviations for survey area B. It is seen that the bathymetric standard deviation and number of soundings per cell are not constant over the swath, see also Chapter 5, both issues will be elaborated in Section 6.4.

A brief discussion on the systems used for data acquisition and bathymetry processing is in order (vertical positioning in particular). A critical element in the accurate estimation of the depth below the transducer is the Sound Speed Profile (SSP) in the water column which varies both spatially and temporally. Therefore, sufficient and accurate measurements of this parameter are required. To ensure the former, the surveyor was asked to acquire a new SSP if there was a difference of more than 2 m/s between the surface sound speed value and the surface sound speed from the latest full SSP, as specified by [108]. The sound velocity profilers employed in areas A and B were manufactured by Valeport and AML oceanographic,
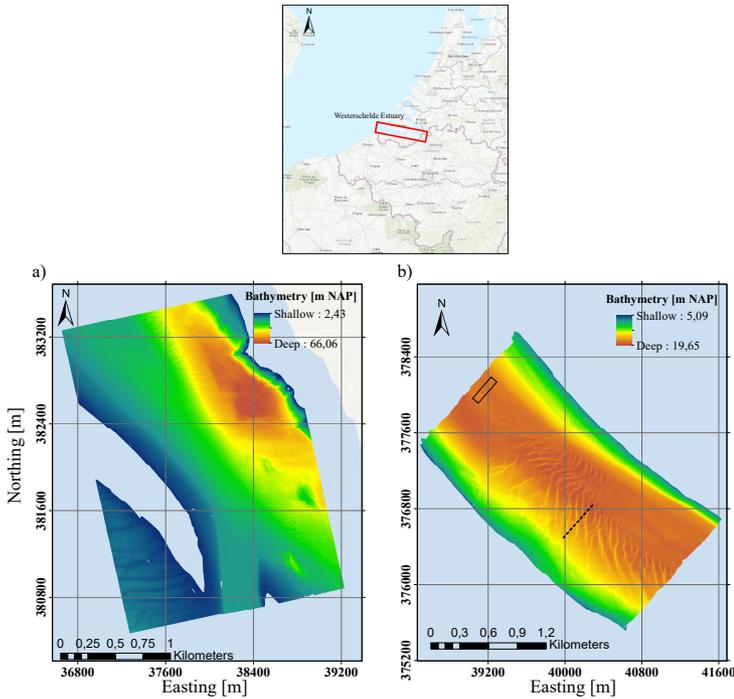
Figure 6.1: Bathymetric maps of the two areas considered (vertically referenced to NAP): a) Honte (omgeving Put van Borssele and b) Pas van Terneuzen (Springergeul ankergebied). The depth is considered positive downward. The black rectangle and black dashed areas in area B consist of 150 and 30 pings and represent a flat and a non-flat areas, respectively, and will be considered in more detail later.
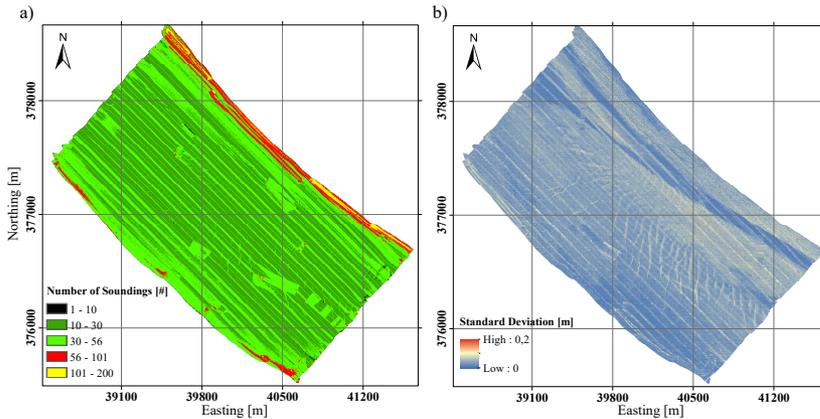
Figure 6.2: Maps of the a) number of soundings and b) the bathymetric standard deviation for area B.

respectively, measuring the sound velocity either directly or as a function of conductivity, temperature and depth. The depth below the transducer was then calculated

using ray-tracing in the processing software. The uncertainty of the sound velocity profilers indicated by the manufacturers is around 0.02 m/s, [144, 161]. However, from measurements in different locations (inland waterways and the North Sea), the uncertainty was found to be 0.2 m/s, and hence this value was chosen as a more realistic description of the systems uncertainty and is used to quantify the resulting depth uncertainty. A discussion on the effect of using an erroneous SSP is also given later on.

Both data sets were acquired using the Quality Integrated Navigation System (QINSy) (developed by Quality Positioning Services, QPS BV) and Global Navigation Satellite System (GNSS) sensors received the correction signal from Real-time Kinematic (RTK) services, Netherlands Positioning Service (NETPOS) in the Netherlands. GNSS RTK provides one with accurate position and ellipsoidal height of the GNSS antenna with an accuracy of a few centimeters in the WGS84 reference frame. The seafloor depth relative to the chart is then derived using the ellipsoidal height, GNSS antenna and transducer offsets from the vessel center of gravity (COG) and chart datum shift, obtained from chart datum models, see as an example [86, 87]. Since NETPOS was used during the data acquisition, the antenna's vertical coordinate is obtained in NAP (Normaal Amsterdam Peil). This means that the uncertainty induced by the chart datum has been already included in the vertical positioning uncertainty, and hence there is no need to add this as a separate contributor to Eq. (2.45). Using GNSS with NETPOS for calculating the seafloor depth implies that the water surface level is directly of no relevance and accounting for height offsets, such as dynamic draft, height above draft reference and tide, is not necessary for this method (however, knowledge of the water surface level is required for computing the entry location for the sound speed profile, and hence it indirectly affects the estimated depth). This means that to obtain the depth uncertainty relative to the chart datum it is not necessary to add their contribution to Eq. (2.45). Heave measurements (short-term variations in the transducer's depth) are, however, used within the processing software to calculate the height of the vessel's center of gravity between two position updates (because the MBES and Inertial Navigation Sensor (INS) have higher unpdate rate than many GNSS system). Therefore, the accuracy of heave measurement acquired by the INS contributes to the uncertainty in the estimate of the depth. Additionally, potential systematic heave errors result in depth errors through a systematic rise and fall of all the beams, see [120] and [40]. A careful assessment of the survey areas shows that such a systematic behavior does not exist. There are also other contributors affecting the quality of depth measurements which will be discussed in Section 6.4.1.

6.4. Results

In this section, the results of determining the shallowest depth in a cell based on the methods described are presented. Before proceeding, the cell size used in this chapter is discussed as it affects the grids derived. In reference [108], the so-called grid resolution (cell size) as a function of depth is specified. Based on the specification (full seafloor coverage), for depths ranging from 0 m to 20 m, a cell

size of 1 m in both directions is required. For depths ranging from 18 m to 40 m and from 36 m to 80 m, the specified cell sizes are 2 m and 4 m, respectively. For area B, a cell size of 1 m was chosen, according to the depth range in Fig. 6.1. For area A, based on the specification, it was possible to use the three aforementioned cell sizes. However, the smallest cell size was chosen to minimize the possibility of not mapping the bathymetric features, a detailed discussion can be found in [167].

For the data sets considered in this chapter with the specifications presented in Table 6.2, the across-track distance between two soundings (in one ping) is around 0.7 m and 0.48 m in areas A and B respectively, i.e., thus smaller than the cell size. For the along-track resolution of the MBES, the operational ping rate should be considered, which depends on the water depth and the angular sector and can be lower than the theoretical maximum ping rate specified by the manufacturer (see Table 6.2). For the deepest parts of areas A and B and the most outer beam, the Two-Way Travel Time (TWTT) equals 0.192 s and 0.073 s respectively (i.e., ping rates of 5 Hz and 13 Hz). The along-track spacing between two consecutive pings with the survey speed of nearly 5 m/s is thus equal to 0.96 m and 0.36 m respectively. Considering the overlap between the adjacent swaths one can conclude that in general multiple measurements will be within the 1 m × 1 m, allowing for extracting the required statistics.

As a first step toward comparing the depths derived from the approaches discussed previously, however, the validity of using the mean is investigated. The shallowest depth using the standard deviation and mean is based on the characteristics of the normal distribution for which it is assumed that a CL percentage of depths appear within the range $E\{y\} \pm D_{CL}\sigma_y$ (as an example, for $CL = 68.3\%$, $D_{CL} = 1$). However, if the distribution of the data is not normal, the mean and standard deviation cannot automatically be considered as the indicators representing the central tendency and variation of the data, respectively. Moreover, the mean and standard deviation are negatively influenced by the outliers [168]. A measure for the central tendency of the data which can be used instead is the median with the advantage of being insensitive to the presence of the outliers. In contrast to the mean which is affected by the presence of even 1 aberrant value (0% breakdown point), the median can resist up to 50% of outliers (50% breakdown point) [169]. As for an indicator of the variability of the data in case of having a skewed (asymmetric) distribution, one can use the Median Absolute Deviation (MAD), with 50% breakdown point in contrast to the standard deviation (with 0% breakdown point). MAD is also a more robust estimate of the data variability than the Interquartile Range (IQR). The latter is defined as the difference between the third and first quartiles of the data and has 25% breakdown point, see [168]. Considering the higher breakdown point of MAD than IQR, the former is investigated as a potential alternative for the standard deviation. Fig. 6.3 shows the depth distribution within four cells with different numbers of soundings. It is seen that for these cells, the distribution of the depth measurements is skewed and varies from one cell to another due to varying bottom characteristics.

Shown in Fig. 6.4 is the map of the differences between the median and mean depths for area A. Varying colors are used to represent the difference. The range of

Table 6.2: Characteristics of Norbit WMBS [170] and EM3002 [171] in the dual head configuration used in area A and B respectively.

| | MBES | |
Parameter	EM3002D	Norbit WMBS
Maximum number of soundings per ping [#]	508	512
Beam spacing mode	equidistant	equidistant
Maximum swath width [°]	200	160
Along-track opening angle [°]	1.5	1.9
Across-track opening angle at nadir [°]	1.5	0.9
Maximum ping rate (Hz)	40	60
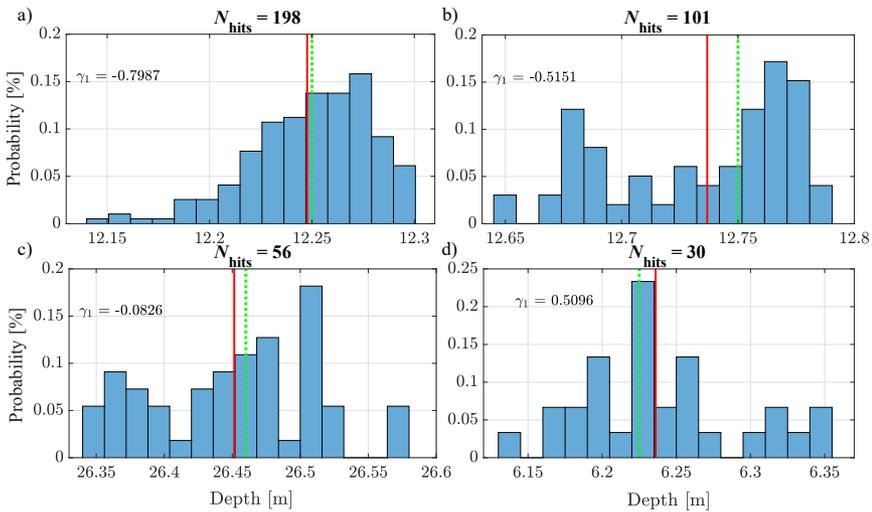
Figure 6.3: Distribution of the depth measurements within four cells with a) 198, b) 101, c) 56 and d) 30 depth measurements. The vertical solid line indicates the median, whereas the dotted line indicates the mean depth. Symbol γ_1 indicates the skewness.

values for each color is such that each color represents a certain percentage (25% in this case) of all data points. It is seen that for 50% of the data, the difference between the depth based on the median and mean varies between $-0.007\,\mathrm{m}$ and $0.005\,\mathrm{m}$. For 25% of the cells, the differences vary between $3.254\,\mathrm{m}$ and $-0.007\,\mathrm{m}$, however, for 97% of these cells the differences are less than $0.05\,\mathrm{m}$. The same situation also holds for the upper bounds of the data, i.e., for 98% of the cells between the 75-percentile and maximum difference, the differences are less than $0.05\,\mathrm{m}$. Observing the color green in Fig. 6.4, which is not present in the color bar, is due to the fact that in some areas the cells with the differences between $-0.007\,\mathrm{m}$ and $0\,\mathrm{m}$ and the ones with the differences between $0\,\mathrm{m}$ and $0.005\,\mathrm{m}$ are located in the close vicinity of each other. Hence, for these areas the colors yellow and light blue are mixed and appear green.

The importance of these differences is to be assessed from a statistical point of view, i.e., whether the difference between the median and mean is statistically
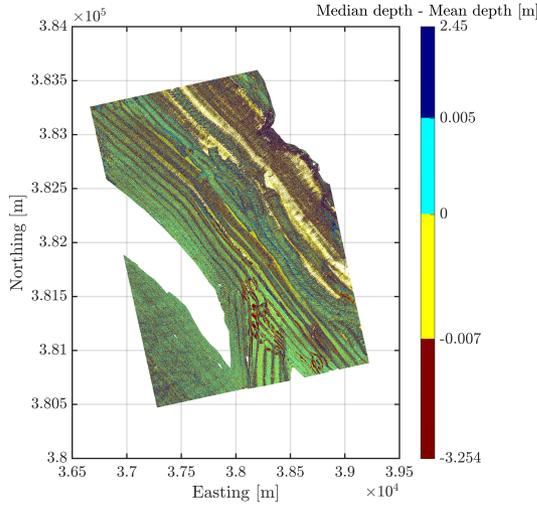
Figure 6.4: Map of the difference between the median and mean depths for area A. The range of values represented by each color is such that each range represents an equal percentage of the data.

significant (meaningful), and hence null and alternative hypotheses are considered

$$\begin{cases} H_0 & : E(\underline{x}) = 0 \\ H_1 & : E(\underline{x}) \neq 0 \end{cases},$$

(6.9)

where $\underline{x}$ is the variable (difference between mean and median). If H_0 is rejected, it means that the expected value of the variable is statistically significant. Hypothesis testing is usually carried out using the Probability Density Function (PDF) of a random variable. However, here, the PDF of the variable is not theoretically known (it varies from cell to cell), and hence one may use Chebyshev's inequality [142] which avoids distributional assumptions for the random variable. However, the bounds provided are quite conservative. Chebyshev's inequality states that for a random variable $(\underline{x})$ with $E(\underline{x})$ and $\sigma_{\underline{x}}$ being its expected value and standard deviation, respectively, the following holds for every ε

$$P\big(|\underline{x} - E(\underline{x})| < \varepsilon \sigma_{\underline{x}}\big) \geq 1 - \frac{1}{\varepsilon^2} .$$

(6.10)

Thus, the probability masses outside the interval $(E(\underline{x}) - \varepsilon \sigma_{\underline{x}}, E(\underline{x}) + \varepsilon \sigma_{\underline{x}})$ are smaller than $\frac{1}{\varepsilon^2}$ for every ε regardless of the form of the PDF of $\underline{x}$. Therefore, under the null hypothesis, the 95% confidence interval is obtained for $\varepsilon = 4.47$, indicating that $4.47\sigma_{\underline{x}} < E(\underline{x}) < 4.47\sigma_{\underline{x}}$. The bounds provided by the Chebyshev's inequality are quite conservative, as an example, the 95% confidence interval is larger than the case with a normal distribution. This means that if the null hypothesis is rejected using the Chebyshev's inequality, it will be indeed rejected for an arbitrary

distribution. However, the reverse situation does not necessarily hold, i.e., if $E(x)$ is within the bounds of Chebyshev's inequality, one cannot state that the difference between the mean and median is not significant for an arbitrary distribution. For the case under consideration, with the mean and standard deviation of the difference between the mean and median equaling -0.001 m and 0.015 m (the null hypothesis is not rejected), one can only state that there is no evidence of the mean and median being different from statistical point of view. Finally, from Fig. 6.4 it is seen that the differences tend to show a 'stripy' behavior. This will be studied in more details in the following section. A similar study was carried out, comparing the differences between standard deviation and MAD, indicating that the standard deviation can be used as a measure for the data variability. A similar conclusion again is drawn from the comparison between mean and median and standard deviation and median absolute deviation of the survey area B.

6.4.1. Mean depth instead of shallowest measured depth

Fig. 6.5a and Fig. 6.5b show the difference between the mean depth and the shallowest depth per cell for areas A and B respectively. The maximum absolute difference between the mean and shallowest depth in Fig. 6.5a (6 m) is significantly larger than that of Fig. 6.5b (0.6 m). Especially Fig. 6.5a clearly demonstrates the need for improved mapping method compared to the shallowest measured depth per cell as it is impossible to have a 6 m difference between the shallowest and mean depth in a 1 m×1 m cell. In addition, the results show a dependency along the sailing direction. This dependency, which was not observed in the bathymetry, exists irrespective of the topography and type of the MBES employed and the difference between the two depths gradually increases from nadir to the outer beams. To closely examine the origin of this dependency, the seafloor profiles for both a flat area and a non-flat area are considered.

Shown in Fig. 6.6a and Fig. 6.6b are the mean and shallowest depths, obtained as an average over nearly 150 pings, and the difference (solid lines) between these two for a relatively flat area (indicated by black rectangle in the bathymetry map B) respectively. It is seen that this difference increases toward the outer parts of the swath (Fig. 6.6b) resulting in the dependency observed. It is hypothesized that this increase is due to the fact that the uncertainties inherent to the MBES, due to uncertainties in, for example, roll and steering angle, increase towards the outer parts of the swaths (i.e., with an increase in the beam angle), see [53, 157] and Chapter 5. The shallowest depth measured per grid cell is more affected by these uncertainties than is the mean depth. This is due to the fact that no averaging is used for the former. The value of 0.01 m, corresponding to measurements directly underneath the MBES, can thus be considered to represent, at least for the considered part of area B, the minimum value of the expected change in estimated water depth (getting deeper) when instead of the shallowest depths, mean depths are presented for flat areas.

An interesting point to address here is the effect of an increase in the cell size. Shown in Fig. 6.7 are the same parameters as shown in Fig. 6.6b with the cell
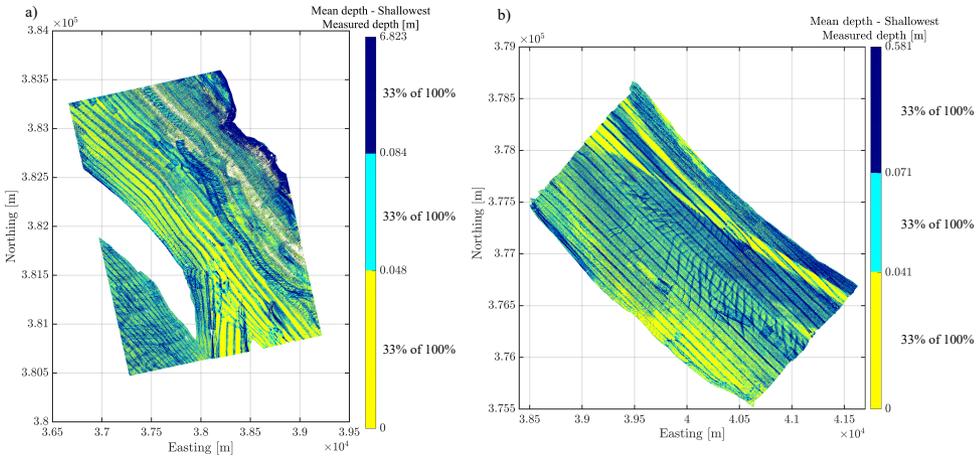
Figure 6.5: Maps of the difference between the mean and shallowest depth a) for area A and b) for area B. The range of values represented by each color is such that each color represents an equal percentage of the data.
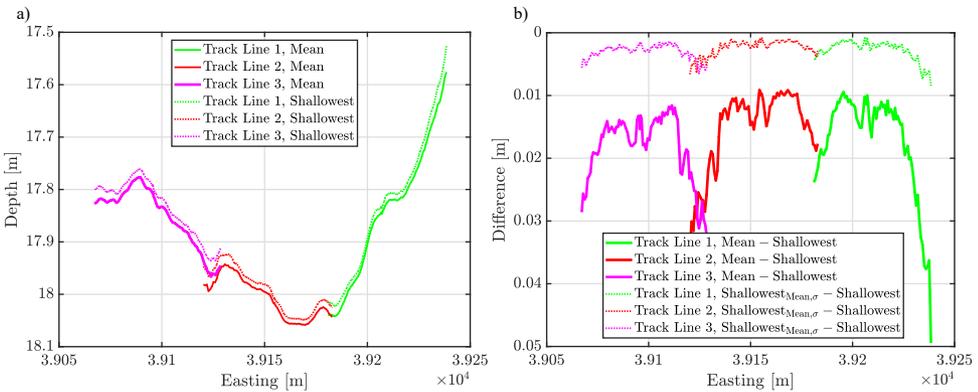
Figure 6.6: a) Mean (solid) and shallowest (dotted) depths, vertically referenced to NAP, for a small area within area B indicated by the black rectangle in Fig. 6.1 consisting of three track lines, and b) the difference between the mean and shallowest depths (solid) and the difference between the mean, corrected for standard deviation, and shallowest depths (dotted).

size of $4\,\mathrm{m} \times 4\,\mathrm{m}$ (instead of $1\,\mathrm{m} \times 1\,\mathrm{m}$). As seen, the coarser grid does not hamper observing the increase in the differences toward the outer part of the swaths (larger beam angles). However, as expected, the level of detail which was observed in Fig. 6.6b has decreased. As for the effect of cell size on the shallowest and mean depths representatives, the former gets shallower when the cell size increases as the shallowest depth is assigned to a larger area. While having a smaller cell size theoretically increases the depth estimate based on the shallowest measured depth (i.e., getting deeper), it does not change the depth estimate derived from the mean to a noticeable extent. However, one should take the MBES along-

track and across-track resolutions into account when choosing a cell size. A more advanced alternative to the fixed resolution gridding is the multi-resolution grid. This leads to the data compression depending on the bottom morphology and enables one to capture the variability of beam footprint and the data density, see as an example [172] and [173]. One can also relate the patches together leading to a smooth surface approximation. This can be done using the theory of polynomial spline approximation. A spline function is a piecewise polynomial interpolation such that these polynomials are joined together under some continuity conditions, see as an example [174] and [175]. However, as this might introduce unwanted depth variations, it is more suitable for morphological studies (where focus is on specific bathymetric features) and not for charting purposes (where the safe navigation is of importance) as considered in this chapter.
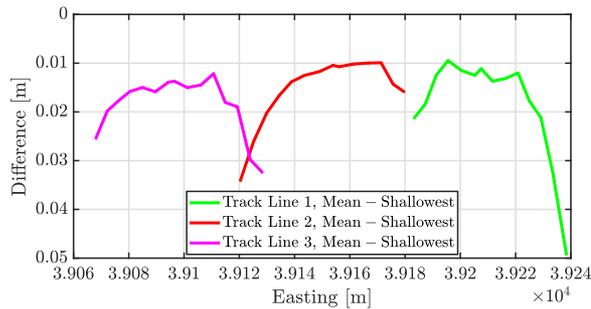
Figure 6.7: Difference between the mean and shallowest depths for the same area shown in Fig. 6.6 with 4 times larger cell size than that of Fig. 6.6b.

It should be noted that generally speaking, the degradation in the quality of the MBES bathymetric measurements is not solely due to the uncertainties inherent to the MBES, but various other error sources can be considered. One of the contributors is the systematic error sources which can be categorized as the static and dynamic ones. The former include (not limited to) the relative heading, pitch and roll misalignments between the MBES and INS and the relative time mis-synchronization between the positioning sensor and MBES clocks, see [120] for a detailed discussion of the various systematic error sources. As an example, the roll offset induces a depth error increasing with the beam angle, and hence its signature is similar to the one observed. Therefore, it is important to properly take them into consideration to avoid any misinterpretation. The correction of the above-mentioned static systematic sources is made using the patch tests, which examines the repeatability of the system over a pre-defined patch of the seafloor. For both survey areas, the patch test was carried out, and therefore these systematic errors (if present) were excluded. The other group of systematic errors is the dynamic ones producing errors which vary either with periods in the ocean wave spectrum or with long period acceleration of the vessel [40]. These errors can be identified using the correlation analysis between the motion time series and depth derivatives. Both data sets were examined carefully and the signatures of the dynamic systematic errors were not found. Another error source with a similar signature as observed (increase

toward the outer parts of the swath) is the SSP. Using an erroneous SSP induces errors both in the estimate of the depth and beamsteering, resulting in the under- or overestimation of the depth for the outer beams, and hence depth artifacts referred to as 'smiley' or 'frowny' are observed in the bathymetry map [96]. This error can be identified using the overlap between the adjacent swaths (Chapter 3, [93, 94]). Considering the fact that the time interval between the measurements of the adjacent lines for both survey areas was maximally up to several hours, the bottom features such as mega ripples and sand dunes did not vary within this relatively short period. Therefore, the depths as determined from the measured travel times along two overlapping swaths should be the same at equal points on the seafloor. Using an erroneous sound speed profile results in discrepancies between these measurement [93, 94, 176] and Chapter 3. A careful assessment of the footprints depth at the overlapping parts for both survey areas over different parts (flat and non-flat) confirmed that the correct SSPs were used. Therefore, it is concluded that the observed increase in the differences toward the outer parts of the swath is not caused by the systematic error sources.

To further investigate the validity of the hypothesis that for the flat area the difference between shallowest and mean depth is caused by the MBES measurement uncertainties, the model of [26, 27], as implemented in *A priori* Multibeam Uncertainty Simulation Tool (AMUST) was used for predicting the bathymetric uncertainties. AMUST is developed by the Acoustics Group of Delft University of Technology in a close cooperation with RWS. Fig. 6.8 shows the predicted uncertainties induced by different uncertainty sources inherent to the MBES for the water depth of around 18 m. The uncertainty sources considered in [26, 27] are the range measurements, roll and steering angle, pitch angle, along track opening angle, sound speed profile and heave, see Section 2.7. It should be noted that in Section 2.7, the depth uncertainty contributors are categorized as the contributions from echosounder, angular motion sensor, motion sonar and transducer alignment, sound speed and heave (which also accounts for the contribution of the GNSS sensor in case of using it for vertical referencing). Another approach for grouping the depth uncertainty sources (considered also in Section 4.4) is to categorize them as range measurements Eq. (2.46), roll and steering angle (Eq. (2.48), first term in Eq. (2.53), Eq. (2.54) and Eq. (2.58)), pitch angle (second term in Eq. (2.53) and Eq. (2.54)), along track opening angle (Eq. (2.51)), sound speed profile (second term in Eq. (2.58)) and heave.

The term describing uncertainties in the range measurements is often considered to result in predicting too high uncertainties [27]. Therefore, this term was scaled by 0.707 compared to [26]. It should be note that as discussed in Chapters 4 and 5, baseline decorrelation and Doppler effect, and Signal-to-Noise Ratio (SNR) are also uncertainty sources contributing to the random depth uncertainty. Although, accounting for them results in a more realistic expectation of the measurements capabilities, it requires knowledge about the pulse shape (its type and bandwidth), speeds of the transducer at transmission and reception projected on the beam direction, sediment composition. For the two data sets used in this chapter, such detailed information was not acquired during the data acquisition and
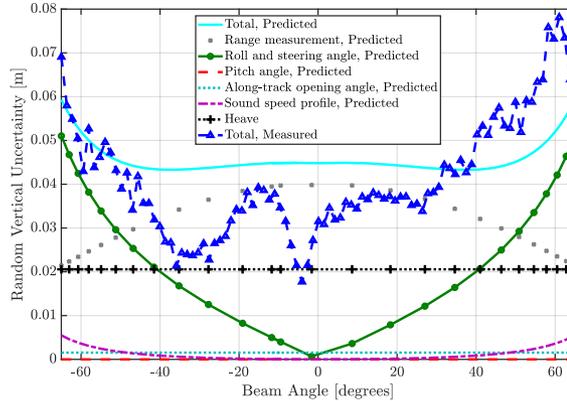
Figure 6.8: Total random vertical uncertainty predicted (cyan curve) due to the contribution of the uncertainty sources inherent to the MBES along with the measured uncertainty from the bathymetry measurement (blue dashed curve with upward triangle marker) for track line 3 in Fig. 6.6.

therefore, these uncertainty sources cannot be considered.

The total uncertainty was derived as the square root of the sum of the square of individual sources (assuming they are independent), see the solid cyan curve in Fig. 6.8. Also shown in this figure is the standard deviation of the depth measurements, see the blue dashed curve with triangles. 150 pings were used to calculate this standard deviation. The comparison between the modeled and measured uncertainties shows good agreement in both the order of magnitude, but also in the behavior of the uncertainties with beam angle, see also Chapter 5. Both the model and the measurements indicate increasing uncertainties with increasing beam angle, reflected in the stripes as observed in Fig. 6.5a and Fig. 6.5b. Discrepancies between the predictions and measurements can, at least partly, be explained by the presence of some bottom features. Although the approaches presented in this chapter are not based on an *a priori* estimates of the depth uncertainties, there are approaches which do need this estimate as an input, such as CUBE, and hence a realistic estimate of this parameter is required. The agreement between the modeled and measured uncertainties indicates that the model can capture the measured standard deviation to a certain extent in agreement with the findings of Chapter 5.

It can be concluded that for flat areas, using the shallowest measured depths results in mapping depths that are affected by measurement uncertainties. It is known that these uncertainties in the measurements change with beam angle, water depth and measurement equipment, see [157] as an example. Thus, the magnitude with which the uncertainties affect the mapped depths will be location and survey dependent.

Regarding the non-flat regions, a small area consisting of 5 track lines and 30 pings was considered, see the black dashed area in Fig. 6.1. A small number of pings was chosen to ensure that the topography did not change. For each ping, the measurements were averaged over five beams and the profile for mean depth

(Fig. 6.9a) was derived by averaging over the 30 pings for each track. From Fig. 6.9c it is seen that now, in contrast to the flat area (see the solid lines in Fig. 6.6b), the larger differences between mean and shallowest do not occur at the outer parts of the swaths. In this case the largest differences are found at the locations of morphological features. Specifically, it is seen that the maximum differences occur at regions with larger slopes (Fig. 6.9b), as expected for a sloping plane. To further assess the correlation between the differences and the slopes, these two parameters along with their linear fit are shown in Fig. 6.10. It is seen that the differences between the mean and shallowest depths increases with an increase in the slope (correlation coefficient between the two parameters is 0.624 which is significant in 95% confidence level). As discussed, an increase in the cell size leads to a less-detailed seafloor representation. This affects non-flat regions to a larger extent than that of flat areas as larger depth variations are expected in a small area, see Fig. 6.11a and Fig. 6.11b where the same parameters as shown in Fig. 6.9b and Fig. 6.9c, respectively, are presented for a four times larger cell size. As an example, for Line 4 (red) in Fig. 6.9b (1 m×1 m cell size) the slope at the beginning of the swath is not very steep, however, if the cell size increases, one might interpret it as a steep slope. Similar to the flat areas, having a coarser grid for the non-flat regions results in a shallower grid compared to that of the fine, however, the magnitude of the change is larger than that of the flat areas.
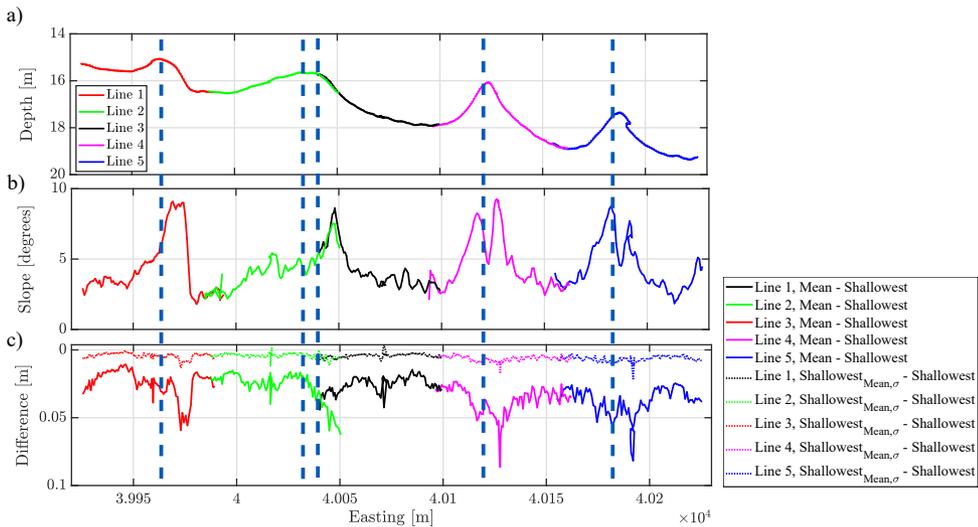
Figure 6.9: a) Mean depth vertically referenced to NAP, b) Mean slope, and c) Mean difference between mean and shallowest depths (solid) and mean difference between mean and standard deviation and shallowest depths (dashed) for the black area shown in area B in Fig. 6.1. This area consists of five track lines and 30 pings. The blue dashed vertical lines indicate the location of the shallowest depth for each swath.

Based on the above, it is concluded that for flat areas, the differences between mean and shallowest measured depths are dominated by the MBES measurement uncertainties. This result in depths that are shallower than the actual shallowest
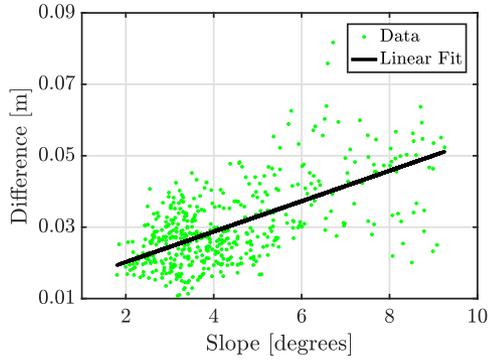
Figure 6.10: Mean Slope versus the mean differences for the black dashed area shown in area B in Fig. 6.1 and its linear fit.
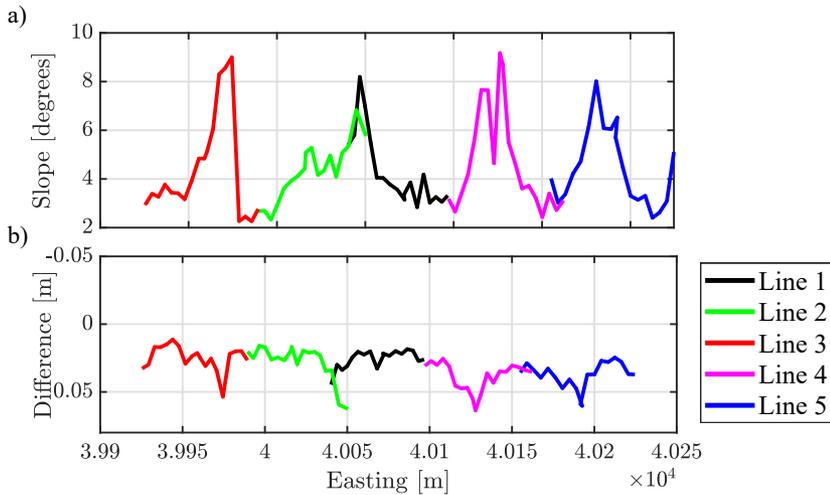
Figure 6.11: a) Mean slope, and b) Mean difference between mean and shallowest depths for the same area shown in Fig. 6.9c with four times larger cell size.

depths, with the magnitude of the offset varying along the MBES swath. For non-flat areas, an additional contribution is due to the presence of slopes that inherently results in a difference between the mean and shallowest depth in a cell. Whereas the effect of measurement uncertainties can be counteracted by using the mean instead of shallowest depth, this will result in an overestimation of the depth in non-flat areas, i.e., it gets deeper. Considering the importance of guaranteeing safe navigation, this can be considered as an undesirable situation. Indeed, assigning a realistic depth value in non-flat regions where steep slopes exist is an issue of great interest and has been discussed by various scholars. Reference [177] found that for areas with extreme seafloor morphology and steep slopes, even the advanced surface estimation approaches, such as CUBE, might fail to provide a realistic and

robust estimate of the depth. Modification of the different CUBE parameters has resulted in a more realistic surface representation. The irregular and non-flat bottom can also complicate the identification and rejection of the outliers such that automatic data cleaning approaches might not be applicable, see reference [166] for a detailed discussion.

6.4.2. Shallowest depth using mean and standard deviation

To account for the overestimation of the depth in non-flat areas, Eq. (6.1) was used. Shown in Fig. 6.12a and Fig. 6.12b are the maps of the differences between the shallowest depth based on the mean and standard deviation and the shallowest measured depth per cell for areas A and B respectively.

Different color bars were used, for the two areas, for representing the difference between the shallowest depth derived (i.e., using the standard deviation) and the one measured. For decreasing difference between the mathematical shallowest depth and the shallowest measured depth while being positive, the color gets lighter. The range of values for each color was selected such that each color represents a certain percentage of all data points (33% here). Dark red in Fig. 6.12 indicates that the resulting depth is shallower than that actually measured. For 17% of the cells in area A, the shallowest depth based on the mean and standard deviation is up to a meter shallower than the shallowest depth measured (only for 0.002% of the cells the difference exceeds 1 m). With regards to area B, the range of the differences is considerably smaller and for a smaller percentage (around 2%) of the cells the shallowest depth derived is shallower than the one measured. Obtaining a shallower representative than the shallowest measured depth indicates that the standard deviation within a cell is larger than the difference between the shallowest and mean depths, see Eq. (6.1). This phenomenon, which is somewhat unexpected, can be explained by the fact that the distribution of depth values within a cell does not necessarily need to be symmetric (Fig. 6.3 and Fig. 6.4) and can be skewed. The standard deviation does not reflect this asymmetry in the distribution, resulting in derived depths that are shallower than the actual shallowest depth.

To investigate in more detail the effect of using this measure in a flat area, Fig. 6.6b shows the difference between the shallowest measured depth and the approach considered in this section, see the dotted lines. For the tracks considered, it is seen that the estimated depths are larger than those obtained when taking the shallowest depth. Also the standard deviation is affected by the MBES measurement uncertainties, as is the shallowest measured depth. However, since the effect is smaller for the standard deviation than for the minimum, the dotted lines in Fig. 6.6 shows a less pronounced dependency along the swath compared to the solid lines Fig. 6.5. More interesting is the effect of using the measure for depth as considered in this section for an area with slopes. The results are shown in Fig. 6.9c as the dotted lines. From this figure it is seen that now the slopes do no longer significantly contribute to the difference. The difference at the locations of the slopes is now comparable to those found for the remaining locations.
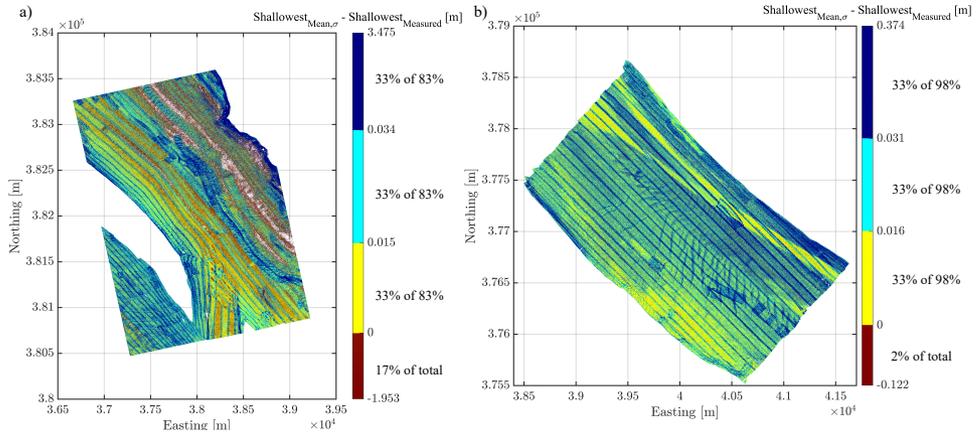
Figure 6.12: Maps of the difference between the shallowest depth based on the mean and standard deviation and the shallowest depth measured a) for area A and b) for area B. The positive range of values represented by each color is such that each color represents an equal percentage of the data for which the derived depths are deeper than the shallowest measured depths. Dark red indicates those data points where the derived depths are shallower than the shallowest measured depths.

Based on the above discussion, it can be concluded that although for flat areas using the combination of mean and standard deviation results in estimates for the water depth that are close to those corresponding to the shallowest measured depth, i.e., underestimating the actual depth, the standard deviation seems an appropriate way to account for the presence of slopes.

6.4.3. Mathematical shallowest depth using regression coefficients

The shallowest depth using the regression coefficients was derived from Eq. (6.8). Theoretically, this measure is a realistic representation of the shallowest depth in a cell as the effect of potential slopes is fully taken into account by calculating the shallowest depth at the corner. It was, however, found that when applying this method to the MBES point cloud data, unrealistic depth values were obtained for some cells, in agreement with [54]. As an example, consider the four depths derived for the corners of a cell in area A, see Table 6.3. Considering the mean for this cell (44.45 m, see Table 6.4) and the cell size 1 m × 1 m, it is impossible to obtain a depth of 10.78 m as the shallowest depth at the upper-left corner. To understand the reason behind obtaining the unrealistic depth values at the cell corners, the distribution of the soundings within a cell having this issue was assessed.

Table 6.3: Depth values at four corners of the cell in area A with parameters as presented in Table 6.4. Depth is considered positive downward.

Corner	LU	LL	RL	RU
Depth [m]	10.78	46.78	78.12	42.12

Table 6.4 presents the coordinates of the cell center, mean depth, number of soundings, regression coefficients and slope angles for a cell in area A with depth values at their corners as shown in Table 6.3. Fig. 6.13 illustrates the distribution of the soundings in this cell. It is seen that the points are not well-distributed within the cell under consideration, and hence the design matrix ($\mathbf{A}$) is badly invertible. As a result, the coefficients should only be used to determine the depth in the vicinity of the points rather than at the corners of the cell [54].

Table 6.4: Easting and northing of the cell center along with mean depth, number of soundings and slope angles for a cell in survey area A with unrealistic depth values at its corners. Depth is considered positive downward.

Parameter	Value
$X_{N_{\text{cent}}}$ [m]	38846.5
$Y_{N_{\text{cent}}}$ [m]	382065.5
Mean Depth [m]	44.45
N_{hits}	7
Slope angle [°]	88.8
Slope Direction [°]	318.96
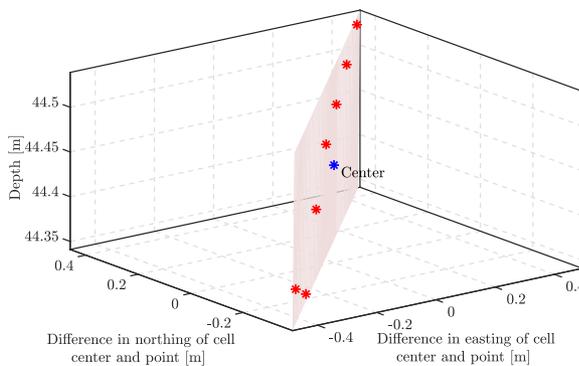
Figure 6.13: Distribution of the points in the cell (red) with the center (blue) coordinates presented in Table 6.4 (area A) along with the plane fitted.

The problem can be addressed by computing the condition number of the normal matrix ($\mathbf{A}^T\mathbf{A}$) of the size 3×3 [17] as done by [178] (using Singular Value Decomposition (SVD) of $\mathbf{A}$). The eigenvalue decomposition of the positive definite normal matrix is

$$\mathbf{A}^T\mathbf{A} = \mathbf{U}\boldsymbol{\Lambda}\mathbf{U}^T , \qquad (6.11)$$

where $\boldsymbol{\Lambda} = \text{diag}(\lambda_{11}, \lambda_{22}, \lambda_{33})$ is a diagonal matrix with diagonal entries the eigenvalues of $\mathbf{A}^T\mathbf{A}$, and $\mathbf{U}$ is a 3×3 matrix of eigenvectors where each column corresponds to one of the eigenvalues, $\lambda_{ii}, i = 1, 2, 3$, of the normal matrix. If the matrix $\mathbf{A}^T\mathbf{A}$ is singular or ill-conditioned, some of the eigenvalues are (almost) zero. The condition number, which is defined as the ratio of the largest (in magnitude) eigenvalue to the smallest eigenvalue, will thus take large values. For areas A and B, the condition number exceeded 10^2, 10^3 and 10^5 in 5%, 3% and 2% and 0.1%

0.07% and 0.02% of the cells, respectively. Here, cells with the condition number larger than 10^2 were excluded from the analysis and their 8 neighboring cells were used to assign the required parameters (such as regression coefficients) to them.

Shown in Fig. 6.14a and Fig. 6.14b are the differences between the shallowest depth based on Eq. (6.8) after excluding the badly-conditioned cells and the measured shallowest depth in a cell for areas A and B, respectively. It is seen that for around 55% and 40% of the cells in areas A and B, respectively, the depth derived is shallower than its measured counterparts. It should be highlighted that for nearly 95% of the cells in area A for which the depth derived is shallower than the one measured, the differences are less than 0.2 m. As for area B, for around 99% of these cells, the differences are less than 0.1 m. This means that the largest differences shown in the color bars (7.516 m and 0.917 m for areas A and B respectively) occur for a negligible portion of the cells.
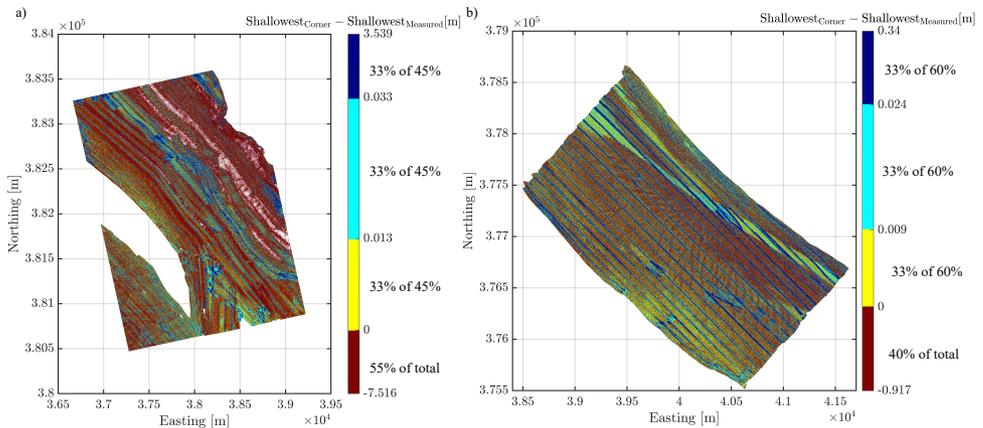
Figure 6.14: Maps of the difference between the shallowest depth at the corner of the cell (based on regression coefficients) and shallowest depth measured a) for area A and b) for area B. The positive range of values represented by each color is such that each range represents an equal percentage of the data for which the derived depths are deeper than the shallowest measured depths. Dark red indicates those data points where the derived depths are shallower than the shallowest measured depths.

To further investigate the performance of the approach based on the regression coefficients, an area consisting of one track line (on a slope) and six consecutive pings was considered (covering one meter along the sailing direction). For each ping, the measurements were averaged over five beams. Shown in Fig. 6.15 are the linear regressions along with the estimate of depth based on the mean, mean and standard deviation and shallowest measured. For a large number of cells, the best fitted planes show a discontinuous and unrealistic representation of the seafloor. As explained, the unrealistic estimate of the regression coefficients is due to the distribution of the soundings within the cells (Fig. 6.13) resulting in a relatively large condition number (see the condition number of 81 shown for the cell in Fig. 6.15). In a small region, right of the peak, a more continuous representation of the bathymetry as derived from the regression coefficients per

cell is found. For this area, lower values of the condition number are found. This result indicates that the applicability of the approach based on the regression is highly sensitive to the distribution of the measurements. Consequently, employing it is not encouraged. One approach to minimize the negative effect of outliers and to decrease the sensitivity of the this method to the distribution of the points is to calculate the regression coefficients for a local window of the cells instead of a single cell, however, this will result in a grid with varying cell size (i.e., multi-resolution) which is not considered in this chapter.
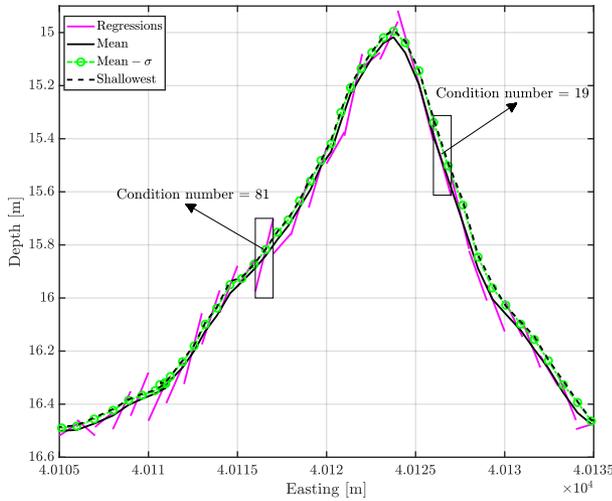
Figure 6.15: Depths vertically referenced to NAP using mean (solid black), mean and standard deviation (dotted green with circle) and shallowest measured (dashed black) along with the linear regressions (magenta). The rectangles indicate two cell with large and small condition numbers.

The average value of the depth based on the mean and standard deviation, regression coefficients, mean and the shallowest measured depth for both survey areas are shown in Table 6.5. It is seen than the deepest and shallowest representatives are based on the mean and the regression coefficients, respectively. The averaged value of the depth based on the mean and standard deviation is between those based on the shallowest measured and mean depths.

Table 6.5: The average value of the shallowest measured, mean and mathematical shallowest depths for survey areas A and B. Depth is considered positive downward.

	Survey Area	
Various Depth Representatives	A	B
Shallowest Measured depth [m]	24.87	14.92
Shallowest depth based on mean and standard deviation [m]	24.89	14.95
Shallowest depth using regression coefficients (at the corner) [m]	24.85	14.91
Mean depth [m]	24.94	14.99

Different approaches presented in this chapter for the estimate of the depth are not to be viewed as a replacement for more sophisticated methods, such as CUBE (developed by [55]). However, the fact that they do not require an *a priori* estimate of the depth uncertainties (i.e., they are based on the statistics from the soundings) and are simple to implement (particularly the depth estimate based the mean, shallowest and mean and standard deviation) make them appropriate alternatives in case a detailed information of the soundings uncertainty is not available. Nevertheless, the depth estimates derived using the shallowest, mean, mean and standard deviation and regression coefficients were compared to that of the CUBE implemented in Qimera processing software (developed by QPS BV) to give an insight into their agreement and possible discrepancies. For CUBE processing, the default Qimera configuration for shallow water was chosen containing the parameters suitable for areas where small scale features are important. Information on the parameters used in Qimera can be found in [179], and an interested reader might also refer to [180] for a detailed description of CUBE. The comparison was carried out for two parts of the seafloor, in non-flat and flat areas. Both parts were chosen such that they correspond to the data for small beam angles, i.e., close to nadir. Regarding the non-flat part, an across-track profile of the length 35 m in the area indicated by dashed line in Fig. 6.1 was chosen. Fig. 6.16a illustrates the depths obtained using different approaches. It is seen that the estimate of CUBE is in a good agreement with that of the mean. This indicates that using CUBE for the slopes with the default settings in Qimera, results in an overestimation of the depth (getting deeper) and therefore the method based on the mean and standard deviation seems to give a more realistic estimate. Regarding the seafloor profile for a flat part, see Fig. 6.16b, the CUBE estimates again closely follows the mean depth. This is somewhat expected as for a flat seafloor with randomly distributed soundings with comparable uncertainties (as the inner part of the swath is considered), the mean depth is close to output of the Kalman Filter.
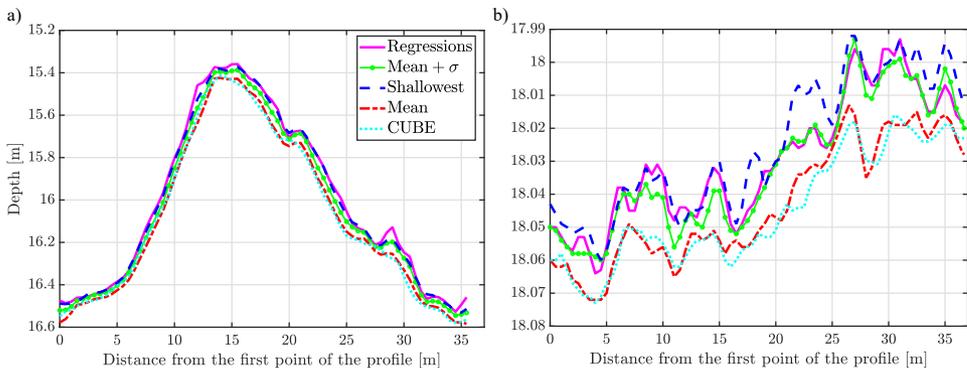
Figure 6.16: Depths vertically referenced to NAP using mean (dotted dashed red), mean and standard deviation (solid green with circle) and shallowest measured (dashed blue), regressions coefficients (magenta) along with the CUBE (dotted cyan) estimate for a) non-flat and b) flat parts.

6.5. Conclusions

A MBES provides a non-destructive and cost-effective way to produce qualitative and quantitative bathymetry maps. The resulting MBES point cloud data contains millions of soundings and is, in general, not directly used for charting. A straightforward approach for equidistant gridding, often adopted, is to consider the shallowest depth at the center of the cell. The grids derived can be artificially shallow due to the presence of erroneous soundings. An approach to address this issue is to use the mean depth instead. However, this may lead to not charting hazardous objects imperative for safe navigation. Within this chapter, approaches to derive depths from the point cloud (in addition to mean and shallowest depths) using the statistical properties of the point cloud were proposed and applied to two different survey areas within the Netherlands which are of importance as they contain critical locations important for shipping. Based on the results, the following conclusions are drawn.

Two issues are found to be of importance for the quality of the resulting estimates for shallowest depth, i.e., the distribution of the soundings in a cell and the MBES measurement uncertainty. Whereas for the approach based on the regression coefficients, a proper distribution of the measurement points within a cell is crucial, the approach of using the mean depth together with the standard deviation requires minimum uncertainties in the depth measurements. For the surveys considered, the distribution of MBES measurements hampered proper estimation of the slopes and thus negatively affected the estimates for shallowest depths based on the regression coefficients. Using the mean is found to counteract the measurement uncertainties, but overestimates the depth for areas with slopes. Using a combination of the mean and standard deviation is found to capture the presence of slopes, while decreasing the influence of measurement uncertainties compared to using the shallowest measured depths. These measurement uncertainties vary with beam angle, depth and survey equipment, and can be predicted using proper modelling. This modelling can be used to select the survey strategy and, potentially a subset of the full point cloud, such that there is minimum variation in the uncertainties over the area.

Another important issue to consider is the effect of the cell size on the grid derived. It was shown that for the flat areas, increasing the cell size results in a shallower depth estimate when using the shallowest measured depth (and consequently a shallower grid is derived). The coarser grid affects the non-flat areas to a larger extent than that of the flat. This can hamper the identification of the morphological features, and hence a realistic cell size based on the depth, angular sector, number of soundings with a ping and the vessel speed is to be chosen.

In addition, it can be concluded that the differences are found to be useful tool for identifying artefacts, but also morphological features, which are not directly observed in the bathymetry map. Especially the morphological features can be of interest, for example, for sediment classification purposes. For this, often a combination of parameters derived from depth measurements and backscatter values are used for discriminating between different sediment types (e.g. [23, 52, 181])

6

7

Conclusion and outlook

Logic will get you from A to B. Imagination will take you everywhere.

Albert Einstein

7.1. Conclusions

This thesis has focused on bringing the insights of the MBES measurement capabilities to a new stage in terms of a reliable and accurate representation of the bottom and a realistic expectation of the associated uncertainties.

It is worthy to revisit the four research objectives stated in Chapter 1 and to assess to what extent they have been fulfilled.

1. **Correct the bathymetric measurements for the errors induced due to inaccurate or insufficient knowledge about the water column sound speed with no *a priori* constraints on bottom topography or additional sound speed measurements;**

   This objective has been met in Chapter 3. The proposed method does not impose constraints on the bottom topography as it exploits the redundancy in the MBES measurements obtained from the overlap of adjacent swaths (equal water depth at the overlapping parts of the adjacent swaths naturally happens when the correct sound speeds are used and is thus not a constraint). It has been shown that even with a simple parametrization of the sound speed profile (constant SSP), the correct bathymetry can be derived from the inversion method. Successful execution of the inversion method was confirmed by the statistically insignificant (95% confidence level) differences between the original depth measurements and those derived after the inversion.

   The SSP inversion method has successfully corrected the bathymetry in areas with existing refraction artefacts and reduced the mean and standard deviation of the derived depths by a factor of around 2.8. Furthermore, it has neither manipulated the existing morphology nor introduced artificial bathymetric features in areas without refraction artefacts. For the areas considered

151

with the assumption of constant SSP, both Differential Evolution (DE) and Gauss-Newton (GN) have given almost identical results with the latter being faster by a factor ranging from 3.3 to 5 (though it is less flexible with regard to varying sound speed parameterizations).

The overlap percentage between the adjacent sailed tracks was found important for a successful application of the inversion method. While for the overlap percentage decreasing from 70% to 35%, the standard deviation of the difference between the original depth measurements and those derived after applying the inversion method only slightly increased, for an overlap less than 35% a more rapid increase was found.

2. **Model and assess the relevance of the bathymetric uncertainties induced due to the use of FM pulse shapes in the framework of the widely used bathymetric uncertainty prediction model of [26, 27], as implemented in AMUST;**

The implications of using Frequency Modulated (FM) pulse types for MBES bathymetric uncertainties has been examined in Chapter 4 by quantifying the induced uncertainties resulting from their use and assessing their relevance for the MBES bathymetric uncertainty predictions. The contribution of the Doppler effect is divided into first-order (effect on beamsteering) and second order (imperfectness of the Doppler-range correction), with the former being independent of the pulse type. The contribution of the Doppler effect to the total bathymetric uncertainty has been found to be significant and dependent on the sea-state (nearly 82% for 'rough' and 68% for 'calm' of the total uncertainty). The total bathymetric uncertainty has been derived from the uncertainty prediction model of [26, 27], as implemented in the *A priori* Multibeam Uncertainty Simulation Tool (AMUST) developed by the Acoustics Group of Delft University of Technology in a close cooperation with RWS. The uncertainty due to the imperfectness of the Doppler-range correction occurs only for the FM pulse shapes and has been found to be much smaller than the contribution of the Doppler effect on beamsteering. Although taking these contributions into account results in a more realistic prediction of the MBES bathymetric uncertainties, detailed information on the transducer motion during transmission and reception and sea-state is required, which might not be always available.

The depth uncertainty induced by the baseline decorrelation is greatly influenced by the shape of the transmitted signal and is not solely a matter of using an FM or a Continuous Wave (CW) pulse shape. For the specifications considered, in general, the depth uncertainty for the former was larger than that of the latter. The results also revealed that depending on the duration of the CW pulses, the effect of a decreased Signal-to-Noise Ratio (SNR) might dominate the depth uncertainty for the outer beams. This means that when choosing the pulse length for a CW signal, a compromise has to be made between the decreased uncertainty due to the baseline decorrelation with decreasing pulse length and the resulting decreased SNR.

3. **Assess the performance of the widely used bathymetric uncertainty prediction model of [26, 27], as implemented in AMUST, using the state-of-the-art MBES system and identify parameters that require modification to obtain a better model-data agreement;**

The comparison between the bathymetric uncertainties derived from modern MBES measurements to those predicted using the uncertainty prediction model of [26, 27], as implemented in AMUST, has been carried out in Chapter 5. The measurements were acquired with three different pulse lengths of 27 µs, 54 µs and 134 µs in water depths of 10 m and 30 m.

To obtain the measured bathymetric uncertainties such that a fair comparison can be made to those modeled, a number of factors have been found of importance. These are the size of the bottom surface patch and the number of phase samples per beam. The size of the surface patch, used for the calculation of the measured bathymetric uncertainty while accounting for the potential presence of the small-scale depth variations, has to be chosen carefully. The optimal size of the surface patch varies with different water depths. As for the number of phase samples, this is used to calculate the contribution of the phase bottom detection method to the depth uncertainty. For the data sets considered, discrepancies were observed between the theoretical and actual number of phase samples resulting in an incorrect predictions of the bathymetric uncertainties in case of using the former.

In general, the magnitude of the bathymetric uncertainties derived from the uncertainty prediction model of [26, 27] are in good agreement with those measured. However, discrepancies have been observed with increasing water depth and for the outer beams. The model tends to underestimate the measured uncertainties for the beams where the amplitude detection was used as the bottom detection technique. As the pulse length increases, the angular range using this detection method increases, and hence an underestimation of the measured uncertainties occurs for a broader angular range.

The most dominant contributor to the depth uncertainty is the echosounder contribution, and hence as a first step toward improving the model, the most recent insights in contributors to the MBES depth uncertainties (i.e., Doppler effect and baseline decorrelation) have been accounted for. The comparison between the situations with and without accounting for these uncertainty sources has shown a decrease in the contribution of the echosunder. The effect on the total bathymetric uncertainty depends also on the magnitude of the Doppler effect (as the observed reduction in the echosounder contribution is counteracted by an increase of the Doppler induced depth uncertainty). This suggest that the good model-data agreement obtained for the situations considered without accounting for these contributions might have been a coincidence as for a different scenario, the two contributor might not counteract each other. Thus, the effect of not accounting for them in the uncertainty prediction model leads to incorrect predictions.

Accounting for the contributions of the Doppler effect and baseline decor-

7

relation improves the performance of the prediction model in capturing the variations of the uncertainty with beam angle. The agreement between the modeled and measured uncertainties for the outer parts of the swath is further improved by accounting for the decreased SNR. Accounting for these new insights improves the performance of the bathymetric uncertainty prediction model. This, however, requires knowledge of additional parameters such as speed of the transducer array at reception and transmission which might not be always available.

4. **Propose methods for gridding the MBES bathymetric measurements to equidistant grids as alternatives to the shallowest measured depth such that safe navigation is not hampered and outliers are rejected simultaneously;**

This objective has been accomplished in Chapter 6. It has been found that the applicability of the approach based on regression coefficients is highly sensitive to the distribution of the measurements. Otherwise, the regression coefficients, derived from ill-distributed soundings, should only be used to determine the depth in the vicinity of the soundings. Consequently, employing this approach is not encouraged.

Another issue requiring careful attention, particularly when using the shallowest depth, is the uncertainty of the depth measurements. It has been shown that for flat areas these uncertainties result in depths that are shallower than the actual shallowest depth and that this can be counteracted when using the mean depth. Considering the factors affecting the MBES uncertainties, the magnitudes with which the uncertainties affect the mapped depths are location and survey dependent. These uncertainties can be predicted in advance using a proper modeling, **objective 1**. The modeling can be used to select a survey strategy or area within the full point cloud with minimum variation in the uncertainties. It has been confirmed that for non-flat areas, an additional contribution is due to the presence of slopes and using the mean depth can result in undesirable situations as it overestimates the depth, i.e., getting deeper. This issue has been counteracted by subtracting the standard deviation of the soundings for non-flat areas. However, for flat areas this has been led to underestimation of the actual depth. This means that when deciding upon whether or not to use the standard deviation, a compromise has to be made.

It has been also shown that, although increasing the size of the grid cells leads to more computationally efficient processing, it affects the non-flat areas such that the identification of the morphological features is hampered. A realistic grid cell size based on the depth, angular sector, number of soundings and vessel speed is to be chosen.

7.2. Outlook

After reviewing the results and statements of this thesis, some recommendations for future work can be made:

- As shown in Chapter 3 from the application of the sound speed inversion method to two different survey areas, a simple representation of the sound speed in the water column (i.e., constant) has been able to retrieve the original bathymetry and correct the existing refraction artefacts. It is indeed interesting to assess the validity of this assumption in more challenging environments, for example in areas with water mass exchanges between ocean basins. The outcome of this assessment determines whether there is a need to modify the inversion algorithm to account for complex representations of the sound speed profile, e.g., using Empirical Orthogonal Functions;

- The SSP inversion method proposed in Chapter 3 is sensitive to vertical offset between the data and tries to solve for it, even if the vertical offset is due to the errors in the vertical referencing (i.e., heave artefacts or GNSS). Therefore, it has been recommended to carefully perform the vertical referencing prior to applying the inversion method. Incorporating a nuisance parameter for a height shift can assist the method to discard these types of errors or to provide an approach to simultaneously address them;

- As pointed out in Chapter 3, GN based inversion method is faster than DE by a factor ranging from 3.3 to 5. To further increase the computational efficiency of the inversion method, one can select a subset of segments, for example, cross line intersections, beginning and end of a sailed track or some distance interval along a sailed track. The feasibility of this approach, however, depends on the variations of the sound speed in the survey area and the performance of the inversion method compared to the results using all segments;

- In Chapter 4, a comparison has been made between the modeled and measured effect of switching from CW to FM pulse shapes. This means that the uncertainties induced by other sources were assumed equal for both pulse types. It is recommended to carry out a survey in a calm sea state in an area with the least variations in the morphology as possible to compare the modeled and measured uncertainties in an absolute sense;

- Considering the dependency of the depth uncertainty induced by the Doppler effect to the sea state, it is beneficial to acquire data sets corresponding to sea states ranging from calm to rough to have a comprehensive assessment of its effect. This can potentially obviate the need for the transducer array speeds at reception and transmission for every survey as the acquired data can be used to model the depth uncertainty induced by the Doppler effect as a function of sea state;

7

- To further improve the depth uncertainty prediction model, the bottom detection model developed in [69] can be used. As an example, the term quantifying the bathymetric uncertainty due to the amplitude bottom detection technique can be empirically modified using the corresponding uncertainties derived from the bottom detection model;

- The contribution of the sound speed uncertainty to the derived depth was modeled based on a two-layered representation of the sound speed profile assuming that the thickness of both layers is the same. It is recommended to assess the effect of this contributor through the Monte Carlo approach with the advantage of enabling the uncertainty estimation without the need for the exact uncertainty model. The Monte Carlo approach can be implemented by repeated random sampling of the sound speed profile in the water column and calculating the corresponding bathymetry uncertainty. Based on the computational complexity of the Monte Carlo approach and the differences between the resulting uncertainties and those predicted assuming a two-layered representation of the sound speed profile, a decision can be made regarding modification of the uncertainty prediction model;

- The bathymetry gridding methods proposed in Chapter 6 assume a fixed grid cell size. The minimum cell size was chosen based on the water depth, beamspacing mode, angular sector and number of beams. Another approach is to consider a multi-resolution grid capturing the variability of the beam footprint and density over the depth. This enables data compression as proposed by [172];

7

- Assess the applicability of the theory of polynomial spline approximation for obtaining a smooth and continuous surface by relating the grid cells together [174]. A spline function is a piecewise polynomial interpolation such that these polynomials are joined together under some continuity conditions. However, this should be carried out with care as it is susceptible to introducing unwanted depth variations.

A

Recalculating launch Angle and azimuth for a new estimate of the sound speed

Traditionally, repointing a beam to account for an update of the sound speed at the transducer is done by correcting the raw steering angles reported by the transducer followed by recalculating the beam launch angle (depression angle) β in Fig. 3.1, see [114, 115]. However, in this thesis the refraction correction is applied to the launch angle, without having to recalculate the steering angle θ_s which improves the computational efficiency. This appendix elaborates on this subject. Consider the situation where the beamsteering is based on the erroneous sound speed (c_m), but that the true sound speed (c) becomes available afterwards. Then the beam vector has to be re-pointed.

Before proceeding, it is necessary to introduce the coordinate systems and rotations used. For the vessel coordinate system, we consider a right-handed system with the positive X and Y axes pointing towards the starboard and bow, respectively. Consequently, the Z points towards up. X, Y and Z belong to the vessel and are thus not shown in Fig. 3.1.

For the navigation frame, shown in Fig. 3.1 with subscript N, again a right-handed coordinate system considered with the positive X_N, Y_N and Z_N pointing toward east, north and up, respectively.

For rotations, heading h, pitch P and roll R are considered to be clockwise or left-handed rotations about the Z axis, counter clockwise or right-handed rotation about the X axis and counter clockwise rotations about the Y axis, respectively. Tait-Bryant ordering of angle rotation is used, i.e. h, P, R. These rotations are both valid in the vessel and navigation frames.

In general, MBES measurements are stored such that the beam vector (dashed line in Fig. 3.1) is reported relative to the navigation frame. Therefore, when accounting for an updated sound speed profile, i.e., a modified value for β, one needs to translate the beam vector from the navigation frame to the transducer frame. For this, two rotation matrices are needed. One for the vessel motion R_{NV} translating the coordinates from the vessel frame (V) to navigation frame (N) using heading,

roll and pitch angles of the vessel relative to the navigation frame measured by the motion sensor. The second rotation required is for the transducer mounting angles (R_{VT}) which translates from the transducer frame (T) to vessel frame (V) using the mounting angles of the MBES receiving array. The rotation matrix from the transducer to the navigation frame is thus derived from the product of these rotation matrices ($R_{NT} = R_{NV}R_{VT}$).

Given the correct launch angle β and azimuth (Az), a beam unit vector is defined in the navigation frame ($\vec{u}_N$) as

$$\begin{aligned}
\vec{u}_N &= \begin{bmatrix} X & Y & Z \end{bmatrix}_N^T \\
&= \begin{bmatrix} \sin \text{Az} \cos \beta & \cos \text{Az} \cos \beta & -\sin \beta \end{bmatrix}^T,
\end{aligned} \tag{A.1}$$

where $[X, Y, Z]_N$ are the components of the beam unit vector in the navigation frame. Eq. (A.1) can be also written for the erroneous sound speed c_m (inducing errors in the launch angle β_m and azimuth Az_m) and is referred to $\vec{u}_{m,N}$. The beam unit vector in the navigation frame is then rotated into the transducer frame $\vec{u}_T$ using $R_{NT}^T \vec{u}_N$. Shown in Fig. A.1 are the components of $\vec{u}_T$ in the transducer frame assuming a) erroneous, and b) correct sound speeds where θ_m and θ_s are the erroneous and correct beam vector angles relative to the transducer frame's normal respectively, i.e., erroneous and correct beam steering angles.
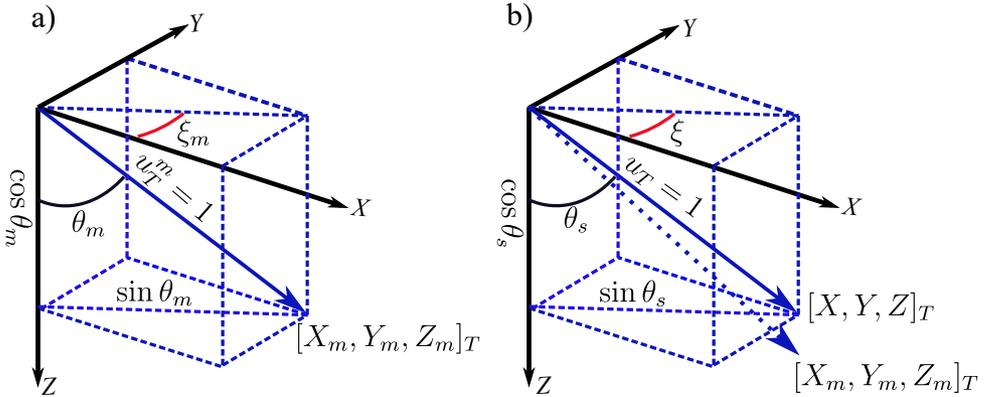
Figure A.1: Beam vector in transducer frame (T) for erroneous a) and correct b) sound speeds.

Whereas in general β is calculated from θ_s, here a different approach is taken as described below. Snell's law of refraction for the erroneous and correct sound speeds states

$$\frac{\sin \theta_m}{\sin \theta_s} = \frac{c_m}{c}. \tag{A.2}$$

This can be rearranged to give the steering angle as

$$\theta_s = \sin^{-1}\left(a_c \sin \theta_m\right), \tag{A.3}$$

where $a_c = \frac{c}{c_m}$ is the ratio of correct to erroneous sound speeds. Considering $\sin \theta_s$ (and $\sin \theta_m$) as the hypotenuse of the right-angled triangle with the catheti legs X_T (or $X_{m,T}$) and Y_T (or $Y_{m,T}$) one can write

$$\sin \theta_m = \sqrt{X_{m,T}^2 + Y_{m,T}^2} \,, \tag{A.4a}$$

$$\sin \theta_s = \sqrt{X_T^2 + Y_T^2} \,. \tag{A.4b}$$

Substituting θ_m and θ_s from Eq. (A.4) in Eq. (A.3) gives

$$\overbrace{\sin^{-1}\left(\sqrt{X_T^2 + Y_T^2}\right)}^{\theta_s} = \sin^{-1}\left(a_c \sin\left[\overbrace{\sin^{-1}\left(\sqrt{X_{m,T}^2 + Y_{m,T}^2}\right)}^{\theta_m}\right]\right) \,, \tag{A.5a}$$

$$\sqrt{X_T^2 + Y_T^2} = a_c \sqrt{X_{m,T}^2 + Y_{m,T}^2} \,. \tag{A.5b}$$

Considering the beam vector in the transducer frame as unitary gives the constraints

$$1 = u_T^2 = X_T^2 + Y_T^2 + Z_T^2 \,, \tag{A.6a}$$
$$1 = u_{m,T}^2 = X_{m,T}^2 + Y_{m,T}^2 + Z_{m,T}^2 \,. \tag{A.6b}$$

Substituting Eq. (A.5) in the expression for u_T^2 in Eq. (A.6)a gives the third component of the beam vector for the correct sound speed (Z_T) as

$$|Z_T| = \sqrt{1 - a_c^2(X_{m,T}^2 + Y_{m,T}^2)} \,, \tag{A.7a}$$

$$= \sqrt{1 - a_c^2(1 - Z_{m,T}^2)} \,. \tag{A.7b}$$

As the refraction only changes the beam vector in the plane formed by the Z-axis and the beam vector, the orientation of the projected beam vector onto the XY-plane of the transducer frame remains unchanged for both erroneous and correct sound speeds ($\xi = \xi_m$ in Fig. A.1). This results in the following expressions for X_T and Y_T

$$X_T = a_c X_{m,T} \,, \tag{A.8a}$$
$$Y_T = a_c Y_{m,T} \,. \tag{A.8b}$$

Eqs. (A.7) and (A.8) give the three components of the unit beam vector in the transducer frame for the correct sound speed ($\vec{u}_T$). This vector is then rotated back into the navigation frame using R_{NT} and the correct launch angle and azimuth are derived as

$$\beta = -\sin^{-1}(Z_N) \,, \tag{A.9a}$$

$$Az = -\tan^{-1}\left(\frac{X_N}{Y_N}\right) \,. \tag{A.9b}$$

A

where X_N, Y_N and Z_N are the components of the beam unit vector in the navigation frame corresponding to the actual (correct) sound speed, see Eq. (A.1).

B

Differential Evolution optimization method

Differential Evolution (DE) introduced by [110] is a technique for optimizing a problem by iteratively improving the candidate solution with respect to a given measure of quality. DE can be classified as a metaheuristic optimization technique used for solving very general classes of problems and makes few or no assumptions about the optimization problem under investigation, and thus can search a very large space of candidate solutions. However, the drawback of this metaheuristic method is that it cannot guarantee convergence to an optimal solution.

DE is a variant of Genetic Algorithm (GN) and starts with an initial population of randomly chosen parameter value combination, making the process stochastic, each containing trial values for unknown parameters. The parameter value combinations are improved each iteration (generation) over a maximum amount of $N_{G_{\mathrm{DE}}}$ successive generations of constant population size q_{DE}. At each generation l, members of the partner population are constructed from the original population members $\boldsymbol{m}_{l,i}$ as

$$\boldsymbol{p}_{l,i} = \boldsymbol{m}_{l,r_1} + F_{\mathrm{DE}}(\boldsymbol{m}_{l,r_2} - \boldsymbol{m}_{l,r_3}) , \tag{B.1}$$

with $i = 1, \dots, q_{\mathrm{DE}}$. Indices $r_1, r_2, r_3 \in [1, 2, \dots, q_{\mathrm{DE}}]$ are randomely chosen integers, differing from each other. $\boldsymbol{p}_{l,i}$ is thus the partner for $\boldsymbol{m}_{l,i}$ with $\boldsymbol{m}_{l,r_1}$, $\boldsymbol{m}_{l,r_2}$ and $\boldsymbol{m}_{l,r_3}$ being three different parameter value combinations. F_{DE} is a scalar multiplication factor between 0 and 1. A higher value of F_{DE} indicates an increased difference between original parameter vector $\boldsymbol{m}_{l,i}$ and those contained in the partner population $\boldsymbol{p}_{l,i}$. On the other hand, small F_{DE} value results in parameters in succeeding generation that differ slightly from those in previous generations, and thus leads to a local search and prevents exploration of the search space.

The descendant is obtained by applying crossover to $\boldsymbol{p}_{l,i}$ and $\boldsymbol{m}_{l,i}$ with a probability of $p_{c_{\mathrm{DE}}}$. For each parameter j of $\boldsymbol{de}_{l,i}$ one gets

$$de_{l,i}^j = \begin{cases} p_{l,i}^j & \text{if } \mathcal{U}(0,1)^j \leq p_{c_{\mathrm{DE}}} \\ m_{l,i}^j & \text{if } \mathcal{U}(0,1)^j > p_{c_{\mathrm{DE}}} \end{cases} , \tag{B.2}$$

where $p_{l,i}^j$, $m_{l,i}^j$ and $de_{l,i}^j$ represent the jth component, i.e., a design variable in the

vectors $\boldsymbol{p}_{l,i}$, $\boldsymbol{m}_{l,i}$ and $\boldsymbol{de}_{l,i}$, respectively. The symbol $\mathcal{U}(0,1)^j$ represents the jth randomized number in the uniform distribution between 0 and 1 and $p_{c_{\text{DE}}} \in [0,1]$ is the crossover probability. A higher value of $p_{c_{\text{DE}}}$ means that more values are replaced by those of the partner population, while a low value of $p_{c_{\text{DE}}}$ results in generations which differ only slightly regardless of values of F_{DE}.

The population of the next generation $l+1$ is created from the previous generation l by replacing $\boldsymbol{m}_{l,i}$ with $\boldsymbol{de}_{l,i}$ only if the latter yields to a smaller value for the objective function G_{DE}.

$$\boldsymbol{m}_{l+1,i} = \begin{cases} \boldsymbol{de}_{l,i} & \text{if } G_{\text{DE}}(\boldsymbol{de}_{l,i}) < G_{\text{DE}}(\boldsymbol{m}_{l,i}) \\ \boldsymbol{m}_{l,i} & \text{if } G_{\text{DE}}(\boldsymbol{de}_{l,i}) \geq G_{\text{DE}}(\boldsymbol{m}_{l,i}) \end{cases}. \tag{B.3}$$

Doing this procedure for all members i in the population, the next generation $l+1$ is created. The optimization is carried out until l reaches $N_{G_{\text{DE}}}$. For decreasing energy values a member would converge to the correct parameter value. The diagram showing the workflow of DE algorithm is presented in Fig. B.1.
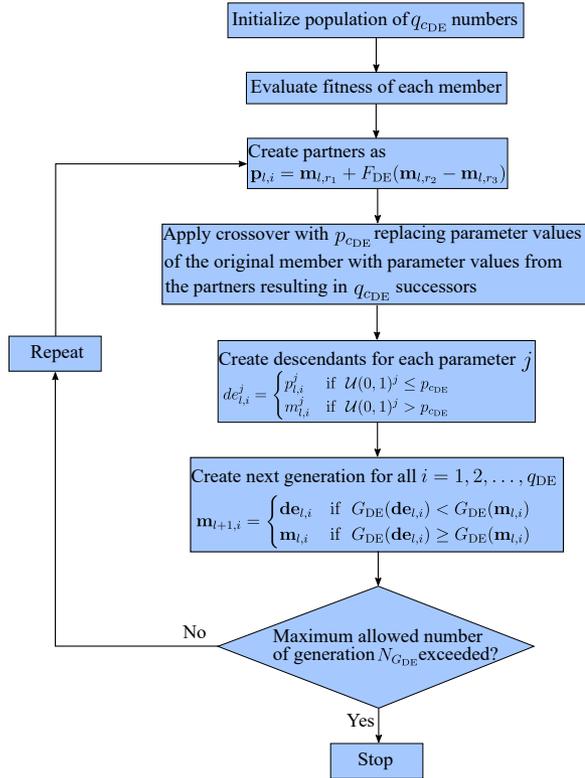
Figure B.1: Flowchart of the DE algorithm.

References

[1] A. K. Rutledge and D. S. Leonard, *Role of multibeam sonar in oil and gas exploration and development,* in *Offshore Technology Conference* (Houston, Texas, USA, 2001) pp. 1–12.

[2] T. J. Anderson, C. Syms, D. A. Roberts, and D. F. Howard, *Multi-scale fish-habitat associations and the use of habitat surrogates to predict the organisation and abundance of deep-water fish assemblages,* Journal of Experimental Marine Biology and Ecology **379**, 34–42 (2009).

[3] R. A. Pickrill and B. J. Todd, *The multiple roles of acoustic mapping in integrated ocean management, Canadian Atlantic continental margin,* Ocean & Coastal Management **46**, 601–614 (2003).

[4] L. J. Poppe, M. L. DiGiacomo-Cohen, S. M. Smith, H. F. Stewart, and N. A. Forfinski, *Seafloor character and sedimentary processes in eastern Long Island Sound and western Block Island Sound,* Geo-Marine Letters **26**, 59–68 (2006).

[5] L. A. Mayer, *Frontiers in seafloor mapping and visualization,* Marine Geophysical Researches **27**, 7–17 (2006).

[6] L. A. Mayer, M. Jakobsson, G. Allen, B. Dorschel, R. Falconer, V. Ferrini, G. Lamarche, H. Snaith, and P. Weatherall, *The Nippon Foundation–GEBCO seabed 2030 project: the quest to see the world's oceans completely mapped by 2030,* Geosciences **8**, 63 (2018).

[7] H. Medwin and C. S. Clay, *Fundamentals of Acoustical Oceanography* (Elsevier Inc., 1998).

[8] D. R. Lyzenga, *Remote sensing of bottom reflectance and water attenuation parameters in shallow water using aircraft and Landsat data,* International Journal of Remote Sensing **2**, 71–82 (1981).

[9] W. H. F. Smith and D. T. Sandwell, *Bathymetric prediction from dense satellite altimetry and sparse shipboard bathymetry,* Journal of Geophysical Research: Solid Earth **99**, 21803–21824 (1994).

[10] I. S. Bogie, *Conduction and magnetic signalling in the sea a background review,* Radio and Electronic Engineer **42**, 447–452 (1972).

[11] X. Lurton, *An Introduction to Underwater Acoustics: Principles and Applications*, 2nd ed. (Springer-Verlag Berlin Heidelberg, 2010).

[12] P. Blondel, *The Handbook of Sidescan Sonar* (Springer-Verlag Berlin Heidelberg, 2009).

[13] P. N. Denbigh, *Swath bathymetry: principles of operation and an analysis of errors,* IEEE Journal of Oceanic Engineering **14**, 289–298 (1989).

[14] J. G. Blackinton, *Bathymetric resolution, precision and accuracy considerations for swath bathymetry mapping sonar systems,* in *OCEANS 91 Proceedings*, Vol. 1 (Honolulu, Hawaii, USA, 2001) pp. 550–557.

[15] P. N. Denbigh, *Signal processing strategies for a bathymetric sidescan sonar,* IEEE Journal of Oceanic Engineering **19**, 382–390 (1994).

[16] X. Lurton, *Swath bathymetry using phase difference: theoretical analysis of acoustical measurement precision,* IEEE Journal of Oceanic Engineering **25**, 351–363 (2000).

[17] A. R. Amiri-Simkooei, M. Snellen, and D. G. Simons, *Principal component analysis of single-beam echo-sounder signal features for seafloor classification,* IEEE Journal of Oceanic Engineering **36**, 259–272 (2011).

[18] M. Snellen, K. Siemes, and D. G. Simons, *Model-based sediment classification using single-beam echosounder signals,* The Journal of the Acoustical Society of America **129**, 2878–2888 (2011).

[19] E. J. Eidem and K. Landmark, *Acoustic seabed classification using QTC IMPACT on single-beam echo sounder data from the Norwegian Channel, northern North Sea,* Continental Shelf Research **68**, 1–14 (2013).

[20] T. Mulder, H. Hüneke, and A. J. van Loon, *Chapter 1 - Progress in Deep-Sea Sedimentology,* in *Deep-Sea Sediments*, Vol. 63 (Elsevier, 2011) pp. 1–24.

[21] D. D. Sternlicht and C. P. de Moustier, *Remote sensing of sediment characteristics by optimized echo-envelope matching,* The Journal of the Acoustical Society of America **114**, 2727–2743 (2003).

[22] L. Fonseca, C. Brown, B. Calder, L. A. Mayer, and Y. Rzhanov, *Angular range analysis of acoustic themes from Stanton Banks Ireland: a link between visual interpretation and multibeam echosounder angular signatures,* Applied Acoustics **70**, 1298–1304 (2009).

[23] D. Eleftherakis, A. R. Amiri-Simkooei, M. Snellen, and D. G. Simons, *Improving riverbed sediment classification using backscatter and depth residual features of multi-beam echo-sounder systems,* The Journal of the Acoustical Society of America **131**, 3710–3725 (2012).

[24] M. Snellen, T. C. Gaida, L. Koop, E. Alevizos, and D. G. Simons, *Performance of multibeam echosounder backscatter-based classification for monitoring sediment distributions using multitemporal large-scale ocean data sets,* IEEE Journal of Oceanic Engineering **44**, 142–155 (2018).

[25] C. P. de Moustier, *Signal processing for swath bathymetry and concurrent seafloor acoustic imaging,* in *Acoustic Signal Processing for Ocean Exploration*, edited by J. M. F. Moura and I. M. G. Lourtie (Springer Netherlands, Dordrecht, 1993) pp. 329–354.

[26] R. Hare, *Depth and position error budgets for multibeam echosounding,* International Hydrographic Review **LXXII**, 37–69 (1995).

[27] R. Hare, *Error Budget Analysis for US Naval Oceanographic Office (NAVOCEANO) Hydrographic Survey Systems*, Tech. Rep. (Hydrographic Science Research Center (HSRC), Mississippi, USA, 2001).

[28] B. R. Calder and L. A. Mayer, *Automatic processing of high-rate, high-density multibeam echosounder data,* Geochemistry, Geophysics, Geosystems **4** (2003).

[29] X. Lurton and J.-M. Augustin, *A measurement quality factor for swath bathymetry sounders,* IEEE Journal of Oceanic Engineering **35**, 852–862 (2010).

[30] V. Renard and P. Allenou, *SEA BEAM multi-beam echo sounding in "Jean Charcot": description, evaluation and first results,* International Hydrographic Review **LVI**, 35–67 (1979).

[31] B. Volberg and T. Meurling, *Evolution and future of multibeam echosounder technology,* in *2007 Symposium on Underwater Technology and Workshop on Scientific Use of Submarine Cables and Related Technologies* (Tokyo, Japan, 2007) pp. 147–155.

[32] D. Mann, *Multi-beam echo sounders: new technology, new capabilities and new Markets,* Hydro International Magazine **March**, 13–17 (2013).

[33] J. E. Hughes Clarke, *Multispectral acoustic backscatter from multibeam, improved classification potential,* in *United States Hydrographic Conference* (National Harbor, Maryland, USA, 2015) pp. 1–18.

[34] T. C. Gaida, T. A. Tengku Ali, M. Snellen, A. R. Amiri-Simkooei, T. A. G. P. van Dijk, and D. G. Simons, *A multispectral bayesian classification method for increased acoustic discrimination of seabed sediments using multi-frequency multibeam backscatter data,* Geosciences **8**, 455 (2018).

[35] G. Wübbena, A. Bagge, and M. Schmitz, *Network-based techniques for RTK applications,* in *Proceedings of the Japan Institute of Navigation, GPS Symposium* (Tokyo, Japan, 2001) pp. 1–14.

[36] G. Seeber, *Satellite geodesy: foundations, methods, and applications*, 2nd ed. (Walter de Gruyter, 2003).

[37] iXblue, Phins subsea: FOG-based high-performance inertial navigation system [Accessed in March 2020].

[38] iXblue, *Octans subsea: high-performance subsea gyrocompass and motion sensor* [Accessed in March 2020].

[39] D. R. Herlihy, B. F. Hillard, and T. D. Rulon, *National oceanic and atmospheric administration SEA BEAM system "patch test",* International Hydrographic Review **LXVI**, 119–139 (1989).

[40] J. E. Hughes Clarke, *Dynamic motion residuals in swath sonar data: ironing out the creases,* International Hydrogrphic Review **4**, 6–23 (2003).

[41] E. Kammerer, *New method for the removal of refraction artifacts in multi-beam echosounder systems,* Ph.D. thesis, University of New Brunswick, Fredericton, Canada (2000).

[42] J. Ding, X. Zhou, and Q. Tang, *A method for the removal of ray refraction effects in multibeam echo sounder systems,* Journal of Ocean University of China **7**, 233–236 (2008).

[43] A. Furlong, B. Beanlands, and M. Chin-Yee, *Moving vessel profiler MVP real time near vertical data profiles at 12 knots,* in *OCEANS '97. MTS/IEEE*, Vol. 1 (Halifax, NS, Canada, 1997) pp. 229–234.

[44] D. L. Rudnick and J. Klinke, *The underway Conductivity–Temperature–Depth Instrument,* Journal of Atmospheric and Oceanic Technology **24**, 1910–1923 (2007).

[45] J. D. Beaudoin, *Real-time monitoring of uncertainty due to refraction in multibeam echo sounding,* The Hydrographic Journal **134**, 9–15 (2010).

[46] J. R. Klauder, A. C. Price, S. Darlington, and W. J. Albersheim, *The theory and design of chirp radars,* The Bell System Technical Journal **39**, 745–808 (1960).

[47] J. D. Beaudoin, P. D. Johnson, X. Lurton, and J.-M. Augustin, *R/V Falkor Multibeam Echosounder System Review,* Tech. Rep. (Center for Coastal and Ocean Mapping/NOAA-UNH Joint Hydrographic Center, Durham, New Hampshire, USA, 2012).

[48] J. D. Beaudoin, P. D. Johnson, and A. F. Flinders, *R/V Falkor Multibeam Echosounder System Review,* Tech. Rep. 12-001 (Center for Coastal and Ocean Mapping/NOAA-UNH Joint Hydrographic Center, Durham, New Hampshire, USA, 2014).

[49] P. Vincent, *Modulated signal impact on multibeam echosounder bathymetry,* Ph.D. thesis, Télécom Bretagne Sous En habilitation conjointe avec ÍUniversité de Rennes 1, Rennes, France (2013).

[50] P. Vincent, F. Maussang, X. Lurton, C. Sintès, and R. Garello, *Bathymetry degradation causes for frequency modulated multibeam echo sounders,* in *2012 Oceans* (Hampton Roads, Virginia, USA, 2012) pp. 1–5.

[51] P. Vincent, F. Maussang, X. Lurton, C. Sintes, and R. Garello, *Multibeam interferometric sounding quality for FM signals: modelling and comparison with field data,* in *2013 MTS/IEEE OCEANS* (Bergen, Norway, 2013) pp. 1–4.

[52] D. Eleftherakis, M. Snellen, A. R. Amiri-Simkooei, D. G. Simons, and K. Siemes, *Observations regarding coarse sediment classification based on multi-beam echo-sounder's backscatter strength and depth residuals in Dutch rivers,* The Journal of the Acoustical Society of America **135**, 3305–3315 (2014).

[53] V. Lucieer, Z. Huang, and J. Siwabessy, *Analyzing uncertainty in multi-beam bathymetric data and the impact on derived seafloor attributes,* Marine Geodesy **39**, 32–52 (2016).

[54] T. H. Mohammadloo, M. Snellen, and D. G. Simons, *Multi-beam echo-sounder bathymetric measurements: implications of using frequency modulated pulses,* The Journal of the Acoustical Society of America **144**, 842–860 (2018).

[55] B. R. Calder and L. A. Mayer, *Robust automatic multi-beam bathymetric processing,* in *U.S. Hydrographic Conference* (Norfolk, Virginia, USA, 2001) pp. 1–20.

[56] B. R. Calder, *Distribution-free, variable resolution depth estimation with composite uncertainty,* in *U.S. Hydrographic Conference* (New Orleans, Louisiana, USA, 2013) pp. 1–8.

[57] G. Brouns, A. De Wulf, and D. Constales, *Multibeam data processing: adding and deleting vertices in a Delaunay triangulation,* Hydrographic Journal , 3–9 (2001).

[58] G. Brouns, A. De Wulf, and D. Constales, *Delaunay triangulation algorithms useful for multibeam echosounding,* Journal of Surveying Engineering **129**, 79–84 (2003).

[59] D. G. Tucker and B. K. Gazey, *Applied Underwater Acoustics* (Pergamon Press, 1967).

[60] M. A. Ainslie, *Principles of Sonar Performance Modeling* (Springer-Verlag Berlin Heidelberg, 2010).

[61] R. E. Francois and G. R. Garrison, *Sound absorption based on ocean measurements: part I: pure water and magnesium sulfate contributions,* The Journal of the Acoustical Society of America **72**, 896–907 (1982).

[62] R. E. Francois and G. R. Garrison, *Sound absorption based on ocean measurements: part II: Boric acid contribution and equation for total absorption,* The Journal of the Acoustical Society of America **72**, 1879–1890 (1982).

[63] W. S. Burdic, *Underwater Acoustic System Analysis*, 2nd ed. (Englewood Cliffs, N.J., Prentice-Hall, 1991).

[64] H. Medwin, *Speed of sound in water: a simple equation for realistic parameters,* The Journal of the Acoustical Society of America **58**, 1318–1319 (1975).

[65] E. L. Hamilton, *Compressional-wave attenuation in marine sediments,* Geophysics **37**, 620–646 (1972).

[66] *APL-UW High-Frequency Ocean Environmental Acoustic Models Handbook*, Tech. Rep. APL-UW TR9407 (Applied Physics Laboratory, University of Washington, Seattle, Washington, USA, 1994).

[67] D. R. Jackson and K. B. Briggs, *High-frequency bottom backscattering: roughness versus sediment volume scattering,* The Journal of the Acoustical Society of America **92**, 962–977 (1992).

[68] K. L. Williams, D. R. Jackson, D. Tang, K. B. Briggs, and E. I. Thorsos, *Acoustic backscattering from a sand and a sand/mud environment: experiments and data/model comparisons,* IEEE Journal of Oceanic Engineering **34**, 388–398 (2009).

[69] T. C. Gaida, T. A. G. P. van Dijk, M. Snellen, T. Vermaas, C. Mesdag, and D. G. Simons, *Monitoring underwater nourishments using multibeam bathymetric and backscatter time series,* Coastal Engineering **158**, 103666 (2020).

[70] P. D. Mourad and D. R. Jackson, *High frequency sonar equation models for bottom backscatter and forward loss,* in *Proceedings OCEANS '89* (Seattle, Washington, USA, 1989) pp. 1168–1175.

[71] R. G. Urick, *Principles of Underwater sound*, 3rd ed. (Peninsula Publishing, 1983).

[72] F. B. Jensen, W. A. Kuperman, M. B. Porter, and H. Schmidt, *Wave Propagation Theory,* in *Computational Ocean Acoustics* (Springer New York, 2011) pp. 65–153.

[73] J. C. Novarini and J. W. Caruther, *A simplified approach to backscattering from a rough seafloor with sediment inhomogeneities,* IEEE Journal of Oceanic Engineering **23**, 157–166 (1998).

[74] D. R. Jackson, D. P. Winebrenner, and A. Ishimaru, *Application of the composite roughness model to high-frequency bottom backscattering,* The Journal of the Acoustical Society of America **79**, 1410–1422 (1986).

[75] R. Yang, H. Li, S. Li, P. Zhang, L. Tan, X. Gao, and X. Kang, *Linear Frequency Modulation Pulse Signal,* in *High-Resolution Microwave Imaging* (Springer Singapore, 2018) pp. 83–118.

[76] T. C. Gaida, *Acoustic mapping and monitoring of the seabed: from single frequency to multispectral multibeam backscatter*, Ph.D. thesis, Delft University of Technology, Delft, The Netherlands (2020).

[77] Kongsberg Maritime, Sector coverage and beam spacing modes for multibeam echosounders [Accessed in March 2020].

[78] Y. Ladroit, X. Lurton, C. Sintès, J.-M. Augustin, and R. Garello, *Definition and application of a quality estimator for multibeam echosounders,* in *2012 Oceans* (Yeosu, South Korea, 2012) pp. 1–7.

[79] X. Lurton, *Theoretical modelling of acoustical measurement accuracy for swath bathymetric sonars,* International Hydrographic Review **4**, 17–30 (2003).

[80] J. E. Hughes Clarke, L. A. Mayer, and D. E. Wells, *Shallow-water imaging multibeam sonars: a new tool for investigating seafloor processes in the coastal zone and on the continental shelf,* Marine Geophysical Researches **18**, 607–629 (1996).

[81] V. E. Kostylev, B. J. Todd, G. B. J. Fader, R. C. Courtney, G. D. M. Cameron, and R. A. Pickrill, *Benthic habitat mapping on the Scotian Shelf based on multibeam bathymetry, surficial geology and sea floor photographs,* Marine Ecology Progress Series **219**, 121–137 (2001).

[82] J. J. Daniell, P. T. Harris, M. G. Hughes, M. Hemer, and A. Heap, *The potential impact of bedform migration on seagrass communities in Torres Strait, northern Australia,* Continental Shelf Research **28**, 2188–2202 (2008).

[83] D. G. Simons and M. Snellen, *A Bayesian approach to seafloor classification using multi-beam echo-sounder backscatter data,* Applied Acoustics **70**, 1258–1268 (2009).

[84] T. H. Mohammadloo, M. Snellen, A. R. Amiri-Simkooei, and D. G. Simons, *Comparing modeled and measured bathymetric uncertainties: effect of Doppler and baseline decorrelation,* in *OCEANS 2019* (Marseille, France, 2019) pp. 1–8.

[85] A. D. Hiroji, *Extracting sonar relative beam patterns for Multi-Sector Multibeam sonar*, M.S. thesis, Department of Geodesy and Geomatics Engineering, University of New Brunswick, Fredericton, Canada (2016).

[86] D. C. Slobbe, R. Klees, M. Verlaan, L. L. Dorst, and H. Gerritsen, *Lowest astronomical tide in the North Sea derived from a vertically referenced shallow water model, and an assessment of its suggested sense of safety,* Marine Geodesy **36**, 31–71 (2013).

[87] D. C. Slobbe, R. Klees, and B. C. Gunter, *Realization of a consistent set of vertical reference surfaces in coastal areas,* Journal of Geodesy **88**, 601–615 (2014).

[88] QPS, *How to Height, Tide and RTK* [Accessed in March 2020].

[89] D. R. Jackson and M. D. Richardson, *High-Frequency Seafloor Acoustics* (Springer-Verlag New York, 2006).

[90] J.-M. Augustin and X. Lurton, *Image amplitude calibration and processing for seafloor mapping sonars,* in *Europe Oceans*, Vol. 1 (Brest, France, 2005) pp. 698–701.

[91] A. C. G. Schimel, J. D. Beaudoin, I. M. Parnum, T. Le Bas, V. Schmidt, G. Keith, and D. Ierodiaconou, *Multibeam sonar backscatter data processing,* Marine Geophysical Research **39**, 121–137 (2018).

[92] A. R. Amiri-Simkooei, M. Snellen, and D. G. Simons, *Riverbed sediment classification using multi-beam echo-sounder backscatter data,* The Journal of the Acoustical Society of America **126**, 1724–1738 (2009).

[93] T. H. Mohammadloo, M. Snellen, W. Renoud, J. D. Beaudoin, and D. G. Simons, *Correcting multibeam echosounder bathymetric measurements for errors induced by inaccurate water column sound speeds,* IEEE Access **7**, 122052–122068 (2019).

[94] J. D. Beaudoin, W. Renoud, T. H. Mohammadloo, and M. Snellen, *Automated correction of refraction residuals,* in *Hydro18 Conference and Trade Exhibition* (Sydney, Australia, 2018) pp. 1–15.

[95] L. Hellequin, J.-M. Boucher, and X. Lurton, *Processing of high-frequency multibeam echo sounder data for seafloor characterization,* IEEE Journal of Oceanic Engineering **28**, 78–89 (2003).

[96] D. F. Dinn, B. D. Loncarevic, and G. Costello, *The effect of sound velocity errors on multi-beam sonar depth accuracy,* in *'Challenges of Our Changing Global Environment'. Conference Proceedings. OCEANS '95 MTS/IEEE*, Vol. 2 (San Diego, California, USA, 1995) pp. 1001–1010.

[97] D. S. Cartwright and J. E. Hughes Clarke, *Multibeam surveys of the Frazer River delta, coping with an extreme refraction environment,* in *Proceedings of the Canadian Hydrographic Conference* (Montreal, Canada, 2002) pp. 1–23.

[98] W. J. Capell, *Determination of sound velocity profile errors using multibeam data,* in *Oceans '99. MTS/IEEE. Riding the Crest into the 21st Century*, Vol. 3 (Seattle, Washington, USA, 1999) pp. 1144–1148.

[99] J. D. Beaudoin, B. Calder, J. Hiebert, and G. Imahori, *Estimation of sounding uncertainty from measurements of water mass variability,* International Hydrographic Review **2**, 20–38 (2009).

[100] G. Masetti, J. G. Kelley, P. Johnson, and J. D. Beaudoin, *A ray-tracing uncertainty estimation tool for ocean mapping,* IEEE Access **6**, 2136–2144 (2018).

[101] X. Geng and A. Zielinski, *Precise multibeam acoustic bathymetry,* Marine Geodesy **22**, 157–167 (1999).

[102] L. R. LeBlanc and F. H. Middleton, *An underwater acoustic sound velocity data model,* The Journal of the Acoustical Society of America **67**, 2055–2062 (1980).

[103] D. B. Cousins and J. Miller, *A model based system for simultaneously estimating bathymetry and sound speed characteristics-simulation results,* in *OCEANS 2000 MTS/IEEE Conference and Exhibition*, Vol. 1 (Providence, Rhode Island, USA, 2000) pp. 213–219.

[104] D. B. Cousins and J. Miller, *A model based system for simultaneously estimating bathymetry and sound speed profile characteristics-non-isovelocity simulation results,* in *OCEANS'02 MTS/IEEE*, Vol. 2 (Biloxi, Mississippi, USA, 2002) pp. 1098–1108.

[105] B. R. Calder, B. J. Kraft, C. P. de Moustier, J. Lewis, and P. Stein, *Model based refraction correction in intermediate depth multibeam echosounder survey,* in *Proceedings of the Seventh European Conference on Underwater Acoustics (ECUA)* (Delft, The Netherlands, 2004) pp. 795–800.

[106] S. Jin, W. Sun, J. Bao, M. Liu, and Y. Cui, *Sound Velocity Profile (SVP) inversion through correcting the terrain distortion,* International Hydrographic Review **13**, 7–16 (2015).

[107] *IHO Standards for Hydrographic Surveys: Special Publication N°, 5th Ed*, Tech. Rep. (International Hydrographic Bureau, Monaco, France, 2008).

[108] *Hydrographic survey specifications and deliverables*, Tech. Rep. (National Oceanic and Atmospheric Administration, Washington, USA, Washington, District of Columbia, USA, 2018) [Accessed in March 2020].

[109] *Contract Specifications for Hydrographic Surveys, version 1.3*, Tech. Rep. (Land Information New Zealand, Wellington, Hamilton, Christchurch, New Zealand, New Zealand, 2016).

[110] R. Storn and K. Price, *Differential Evolution – A simple and efficient heuristic for global optimization over Continuous Spaces,* Journal of Global Optimization **11**, 341–359 (1997).

[111] J. Nocedal and S. J. Wright, *Numerical Optimization*, 2nd ed. (Springer-Verlag New York, 2006).

[112] C. van Moll and D. G. Simons, *Improved performance of global optimisation methods for inversion problems in underwater acoustics,* in *Proceedings of the Seventh European Conference on Underwater Acoustics (ECUA)* (Delft, The Netherlands, 2004) pp. 715–720.

[113] M. Snellen, D. G. Simons, and C. van Moll, *Application of Differential Evolution as an optimisation method for geo-acoustic inversion,* in *Proceedings of the Seventh European Conference on Underwater Acoustics (ECUA)* (Delft, The Netherlands, 2004) pp. 1–6.

[114] J. D. Beaudoin, J. E. Hughes Clarke, and J. E. Bartlett, *Retracing (and re-raytracing) Amundsen's journey through the northwest passage,* in *Proceedings of the 2004 Canadian Hydrographic Conference* (Ottawa, Canada, 2004) pp. 1–35.

[115] J. D. Beaudoin, J. E. Hughes Clarke, and J. E. Bartlett, *Application of surface sound speed measurements in post-processing for multi-sector multibeam echosounders,* International hydrographic review **5**, 17–32 (2004).

[116] M. Snellen and D. G. Simons, *An assessment of the performance of global optimization methods for geo-acoustic inversion,* Journal of Computational Acoustics **16**, 199–223 (2008).

[117] P. J. G. Teunissen, *Adjustment Theory: An Introduction*, Mathematical Geodesy and Positioning (Delft Academic Press, 2000).

[118] D. Buscombe and P. E. Grams, *Probabilistic substrate classification with multi-spectral acoustic backscatter: a comparison of discriminative and generative models,* Geosciences **8**, 395 (2018).

[119] W. K. W. Li and W. Glen Harrison, *Propagation of an atmospheric climate signal to phytoplankton in a small marine basin,* Limnology and Oceanography **53**, 1734–1745 (2008).

[120] A. Godin, *The calibration of shallow water multibeam echo-sounding systems*, M.S. thesis, Department of Geodesy and Geomatics Engineering, University of New Brunswick, Fredericton, Canada (1998).

[121] T. H. Mohammadloo, M. Snellen, and D. G. Simons, *An uncertainty assessment of the effect of using FM pulses on MBES depth measurements,* in *4th Underwater Acoustics Conference and Exhibition* (Skiathos, Greece, 2017) pp. 1043–1048.

[122] P. Johnson and K. Jerram, *E/V Nautilus EM302 Multibeam Echosounder System Review*, Tech. Rep. NA040 (Center for Coastal and Ocean Mapping/NOAA-UNH Joint Hydrographic Center, Durham, New Hampshire, USA, 2014).

[123] P. Vincent, C. Sintès, F. Maussang, X. Lurton, and R. Garello, *Doppler effect on bathymetry using frequency modulated multibeam echo sounders,* in *OCEANS 2011 IEEE* (Santander, Spain, 2011) pp. 1–5.

[124] Kongsberg Maritime, Instruction manual: EM series multibeam echo sounder, datagram formats [Accessed in March 2020].

[125] C. P. de Moustier, *State of the art in swath bathymetry survey systems,* International Hydrographic Review **65**, 25–54 (1988).

[126] J. S. Bird and G. K. Mullins, *Analysis of swath bathymetry sonar accuracy,* IEEE Journal of Oceanic Engineering **30**, 372–390 (2005).

[127] G. Llort-Pujol, *Amélioration de la résolution spatiale des sondeurs multifaisceaux,* Ph.D. thesis, Télécom Bretagne en Habilitation conjointe avec ÍUniversité de Rennes 1, Rennes, France (2007).

[128] R. O. Nielsen, *Azimuth and elevation angle estimation with a three-dimensional array,* IEEE Journal of Oceanic Engineering **19**, 84–86 (1994).

[129] R. O. Nielsen, *Accuracy of angle estimation with monopulse processing using two beams,* IEEE Transactions on Aerospace and Electronic Systems **37**, 1419–1423 (2001).

[130] C. Sintes, G. Llort-Pujol, and D. Gueriot, *Coherent probabilistic error model for interferometric sidescan sonars,* IEEE Journal of Oceanic Engineering **35**, 412–423 (2010).

[131] G. L. Jin and D. J. Tang, *Uncertainties of differential phase estimation associated with interferometric sonars,* IEEE Journal of Oceanic Engineering **21**, 53–63 (1996).

[132] W. Rihaczek, *Principles of High-Resolution Radar* (McGraw-Hill New York, 1969).

[133] L. Bruno, P. Braca, J. Horstmann, and M. Vespe, *Experimental evaluation of the Range–Doppler coupling on HF surface wave radars,* IEEE Geoscience and Remote Sensing Letters **10**, 850–854 (2013).

[134] Y. Pailhas, S. Dugelay, and C. Capus, *Impact of temporal Doppler on synthetic aperture sonar imagery,* The Journal of the Acoustical Society of America **143**, 318–329 (2018).

[135] G. Yufit and E. Maillard, *The influence of ship motion on bathymetric sonar performance in FM mode of operation,* in *OCEANS'11 MTS/IEEE KONA* (Waikoloa, Hawaii, USA, 2011) pp. 1–5.

[136] L. C. van Rijn, *Principles of Fluid Flow and Surface Waves in Rivers, Estuaries, Seas and Oceans* (Aqua Publication, 2011).

[137] J. A. Tough, D. Balcknell, and S. Quegan, *A statistical description of polarimetric and interferometric synthetic aperture radar data,* Proceedings of the Royal Society of London A: Mathematical, Physical and Engineering Sciences **449**, 567–589 (1995).

[138] D. G. Simons and M. Snellen, *A comparison between modeled and measured high frequency bottom backscattering,* The Journal of the Acoustical Society of America **123**, 3895–3895 (2008).

[139] D. D. Sternlicht and C. P. de Moustier, *Time-dependent seafloor acoustic backscatter (10–100 kHz),* The Journal of the Acoustical Society of America **114**, 2709–2725 (2003).

[140] C. P. de Moustier and H. Matsumoto, *Seafloor acoustic remote sensing with multibeam echo-sounders and bathymetric sidescan sonar systems,* Marine Geophysical Researches **15**, 27–42 (1993).

[141] Kongsberg Maritime, EM2040C MKII [Accessed in March 2020].

[142] P. J. G. Teunissen, D. G. Simons, and C. C. J. M. Tiberius, *Probability and Observation Theory: An Introduction* (Faculty of Aerospace Engineering, Delft University of Technology: Delft University. Lecture notes AE2-E01, 2006).

[143] C. P. de Moustier and D. Alexandrou, *Angular dependence of 12-kHz seafloor acoustic backscatter,* The Journal of the Acoustical Society of America **90**, 522–531 (1991).

[144] Valeport, miniSVP - sound velocity profiler [Accessed in March 2020].

[145] Kongsberg Maritime, EM technical note: filters and gains for EM 2040, EM 710, EM 302 and EM 122, [Accessed in March 2020].

[146] Kongsberg Maritime, EM technical note: advanced filters and gains for EM 2040, EM 710, EM 302 and EM 122 [Accessed in March 2020].

[147] J. E. Hughes Clarke, *The impact of acoustic imaging geometry on the fidelity of seabed bathymetric models,* Geosciences **8**, 109 (2018).

[148] T. H. Mohammadloo, M. Snellen, and D. G. Simons, *Assessing the performance of the multi-beam echo-sounder bathymetric uncertainty prediction model,* Applied Sciences **10**, 4671 (2020).

[149] T. H. Mohammadloo, M. Snellen, A. Amiri-Simkooei, and D. G. Simons, *Comparing modeled and measured bathymetric uncertainties: effect of Doppler and baseline decorrelation,* in *OCEANS 2019* (Marseille, France, 2019) pp. 1–8.

[150] T. H. Mohammadloo, M. Snellen, A. Amiri-Simkooei, and D. G. Simons, *Assessment of reliability of multi-beam echo-sounder bathymetric uncertainty prediction models,* in *5th Underwater Acoustics Conference and Exhibition* (Crete, Greece, 2019) pp. 783–790.

[151] T. Komatsu, C. Igarashi, K. Tatsukawa, S. Sultana, Y. Matsuoka, and S. Harada, *Use of multi-beam sonar to map seagrass beds in Otsuchi Bay on the Sanriku Coast of Japan,* Aquatic Living Resources **16**, 223–230 (2003).

[152] G. Di Maida, A. Tomasello, F. Luzzu, A. Scannavino, M. Pirrotta, C. Orestano, and S. Calvo, *Discriminating between Posidonia oceanica meadows and sand substratum using multibeam sonar,* ICES Journal of Marine Science **68**, 12–19 (2011).

[153] B. W. Eakins and L. A. Taylor, *Seessly integrating bathymetric and topographic data to support tsunami modeling and forecasting efforts,* in *Ocean Globe,* edited by J. Breman (Esri Press, 2010) Chap. 2, pp. 37–56.

[154] R. Hare, B. W. Eakins, C. Amante, and L. A. Taylor, *Modeling bathymetric uncertainty,* International Hydrographic Review **6**, 31–42 (2011).

[155] M. Jakobsson, B. R. Calder, and L. A. Mayer, *On the effect of random errors in gridded bathymetric compilations,* Journal of Geophysical Research: Solid Earth **107**, ETG 14–1-ETG 14–11 (2002).

[156] K. M. Marks and W. H. F. Smith, *An uncertainty model for deep ocean single beam and multibeam echo sounder data,* Marine Geophysical Researches **29**, 239–250 (2008).

[157] W. Maleika, *The influence of track configuration and multibeam echosounder parameters on the accuracy of seabed DTMs obtained in shallow water,* Earth Science Informatics **6**, 47–69 (2013).

[158] T. H. Mohammadloo, M. Snellen, D. G. Simons, B. Dierikx, and S. Bicknese, *Using alternatives to determine the shallowest depth for bathymetric charting: case study,* Journal of Surveying Engineering **145**, 05019004–1–05019004–1 (2019).

[159] E. R. Lundblad, D. J. Wright, J. Miller, E. M. Larkin, R. Rinehart, D. F. Naar, B. T. Donahue, S. M. Anderson, and T. Battista, *A benthic terrain classification scheme for American Samoa,* Marine Geodesy **29**, 89–111 (2006).

[160] M. F. J. Wilson, B. O'Connell, C. Brown, J. C. Guinan, and A. J. Grehan, *Multiscale terrain analysis of multibeam bathymetry data for habitat mapping on the continental slope,* Marine Geodesy **30**, 3–35 (2007).

[161] AML Oceanographic, SV & CTD profilers: Base X2 and Minos X, [Accessed in March 2020].

[162] T. H. Mohammadloo, M. Snellen, D. G. Simons, B. Dierikx, and S. Bicknese, *Minimum depth, mean depth or something in between?* International Hydrogaphic Review **19**, 45–53 (2018).

[163] R. Kannan, G.Latha, and M. P. Devi, *Optimum statistical gridding technique for multi beam echo sounder (MBES) data processing,* in *2015 International Symposium on Ocean Electronics (SYMPOL)* (Kochi, India, 2015) pp. 1–10.

[164] A. De Wulf, D. Constales, C. Stal, and T. Nuttens, *Accuracy aspects of processing and filtering of multibeam data: grid modeling versus TIN based modeling,* in *FIG working week 2012, Knowing to manage the territory, protect the environment, evaluate the cultural heritage* (Rome, Italy, 2012) pp. 1–15.

[165] A. De Wulf, D. Constales, T. Nuttens, and C. Stal, *Grid models versus TIN: geometric accuracy of multibeam data processing,* in *Hydro12 proceedings* (Rotterdam, The Netherlands, 2012) pp. 1–6.

[166] F. M. F. Artilheiro, *Analysis and procedures of multibeam data cleaning for bathymetric charting*, M.S. thesis, Department of Geodesy and Geomatics Engineering, University of New Brunswick, Fredericton, Canada, Fredericton, Canada (1998).

[167] W. Maleika, *The influence of the grid resolution on the accuracy of the digital terrain model used in seabed modeling,* Marine Geophysical Research **36**, 35–44 (2015).

[168] P. J. Rousseeuw and M. Hubert, *Robust statistics for outlier detection,* WIREs Data Mining and Knowledge Discovery **1**, 73–79 (2011).

[169] R. A. Maronna, R. D. Martin, and V. J. Yohai, *Robust Statistics: Theory and Methods* (John Wiley & Sons, Chichester, 2006).

[170] Norbit, Wideband multibean sonar for high resolution bathymetry [Accessed in March 2020].

[171] Kongsberg Maritime, EM 3002 Multibeam echo sounder: the new generation high performance shallow water multibeam [Accessed in March 2020].

[172] W. Maleika, M. Koziarski, and P. Forczmański, *A multiresolution grid structure applied to seafloor shape modeling,* ISPRS International Journal of Geo-Information **7**, 119–133 (2018).

[173] N. Debese, R. Moitié, and N. Seube, *Multibeam echosounder data cleaning through a hierarchic adaptive and robust local surfacing,* Computers & Geosciences **46**, 330–339 (2012).

[174] A. R. Amiri-Simkooei, M. Hosseini-Asl, and A. Safari, *Least squares 2D bi-cubic spline approximation: theory and applications,* Measurement **127**, 366–378 (2018).

[175] F. Zangeneh-Nejad, A. R. Amiri-Simkooei, M. A. Sharifi, and J. Asgari, *Cycle slip detection and repair of undifferenced single-frequency GPS carrier phase observations,* GPS Solutions **21**, 1593–1603 (2017).

[176] M. Snellen, K. Siemes, and D. G. Simons, *An efficient method for reducing the sound speed induced errors in multibeam echosounder bathymetric measurements,* in *Proceedings of the 3rd International Conference & Exhibition on Underwater Acoustic Measurements: Technologies and Results*, Vol. 3 (Nafplion, Greece, 2009) pp. 1–8.

[177] M. E. Vásquez, *Tuning the CARIS implementation of CUBE for Patagonian Waters*, M.S. thesis, Department of Geodesy and Geomatics Engineering, University of New Brunswick, Fredericton, Canada (2007).

[178] L. Biagi and L. Carcano, *Re-gridding and merging overlapping DTMS: Problems and solutions in HELI-DEM,* in *VIII Hotine-Marussi Symposium on Mathematical Geodesy* (Rome, Italy, 2015) pp. 257–262.

[179] QPS, Qimera CUBE dialogs [Accessed in March 2020].

[180] R. B. Calder and D. Wells, *CUBE user's manual: version 1.13,* University of New Hampshire, New Hampshire, USA (2007), [Accessed in February 2020].

[181] J. M. Preston, A. C. Christney, S. F. Bloomer, and I. L. Beaudet, *Seabed classification of multibeam sonar images,* in *MTS/IEEE Oceans 2001. An Ocean Odyssey*, Vol. 4 (Honolulu, Hawaii, USA, 2001) pp. 2616–2623.

Acknowledgements

critical comments on my articles are truly appreciated.

It has been a great pleasure to be a part of the ANCE group and be surrounded by great colleagues. I would like to thank my two office-mates, Anwar and Salil, for their patience, cheerful spirit, kindness and assistance with translating Dutch documents. Special thanks goes to Timo for all the fruitful and long discussion and all the five-minute questions which lasted for hours. Thanks for being a brilliant colleague, a great friend, and a critical reader. Additional thanks to Alejandro, Ana, Bieke (thanks also for your Dutch translation), Colin, Feijia, Irene, Kathrin, Leo, Mahrad and Roberto for all the fun moments and emotional support. I would like to thank our secretary, Lisette, for all the help and kindness. The ANCE group has been my home away from home and I am grateful for all the lunches we had, all the memories we made in group outings, Christmas dinners, and all the conversations we shared while enjoying our coffees.

During the last four years in the Netherlands, I have made good friends that I would like to thank. Vivian, you are indeed a true friend and an amazing person. Your sense of humor and kindness along with helpful life suggestions helped me in tough times. Farzam, we first met in one of the expat gathering events in 2016 and I am glad that I attended that one as it was the first and last time I joined. Mojdeh and Mostafa, I met you by coincidence in our apartment's elevator and since then you have become one of our closest friends.

Despite the long-distance, I value all my good friends in Tehran and Esfahan. The list is too long, but I want to particularly thank Sepideh for all her emotional support during the past 22 years. I would also like to thank Mohsen, Khashayar, Mohammad, Yassi, Iman, Helia, Bahram, Farinaz, and Moosa for your support, care and listening to me complaining about being homesick.

My kindest gratitude goes to my best friend and husband, Alireza. We had quite an adventure during the past eight years. If it were not for you, I would not be standing here today. Your unconditional love and support have always motivated me to take risks and big leaps in life. Words cannot describe how lucky I feel to have you in my life. I am looking forward to all the adventures and challenges to come in the future. I love you so much.

<div dir="rtl" align="center">سر مرا به جز این در حواله گاهی نیست   جز آستان توام در جهان پناهی نیست</div>

My boundless love and appreciation go to my parents, Maman and Baba. You have never failed to support me and the decisions I made throughout my life. Although we are kilometers apart, your selfless love has remained a constant source of endorsement and reassurance for me. Heartfelt thanks to my always cheerful and high-spirited sister Farnaz, for always cheering me up. I would also like to thank Zari joon for her emotional support and encouragement and Samin and Samar for all the jokes, laughs, memorable moments, and listening to me while calming me down when I was stressed out.

Tannaz,
Delft, May 2020

Curriculum Vitæ

Tannaz HAJI MOHAMMADLOO

12-11-1987   Born in Tehran, Iran

Education

2002–2006   Adib Farzaneh Secondary School, Tehran (2002–2005)
Bahar Elm Amoozan Secondary School, Tehran (2005–2006)

2006–2010   Bachelor of Science in Geomatics Engineering,
University of Esfahan, Esfahan, Iran

2011–2013   Master of Science in Geomatics Engineering: Geodesy,
University of Esfahan, Esfahan, Iran
Thesis: Constrained Kinematic Positioning
Promotor: Dr. J. Asgari

2016–2020   Doctor of Philosophy (Ph.D.) in Underwater Acoustics,
Delft University of Technology, Delft, The Netherlands
Thesis: Optimizing hydrographic operations for bathymet-
ric measurements using multibeam echosounders
Promotors: Prof. dr. D. G. Simons and Prof. dr. ir. M. Snellen

Awards

Leif Bjørnø   Best Student Paper in 4th Underwater Acoustics Conference
and Exhibition, Skiathos, Greece.

List of Publications

Peer-reviewed journal articles

8. **T. H. Mohammadloo**, M. Snellen, D. G. Simons, *Assessing the performance of the Multi-beam Echo-Sounder bathymetric uncertainty prediction model*, Applied Sciences **10**, 13, 4671 (2020).

7. Timo C. Gaida **T. H. Mohammadloo**, M. Snellen, D. G. Simons, *Mapping the seabed and shallow subsurface with multi-Frequency multibeam echosounders*, Remote Sensing **12**, 1, 52 (2020).

6. **T. H. Mohammadloo**, M. Snellen, W. Renoud, J. Beaudoin, D. G. Simons, *Correcting multibeam echosounder bathymetric measurements for errors induced by inaccurate water column sound speeds*, IEEE Access **144**, 7, 122052-122068 (2019).

5. **T. H. Mohammadloo**, M. Snellen, D. G. Simons, B. Dierikx, S. Bicknese *Using alternatives to determine the shallowest depth for bathymetric charting: case Study*, Journal of Surveying Engineering **145**, 4 (2019).

4. **T. H. Mohammadloo**, M. Snellen, D. G. Simons, *Multi-beam echo-sounder bathymetric measurements: implications of using frequency modulated pulses*, Journal of the Acoustical Society of America **144**(2), 842-860 (2018).

3. **T. H. Mohammadloo**, M. Snellen, D. G. Simons, B. Dierikx, S. Bicknese, *Minimum depth, mean depth or something in between?*, International Hydrogaphic Review **19**, 45-53 (2018).

2. A. R. Amiri-Simkooei, **T. H. Mohammadloo**, D. F. Argus *Multivariate analysis of GPS position time series of JPL second reprocessing campaign*, Journal of Geodesy **91**(6), 685-704.

1. J. Asgari, **T. H. Mohammadloo**, A. R. Amiri-Simkooei *Geometrically constrained kinematic global navigation satellite systems positioning: Implementation and performance*, Advances in Space Research **56**(6), 1067-1078.

Conference papers and published abstracts

6. **T. H. Mohammadloo**, M. Snellen, A. R. Amiri-Simkooei, D. G. Simons, *Assessment of reliability of multi-beam echo-sounder bathymetric uncertainty prediction models*, 5th Underwater Acoustics Conference and Exhibition, Crete, Greece, 2019.

5. **T. H. Mohammadloo**, M. Snellen, A. R. Amiri-Simkooei, D. G. Simons, *Comparing modeled and measured bathymetric uncertainties: effect of Doppler and baseline decorrelation*, OCEANS 2019, Marseille, France, 2019.

4. Timo C. Gaida **T. H. Mohammadloo**, M. Snellen, D. G. Simons, *An improved understanding of multispectral multibeam echosounders*, GeoHab Conference –Marine Geological and Biological Habitat Mapping Conference, St. Petersburg, Russia, 2019 .

3. J. Beaudoin, W. Renoud, **T. H. Mohammadloo**, M. Snellen, *Automated correction of refraction residuals*, Hydro18 Conference and Trade Exhibition, Sydney, Australia, 2018.

2. **T. H. Mohammadloo**, M. Snellen, D. G. Simons, *An uncertainty assessment of the effect of using FM pulses on MBES depth measurements*, 4th Underwater Acoustics Conference and Exhibition, Skiathos, Greece, 2017.

1. A. R. Amiri-Simkooei **T. H. Mohammadloo**, J. Asgari, *Optimal analysis of GPS position time series*, Iranian Geophysics Conference, Tehran, Iran, 2016.